The Dissertation Committee for Ju Liu
certifies that this is the approved version of the following dissertation:

Thermodynamically Consistent Modeling and Simulation of Multiphase Flows

Committee:

Thomas J.R. Hughes, Supervisor

Todd Arbogast

Omar Ghattas

Hector Gomez

Chad M. Landis

Alexis F. Vasseur

Thermodynamically Consistent Modeling and Simulation of Multiphase Flows

by

Ju Liu, B.S.; M.S.C.A.M.

DISSERTATION

Presented to the Faculty of the Graduate School of

The University of Texas at Austin

in Partial Fulfillment

of the Requirements

for the Degree of

DOCTOR OF PHILOSOPHY

THE UNIVERSITY OF TEXAS AT AUSTIN

December 2014

Dedicated to my parents.

Acknowledgments

Foremost, I want to express my greatest gratitude to my supervisor, Professor Thomas J.R. Hughes, for his guidance and inspiration. This work truly benefits from his profound insights in the broad areas of mechanics, mathematics, and scientific computing.

I would like to thank Professors Todd Arbogast, Omar Ghattas, Hector Gomez, Chad M. Landis, and Alexis F. Vasseur for serving my dissertation committee.

I am indebted to Dr. Luca Dedè and Prof. John A. Evans for teaching me the surviving skills in computational mechanics. I want to thank Prof. Mike Borden for many helpful suggestions on finite element programming. I am grateful to Dr. Shaolie Hossain and Mr. Fred Nugen for their continuing encouragement during my Ph.D. study.

I am thankful to all my friends in Austin, in particular Nick Alger, Jie Bai, Henry Chang, Mike Harmon, Ying He, Talea Mayo, Yusuke Sakamoto, Kent van Vels, Ni Wang, Wenhao Wang, Hailong Xiao, Shan Yang, Wenqi Zhao, and Hongyu Zhu.

I want to thank my parents and my girlfriend. My accomplishment is impossible without your sacrifices and love.

Thermodynamically Consistent Modeling and Simulation of Multiphase Flows

Publication No. _____

Ju Liu, Ph.D.
The University of Texas at Austin, 2014

Supervisor: Thomas J.R. Hughes

Multiphase flow is a familiar phenomenon from daily life and occupies an important role in physics, engineering, and medicine. The understanding of multiphase flows relies largely on the theory of interfaces, which is not well understood in many cases. To date, the Navier-Stokes-Korteweg equations [127, 198] and the Cahn-Hilliard equation [41] have represented two major branches of phase-field modeling. The Navier-Stokes-Korteweg equations describe a single component fluid material with multiple states of matter, e.g., water and water vapor; the Cahn-Hilliard type models describe multi-component materials with immiscible interfaces, e.g., air and water. In this dissertation, a unified multiphase fluid modeling framework is developed based on rigorous mathematical and thermodynamic principles. This framework does not assume any ad hoc modeling procedures and is capable of formulating meaningful new models with an arbitrary number of different types of interfaces.

In addition to the modeling, novel numerical technologies are developed in this dissertation focusing on the Navier-Stokes-Korteweg equations. First, the notion of entropy variables is properly generalized to the functional setting, which results in an entropy-dissipative semi-discrete formulation. Second, a family of quadrature rules is developed and applied to generate fully discrete schemes. The resulting schemes are featured with two main properties: they are provably dissipative in entropy and second-order accurate in time. In the presence of complex geometries and high-order differential terms, isogeometric analysis [108] is invoked to provide accurate representations of computational geometries and robust numerical tools. A novel periodic transformation operator technology is also developed within the isogeometric context. It significantly simplifies the procedure of the strong imposition of periodic boundary conditions. These attributes make the proposed technologies an ideal candidate for credible numerical simulation of multiphase flows.

A general-purpose parallel computing software, named `PERIGEE`, is developed in this work to provide an implementation framework for the above numerical methods. A comprehensive set of numerical examples has been studied to corroborate the aforementioned theories. Additionally, a variety of application examples have been investigated, culminating with the boiling simulation. Importantly, the boiling model overcomes several challenges for traditional boiling models, owing to its thermodynamically consistent nature. The numerical results indicate the promising potential of the proposed methodology for a wide range of multiphase flow problems.

Table of Contents

List of Tables

List of Figures

Chapter 1

Introduction

"Physics is really nothing more than a search for ultimate simplicity, but so far all we have is a kind of elegant messiness."

— William M. Bryson, 2003

1.1 Background and motivation

1.1.1 Multiphase flows and modeling

Multiphase flows are ubiquitous in the natural world, as well as in engineering practice. Researches on multiphase flows have spanned over many different disciplines, and each discipline focuses on very different aspect of the phenomena. Typical research topics include heat and mass transfer, capillarity effects, morphology, etc. Therefore, it is necessary to clarify the scope of this research before getting involved with further details.

In general, "phase" refers to a substance with a uniform and distinct chemical or physical property. The specific property that serves as an indicator is chosen based on a particular research goal. For instance, in chemistry, carbon is usually considered to have two stable phases: diamond, and graphite [35], where the crystal structure indicates the phases. In the study of ferroelectric ceramics, however, the electrical polarization is often used to identify

1

ferroelectric phases [185]. In fluid mechanics, mass fractions of chemically distinct substances are often selected to serve as an order parameter, since different substances usually have different fluid properties (like viscosity, thermal conductivity, capillarity, etc.). On the other hand, fluid density, which is related to the state of matter, is another phase indicator used to distinguish liquid and gaseous phases.

Phase transformation refers to a sharp change of the chemical or physical property due to environmental transition. Fluid phase transformations due to temperature changes are evaporation and condensation. Evaporation happens when the temperature reaches above the boiling point and the gaseous phase becomes more stable than the liquid phase; conversely, condensation is induced by dropping the temperature below the boiling point. In industrial plants, evaporation and condensation take place everyday in steam generators, heat exchangers, and various liquid-vapor pipelines. Extensive studies have been performed to improve the efficiency of heat and mass transfers in these industrial facilities. On the other side, liquid-vapor phase transformation caused by pressure variation is another widespread phenomenon. This transformation has been observed, for instance, near fast rotating ship propellers. When the propeller rotates fast enough, the local pressure near the blades will drop below the boiling pressure, and vapor bubbles will be generated near the blades. Figure 1.1 shows the cavitation of water near a ship propeller. The collapse of vapor bubbles will lead to heat and pressure emissions, which may generate noise and even damage to the blades. Till now, cavitation is still a

key factor limiting ship speed, and is thus under keen investigation by naval engineers [129].
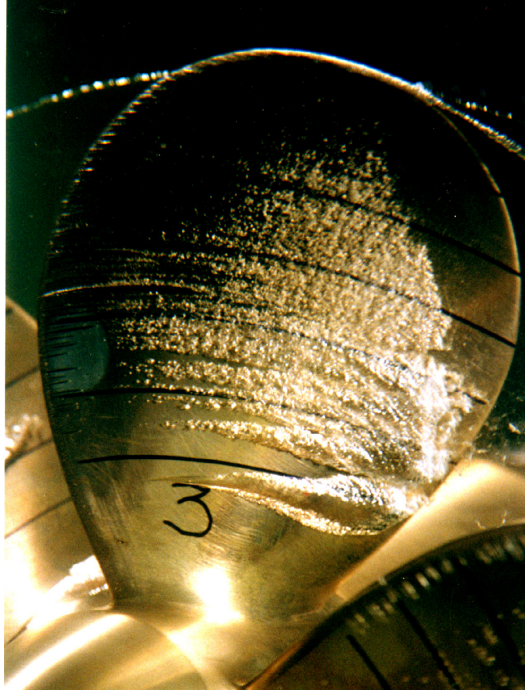
Figure 1.1: Vapor bubbles generated by cavitation near a ship propeller. Photograph used by permission of Dr. Ir. G. Kuiper [129].

Phase dynamics involving multiple substances may become even more complicated. Besides each single substance's change of the state of matter, phase separation takes place among different substances. When the temperature drops below a critical value, the attraction force between similar molecules gets stronger than between different molecules. Consequently, at macroscopic scale, a homogeneous mixture will spontaneously separate into domains rich in pure substances with finite-width interfaces. Unlike the changes of the state

of matter for a single substance, phase separations for multiple components do not allow mass transfer across the interface, and such type of interface is termed immiscible. Multiphase flows with immiscible interfaces are specifically called *multicomponent flows* in the succeeding text. In fluid mechanics, this type of phase dynamics has received special attention by petroleum engineers. In the oil production industry nowadays, water, carbon-dioxide, and air are injected into reservoirs to maintain a necessary reservoir pressure. The mixture of hydrocarbons, water, and gas has intricate interactions with each other, which makes their studies crucial for the enhancement of oil production [10, 80].

The aforementioned two types of phase dynamics are the primary research subjects in this dissertation. Many techniques have been designed to model and simulate multicomponent multiphase flows. These methods fall into the category of either the interface-tracking methods or the interface-capturing methods [167].

The interface-tracking methods keep track of the interface by aligning the computational nodes along the interface and move the mesh with the fluid flow [190]. Such methods produce very accurate descriptions of the interface, since the interface is explicitly traced by the mesh. Despite that, sophisticated re-meshing techniques are always needed, which are usually prohibitively expensive. Moreover, for problems involving severe topological changes, such as interface pinch-off and connection, ad hoc rules are necessary for mesh updating. To date, three-dimensional problems with topological transitions are still

4

notoriously difficult to solve with the interface-tracking methods.

The interface-capturing methods, on the other side, use additional unknowns to identify different phases, while the whole fluid domain is immersed in the computation mesh. With a commensurate spatial mesh size, the interface-capturing methods generally produce less accurate representations of the interface than the interface-tracking methods. In spite of that, the interface-capturing methods enjoy various advantages: they are relatively convenient to implement and efficient to compute, since there is no need to constantly update the mesh, and they are capable of handling topological transitions naturally without ad hoc procedures. The volume-of-fluid (VOF) method [105, 184] is among the early versions of the interface-capturing methods. It uses the volume fraction of one fluid component in each cell to identify different phases, and this volume fraction convects with the fluid flow. The shape of the interface can be obtained by post-processing the volume fraction field in each cell. Along with the VOF technique, a continuous model for the surface tension [31] has been developed to take capillarity into account in the interface-capturing framework. Recently, the level-set methods [161, 176] enjoy increasingly popularity in the multiphase flow community. The level-set function is a scalar function whose zero value contours the interface, and it convects with the velocity field, whose governing equations are of the Hamilton-Jacobi type. Unlike the VOF method, the level-set function's contour readily gives a sharp description of the interface and post-processing is no more needed here. Existing numerical methods for hyperbolic problems can be applied to the

level-set's governing equations straightforwardly [3, 46, 189]. Even though the level-set methods have achieved great success in multiphase modeling, they still face several challenging issues. First of all, the level-set function will be distorted when evolving with time, which necessitates ad hoc reinitialization procedures for the level-set function. Second, the level-set methods are not mass conservative, which demands the design of intricate numerical techniques to remedy this issue [122, 197].

1.1.2 Phase-field methods

Phase-field models begin with the research on fluid interfaces by van der Waals. Based on early observations made by Maxwell and Gibbs, van der Waals proposed a continuous equation of state describing the thermodynamic properties of water in both liquid and vapor phases [198]. This model could be viewed as a high-order correction of the perfect gas law by taking both short-range and long-range molecular interactions into account. One fundamental postulate of the van der Waals fluid model is that the interface has non-zero thickness, across which fluid properties are smoothly distributed. In light of that, this theory is also termed the diffuse-interface theory [5]. In contrast, traditional theories assume sharp interfaces between fluids. Namely, the bulk properties of the material are discontinuous. This assumption entails moving boundary conditions for the fluids in mathematics, which is properly avoided in the van der Waals model. Within this new theory, van der Waals successfully calculated the capillarity and estimated the liquid-vapor interface width.

This new equation of state was further validated by statistical mechanics and non-equilibrium thermodynamics [170]. In 1901, Korteweg derived an explicit form for the capillarity stress tensor [127], and henceforth the governing equations for the van der Waals fluid had been established. A non-local density gradient-squared term was introduced to model the interface energy, which in mathematics regularizes the singularity introduced by the non-convex local free energy (see Section 6.3). In modern continuum mechanics, Korteweg's model is regarded as a *grade-N* fluid model [194]. In 1985, Dunn and Serrin analyzed the continuum mechanics model from the thermodynamics perspective, and they added an "interstitial working" term to the energy equation to enforce thermodynamic consistency [69].

Parallel to the development of the van der Waals fluid model, Cahn and Hilliard developed a fourth-order parabolic equation to describe the spinodal decomposition of a two-component mixture [41, 42]. This equation could be viewed as a gradient flow problem minimizing a double-well chemical energy and a gradient-squared surface energy altogether. These two energy minimization processes correspond to the phase separation and coarsening respectively. The Cahn-Hilliard model gained its initial success in the study of metallurgy, and soon it was generalized to model ferroelectric ceramics [130], planet formation [193], microstructure evolution [48], solidification [90], and cancer growth [156, 200], to list a few.

Coupling the Cahn-Hilliard model with hydrodynamics has been continuously investigated in the past decades, and there are several works worth

mentioning. The first successful attempt should be credited to the so-called model H [106], which was developed in 1977. In 1996, Gurtin gives a continuum mechanics explanation of this model by introducing the notion of microforces [98]. This model prevails in the two-phase flow simulations [111, 141, 208] because it has a relatively simple mathematical structure. However, it must be noted that this model assumes a solenoidal velocity field, which is only true for fluid components which are incompressible and have equal densities. Practical multiphase flows are usually characterized with very high density ratios, and the density differences will inevitably lead to a non-solenoidal velocity field [117]. In 1997, Lowengrub and Truskinovsky proposed the so-called quasi-incompressible two-phase fluid model [145]. This is the first model that systematically treats unequal density cases. Later, Lowengrub and Kim proposed a multicomponent fluid flow model using a similar approach [125]. Unfortunately, there have been very limited numerical simulations based on these models heretofore.

Nowadays, the van der Waals fluid model and the Cahn-Hilliard type multicomponent fluid model have represented two major branches of phase-field multiphase fluid modeling. The van der Waals fluid model describes a single material undergoing phase transition (e.g. evaporation, condensation, cavitation, etc.); the Cahn-Hilliard model is considered well-suited for modeling a mixture of different substances [5] (e.g. water and air). Compared with other types of multiphase fluid modeling techniques, the phase-field approach enjoys several advantages: (1) It has solid theoretical foundations in thermo-

dynamics and statistical mechanics. (2) In scientific simulations, this method is capable of describing problems with severe topological changes, since these phenomena fundamentally involve "mechanisms acting on length scale commensurate with the interface width" [5]. In contrast to the previous existing techniques, artificial numerical surgery is no longer necessary.

Despite its great success in modeling physical phenomena, the phase-field methods still face great challenges in mathematics as well as in scientific computing. They are highly nonlinear; in the vanishing limit of capillarity and viscosity, the type of the equations switches between hyperbolic and mixed (hyperbolic-elliptic) according to the temperature. Due to these difficulties, the existence, uniqueness, regularity, and admissible criteria for these problems are still lacking. For real-world problems, the interfaces are usually at the length scale of a few nanometres. Hence, extremely fine meshes or sophisticated adaptivity techniques are demanded to capture these interfaces.

1.1.3 Numerical stability

Stability is among the most important notions for partial differential equations and numerical analysis. In the theory of partial differential equations, stability is directly linked to the uniqueness of solutions [74]. In numerical analysis, the role of stability for linear problems has been revealed by the Lax equivalence theorem, i.e., for a consistent scheme, stability is necessary and sufficient for convergence [132]. For nonlinear problems, the notion of stability has become more intricate. It has been realized that the concept of

linear stability is not sufficient to guarantee convergence for nonlinear problems [21]. Moreover, for nonlinear hyperbolic type equations, weak solutions are non-unique, and stability plays an additional role of singling out physically relevant solutions. The most significant example is the study of entropy stability for gas dynamics. In the pioneering works on the symmetrization of the Euler and Navier-Stokes equations [100, 109], it has been shown that the weighted residual form of the symmetrized Navier-Stokes equations will automatically satisfy the Clausius-Duhem inequality. The symmetrized form of the Navier-Stokes equations invokes a particular set of fluid variables that are referred to as entropy variables. In the late 1980s, it was proven that the weighted residual form of the symmetrized Navier-Stokes equations in conjunction with a space-time formulation constitutes a fully discrete scheme which is provably unconditionally stable-in-entropy [178]. Over the years, a significant amount of research work has been made in the study of entropy variables, and readers are referred to [110] for further references.

For phase-field models, however, the situation becomes more complicated. Under critical temperatures, phase-field problems are always endowed with a non-convex local entropy function. This non-convexity essentially precludes the possibility of directly applying the techniques developed for gas dynamics. The first reason is that the mapping between conservation variables and classical entropy variables is not invertible. Thus, the classical way of defining entropy variables does not result in a viable variable set here. Second, the space-time method is no longer guaranteed to be unconditionally

stable-in-entropy as its stability relies on one crucial fact – that the Jacobian matrix describing the mapping from conservation variables to classical entropy variables is positive definite. In the context of phase-field models, the Jacobian matrix can be singular or even negative definite within the interface region.

In Chapters 6 and 7, the two difficulties mentioned above are addressed for the isothermal Navier-Stokes-Korteweg equations and the thermal Navier-Stokes-Korteweg equations respectively. First, in the presence of a non-local surface energy term, the standard mathematical entropy function is supplemented with a regularization term. New entropy variables are defined as the functional derivatives of this new mathematical entropy functional with respect to conservation variables. A calculation will reveal that the entropy variable corresponding to density is a complicated and nonlinear function of density, velocity, temperature, and the density gradient. This non-trivial entropy variable is introduced as a new independent variable and is coupled with the conservation laws by replacing the pressure term with this new variable. In doing so, the equation associated with the entropy variable plays an analogous role to the equation of state, and the degenerate change-of-variables from conservation variables to entropy variables is avoided. The weighted residual formulation of this alternative statement of the strong problem will lead to an unconditionally entropy-dissipative weak formulation. Second, it is noteworthy that a stable time integration scheme based on a pair of new quadrature rules was developed recently by Gomez and Hughes [85]. This new temporal scheme has several appealing features: (1) the dissipation property of the semi-

discrete scheme is inherited at the fully discrete level; (2) it is second-order time accurate; (3) there is no convexity requirement for the entropy function. Hence, this time marching scheme is readily applicable to a wide class of nonlinear problems. In this work, two more pairs of special quadrature rules are developed and are invoked to construct fully discrete schemes for the Navier-Stokes-Korteweg equations. Detailed proofs of the aforesaid properties and a suite of numerical tests are performed in Chapters 6 and 7. The generalized notion of entropy variables and the quadrature-based time integration scheme are two novel numerical technologies developed in this dissertation. They should be by no means confined to the Navier-Stokes-Korteweg equations and are expected to be applicable to more general phase-field problems.

1.1.4 Isogeometric analysis

Isogeometric analysis was initially proposed to create a pathway for breaking down the barriers between Computer Aided Design (CAD) and Computer Aided Engineering (CAE) [108]. The fundamental philosophy of isogeometric analysis is to use the same basis functions that are used in CAD as the basis functions in engineering analysis within the isoparametric framework. The primary objective of this approach is to avoid the costly communication process between CAD and CAE. Indeed, in isogeometric analysis, exact geometric representation is retained at every level of discretization in contrast to traditional grid or element based numerical methods. Once the coarse but exact geometric description is generated, there is no need to communicate with

the CAD system at refinement levels in isogeometric analysis. In contrast, traditional numerical methods require constantly communications with the CAD file at each refinement level, which is not only time consuming but also error prone. Moreover, isogeometric analysis possesses the unique k-refinement technology, which enables the generation of high-order, high-continuity basis functions without a proliferation of degrees-of-freedom. This enhanced continuity of basis functions in isogeometric analysis allows direct Galerkin discretizations of high-order differential equations, which are often encountered in, for example, phase-field models [83, 86], thin shell theory [123], etc. The k-refinement concept has also been shown to exhibit superior robustness [53] and accuracy [73] in comparison with C^0 finite elements. Particularly, it has been shown that smooth basis functions may actually result in sharp oscillation-free interface descriptions in phase-field models [83].

The first instantiation of isogeometric analysis were based on Non-Uniform Rational B-Splines (NURBS), since the NURBS technology is mature and standard in the CAD community. So far, NURBS-based isogeometric analysis has been shown to be computationally superior to traditional numerical techniques. Successful applications include turbulence [16], fluid-structure interaction [17], complex fluids [86], phase-field modeling [142], structural analysis [54], shape optimization [60], and electromagnetics [34]. Although NURBS technology can underpin most engineering designs, its practicability is often severely restricted by its algebraic structure. The algebraic structure of NURBS necessitates the control points to be aligned in a topological rect-

angular structure, which demands geometrically redundant control points to maintain the topology. Additionally, this structure obviate local refinement possibility, since inserting new control points often leads to a global degrees-of-freedom proliferation. This makes NURBS technology unfavorable in analysis, especially when adaptivity is needed. T-splines were originally introduced to remedy the limitations of NURBS in geometric modeling [174]. It can create single watertight geometric models for complicated engineering designs. Soon, its analysis suitability was analyzed in [171], where the topological flexibility and local refinement capability were explored in detail. These features make T-splines a promising technology in isogeometric analysis.

Recent advancements of isogeometric analysis include the divergence-conforming B-splines [72] and the isogeometric collocation methods [169]. It has been shown that for incompressible flows, divergence-conforming B-splines generate pointwise divergence-free velocity solutions. This property further guarantees full respect of the conservation structures of the Navier-Stokes equations at discrete levels. It is anticipated such technology may be applied to compressible flow simulations as well in the hope of attaining a well-behaved discretization in the incompressible limit, which is often the bane for current compressible flow simulations. Isogeometric collocation methods have been shown to be an efficient alternate to the isogeometric Galerkin methods [169]. This attribute makes the isogeometric collocation methods potentially cost-effective for large-scale phase-field simulations [88].

1.2   Outline of this dissertation

This dissertation is outlined as follows. In Chapter 2, a unified continuum mechanics framework for multicomponent multiphase flows is developed. In Chapter 3, several classical models will be recovered and new models will be proposed within the framework. In Chapter 4, isogeometric analysis is first briefly reviewed, then the notion of periodic transformation operator technology is introduced within the isogeometric context. The software design and parallel implementation are discussed after that. In Chapter 5, a simplified two-component fluid model is derived and numerically analyzed using the isogeometric Galerkin method. In Chapters 6 and 7, provably entropy-dissipative, second-order time accurate numerical schemes are developed and analyzed for the isothermal Navier-Stokes-Korteweg equations and the thermal Navier-Stokes-Korteweg equations. Several benchmark problems are studied numerically to corroborate the properties of the proposed numerical scheme. A variety of application examples are explored, utilizing the developed numerical technologies. Finally, in Chapter 8, conclusions are drawn and future research directions are discussed.

1.3   Nomenclature

When organizing ideas from diverse disciplines, it is a great challenge to synthesize and establish coherent notational conventions. The most common notations are listed in Tables 1.1-1.4 for references, and I hope any ambiguities throughout the succeeding text may be clarified in their own context.

Table 1.1: Roman symbols

a, b	Parameters in the van der Waals fluid model
$\mathcal{B}$	Reference configuration
$\mathcal{B}_t$	Current configuration
$\mathfrak{B}$	Material modulus
$\mathbf{b}$	External body force per unit mass
B	Bernstein polynomial
$\mathcal{C}$	Time integration parameter
$\mathbb{C}$	Bézier extraction operator
C_v	Specific heat at constant volume
$\mathbf{c}$	Mass fraction vector
c_α	Mass fraction of the α-th component
$\mathcal{D}$	Dissipation
$\mathbb{D}$	Material modulus
$\mathfrak{D}_\alpha$	Material modulus
d	Spatial dimension
E	Total energy density per unit mass
$\mathcal{E}$	Lyapunov functional
$\mathcal{G}$	Gibbs region
$\mathfrak{g}_\alpha$	External microforce associated with c_α
$\mathfrak{h}$	Prescribed boundary heat flux
$\mathcal{H}$	Lyapunov functional
$\mathfrak{H}$	Mathematical entropy function
$\mathbf{I}$	Identity tensor
$\mathbb{I}$	Identity matrix
$\mathbf{L}$	Rate of strain tensor
L_0	Reference length scale
i, j, k, l	Tensor/vector component indices
$\mathfrak{l}$	External microforce associated with ρ
$\mathbf{M}_\alpha$	Mobility tensor of the α-th component
M_0	Reference mass scale
$\mathfrak{m}_\alpha$	Mass source of the α-th component

Table 1.2: Roman symbols, continued

N	Number of material components
N	B-spline basis function
n	Basis function space's dimensionality
n	Unit outward normal vector
$\mathfrak{p}, \mathfrak{q}, \mathfrak{r}$	Basis function's polynomial degree
p	Thermodynamic pressure
q	Heat flux
R	Universal gas constant
R	NURBS basis function
$\mathbb{R}$	Set of real numbers
r	Heat source per unit mass
s	Entropy density per unit mass
$\mathfrak{s}$	Shear rate
T	Cauchy stress tensor
$\mathbb{T}$	Periodic transformation operator
T_0	Reference time scale
t	Time
$\mathcal{U}$	Conservation variable vector
u	Spatial velocity field
$\mathcal{V}$	Trial solution/test function space
$\mathfrak{V}$	Entropy variable vector for the isothermal problem
v	Auxiliary variable for the isothermal problem
V	Entropy variable vector for the thermal problem
V	Auxiliary variable for the thermal problem
w_i	Test function
$\mathbf{w} = (w_2, w_3, w_4)$	Test function vector
W	Local Helmholtz free energy
W	Spin tensor
W	Weight function
$\mathbf{X} = (X_1, X_2, X_3)$	Material coordinate
$\mathbf{x} = (x_1, x_2, x_3)$	Spatial coordinate

Table 1.3: Greek symbols

α, β	Indices for material components
γ	Heat capacity ratio
γ_α	Interface parameter associated with c_α
δ	Kronecker delta
$\boldsymbol{\zeta}_\alpha$	Microstress associated with c_α
θ	Temperature
θ_0	Reference temperature scale
ι	Internal energy density per unit mass
$\boldsymbol{\kappa}$	Thermal conductivity
λ	Interface parameter associated with ρ
$\bar{\lambda}, \bar{\mu}$	Viscosity coefficients
μ_α	Chemical potential of the α-th component
ν	Electrochemical potential
Ξ	Knot vector
$\boldsymbol{\xi}$	Microstress associated with ρ
$\boldsymbol{\Pi}$	Power expenditure due to microforces and component fluxes
π	Ratio of a circle's circumference to its diameter
ϖ	Capillarity stress due to mass fraction gradients
ρ	Density
ϱ	Internal microforce associated with ρ
σ	Surface energy
$\boldsymbol{\sigma}$	Cauchy stress vector
ς	Korteweg stress
τ	Local truncation error in time
$\boldsymbol{\tau}$	Viscous shear stress
ϕ	Contact angle
φ_α	Internal microforce associated with c_α
Ψ	Helmholtz free energy density per unit mass
ψ	Helmholtz free energy density of pure materials

Table 1.4: Subscripts and supercripts

awv	Air, water, water vapor model
$ch2$	Binary Cahn-Hilliard model
$ch\mathbf{N}$	**N**-component Cahn-Hilliard model
$crit$	Critical value
loc	Local thermodynamic property
pg	Perfect gas
ref	Reference value
T	Transpose
vdw	van der Waals fluid model
$*$	Dimensionless quantity

Chapter 2

The continuum theory of multiphase flows

"If someone points out to you that your pet theory of the universe is in disagreement with Maxwell's equations – then so much the worse for Maxwell's equations. If it is found to be contradicted by observation – well, these experimentalists do bungle things sometimes. But if your theory is found to be against the second law of thermodynamics I can give you no hope; there is nothing for it but to collapse in deepest humiliation."

— Sir Arthur S. Eddington, 1915

2.1 Balance laws

My discussion is based on the fundamental hypothesis of continuum mechanics [89] and is restricted to the Euclidean space $\mathbb{R}^3$, which is described by a fixed orthonormal vector set $\mathbf{e}_i$, $i = 1, 2, 3$. The considered body occupies a continuous region $\mathcal{B} \subset \mathbb{R}^3$, which is referred to as the reference configuration. The material points in this reference configuration $\mathcal{B}$ is labeled by $\mathbf{X} = (X_1, X_2, X_3)^T$. This continuum body undergoes a motion $\mathcal{X} : \mathcal{B} \times [0, \infty) \to \mathbb{R}^3$, which maps the reference configuration $\mathcal{B}$ onto a current configuration $\mathcal{B}_t$, with the spatial position of material points $\mathbf{X}$ at time t given

by the following relation

$$\mathbf{x} = \mathcal{X}\left(\mathbf{X}, t\right).$$

(2.1)

Here $\mathbf{x} = (x_1, x_2, x_3)^T$ represents the spatial coordinates. The map $\mathcal{X}$ is postulated to be differentiable, one-to-one, and orientation preserving for each fixed $t \geq 0$. For the purpose of describing multiphase systems, I follow the idea of classical mixture theory that each spatial position is occupied by $\mathbf{N}$ different components. At the spatial position $\mathbf{x}$, each component has density $\hat{\rho}_\alpha(\mathbf{x}, t)$ at time t, and the mixture as a whole has density $\rho(\mathbf{x}, t)$. Consider an infinitesimal volume element dv containing $\mathbf{x}$ at time t, material α occupies dv_α within dv. Then the following relation holds,

$$\rho(\mathbf{x}, t)dv = \sum_{\alpha=1}^{\mathbf{N}} \hat{\rho}_\alpha(\mathbf{x}, t)dv_\alpha.$$

(2.2)

Let $\rho_\alpha(\mathbf{x}, t)$ denote

$$\rho_\alpha(\mathbf{x}, t) := \hat{\rho}_\alpha(\mathbf{x}, t)\frac{dv_\alpha}{dv},$$

(2.3)

then

$$\rho(\mathbf{x}, t) = \sum_{\alpha=1}^{\mathbf{N}} \rho_\alpha(\mathbf{x}, t).$$

(2.4)

Consequently the mass fraction for the α-th component is defined as

$$c_\alpha(\mathbf{x}, t) := \frac{\rho_\alpha(\mathbf{x}, t)}{\rho(\mathbf{x}, t)}.$$

(2.5)

Consider an arbitrary open set Ω of $\mathcal{B}$, with image at time t being $\Omega_t = \mathcal{X}(\Omega, t)$. The boundary $\partial\Omega_t$ is oriented with a unit outward normal vector $\mathbf{n}(\mathbf{x})$. In

21

the following text, it is understood that d/dt represents the material time derivative, i.e.,

$$\frac{d}{dt}(\cdot) := \frac{\partial}{\partial t}(\cdot) + \mathbf{u} \cdot \nabla(\cdot), \tag{2.6}$$

where $\mathbf{u}$ is the spatial velocity field. Then I have the following balance laws that govern the thermomechanical behavior of the considered continuum body.

- **Conservation of Mass**

$$\frac{d}{dt} \int_{\Omega_t} \rho(\mathbf{x}, t) dV_\mathbf{x} = 0. \tag{2.7}$$

- **Conservation of Components**

$$\frac{d}{dt} \int_{\Omega_t} \rho(\mathbf{x}, t) c_\alpha(\mathbf{x}, t) dV_\mathbf{x} = \int_{\partial \Omega_t} - \mathbf{h}_\alpha(\mathbf{x}, t) \cdot \mathbf{n}(\mathbf{x}) dA_\mathbf{x} + \int_{\Omega_t} \mathfrak{m}_\alpha(\mathbf{x}, t) dV_\mathbf{x},$$
$$\text{for } \alpha = 1, \cdots, \mathbf{N} - 1. \tag{2.8}$$

Here the vector function $\mathbf{h}_\alpha$ and the scalar function $\mathfrak{m}_\alpha$ represent the α-th component's mass flux and mass source.

Remark 2.1.1. *Notice that relations (2.4)-(2.5) imply that*

$$\rho(\mathbf{x}, t) = \sum_{\alpha=1}^{\mathbf{N}} \rho(\mathbf{x}, t) c_\alpha(\mathbf{x}, t). \tag{2.9}$$

Therefore, the $\mathbf{N}$-th component's mass fraction $c_\mathbf{N}$ is not independent. Conservation of mass (2.7) and conservation of the first $\mathbf{N} - 1$ components' mass

(2.8) *lead to the balance equation for $c_{\mathbf{N}}$ as*

$$\frac{d}{dt}\int_{\Omega_t}\rho(\mathbf{x},t)c_{\mathbf{N}}(\mathbf{x},t)dV_{\mathbf{x}} = \sum_{\alpha=1}^{\mathbf{N}-1}\int_{\partial\Omega_t}\mathbf{h}_\alpha(\mathbf{x},t)\cdot\mathbf{n}(\mathbf{x})dA_{\mathbf{x}}$$
$$-\sum_{\alpha=1}^{\mathbf{N}-1}\int_{\Omega_t}\mathfrak{m}_\alpha(\mathbf{x},t)dV_{\mathbf{x}}. \qquad (2.10)$$

It is viable to replace the mass conservation equation with (2.10). Then the $\mathbf{N}$ *equations of component conservation imply mass conservation (2.8) inherently (see discussion in [103]).*

- **Balance of Linear Momentum**

$$\frac{d}{dt}\int_{\Omega_t}\rho(\mathbf{x},t)\mathbf{u}(\mathbf{x},t)dV_{\mathbf{x}} = \int_{\partial\Omega_t}\boldsymbol{\sigma}(\mathbf{x},t)dA_{\mathbf{x}} + \int_{\Omega_t}\rho(\mathbf{x},t)\mathbf{b}(\mathbf{x},t)dV_{\mathbf{x}}. \qquad (2.11)$$

Here $\boldsymbol{\sigma}(\mathbf{x},t) = \mathbf{T}(\mathbf{x},t)\mathbf{n}(\mathbf{x})$, where $\mathbf{T}(\mathbf{x},t)$ is the Cauchy stress tensor.

- **Balance of Angular Momentum**

$$\frac{d}{dt}\int_{\Omega_t}\mathbf{x}\times\rho(\mathbf{x},t)\mathbf{u}(\mathbf{x},t)dV_{\mathbf{x}} = \int_{\partial\Omega_t}\mathbf{x}\times\boldsymbol{\sigma}(\mathbf{x},t)dA_{\mathbf{x}}$$
$$+\int_{\Omega_t}\mathbf{x}\times\rho(\mathbf{x},t)\mathbf{b}(\mathbf{x},t)dV_{\mathbf{x}}. \qquad (2.12)$$

Two types of phase dynamics are taken into consideration in this work. One is the phase separation and mixing of different fluid components, whose phase-field order parameters are the mass fractions c_α, $1 \leq \alpha \leq \mathbf{N}-1$. The other one is the phase transition associated with the change of the state of matter,

23

whose phase-field order parameter is the density ρ. To describe these phenomena, I make one basic postulate: there exists a set of microscopic forces that accompany the evolution of each phase-field order parameter. Indeed, Gurtin argues [94] that " fundamental physical laws involving energy should account for the working associated with each operative kinematical process [...] and it seems plausible that there should be 'microforces' whose working accompanies changes in ρ." These forces are termed microscopic because they are involved with local changes of the material, instead of macroscopic movements. The notion of microscopic forces or microforces has been successfully applied to recover or generalize the Cahn-Hilliard equation [94], plasticity of single crystals [95, 96], fracture modeling [28], gradient elasticity theories [148, 162], and ferroelectric modeling [185]. In this work, I assume that the kinematics of ρ is associated with the following forces:

$\boldsymbol{\xi}$, the microstress associated ρ,
ϱ, the internal microforce associated with ρ,
$\mathfrak{l}$, the external microforce associated with ρ.

And this set of microforces is balanced as is stated in the following equation.

- **Balance of Microforces Associated with Density**

$$\int_{\partial\Omega_t} \boldsymbol{\xi}(\mathbf{x},t) \cdot \mathbf{n}(\mathbf{x})dA_{\mathbf{x}} + \int_{\Omega_t} \varrho dV_{\mathbf{x}} + \int_{\Omega_t} \mathfrak{l}dV_{\mathbf{x}} = 0. \qquad (2.13)$$

Analogously, the kinematics of c_α is accompanied with the following forces for each $1 \leq \alpha \leq \mathbf{N} - 1$,

24

$\boldsymbol{\zeta}_\alpha$, the microstress associated with c_α,
φ_α, the internal microforce associated with c_α,
$\mathfrak{g}_\alpha$, the external microforce associated with c_α.

These forces follow the microforce balance law for each of the $\mathbf{N}-1$ components in the following sense.

- **Balance of Microforces Associated with** c_α

$$
\int_{\partial\Omega_t} \boldsymbol{\zeta}_\alpha(\mathbf{x}, t) \cdot \mathbf{n}(\mathbf{x}) dA_{\mathbf{x}} + \int_{\Omega_t} \varphi_\alpha dV_{\mathbf{x}} + \int_{\Omega_t} \mathfrak{g}_\alpha dV_{\mathbf{x}} = 0,
$$
$$
\text{for } 1 \leq \alpha \leq \mathbf{N} - 1. \tag{2.14}
$$

- **Conservation of Energy**

$$
\frac{d}{dt} \int_{\Omega_t} \rho(\mathbf{x}, t) E(\mathbf{x}, t) dV_{\mathbf{x}} := \frac{d}{dt} \int_{\Omega_t} \rho(\mathbf{x}, t) \left(\frac{1}{2} |\mathbf{u}(\mathbf{x}, t)|^2 + \iota(\mathbf{x}, t) \right) dV_{\mathbf{x}}
$$
$$
= \int_{\partial\Omega_t} \left(\mathbf{T}(\mathbf{x}, t)\mathbf{u}(\mathbf{x}, t) + \frac{d}{dt}\rho(\mathbf{x}, t)\boldsymbol{\xi}(\mathbf{x}, t) \right.
$$
$$
+ \sum_{\alpha=1}^{\mathbf{N}-1} \left(\frac{d}{dt} c_\alpha(\mathbf{x}, t)\boldsymbol{\zeta}_\alpha(\mathbf{x}, t) - \mu_\alpha(\mathbf{x}, t)\mathbf{h}_\alpha(\mathbf{x}, t) \right) - \mathbf{q}(\mathbf{x}, t) \bigg) \cdot \mathbf{n}(\mathbf{x}) dA_{\mathbf{x}}
$$
$$
+ \int_{\Omega_t} \rho(\mathbf{x}, t)\mathbf{b}(\mathbf{x}, t) \cdot \mathbf{u}(\mathbf{x}, t) + \mathfrak{l}(\mathbf{x}, t)\frac{d}{dt}\rho(\mathbf{x}, t)
$$
$$
+ \sum_{\alpha=1}^{\mathbf{N}-1} \left(\mathfrak{g}_\alpha \frac{d}{dt} c_\alpha(\mathbf{x}, t) + \mu_\alpha \mathfrak{m}_\alpha \right) + \rho(\mathbf{x}, t)r(\mathbf{x}, t) dV_{\mathbf{x}}. \tag{2.15}
$$

Here in equation (2.15), the following new notations are introduced,

$E(\mathbf{x}, t)$, the total energy density per unit mass,
$\iota(\mathbf{x}, t)$, the internal energy density per unit mass,
$\mu_\alpha(\mathbf{x}, t)$, the chemical potential of the α-th component,
$\mathbf{q}(\mathbf{x}, t)$, the heat flux,
$r(\mathbf{x}, t)$, the heat source per unit mass.

The total energy density is the sum of the kinetic energy density and the internal energy density, i.e.,

$$E(\mathbf{x}, t) = \iota(\mathbf{x}, t) + \frac{1}{2}|\mathbf{u}(\mathbf{x}, t)|^2. \tag{2.16}$$

It is noteworthy that besides the traditional working terms of macroscopic forces and macroscopic energy sources, there are non-classical terms contributing to the balance of total energy. First, there are power expenditures of the microforces [94, 96] given by

$$\int_{\partial\Omega_t} \frac{d}{dt}\rho(\mathbf{x}, t)\boldsymbol{\xi}(\mathbf{x}, t)dA_\mathbf{x}, \quad \int_{\partial\Omega_t} \frac{d}{dt}c_\alpha(\mathbf{x}, t)\boldsymbol{\zeta}_\alpha(\mathbf{x}, t)dA_\mathbf{x},$$

$$\int_{\Omega_t} \mathfrak{l}(\mathbf{x}, t)\frac{d}{dt}\rho(\mathbf{x}, t)dV_\mathbf{x}, \quad \int_{\Omega_t} \mathfrak{g}_\alpha \frac{d}{dt}c_\alpha(\mathbf{x}, t)dV_\mathbf{x}.$$

Second, there are energy fluxes due to the component fluxes and component sources,

$$\int_{\partial\Omega_t} \mu_\alpha\mathbf{h}_\alpha dA_\mathbf{x}, \quad \int_{\Omega_t} \mu_\alpha\mathfrak{m}_\alpha dV_\mathbf{x}.$$

Remark 2.1.2. *Internal microforces are not present in the working terms, see [94] for a conceptual interpretation.*

- **Second Law of Thermodynamics**

$$\int_{\Omega_t} \mathcal{D}(\mathbf{x}, t)dV_\mathbf{x} := \frac{d}{dt}\int_{\Omega_t} \rho(\mathbf{x}, t)s(\mathbf{x}, t)dV_\mathbf{x} + \int_{\partial\Omega_t} \frac{\mathbf{q}(\mathbf{x}, t) \cdot \mathbf{n}(\mathbf{x})}{\theta(\mathbf{x}, t)}dA_\mathbf{x}$$

$$- \int_{\Omega_t} \frac{\rho(\mathbf{x}, t)r(\mathbf{x}, t)}{\theta(\mathbf{x}, t)}dV_\mathbf{x} \geq 0. \tag{2.17}$$

Here $\mathcal{D}(\mathbf{x}, t)$ denotes the total dissipation, $s(\mathbf{x}, t)$ stands for the entropy density per unit mass, and $\theta(\mathbf{x}, t)$ is the absolute temperature. The above inequality is called the second law of thermodynamics, or the Clausius-Duhem inequality.

By applying the divergence and Reynolds' transport theorems, local forms of the balance equations and the Clausius-Duhem inequality can be written as (omitting the arguments $\mathbf{x}$ and t for simplicity)

$$\frac{d\rho}{dt} + \rho \nabla \cdot \mathbf{u} = 0, \tag{2.18}$$

$$\rho \frac{dc_\alpha}{dt} = -\nabla \cdot \mathbf{h}_\alpha + m_\alpha, \qquad \text{for } 1 \leq \alpha \leq \mathbf{N} - 1, \tag{2.19}$$

$$\rho \frac{d\mathbf{u}}{dt} = \nabla \cdot \mathbf{T} + \rho \mathbf{b}, \tag{2.20}$$

$$\mathbf{T} = \mathbf{T}^T, \tag{2.21}$$

$$\nabla \cdot \boldsymbol{\xi} + \varrho + \mathfrak{l} = 0, \tag{2.22}$$

$$\nabla \cdot \boldsymbol{\zeta}_\alpha + \varphi_\alpha + \mathfrak{g}_\alpha = 0, \qquad \text{for } 1 \leq \alpha \leq \mathbf{N} - 1, \tag{2.23}$$

$$\rho \frac{dE}{dt} = \rho \frac{d\iota}{dt} + \rho \mathbf{u} \cdot \frac{d\mathbf{u}}{dt} = \nabla \cdot \left(\mathbf{T}\mathbf{u} + \frac{d\rho}{dt} \boldsymbol{\xi} + \sum_{\alpha=1}^{\mathbf{N}-1} \left(\frac{dc_\alpha}{dt} \boldsymbol{\zeta}_\alpha - \mu_\alpha \mathbf{h}_\alpha \right) - \mathbf{q} \right)$$

$$+ \rho \mathbf{b} \cdot \mathbf{u} + \mathfrak{l} \frac{d\rho}{dt} + \sum_{\alpha=1}^{\mathbf{N}-1} \left(\mathfrak{g}_\alpha \frac{dc_\alpha}{dt} + \mu_\alpha \mathfrak{m}_\alpha \right) + \rho r, \tag{2.24}$$

$$\mathcal{D} := \rho \frac{ds}{dt} + \nabla \cdot \left(\frac{\mathbf{q}}{\theta} \right) - \frac{\rho r}{\theta} \geq 0. \tag{2.25}$$

In addition to the governing equations (2.18)-(2.25), a balance equation for the internal energy density ι can be readily obtained, which will play a vital role in the coming discussion. The balance of total energy can be expanded as

$$
\rho\frac{d\iota}{dt} + \rho\mathbf{u}\cdot\frac{d\mathbf{u}}{dt} = \nabla\cdot\mathbf{T}\cdot\mathbf{u} + \mathbf{T}:\nabla\mathbf{u} + \nabla\cdot\boldsymbol{\xi}\frac{d\rho}{dt} + \boldsymbol{\xi}\cdot\nabla\left(\frac{d\rho}{dt}\right)
$$
$$
+ \sum_{\alpha=1}^{\mathbf{N}-1}\left(\nabla\cdot\boldsymbol{\zeta}_\alpha\frac{dc_\alpha}{dt} + \boldsymbol{\zeta}_\alpha\cdot\nabla\left(\frac{dc_\alpha}{dt}\right) - \nabla\mu_\alpha\mathbf{h}_\alpha - \mu_\alpha\nabla\cdot\mathbf{h}_\alpha\right.
$$
$$
\left. + \mathfrak{g}_\alpha\frac{dc_\alpha}{dt} + \mu_\alpha\mathfrak{m}_\alpha\right) - \nabla\cdot\mathbf{q} + \rho\mathbf{b}\cdot\mathbf{u} + \iota\frac{d\rho}{dt} + \rho r. \tag{2.26}
$$

The linear momentum balance equations, the microforce balance equations, and the component balance equations lead to the following relations

$$
\rho\mathbf{u}\cdot\frac{d\mathbf{u}}{dt} = \nabla\cdot\mathbf{T}\cdot\mathbf{u} + \rho\mathbf{b}\cdot\mathbf{u}, \tag{2.27}
$$

$$
\nabla\cdot\boldsymbol{\xi}\frac{d\rho}{dt} + \iota\frac{d\rho}{dt} = -\varrho\frac{d\rho}{dt}, \tag{2.28}
$$

$$
\nabla\cdot\boldsymbol{\zeta}_\alpha\frac{dc_\alpha}{dt} + \mathfrak{g}_\alpha\frac{dc_\alpha}{dt} = -\varphi_\alpha\frac{dc_\alpha}{dt}, \tag{2.29}
$$

$$
-\mu_\alpha\nabla\cdot\mathbf{h}_\alpha + \mu_\alpha\mathfrak{m}_\alpha = \mu_\alpha\rho\frac{dc_\alpha}{dt}. \tag{2.30}
$$

Substituting (2.27)-(2.30) into (2.26), the balance equation for the internal energy is given by

$$
\rho\frac{d\iota}{dt} = \mathbf{T}:\nabla\mathbf{u} - \varrho\frac{d\rho}{dt} + \boldsymbol{\xi}\cdot\nabla\left(\frac{d\rho}{dt}\right) + \sum_{\alpha=1}^{\mathbf{N}-1}\left(-\varphi_\alpha\frac{dc_\alpha}{dt} + \boldsymbol{\zeta}_\alpha\cdot\nabla\left(\frac{dc_\alpha}{dt}\right)\right.
$$
$$
\left. + \rho\mu_\alpha\frac{dc_\alpha}{dt} - \nabla\mu_\alpha\cdot\mathbf{h}_\alpha\right) - \nabla\cdot\mathbf{q} + \rho r. \tag{2.31}
$$

28

2.2 Constitutive relations

2.2.1 Free energy imbalance

To describe the material behaviors, I need to provide constitutive relations for the Cauchy stress, internal energy density, entropy density, heat flux, component fluxes, and microforces. The constitutive relations have to obey restrictions imposed by classical principles. It is demanded that the objectivity and the second law of thermodynamics are satisfied identically. Before proceeding further, let me introduce the Helmholtz free energy density per unit mass $\Psi(\mathbf{x}, t)$ as

$$\Psi(\mathbf{x}, t) := \iota(\mathbf{x}, t) - \theta(\mathbf{x}, t)s(\mathbf{x}, t). \tag{2.32}$$

Taking material time derivatives at both sides of (2.32) leads to

$$\frac{d\iota}{dt} - \theta\frac{ds}{dt} = \frac{d\Psi}{dt} + s\frac{d\theta}{dt}. \tag{2.33}$$

Substituting the internal energy balance law (2.31) and the second law of thermodynamics (2.25) into the above relation, an inequality is obtained

$$\rho\frac{d\Psi}{dt} + \rho s\frac{d\theta}{dt} \leq \mathbf{T} : \nabla\mathbf{u} - \varrho\frac{d\rho}{dt} + \boldsymbol{\xi} \cdot \nabla\left(\frac{d\rho}{dt}\right) + \sum_{\alpha=1}^{\mathbf{N}-1}\left(-\varphi_\alpha\frac{dc_\alpha}{dt} + \boldsymbol{\zeta}_\alpha \cdot \nabla\left(\frac{dc_\alpha}{dt}\right)\right)$$
$$+ \rho\mu_\alpha\frac{dc_\alpha}{dt} - \nabla\mu_\alpha \cdot \mathbf{h}_\alpha\right) - \frac{\mathbf{q} \cdot \nabla\theta}{\theta}. \tag{2.34}$$

Moving $\rho s d\theta/dt$ to the right hand side, an inequality for Ψ can be obtained

$$\rho\frac{d\Psi}{dt} \leq \mathbf{T} : \nabla\mathbf{u} - \varrho\frac{d\rho}{dt} + \boldsymbol{\xi} \cdot \nabla\left(\frac{d\rho}{dt}\right) + \sum_{\alpha=1}^{\mathbf{N}-1}\left(-\varphi_\alpha\frac{dc_\alpha}{dt} + \boldsymbol{\zeta}_\alpha \cdot \nabla\left(\frac{dc_\alpha}{dt}\right)\right)$$
$$+ \rho\mu_\alpha\frac{dc_\alpha}{dt} - \nabla\mu_\alpha \cdot \mathbf{h}_\alpha\right) - \frac{\mathbf{q} \cdot \nabla\theta}{\theta} - \rho s\frac{d\theta}{dt}, \tag{2.35}$$

29

which is often referred to as the Helmholtz free energy imbalance. For pure mechanical processes when thermal effects are neglected, the Helmholtz free energy becomes the thermodynamic potential that characterizes the dissipation behavior of the isothermal mechanical system [43, 96]. As will be shown, the Helmholtz free energy imbalance plays a critical role in restricting mechanical constitutive relations as well.

2.2.2 Coleman-Noll type analysis

For convenience, let me split the stress tensor $\mathbf{T}$ and the velocity gradient tensor $\nabla \mathbf{u}$ into deviatoric and hydrostatic parts. New tensor notations are introduced in below.

1. The Cauchy stress $\mathbf{T}$ can be split into deviatoric and hydrostatic parts,

$$\mathbf{T} = \mathbf{T}^d + \mathbf{T}^h, \tag{2.36}$$

where

$$\mathbf{T}^d = \mathbf{T} - \frac{1}{3} \left(\mathrm{tr} \mathbf{T} \right) \mathbf{I}, \tag{2.37}$$

$$\mathbf{T}^h = \frac{1}{3} \left(\mathrm{tr} \mathbf{T} \right) \mathbf{I}. \tag{2.38}$$

Here $\mathbf{I}$ is the identity tensor, and tr represents the trace operator.

2. The velocity gradient tensor can also be split into three parts,

$$\nabla \mathbf{u} = \mathbf{L}^d + \mathbf{L}^h + \mathbf{W}, \tag{2.39}$$

wherein

$$\mathbf{L}^d = \frac{1}{2}\left(\nabla\mathbf{u} + \nabla\mathbf{u}^T\right) - \frac{1}{3}\nabla\cdot\mathbf{u}\mathbf{I}, \tag{2.40}$$

$$\mathbf{L}^h = \frac{1}{3}\nabla\cdot\mathbf{u}\mathbf{I}, \tag{2.41}$$

$$\mathbf{W} = \frac{1}{2}\left(\nabla\mathbf{u} - \nabla\mathbf{u}^T\right). \tag{2.42}$$

Notice that $\mathbf{L}^d$ and $\mathbf{L}^h$ are the deviatoric and hydrostatic parts of the rate of strain tensor $\mathbf{L}$; $\mathbf{W}$ is the spin tensor.

Furthermore, the following observations are made which will be helpful in the subsequent discussion.

1. From the mass balance equation (2.18), one has

$$\nabla\cdot\mathbf{u} = -\frac{d\rho/dt}{\rho}. \tag{2.43}$$

2. The gradient of material time derivatives can be expressed as

$$\nabla\left(\frac{d\rho}{dt}\right) = \frac{d}{dt}\left(\nabla\rho\right) + \nabla\mathbf{u}^T\nabla\rho = \frac{d}{dt}\left(\nabla\rho\right) + \mathbf{L}^d\nabla\rho + \mathbf{W}^T\nabla\rho$$
$$- \frac{d\rho/dt}{3\rho}\nabla\rho, \tag{2.44}$$

$$\nabla\left(\frac{dc_\alpha}{dt}\right) = \frac{d}{dt}\left(\nabla c_\alpha\right) + \nabla\mathbf{u}^T\nabla c_\alpha = \frac{d}{dt}\left(\nabla c_\alpha\right) + \mathbf{L}^d\nabla c_\alpha + \mathbf{W}^T\nabla c_\alpha$$
$$- \frac{d\rho/dt}{3\rho}\nabla c_\alpha. \tag{2.45}$$

3. The inner product of $\mathbf{T}$ and $\nabla\mathbf{u}$ can be expressed as

$$\mathbf{T}:\nabla\mathbf{u} = \mathbf{T}^d:\mathbf{L}^d + \mathbf{T}^h:\mathbf{L}^h = \mathbf{T}^d:\mathbf{L}^d + \frac{1}{3}(\mathrm{tr}\mathbf{T})\nabla\cdot\mathbf{u}. \tag{2.46}$$

31

Making use of the above observations, the free energy imbalance (2.35) can be rewritten as

$$\rho \frac{d\Psi}{dt} \leq \mathbf{T}^d : \mathbf{L}^d - \frac{\mathrm{tr}\mathbf{T}}{3\rho}\frac{d\rho}{dt} - \varrho\frac{d\rho}{dt} + \boldsymbol{\xi} \cdot \frac{d}{dt}\left(\nabla\rho\right) + \nabla\rho \cdot \mathbf{L}^d\boldsymbol{\xi} + \nabla\rho \cdot \mathbf{W}\boldsymbol{\xi}$$

$$- \frac{1}{3\rho}\nabla\rho \cdot \boldsymbol{\xi}\frac{d\rho}{dt} + \sum_{\alpha=1}^{\mathbf{N}-1}\left(-\varphi_\alpha\frac{dc_\alpha}{dt} + \boldsymbol{\zeta}_\alpha \cdot \frac{d}{dt}\left(\nabla c_\alpha\right) + \nabla c_\alpha \cdot \mathbf{L}^d\boldsymbol{\zeta}_\alpha\right.$$

$$\left. + \nabla c_\alpha\mathbf{W}\boldsymbol{\zeta}_\alpha - \frac{1}{3\rho}\boldsymbol{\zeta}_\alpha \cdot \nabla c_\alpha\frac{d\rho}{dt} - \nabla\mu_\alpha \cdot \mathbf{h}_\alpha + \rho\mu_\alpha\frac{dc_\alpha}{dt}\right)$$

$$- \frac{\mathbf{q} \cdot \nabla\theta}{\theta} - \rho s\frac{d\theta}{dt}. \tag{2.47}$$

Following the principle of equipresence [194], I demand that the Helmholtz free energy density Ψ, entropy density s, Cauchy stress $\mathbf{T}$, components' flux $\mathbf{h}_\alpha$, heat flux $\mathbf{q}$, and microforces $\boldsymbol{\xi}$, $\boldsymbol{\zeta}_\alpha$, ϱ, φ_α are functions depending on ρ, $\nabla\rho$, $d\rho/dt$, c_α, ∇c_α, dc_α/dt, θ, $\nabla\theta$, μ_α, $\nabla\mu_\alpha$, and $\nabla\mathbf{u}$. Hence, the Helmholtz free energy density can be expressed as

$$\Psi = \Psi\left(\rho, \nabla\rho, \frac{d\rho}{dt}, c_1, \cdots, c_{\mathbf{N}-1}, \nabla c_1, \cdots, \nabla c_{\mathbf{N}-1}, \frac{dc_1}{dt}, \cdots, \frac{c_{\mathbf{N}-1}}{dt},\right.$$

$$\left.\theta, \nabla\theta, \mu_1, \cdots, \mu_{\mathbf{N}-1}, \nabla\mu_1, \cdots, \nabla\mu_{\mathbf{N}-1}, \mathbf{L}^d, \mathbf{W}\right). \tag{2.48}$$

Following the approach of Coleman and Noll [51], taking material time derivative with respect to Ψ leads to

$$\frac{d\Psi}{dt} = \frac{\partial\Psi}{\partial\rho}\frac{d\rho}{dt} + \frac{\partial\Psi}{\partial(\nabla\rho)} \cdot \frac{d\left(\nabla\rho\right)}{dt} + \frac{\partial\Psi}{\partial\left(d\rho/dt\right)}\frac{d^2\rho}{dt^2} + \sum_{\alpha=1}^{\mathbf{N}-1}\left(\frac{\partial\Psi}{\partial c_\alpha}\frac{dc_\alpha}{dt}\right.$$

$$\left. + \frac{\partial\Psi}{\partial\left(\nabla c_\alpha\right)} \cdot \frac{d\left(\nabla c_\alpha\right)}{dt} + \frac{\partial\Psi}{\partial\left(dc_\alpha/dt\right)}\frac{d^2c_\alpha}{dt^2} + \frac{\partial\Psi}{\partial\mu_\alpha}\frac{d\mu_\alpha}{dt} + \frac{\partial\Psi}{\partial\left(\nabla\mu_\alpha\right)}\frac{d\left(\nabla\mu_\alpha\right)}{dt}\right)$$

$$+ \frac{\partial \Psi}{\partial \theta} \frac{d\theta}{dt} + \frac{\partial \Psi}{\partial (\nabla \theta)} \cdot \frac{d(\nabla \theta)}{dt} + \frac{\partial \Psi}{\partial \mathbf{L}^d} \frac{d\mathbf{L}^d}{dt} + \frac{\partial \Psi}{\partial \mathbf{W}} \frac{d\mathbf{W}}{dt}. \tag{2.49}$$

By substituting (2.49) into the free energy imbalance relation (2.47) and making use of the relations (2.36)-(2.45), it can be obtained that

$$
\begin{aligned}
\rho \frac{d\Psi}{dt} = & \rho \left(\frac{\partial \Psi}{\partial \rho} \frac{d\rho}{dt} + \frac{\partial \Psi}{\partial (\nabla \rho)} \cdot \frac{d(\nabla \rho)}{dt} + \frac{\partial \Psi}{\partial (d\rho/dt)} \frac{d^2 \rho}{dt^2} + \sum_{\alpha=1}^{\mathbf{N}-1} \left(\frac{\partial \Psi}{\partial c_\alpha} \frac{dc_\alpha}{dt} \right. \right. \\
& + \frac{\partial \Psi}{\partial (\nabla c_\alpha)} \cdot \frac{d(\nabla c_\alpha)}{dt} + \frac{\partial \Psi}{\partial (dc_\alpha/dt)} \frac{d^2 c_\alpha}{dt^2} + \frac{\partial \Psi}{\partial \mu_\alpha} \frac{d\mu_\alpha}{dt} \\
& \left. + \frac{\partial \Psi}{\partial (\nabla \mu_\alpha)} \frac{d(\nabla \mu_\alpha)}{dt} \right) + \frac{\partial \Psi}{\partial \theta} \frac{d\theta}{dt} + \frac{\partial \Psi}{\partial (\nabla \theta)} \frac{d(\nabla \theta)}{dt} + \frac{\partial \Psi}{\partial \mathbf{L}^d} \frac{d\mathbf{L}^d}{dt} \\
& \left. + \frac{\partial \Psi}{\partial \mathbf{W}} \frac{d\mathbf{W}}{dt} \right) \leq \mathbf{T}^d : \mathbf{L}^d - \frac{\mathrm{tr}\mathbf{T}}{3\rho} \frac{d\rho}{dt} - \varrho \frac{d\rho}{dt} + \boldsymbol{\xi} \cdot \frac{d}{dt} (\nabla \rho) + \nabla \rho \cdot \mathbf{L}^d \boldsymbol{\xi} \\
& + \nabla \rho \cdot \mathbf{W} \boldsymbol{\xi} - \frac{1}{3\rho} \nabla \rho \cdot \boldsymbol{\xi} \frac{d\rho}{dt} + \sum_{\alpha=1}^{\mathbf{N}-1} \left(-\varphi_\alpha \frac{dc_\alpha}{dt} + \boldsymbol{\zeta}_\alpha \cdot \frac{d}{dt} (\nabla c_\alpha) \right. \\
& + \nabla c_\alpha \cdot \mathbf{L}^d \boldsymbol{\zeta}_\alpha + \nabla c_\alpha \cdot \mathbf{W} \boldsymbol{\zeta}_\alpha - \frac{1}{3\rho} \boldsymbol{\zeta}_\alpha \cdot \nabla c_\alpha \frac{d\rho}{dt} - \nabla \mu_\alpha \cdot \mathbf{h}_\alpha \\
& \left. + \rho \mu_\alpha \frac{dc_\alpha}{dt} \right) - \frac{\mathbf{q} \cdot \nabla \theta}{\theta} - \rho s \frac{d\theta}{dt}. \tag{2.50}
\end{aligned}
$$

Grouping terms together results in the following inequality

$$
\begin{aligned}
& \left(\rho \frac{\partial \Psi}{\partial \rho} + \frac{\mathrm{tr}\mathbf{T}}{3\rho} + \varrho + \frac{1}{3\rho} \nabla \rho \cdot \boldsymbol{\xi} + \left(\sum_{\alpha=1}^{\mathbf{N}-1} \boldsymbol{\zeta}_\alpha \cdot \nabla c_\alpha \right) \frac{1}{3\rho} \right) \frac{d\rho}{dt} \\
& + \left(\rho \frac{\partial \Psi}{\partial (\nabla \rho)} - \boldsymbol{\xi} \right) \frac{d}{dt} (\nabla \rho) + \rho \frac{\partial \Psi}{\partial (d\rho/dt)} \frac{d^2 \rho}{dt^2} + \sum_{\alpha=1}^{\mathbf{N}-1} \left(\left(\rho \frac{\partial \Psi}{\partial c_\alpha} + \varphi_\alpha - \rho \mu_\alpha \right) \frac{dc_\alpha}{dt} \right. \\
& + \left(\rho \frac{\partial \Psi}{\partial (\nabla c_\alpha)} - \boldsymbol{\zeta}_\alpha \right) \cdot \frac{d(\nabla c_\alpha)}{dt} + \rho \frac{\partial \Psi}{\partial (dc_\alpha/dt)} \frac{d^2 c_\alpha}{dt^2} + \rho \frac{\partial \Psi}{\partial \mu_\alpha} \frac{d\mu_\alpha}{dt} \\
& \left. + \rho \frac{\partial \Psi}{\partial (\nabla \mu_\alpha)} \cdot \frac{d(\nabla \mu_\alpha)}{dt} + \nabla \mu_\alpha \cdot \mathbf{h}_\alpha \right) + \left(\rho \frac{\partial \Psi}{\partial \theta} + \rho s \right) \frac{d\theta}{dt} + \rho \frac{\partial \Psi}{\partial (\nabla \theta)} \frac{d(\nabla \theta)}{dt}
\end{aligned}
$$

$$+ \frac{\mathbf{q} \cdot \nabla \theta}{\theta} + \frac{\partial \Psi}{\partial \mathbf{L}^d} \frac{d \mathbf{L}^d}{dt} + \frac{\partial \Psi}{\partial \mathbf{W}} \frac{d \mathbf{W}}{dt} - \mathbf{L}^d : \left(\mathbf{T}^d + \nabla \rho \otimes \boldsymbol{\xi} + \sum_{\alpha=1}^{\mathbf{N}-1} \left(\nabla c_\alpha \otimes \boldsymbol{\zeta}_\alpha \right) \right)$$

$$- \mathbf{W} : \left(\nabla \rho \otimes \boldsymbol{\xi} + \sum_\alpha \left(\nabla c_\alpha \otimes \boldsymbol{\zeta}_\alpha \right) \right) \le 0. \tag{2.51}$$

Through appropriate choices of external forces and sources, arbitrary levels of the material rates of the state variables in (2.51) are attainable at a particular time. Invoking the classical Coleman-Noll argument [51], the arbitrarinesses of $d^2\rho/dt^2$, d^2c_α/dt^2, $d\mu_\alpha/dt$, $d(\nabla\mu_\alpha)/dt$, $d(\nabla\theta)/dt$, $d\mathbf{L}^d/dt$, and $d\mathbf{W}/dt$ lead to

$$\frac{\partial \Psi}{\partial \left(d\rho/dt \right)} = 0, \tag{2.52}$$

$$\frac{\partial \Psi}{\partial \left(dc_\alpha/dt \right)} = 0, \tag{2.53}$$

$$\frac{\partial \Psi}{\partial \mu_\alpha} = 0, \tag{2.54}$$

$$\frac{\partial \Psi}{\partial \left(\nabla \mu_\alpha \right)} = \mathbf{0}, \tag{2.55}$$

$$\frac{\partial \Psi}{\partial \left(\nabla \theta \right)} = \mathbf{0}, \tag{2.56}$$

$$\frac{\partial \Psi}{\partial \mathbf{L}^d} = \mathbf{0}, \tag{2.57}$$

$$\frac{\partial \Psi}{\partial \mathbf{W}} = \mathbf{0}. \tag{2.58}$$

Above relations suggest that the Helmholtz free energy density Ψ is actually independent of $d\rho/dt$, dc_α/dt, μ_α, $\nabla\mu_\alpha$, $\mathbf{L}^d$, and $\mathbf{W}$, and thus it takes a simpler form

$$\Psi = \Psi \left(\rho, \nabla\rho, c_1, \cdots, c_{N-1}, \nabla c_1, \cdots, \nabla c_{N-1}, \theta \right). \tag{2.59}$$

34

Accordingly, the relation (2.51) is simplified to

$$\left(\rho\frac{\partial\Psi}{\partial\rho} + \frac{\text{tr}\mathbf{T}}{3\rho} + \varrho + \frac{1}{3\rho}\nabla\rho\cdot\boldsymbol{\xi} + \left(\sum_{\alpha=1}^{\mathbf{N}-1}\boldsymbol{\zeta}_\alpha\cdot\nabla c_\alpha\right)\frac{1}{3\rho}\right)\frac{d\rho}{dt}$$

$$+ \left(\rho\frac{\partial\Psi}{\partial(\nabla\rho)} - \boldsymbol{\xi}\right)\frac{d}{dt}(\nabla\rho) + \sum_{\alpha=1}^{\mathbf{N}-1}\left(\left(\rho\frac{\partial\Psi}{\partial c_\alpha} + \varphi_\alpha - \rho\mu_\alpha\right)\frac{dc_\alpha}{dt}\right.$$

$$+ \left(\rho\frac{\partial\Psi}{\partial(\nabla c_\alpha)} - \boldsymbol{\zeta}_\alpha\right)\cdot\frac{d(\nabla c_\alpha)}{dt} + \nabla\mu_\alpha\cdot\mathbf{h}_\alpha\right) + \left(\rho\frac{\partial\Psi}{\partial\theta} + \rho s\right)\frac{d\theta}{dt}$$

$$+ \frac{\mathbf{q}\cdot\nabla\theta}{\theta} - \mathbf{L}^d : \left(\mathbf{T}^d + \nabla\rho\otimes\boldsymbol{\xi} + \sum_{\alpha=1}^{\mathbf{N}-1}(\nabla c_\alpha\otimes\boldsymbol{\zeta}_\alpha)\right)$$

$$- \mathbf{W} : \left(\nabla\rho\otimes\boldsymbol{\xi} + \sum_{\alpha=1}^{\mathbf{N}-1}(\nabla c_\alpha\otimes\boldsymbol{\zeta}_\alpha)\right) \leq 0. \tag{2.60}$$

The following choices are sufficient to ensure the above inequality

$$\varrho = -\frac{\text{tr}\mathbf{T}}{3\rho} - \rho\frac{\partial\Psi}{\partial\rho} - \frac{1}{3\rho}\nabla\rho\cdot\boldsymbol{\xi} - \frac{1}{3\rho}\left(\sum_{\alpha=1}^{\mathbf{N}-1}\boldsymbol{\zeta}_\alpha\cdot\nabla c_\alpha\right) - \mathfrak{B}\frac{d\rho}{dt}, \tag{2.61}$$

$$\boldsymbol{\xi} = \rho\frac{\partial\Psi}{\partial(\nabla\rho)}, \tag{2.62}$$

$$\varphi_\alpha = \rho\mu_\alpha - \rho\frac{\partial\Psi}{\partial c_\alpha} - \mathfrak{D}_\alpha\frac{dc_\alpha}{dt}, \tag{2.63}$$

$$\boldsymbol{\zeta}_\alpha = \rho\frac{\partial\Psi}{\partial(\nabla c_\alpha)}, \tag{2.64}$$

$$\mathbf{h}_\alpha = -\mathbf{M}_\alpha\nabla\mu_\alpha, \tag{2.65}$$

$$s = -\frac{\partial\Psi}{\partial\theta}, \tag{2.66}$$

$$\mathbf{q} = -\boldsymbol{\kappa}\nabla\theta, \tag{2.67}$$

$$\mathbf{T}^d = \mathbb{D}\mathbf{L}^d - \frac{1}{3}\text{tr}(\mathbb{D}\mathbf{L}^d)\mathbf{I} - \frac{1}{2}(\nabla\rho\otimes\boldsymbol{\xi} + \boldsymbol{\xi}\otimes\nabla\rho) + \frac{1}{3}\nabla\rho\cdot\boldsymbol{\xi}\mathbf{I}$$

$$- \sum_{\alpha=1}^{\mathbf{N}-1}\left(\frac{1}{2}(\nabla c_\alpha\otimes\boldsymbol{\zeta}_\alpha + \boldsymbol{\zeta}_\alpha\otimes\nabla c_\alpha) + \frac{1}{3}\nabla c_\alpha\cdot\boldsymbol{\zeta}_\alpha\mathbf{I}\right), \tag{2.68}$$

35

$$\nabla\rho\otimes\boldsymbol{\xi}+\sum_{\alpha=1}^{\mathbf{N}-1}\left(\nabla c_\alpha\otimes\boldsymbol{\zeta}_\alpha\right)=\boldsymbol{\xi}\otimes\nabla\rho+\sum_{\alpha=1}^{\mathbf{N}-1}\left(\boldsymbol{\zeta}_\alpha\otimes\nabla c_\alpha\right). \qquad (2.69)$$

In the above, $\mathfrak{B}$ and $\mathfrak{D}_\alpha$ are positive scalars, $\mathbf{M}_\alpha$ and $\boldsymbol{\kappa}$ are positive semi-definite second-order tensors, and $\mathbb{D}$ is a positive semi-definite fourth-order tensor. All of them are moduli characterizing material properties.

Remark 2.2.1. *The last requirement (2.69) disallows anisotropic materials in this model. This constraint should also come from the frame indifference argument.*

Remark 2.2.2. *The relations (2.52)-(2.58) and (2.61)-(2.69) are choices that are only sufficient to satisfy the inequality (2.60). In Chapter 3, I will show that these choices can recover a variety of classical models. However, they are by no means necessary conditions. Other choices conforming to (2.51) can be made by adding or removing terms in (2.52)-(2.58) and (2.61)-(2.69), which may generate other sophisticated constitutive relations.*

2.2.3   Constitutive relations

Based on the relations (2.61)-(2.69), constitutive relations for the multiphase fluid system are summarized as follows.

Microstresses

From the relations (2.62) and (2.64), the microstresses are defined as

$$\boldsymbol{\xi}=\rho\frac{\partial\Psi}{\partial\left(\nabla\rho\right)}, \qquad (2.70)$$

$$\boldsymbol{\zeta}_\alpha=\rho\frac{\partial\Psi}{\partial\left(\nabla c_\alpha\right)}, \qquad (2.71)$$

36

for $1 \leq \alpha \leq \mathbf{N} - 1$.

Chemical potentials and component fluxes

Due to the relations (2.63), (2.64) and the microforce balance equations (2.23), the chemical potential for the α-th component can be expressed as

$$\mu_\alpha = \frac{\partial \Psi}{\partial c_\alpha} - \frac{1}{\rho} \nabla \cdot \left(\rho \frac{\partial \Psi}{\partial (\nabla c_\alpha)} \right) - \frac{\mathfrak{g}_\alpha}{\rho} + \mathfrak{D}_\alpha \frac{dc_\alpha}{dt}, \qquad (2.72)$$

where the internal microforce φ_α is substituted by the external microforce $\mathfrak{g}_\alpha$ and microstress $\boldsymbol{\zeta}_\alpha$. Based on (2.65), the α-th component's flux is

$$\mathbf{h}_\alpha = -\mathbf{M}_\alpha \nabla \mu_\alpha. \qquad (2.73)$$

Relation (2.73) is a generalization of the Fick's law to the multicomponent system. $\mathbf{M}_\alpha$ is the mobility tensor for the α-th component.

Cauchy stress

From the relations (2.61), (2.62), (2.64), and the microforce balance equation (2.22), one has the constitutive relation for $\mathrm{tr}\mathbf{T}$ as

$$\begin{aligned}
\frac{\mathrm{tr}\mathbf{T}}{3} =& \rho \nabla \cdot \left(\rho \frac{\partial \Psi}{\partial (\nabla \rho)} \right) - \rho^2 \frac{\partial \Psi}{\partial \rho} - \frac{1}{3} \rho \frac{\partial \Psi}{\partial (\nabla \rho)} \cdot \nabla \rho \\
& - \frac{1}{3} \rho \sum_{\alpha=1}^{\mathbf{N}-1} \frac{\partial \Psi}{\partial (\nabla c_\alpha)} \cdot \nabla c_\alpha + \rho \mathfrak{l} - \mathfrak{B} \rho \frac{d\rho}{dt}.
\end{aligned} \qquad (2.74)$$

Making use of the relations (2.70) and (2.71), the deviatoric part of the

Cauchy stress can be rewritten in terms of Ψ as

$$
\begin{aligned}
\mathbf{T}^d =& \mathbb{D}\mathbf{L}^d - \frac{1}{3}tr(\mathbb{D}\mathbf{L}^d)\mathbf{I} - \frac{\rho}{2}\left(\nabla\rho \otimes \frac{\partial\Psi}{\partial\left(\nabla\rho\right)} + \frac{\partial\Psi}{\partial\left(\nabla\rho\right)} \otimes \nabla\rho\right) \\
& + \frac{\rho}{3}\nabla\rho \cdot \frac{\partial\Psi}{\partial\left(\nabla\rho\right)}\mathbf{I} - \sum_{\alpha=1}^{\mathbf{N}-1}\left(\frac{\rho}{2}\left(\nabla c_\alpha \otimes \frac{\partial\Psi}{\partial\left(\nabla c_\alpha\right)} + \frac{\partial\Psi}{\partial\left(\nabla c_\alpha\right)} \otimes \nabla c_\alpha\right)\right. \\
& \left. + \frac{\rho}{3}\nabla c_\alpha \cdot \frac{\partial\Psi}{\partial\left(\nabla c_\alpha\right)}\mathbf{I}\right).
\end{aligned}
\tag{2.75}
$$

Combining (2.74) and (2.75), the explicit form of the Cauchy stress $\mathbf{T}$ reads

$$
\begin{aligned}
\mathbf{T} =& \mathbf{T}^d + \frac{tr\mathbf{T}}{3}\mathbf{I} \\
=& \mathbb{D}\mathbf{L}^d - \frac{1}{3}tr(\mathbb{D}\mathbf{L}^d)\mathbf{I} - \frac{\rho}{2}\left(\nabla\rho \otimes \frac{\partial\Psi}{\partial\left(\nabla\rho\right)} + \frac{\partial\Psi}{\partial\left(\nabla\rho\right)} \otimes \nabla\rho\right) \\
& - \frac{\rho}{2}\sum_{\alpha=1}^{\mathbf{N}-1}\left(\nabla c_\alpha \otimes \frac{\partial\Psi}{\partial\left(\nabla c_\alpha\right)} + \frac{\partial\Psi}{\partial\left(\nabla c_\alpha\right)} \otimes \nabla c_\alpha\right) \\
& + \left(\rho\nabla \cdot \left(\rho\frac{\partial\Psi}{\partial\left(\nabla\rho\right)}\right) - \rho^2\frac{\partial\Psi}{\partial\rho} + \rho\iota + \mathfrak{B}\rho^2\nabla \cdot \mathbf{u}\right)\mathbf{I}.
\end{aligned}
\tag{2.76}
$$

Heat flux

According to (2.67), the heat flux is

$$
\mathbf{q} = -\boldsymbol{\kappa}\nabla\theta,
\tag{2.77}
$$

which coincides with the classical Fourier's law.

Entropy

Following (2.66), the entropy density is defined as

$$
s = -\frac{\partial\Psi}{\partial\theta}.
\tag{2.78}
$$

This definition agrees with the classical thermodynamics relation for the entropy density s and Helmholtz free energy density Ψ [96].

Internal Energy

According to (2.32), one has the internal energy density defined as

$$\iota = \Psi + \theta s = \Psi - \theta \frac{\partial \Psi}{\partial \theta}. \tag{2.79}$$

Notice that the microforce balance equations (2.22) (2.23) have been utilized to represent the internal microforces in the above derivation. Therefore, the microforce balance equations are inherently satisfied in the constitutive relations, and thus decoupled from the system. Also, the angular momentum balance equation (2.21) is automatically satisfied due to the form of the constitutive relation (2.76). Here, all of the constitutive relations are still represented in terms of the Helmholtz free energy density Ψ. To close the system, one needs to give an explicit form of Ψ together with the material moduli $\mathfrak{B}$, $\mathfrak{D}_\alpha$, $\mathbb{D}$, $\boldsymbol{\kappa}$, and $\mathbf{M}_\alpha$ for $1 \leq \alpha \leq \mathbf{N} - 1$.

2.2.4 A particular form of the Helmholtz free energy

There is still a relation (2.69) that does not necessarily hold true for the constitutive relations. In this section, I discuss a particular form of the Helmholtz free energy function which is general enough for constructing meaningful models and satisfies the constraint relation (2.69) intrinsically. Consider

the Helmholtz free energy taking the form

$$\Psi(\rho, \nabla\rho, c_1, \cdots, c_{\mathbf{N}-1}, \nabla c_1, \cdots, \nabla c_{\mathbf{N}-1}, \theta) = \Psi_{loc}(\rho, c_1, \cdots, c_{\mathbf{N}-1}, \theta) + \frac{\lambda}{2\rho}|\nabla\rho|^2$$

$$+ \sum_{\alpha=1}^{\mathbf{N}-1} \frac{\gamma_\alpha}{2}|\nabla c_\alpha|^2. \qquad (2.80)$$

The term Ψ_{loc} is named as the local Helmholtz free energy density, since it is a function of local thermodynamic state variables. (It is sometimes referred to as the "coarse-grain" free energy [94].) The extra gradient-squared terms are inspired by the early work on phase-field models. In the seminal work of van der Waals [198], a non-local term $\lambda|\nabla\rho|^2/2\rho$ is added to the free energy density function to model the capillarity effect. In a later work, Cahn and Hilliard [41] considered the free energy function for a two-component system using the same diffuse-interface assumption. In their work, it has been shown that terms in the form of $\tilde{\mathfrak{P}} \cdot \nabla c_1$ or $\tilde{\mathfrak{K}} : \nabla^2 c_1$, where $\tilde{\mathfrak{P}}$ is a constant vector and $\tilde{\mathfrak{K}}$ is a constant second-order tensor, cannot enter into the free energy density function Ψ, since the presence of these terms obviates the invariance of symmetry operations. Therefore, I consider the free energy density function taking the form of (2.80). In (2.80), λ and γ_α are functions of the state variables ρ, c_α, $1 \leq \alpha \leq \mathbf{N} - 1$, and θ in general, and they have dimensions such that the gradient-squared terms have energy density dimensions. In the following part of this work, λ is assumed to be a function of $c_1, \cdots, c_{\mathbf{N}-1}$ and γ_α are assumed to be constants for all α.

Remark 2.2.3. *Notice that that higher order terms such as $\tilde{\lambda}|\nabla\rho|^4/2\rho$ is consistent with Cahn and Hilliard's argument. In this work, I restrict my*

attention to the case when Ψ includes only the gradient-squared terms of ρ and c_α.

Applying the particular form of Ψ in (2.80), the microstresses can be written explicitly as

$$\boldsymbol{\xi} = \lambda \nabla \rho, \tag{2.81}$$

$$\boldsymbol{\zeta}_\alpha = \gamma_\alpha \nabla c_\alpha. \tag{2.82}$$

Simple calculations show that

$$\nabla \rho \otimes \boldsymbol{\xi} + \sum_{\alpha=1}^{\mathbf{N}-1} \left(\nabla c_\alpha \otimes \boldsymbol{\zeta}_\alpha\right) = \lambda \nabla \rho \otimes \nabla \rho + \sum_{\alpha=1}^{\mathbf{N}-1} \left(\gamma_\alpha \rho \nabla c_\alpha \otimes \nabla c_\alpha\right)$$

$$= \boldsymbol{\xi} \otimes \nabla \rho + \sum_{\alpha=1}^{\mathbf{N}-1} \left(\boldsymbol{\zeta}_\alpha \otimes \nabla c_\alpha\right). \tag{2.83}$$

Hence, the relation (2.69) is inherently satisfied for the particular form of Ψ given in (2.80). Furthermore, constitutive relations for the chemical potentials, the Cauchy stress, the entropy density and the internal energy density can be further simplified as

$$\mu_\alpha = \frac{\partial \Psi_{loc}}{\partial c_\alpha} - \frac{1}{\rho} \nabla \cdot \left(\gamma_\alpha \rho \nabla c_\alpha\right) - \frac{\mathfrak{g}_\alpha}{\rho} + \mathfrak{D}_\alpha \frac{dc_\alpha}{dt} + \frac{\partial \lambda}{\partial c_\alpha} \frac{|\nabla \rho|^2}{2\rho}, \tag{2.84}$$

$$\mathbf{T} = \mathbb{D}\mathbf{L}^d - \frac{1}{3} \mathrm{tr}\left(\mathbb{D}\mathbf{L}^d\right) \mathbf{I} - \lambda \rho \nabla \rho \otimes \nabla \rho - \rho \sum_{\alpha=1}^{\mathbf{N}-1} \left(\gamma_\alpha \nabla c_\alpha \otimes \nabla c_\alpha\right)$$

$$+ \left(\lambda \rho \Delta \rho + \frac{\lambda}{2} |\nabla \rho|^2 - \rho^2 \frac{\partial \Psi_{loc}}{\partial \rho} + \rho \mathfrak{l} + \mathfrak{B} \rho^2 \nabla \cdot \mathbf{u}\right) \mathbf{I}, \tag{2.85}$$

$$s = -\frac{\partial \Psi_{loc}}{\partial \theta}, \tag{2.86}$$

$$\iota = \Psi_{loc} - \theta \frac{\partial \Psi_{loc}}{\partial \theta} + \frac{\lambda}{2\rho} |\nabla \rho|^2 + \sum_{\alpha=1}^{\mathbf{N}-1} \frac{\gamma_\alpha}{2} |\nabla c_\alpha|^2. \tag{2.87}$$

41

For convenience, the stress tensor $\mathbf{T}$ can be split into four parts

$$\mathbf{T} = \boldsymbol{\tau} + \boldsymbol{\varpi} + \boldsymbol{\varsigma} - p\mathbf{I}, \tag{2.88}$$

wherein

$$\boldsymbol{\tau} = \mathbb{D}\mathbf{L}^d - \frac{1}{3}\mathrm{tr}\left(\mathbb{D}\mathbf{L}^d\right)\mathbf{I} + \mathfrak{B}\rho^2\nabla\cdot\mathbf{u}\mathbf{I}, \tag{2.89}$$

$$p = \rho^2\frac{\partial\Psi_{loc}}{\partial\rho}, \tag{2.90}$$

$$\boldsymbol{\varpi} = -\rho\sum_{\alpha=1}^{\mathbf{N}-1}\left(\gamma_\alpha\nabla c_\alpha\otimes\nabla c_\alpha\right), \tag{2.91}$$

$$\boldsymbol{\varsigma} = -\lambda\rho\nabla\rho\otimes\nabla\rho + \left(\lambda\rho\Delta\rho + \frac{\lambda}{2}|\nabla\rho|^2 + \rho\mathfrak{l}\right)\mathbf{I}. \tag{2.92}$$

Here $\boldsymbol{\tau}$ represents the viscous shear stress, $\boldsymbol{\varpi}$ is the capillarity stress associated with mass fractions, $\boldsymbol{\varsigma}$ is the Korteweg stress [127], and p stands for the thermodynamic pressure.

2.3   Dissipation inequalities

In this section, I analyze the dissipation properties of the model for both isolated and isothermal cases. It will be clear to see how different terms enter into the dissipative mechanisms in this theory. Let me start by considering an isolated system and analyze the dissipation $\mathcal{D}$ given in the second law of thermodynamics (2.17).

Theorem 2.3.1. *Given the constitutive relations* (2.72)-(2.77), *the dissipation*

$\mathcal{D}$ *defined in* (2.17) *takes the following form*

$$\mathcal{D} = \frac{1}{\theta} \mathbf{L}^d : \mathbb{D}\mathbf{L}^d + \frac{1}{\theta} \mathcal{B}\rho^2 (\nabla \cdot \mathbf{u})^2 + \frac{1}{\theta} \sum_{\alpha=1}^{N-1} \left(\mathfrak{D}_\alpha \left(\frac{dc_\alpha}{dt} \right)^2 + \nabla \mu_\alpha \cdot \mathbf{M}_\alpha \nabla \mu_\alpha \right)$$
$$+ \frac{1}{\theta^2} \nabla \theta \cdot \boldsymbol{\kappa} \nabla \theta. \tag{2.93}$$

Proof. Consider the internal energy balance equation (2.31)

$$\rho \frac{d\iota}{dt} = \mathbf{T} : \nabla \mathbf{u} - \varrho \frac{d\rho}{dt} + \boldsymbol{\xi} \cdot \nabla \left(\frac{d\rho}{dt} \right) + \sum_{\alpha=1}^{N-1} \left(-\varphi_\alpha \frac{dc_\alpha}{dt} + \boldsymbol{\zeta}_\alpha \cdot \nabla \left(\frac{dc_\alpha}{dt} \right) \right.$$
$$\left. + \rho \mu_\alpha \frac{dc_\alpha}{dt} - \nabla \mu_\alpha \cdot \mathbf{h}_\alpha \right) - \nabla \cdot \mathbf{q} + \rho r. \tag{2.94}$$

First, following (2.46),

$$\mathbf{T} : \nabla \mathbf{u} = \mathbf{T}^d : \mathbf{L}^d + \frac{\text{tr}\mathbf{T}}{3} \nabla \cdot \mathbf{u}. \tag{2.95}$$

Then by utilizing the constitutive relation (2.75) for $\mathbf{T}^d$, one can get

$$\mathbf{T}^d : \mathbf{L}^d = \mathbf{L}^d : \mathbb{D}\mathbf{L}^d - \frac{\rho}{2} \left(\nabla \rho \otimes \frac{\partial \Psi}{\partial (\nabla \rho)} + \frac{\partial \Psi}{\partial (\nabla \rho)} \otimes \nabla \rho \right) : \mathbf{L}^d$$
$$- \sum_{\alpha=1}^{N-1} \left(\frac{\rho}{2} \left(\nabla c_\alpha \otimes \frac{\partial \Psi}{\partial (\nabla c_\alpha)} + \frac{\partial \Psi}{\partial (\nabla c_\alpha)} \otimes \nabla c_\alpha \right) : \mathbf{L}^d \right)$$
$$= \mathbf{L}^d : \mathbb{D}\mathbf{L}^d - \frac{1}{2} (\nabla \rho \otimes \boldsymbol{\xi} + \boldsymbol{\xi} \otimes \nabla \rho) : \mathbf{L}^d$$
$$- \sum_{\alpha=1}^{N-1} \left(\frac{1}{2} (\nabla c_\alpha \otimes \boldsymbol{\zeta}_\alpha + \boldsymbol{\zeta}_\alpha \otimes \nabla c_\alpha) : \mathbf{L}^d \right). \tag{2.96}$$

Recalling previous observations (2.44)-(2.45), one has

$$\boldsymbol{\xi} \cdot \nabla \left(\frac{d\rho}{dt} \right) = \boldsymbol{\xi} \cdot \left[\frac{d}{dt} (\nabla \rho) + \mathbf{L}^d \nabla \rho + \mathbf{W}^T \nabla \rho - \frac{d\rho/dt}{3\rho} \nabla \rho \right], \tag{2.97}$$

$$\boldsymbol{\zeta}_\alpha \cdot \nabla \left(\frac{dc_\alpha}{dt} \right) = \boldsymbol{\zeta}_\alpha \cdot \left[\frac{d}{dt} (\nabla c_\alpha) + \mathbf{L}^d \nabla c_\alpha + \mathbf{W}^T \nabla c_\alpha - \frac{d\rho/dt}{3\rho} \nabla c_\alpha \right]. \tag{2.98}$$

According to the constitutive relations (2.61) and (2.63),

$$\varrho\frac{d\rho}{dt} = \frac{p}{\rho}\frac{d\rho}{dt} - \rho\frac{\partial\Psi}{\partial\rho}\frac{d\rho}{dt} - \frac{1}{3\rho}\nabla\rho\cdot\boldsymbol{\xi}\frac{d\rho}{dt}$$
$$- \frac{1}{3\rho}\frac{d\rho}{dt}\left(\sum_{\alpha=1}^{\mathbf{N-1}}\boldsymbol{\zeta}_\alpha\cdot\nabla c_\alpha\right) - \mathfrak{B}\left(\frac{d\rho}{dt}\right)^2, \qquad (2.99)$$

$$\varphi_\alpha\frac{dc_\alpha}{dt} = \rho\mu_\alpha\frac{dc_\alpha}{dt} - \rho\frac{\partial\Psi}{\partial c_\alpha}\frac{dc_\alpha}{dt} - \mathfrak{D}_\alpha\left(\frac{dc_\alpha}{dt}\right)^2. \qquad (2.100)$$

Now substituting (2.95)-(2.100) into (2.94) yields

$$\rho\frac{d\iota}{dt} = \mathbf{L}^d:\mathbb{D}\mathbf{L}^d - \frac{1}{2}\left(\nabla\rho\otimes\boldsymbol{\xi}+\boldsymbol{\xi}\otimes\nabla\rho\right):\mathbf{L}^d$$
$$- \sum_{\alpha=1}^{\mathbf{N-1}}\left(\frac{1}{2}\left(\nabla c_\alpha\otimes\boldsymbol{\zeta}_\alpha+\boldsymbol{\zeta}_\alpha\otimes\nabla c_\alpha\right):\mathbf{L}^d\right) + \frac{\mathrm{tr}\mathbf{T}}{3}\nabla\cdot\mathbf{u} + \frac{\mathrm{tr}\mathbf{T}}{3\rho}\frac{d\rho}{dt}$$
$$+ \rho\frac{\partial\Psi}{\partial\rho}\frac{d\rho}{dt} + \frac{1}{3\rho}\nabla\rho\cdot\boldsymbol{\xi}\frac{d\rho}{dt} + \frac{1}{3\rho}\frac{d\rho}{dt}\left(\sum_{\alpha=1}^{\mathbf{N-1}}\boldsymbol{\zeta}_\alpha\cdot\nabla c_\alpha\right) + \mathfrak{B}\left(\frac{d\rho}{dt}\right)^2$$
$$+ \boldsymbol{\xi}\cdot\frac{d}{dt}\left(\nabla\rho\right) + \boldsymbol{\xi}\otimes\nabla\rho:\mathbf{L}^d + \boldsymbol{\xi}\otimes\nabla\rho:\mathbf{W}^T - \frac{1}{3\rho}\frac{d\rho}{dt}\boldsymbol{\xi}\cdot\nabla\rho$$
$$+ \sum_{\alpha=1}^{\mathbf{N-1}}\left[-\rho\mu_\alpha\frac{dc_\alpha}{dt} + \rho\frac{\partial\Psi}{\partial c_\alpha}\frac{dc_\alpha}{dt} + \mathfrak{D}_\alpha\left(\frac{dc_\alpha}{dt}\right)^2 + \boldsymbol{\zeta}_\alpha\cdot\frac{d}{dt}\left(\nabla c_\alpha\right)\right.$$
$$+ \boldsymbol{\zeta}_\alpha\otimes\nabla c_\alpha:\mathbf{L}^d + \boldsymbol{\zeta}_\alpha\otimes\nabla c_\alpha:\mathbf{W}^T - \frac{1}{3\rho}\frac{d\rho}{dt}\boldsymbol{\zeta}_\alpha\cdot\nabla c_\alpha + \rho\mu_\alpha\frac{dc_\alpha}{dt}$$
$$\left. - \nabla\mu_\alpha\cdot\mathbf{h}_\alpha\right] - \nabla\cdot\mathbf{q} + \rho r. \qquad (2.101)$$

Due to the constraint relation (2.69)

$$\nabla\rho\otimes\boldsymbol{\xi} + \sum_{\alpha=1}^{\mathbf{N-1}}\left(\nabla c_\alpha\otimes\boldsymbol{\zeta}_\alpha\right) = \boldsymbol{\xi}\otimes\nabla\rho + \sum_{\alpha=1}^{\mathbf{N-1}}\left(\boldsymbol{\zeta}_\alpha\otimes\nabla c_\alpha\right), \qquad (2.102)$$

it is obvious to get

$$\boldsymbol{\xi}\otimes\nabla\rho:\mathbf{W}^T + \sum_{\alpha=1}^{\mathbf{N-1}}\left(\boldsymbol{\zeta}_\alpha\otimes\nabla c_\alpha:\mathbf{W}^T\right) = 0, \qquad (2.103)$$

44

and

$$
-\frac{1}{2}\left(\nabla\rho\otimes\boldsymbol{\xi}+\boldsymbol{\xi}\otimes\nabla\rho\right):\mathbf{L}^d-\sum_{\alpha=1}^{\mathbf{N}-1}\left(\frac{1}{2}\left(\nabla c_\alpha\otimes\boldsymbol{\zeta}_\alpha+\boldsymbol{\zeta}_\alpha\otimes\nabla c_\alpha\right):\mathbf{L}^d\right)
$$

$$
+\boldsymbol{\xi}\otimes\nabla\rho:\mathbf{L}^d+\boldsymbol{\zeta}_\alpha\otimes\nabla c_\alpha:\mathbf{L}^d+\sum_{\alpha=1}^{\mathbf{N}-1}\left(\boldsymbol{\zeta}_\alpha\otimes\nabla c_\alpha:\mathbf{L}^d\right)
$$

$$
=-\frac{1}{2}\left(\nabla\rho\otimes\boldsymbol{\xi}-\boldsymbol{\xi}\otimes\nabla\rho\right):\mathbf{L}^d-\sum_{\alpha=1}^{\mathbf{N}-1}\left(\frac{1}{2}\left(\nabla c_\alpha\otimes\boldsymbol{\zeta}_\alpha-\boldsymbol{\zeta}_\alpha\otimes\nabla c_\alpha\right):\mathbf{L}^d\right)
$$

$$
=0. \tag{2.104}
$$

Recalling the relation (2.43), it is obvious that

$$
\frac{\mathrm{tr}\mathbf{T}}{3}\nabla\cdot\mathbf{u}+\frac{\mathrm{tr}\mathbf{T}}{3\rho}\frac{d\rho}{dt}=0. \tag{2.105}
$$

Therefore, (2.101) can be rewritten as

$$
\begin{aligned}
\rho\frac{d\iota}{dt}=&\mathbf{L}^d:\mathbb{D}\mathbf{L}^d+\rho\frac{\partial\Psi}{\partial\rho}\frac{d\rho}{dt}+\mathfrak{B}\left(\frac{d\rho}{dt}\right)^2+\boldsymbol{\xi}\cdot\frac{d}{dt}\left(\nabla\rho\right)-\nabla\cdot\mathbf{q}+\rho r\\
&+\sum_{\alpha=1}^{\mathbf{N}-1}\left[\rho\frac{\partial\Psi}{\partial c_\alpha}\frac{dc_\alpha}{dt}+\mathfrak{D}_\alpha\left(\frac{dc_\alpha}{dt}\right)^2+\boldsymbol{\zeta}_\alpha\cdot\frac{d}{dt}\left(\nabla c_\alpha\right)-\nabla\mu_\alpha\cdot\mathbf{h}_\alpha\right]\\
=&\mathbf{L}^d:\mathbb{D}\mathbf{L}^d+\mathfrak{B}\left(\frac{d\rho}{dt}\right)^2+\sum_{\alpha=1}^{\mathbf{N}-1}\left[\mathfrak{D}_\alpha\left(\frac{dc_\alpha}{dt}\right)^2-\nabla\mu_\alpha\cdot\mathbf{h}_\alpha\right]-\nabla\cdot\mathbf{q}+\rho r\\
&+\rho\frac{\partial\Psi}{\partial\rho}\frac{d\rho}{dt}+\boldsymbol{\xi}\cdot\frac{d}{dt}\left(\nabla\rho\right)+\sum_{\alpha=1}^{\mathbf{N}-1}\left[\rho\frac{\partial\Psi}{\partial c_\alpha}\frac{dc_\alpha}{dt}+\boldsymbol{\zeta}_\alpha\cdot\frac{d}{dt}\left(\nabla c_\alpha\right)\right]. \tag{2.106}
\end{aligned}
$$

Making use of the constitutive relations (2.62),(2.64), and (2.65), the equation (2.106) can be rewritten as

$$
\begin{aligned}
\rho\frac{d\iota}{dt}=&\mathbf{L}^d:\mathbb{D}\mathbf{L}^d+\mathfrak{B}\left(\frac{d\rho}{dt}\right)^2+\sum_{\alpha=1}^{\mathbf{N}-1}\left[\mathfrak{D}_\alpha\left(\frac{dc_\alpha}{dt}\right)^2+\nabla\mu_\alpha\cdot\mathbf{M}_\alpha\nabla\mu_\alpha\right]\\
&-\nabla\cdot\mathbf{q}+\rho r+\rho\frac{\partial\Psi}{\partial\rho}\frac{d\rho}{dt}+\rho\frac{\partial\Psi}{\partial\left(\nabla\rho\right)}\cdot\frac{d}{dt}\left(\nabla\rho\right)
\end{aligned}
$$

45

$$+ \sum_{\alpha=1}^{\mathbf{N}-1} \left[\rho \frac{\partial \Psi}{\partial c_\alpha} \frac{dc_\alpha}{dt} + \rho \frac{\partial \Psi}{\partial (\nabla c_\alpha)} \cdot \frac{d}{dt} (\nabla c_\alpha) \right]. \tag{2.107}$$

It has been revealed that the free energy density function Ψ is a function of ρ, $\nabla \rho$, c_α, ∇c_α, and θ in (2.59). Therefore,

$$\rho \frac{\partial \Psi}{\partial \rho} \frac{d\rho}{dt} + \rho \frac{\partial \Psi}{\partial (\nabla \rho)} \cdot \frac{d}{dt} (\nabla \rho) + \sum_{\alpha=1}^{\mathbf{N}-1} \left[\rho \frac{\partial \Psi}{\partial c_\alpha} \frac{dc_\alpha}{dt} + \rho \frac{\partial \Psi}{\partial (\nabla c_\alpha)} \cdot \frac{d}{dt} (\nabla c_\alpha) \right]$$
$$= \rho \frac{d\Psi}{dt} - \rho \frac{\partial \Psi}{\partial \theta} \frac{d\theta}{dt}. \tag{2.108}$$

Consequently, one may continue simplifying the equation (2.107) as

$$\rho \frac{d\iota}{dt} = \mathbf{L}^d : \mathbb{D} \mathbf{L}^d + \mathfrak{B} \left(\frac{d\rho}{dt} \right)^2 + \sum_{\alpha=1}^{\mathbf{N}-1} \left[\mathfrak{D}_\alpha \left(\frac{dc_\alpha}{dt} \right)^2 + \nabla \mu_\alpha \cdot \mathbf{M}_\alpha \nabla \mu_\alpha \right] - \nabla \cdot \mathbf{q}$$
$$+ \rho r + \rho \frac{d\Psi}{dt} - \rho \frac{\partial \Psi}{\partial \theta} \frac{d\theta}{dt}$$
$$= \mathbf{L}^d : \mathbb{D} \mathbf{L}^d + \mathfrak{B} \left(\frac{d\rho}{dt} \right)^2 + \sum_{\alpha=1}^{\mathbf{N}-1} \left[\mathfrak{D}_\alpha \left(\frac{dc_\alpha}{dt} \right)^2 + \nabla \mu_\alpha \cdot \mathbf{M}_\alpha \nabla \mu_\alpha \right] - \nabla \cdot \mathbf{q}$$
$$+ \rho r + \rho \frac{d\Psi}{dt} + \rho s \frac{d\theta}{dt}$$
$$= \mathbf{L}^d : \mathbb{D} \mathbf{L}^d + \mathfrak{B} \left(\frac{d\rho}{dt} \right)^2 + \sum_{\alpha=1}^{\mathbf{N}-1} \left[\mathfrak{D}_\alpha \left(\frac{dc_\alpha}{dt} \right)^2 + \nabla \mu_\alpha \cdot \mathbf{M}_\alpha \nabla \mu_\alpha \right] - \nabla \cdot \mathbf{q}$$
$$+ \rho r + \rho \frac{d\iota}{dt} - \rho \theta \frac{ds}{dt}. \tag{2.109}$$

In the above equation, the second equality is due to the constitutive relation (2.66), and the third equality is due to the equation (2.33). By moving all the terms that include material time derivatives to the left hand side, it follows that

$$\rho \theta \frac{ds}{dt} = \mathbf{L}^d : \mathbb{D} \mathbf{L}^d + \mathfrak{B} \left(\frac{d\rho}{dt} \right)^2 + \sum_{\alpha=1}^{\mathbf{N}-1} \left[\mathfrak{D}_\alpha \left(\frac{dc_\alpha}{dt} \right)^2 + \nabla \mu_\alpha \cdot \mathbf{M}_\alpha \nabla \mu_\alpha \right]$$

$$- \nabla \cdot \mathbf{q} + \rho r \tag{2.110}$$

$$= \mathbf{L}^d : \mathbb{D} \mathbf{L}^d + \mathfrak{B} \rho^2 \left(\nabla \cdot \mathbf{u} \right)^2 + \sum_{\alpha=1}^{\mathbf{N}-1} \left[\mathfrak{D}_\alpha \left(\frac{dc_\alpha}{dt} \right)^2 + \nabla \mu_\alpha \cdot \mathbf{M}_\alpha \nabla \mu_\alpha \right]$$

$$- \nabla \cdot \mathbf{q} + \rho r. \tag{2.111}$$

Substituting above relation into the definition of dissipation $\mathcal{D}$ (2.25), one has

$$\mathcal{D} = \frac{1}{\theta} \mathbf{L}^d : \mathbb{D} \mathbf{L}^d + \frac{1}{\theta} \mathfrak{B} \rho^2 \left(\nabla \cdot \mathbf{u} \right)^2 + \frac{1}{\theta} \sum_{\alpha=1}^{\mathbf{N}-1} \left(\mathfrak{D}_\alpha \left(\frac{dc_\alpha}{dt} \right)^2 + \nabla \mu_\alpha \cdot \mathbf{M}_\alpha \nabla \mu_\alpha \right)$$

$$- \frac{1}{\theta^2} \nabla \theta \cdot \mathbf{q}$$

$$= \frac{1}{\theta} \mathbf{L}^d : \mathbb{D} \mathbf{L}^d + \frac{1}{\theta} \mathfrak{B} \rho^2 \left(\nabla \cdot \mathbf{u} \right)^2 + \frac{1}{\theta} \sum_{\alpha=1}^{\mathbf{N}-1} \left(\mathfrak{D}_\alpha \left(\frac{dc_\alpha}{dt} \right)^2 + \nabla \mu_\alpha \cdot \mathbf{M}_\alpha \nabla \mu_\alpha \right)$$

$$+ \frac{1}{\theta^2} \nabla \theta \cdot \boldsymbol{\kappa} \nabla \theta. \tag{2.112}$$

The last equality is obtained by invoking the constitutive relation (2.67). $\qquad \square$

Theorem 2.3.1 gives an explicit form of the dissipation $\mathcal{D}$ when adopting the constitutive relations in Section 2.2.3. To enforce the second law of thermodynamics for my model, the material moduli have to be positive semi-definite, as is summarized in the next theorem.

Theorem 2.3.2. *If the material moduli $\mathbb{D}$ is a positive semi-definite fourth-order tensor, $\mathbf{M}_\alpha$ and $\boldsymbol{\kappa}$ are positive semi-definite second-order tensors, and $\mathfrak{B} \geq 0$, $\mathfrak{D}_\alpha \geq 0$ for $1 \leq \alpha \leq \mathbf{N} - 1$, then the system of balance equations (2.18) - (2.24) satisfies the second law of thermodynamics, and the amount of dissipation is*

$$\mathcal{D} = \frac{1}{\theta} \mathbf{L}^d : \mathbb{D} \mathbf{L}^d + \frac{1}{\theta} \mathfrak{B} \rho^2 \left(\nabla \cdot \mathbf{u} \right)^2 + \frac{1}{\theta} \sum_{\alpha=1}^{\mathbf{N}-1} \left(\mathfrak{D}_\alpha \left(\frac{dc_\alpha}{dt} \right)^2 + \nabla \mu_\alpha \cdot \mathbf{M}_\alpha \nabla \mu_\alpha \right)$$

$$+ \frac{1}{\theta^2} \nabla \theta \cdot \boldsymbol{\kappa} \nabla \theta \geq 0. \tag{2.113}$$

The dissipation analysis provides a rational tool for designing models with specific dissipation amounts. Once the free energy density function is given for a specific material, the system of equations is closed with positive dissipation.

Under the isothermal condition, the entropy dissipation relation degenerates to the free energy imbalance. The Helmholtz free energy together with the kinetic energy plays an analogous role to the entropy. As will be evident in below, $\theta \mathcal{D}$ becomes the energy dissipation rate under the isothermal case. Under special boundary and external force conditions, the Helmholtz free energy $\rho \Psi$ together with the kinetic energy $\rho |\mathbf{u}|^2 / 2$ constitutes a Lyapunov function for the system.

Lemma 2.3.1. *Under the isothermal condition (i.e., θ is constant), if the system is imposed with boundary conditions $\mathbf{u} = \mathbf{0}$, $\boldsymbol{\xi} \cdot \mathbf{n} = 0$, $\boldsymbol{\zeta}_\alpha \cdot \mathbf{n} = 0$, and $\mathbf{h}_\alpha \cdot \mathbf{n} = 0$ on $\partial \Omega_t$, the following relation holds.*

$$\frac{d}{dt} \int_{\Omega_t} \rho \left(\Psi + \frac{|\mathbf{u}|^2}{2} \right) dV_{\mathbf{x}} = \int_{\Omega_t} \rho \mathbf{b} \cdot \mathbf{u} + \iota \frac{d\rho}{dt} + \sum_{\alpha=1}^{\mathbf{N}-1} \left(\mathfrak{g}_\alpha \frac{dc_\alpha}{dt} + \mu_\alpha \mathfrak{m}_\alpha \right)$$
$$- \theta \mathcal{D} dV_{\mathbf{x}}. \tag{2.114}$$

Proof. From (2.33), if θ is constant,

$$\frac{d\iota}{dt} = \frac{d\Psi}{dt} + \theta \frac{ds}{dt}. \tag{2.115}$$

48

Therefore,

$$\rho \frac{d\iota}{dt} + \rho \mathbf{u} \cdot \frac{d\mathbf{u}}{dt} - \rho\theta \frac{ds}{dt} = \rho \frac{d\Psi}{dt} + \rho \mathbf{u} \cdot \frac{d\mathbf{u}}{dt}. \tag{2.116}$$

Integrating (2.116) over Ω_t, one has the following

$$\begin{aligned}
& \frac{d}{dt} \int_{\Omega_t} \rho \left(\Psi + \frac{1}{2}|\mathbf{u}|^2 \right) dV_{\mathbf{x}} \\
=& \frac{d}{dt} \int_{\Omega_t} \rho \left(\iota + \frac{1}{2}|\mathbf{u}|^2 - \theta s \right) dV_{\mathbf{x}} \\
=& \int_{\partial\Omega_t} \left(\mathbf{Tu} + \frac{d}{dt}\rho\boldsymbol{\xi} + \sum_{\alpha=1}^{\mathbf{N}-1} \left(\frac{d}{dt} c_\alpha \boldsymbol{\zeta}_\alpha - \mu_\alpha \mathbf{h}_\alpha \right) \right) \cdot \mathbf{n} dA_{\mathbf{x}} \\
& + \int_{\Omega_t} \rho \mathbf{b} \cdot \mathbf{u} + \iota \frac{d}{dt}\rho + \sum_{\alpha=1}^{\mathbf{N}-1} \left(\mathfrak{g}_\alpha \frac{d}{dt} c_\alpha + \mu_\alpha \mathfrak{m}_\alpha \right) - \theta \mathcal{D} dV_{\mathbf{x}}. \tag{2.117}
\end{aligned}$$

Boundary integral terms are cancelled due to the given boundary conditions, and hence one has

$$\begin{aligned}
\frac{d}{dt} \int_{\Omega_t} \rho \left(\Psi + \frac{|\mathbf{u}|^2}{2} \right) dV_{\mathbf{x}} = \int_{\Omega_t} \rho \mathbf{b} \cdot \mathbf{u} + \iota \frac{d\rho}{dt} + \sum_{\alpha=1}^{\mathbf{N}-1} \left(\mathfrak{g}_\alpha \frac{dc_\alpha}{dt} + \mu_\alpha \mathfrak{m}_\alpha \right) \\
- \theta \mathcal{D} dV_{\mathbf{x}}, \tag{2.118}
\end{aligned}$$

which completes the proof of the lemma. $\qquad\square$

Theorem 2.3.3. *If (1) the system undergoes an isothermal process, (2) boundary conditions* $\mathbf{u} = \mathbf{0}$, $\boldsymbol{\xi} \cdot \mathbf{n} = 0$, $\boldsymbol{\zeta}_\alpha \cdot \mathbf{n} = 0$, *and* $\mathbf{h}_\alpha \cdot \mathbf{n} = 0$ *are held on* $\partial\Omega_t$, *(3) the forces* $\mathbf{b}$, ι, $\mathfrak{g}_\alpha$, *and component sources* $\mathfrak{m}_\alpha$ *are all negligible, and (4) the material moduli* $\mathbb{D}$, $\mathfrak{B}$, $\mathfrak{D}_\alpha$, $1 \leq \alpha \leq \mathbf{N} - 1$, $\boldsymbol{\kappa}$ *are positive semi-definite, the following dissipation relation gives the Lyapunov function for system.*

$$\frac{d}{dt} \int_{\Omega_t} \rho \left(\Psi + \frac{|\mathbf{u}|^2}{2} \right) dV_{\mathbf{x}} = - \int_{\Omega_t} \theta \mathcal{D} dV_{\mathbf{x}} \leq 0. \tag{2.119}$$

49

The proof of Theorem 2.3.3 follows straightforwardly from Lemma 2.3.1.

Remark 2.3.1. *The relations (2.114) and (2.119) plays a fundamental role in analysing nonlinear stability of isothermal systems. It should be noted that the dissipation relation (2.119) is weaker than the second law of thermodynamics (2.25), since it is in an integral form and requires proper boundary conditions.*

Remark 2.3.2. *As will be shown in Chapter 3, the assumptions made in Theorem 2.3.3 are common. For example, internal microforces l, g_α, and component sources m_α are neglected in most existing models; $\boldsymbol{\xi} \cdot \mathbf{n} = 0$ is equivalent to the contact-angle boundary condition $\nabla \rho \cdot \mathbf{n} = 0$ in the van der Waals fluid model; $\boldsymbol{\zeta}_\alpha \cdot \mathbf{n} = 0$ and $\mathbf{h}_\alpha \cdot \mathbf{n} = 0$ are widely used in the analysis of the Cahn-Hilliard type phase-field models.*

2.4   Governing equations in conservation variables

In Section 2.1, I have given the governing equations using the material time derivatives (see (2.18)-(2.25)). However, the Lagrangian description is not the most suitable way for representing governing equations in fluid mechanics. In this section, let me give the governing equations in terms of conservation variables. Recalling that the microforce balance equations (2.22)-(2.23) and the angular momentum balance equations (2.21) are already decoupled due to the choices of the constitutive relations. The system now consists of the mass balance equation (2.18), the component balance equations (2.19) ($\mathbf{N} - 1$ equations), the linear momentum balance equations (2.20), and the energy

balance equation (2.24). The conservation variables are denoted as

$$\mathcal{U}^T := \rho \left[1; c_1; \cdots, c_{\mathbf{N}-1}; \mathbf{u}; E \right]. \tag{2.120}$$

And the governing equations can be written in terms of the conservation variables as follows.

$$\frac{\partial \rho}{\partial t} + \nabla \cdot (\rho \mathbf{u}) = 0, \tag{2.121}$$

$$\frac{\partial (\rho c_\alpha)}{\partial t} + \nabla \cdot (\rho c_\alpha \mathbf{u}) = -\nabla \cdot \mathbf{h}_\alpha + \mathfrak{m}_\alpha, \qquad \text{for } 1 \leq \alpha \leq \mathbf{N} - 1, \tag{2.122}$$

$$\frac{\partial (\rho \mathbf{u})}{\partial t} + \nabla \cdot (\rho \mathbf{u} \otimes \mathbf{u} + p\mathbf{I}) = \nabla \cdot \boldsymbol{\tau} + \nabla \cdot \boldsymbol{\varpi} + \nabla \cdot \boldsymbol{\varsigma} + \rho \mathbf{b}, \tag{2.123}$$

$$\frac{\partial (\rho E)}{\partial t} + \nabla \cdot ((\rho E + p)\mathbf{u}) = \nabla \cdot \left((\boldsymbol{\tau} + \boldsymbol{\varpi} + \boldsymbol{\varsigma}) \mathbf{u} - \rho \nabla \cdot \mathbf{u} \boldsymbol{\xi} \right.$$

$$+ \sum_{\alpha=1}^{\mathbf{N}-1} \left(\frac{1}{\rho} \left(\mathfrak{m}_\alpha - \nabla \cdot \mathbf{h}_\alpha \right) \boldsymbol{\zeta}_\alpha - \mu_\alpha \mathbf{h}_\alpha \right) - \mathbf{q} \right)$$

$$+ \rho \mathbf{b} \cdot \mathbf{u} + \sum_{\alpha=1}^{\mathbf{N}-1} \mu_\alpha \mathfrak{m}_\alpha + \rho r. \tag{2.124}$$

Chapter 3

Examples of closed systems of equations

A unified continuum mechanics framework for multiphase flow problems has been established in Chapter 2. In this framework, the constitutive relations are expressed in terms of the Helmholtz free energy density. Thus, the modeling work is reduced to the design of a proper formulation of the Helmholtz free energy density function. This design procedure is primarily based on thermodynamic considerations. In this chapter, I recover several meaningful fluid models and propose a novel multicomponent multiphase fluid model with the objective of describing the air, water, water vapor fluid flow. In particular, I analyze thermodynamic properties, construct governing equations, and provide basic mathematical preliminaries for these models. Before proceeding further, the following assumptions are made throughout this chapter:

$$\mathfrak{l} = 0, \tag{3.1}$$

$$\mathfrak{g}_\alpha = 0, \tag{3.2}$$

$$\mathfrak{m}_\alpha = 0, \tag{3.3}$$

$$\mathfrak{D}_\alpha = 0, \tag{3.4}$$

$$\mathbb{D}_{ijkl} = 2\bar{\mu}\delta_{ik}\delta_{jl}, \tag{3.5}$$

$$\mathfrak{B} = \left(\bar{\lambda} + \frac{2}{3}\bar{\mu}\right)\frac{1}{\rho^2}, \tag{3.6}$$

for $\alpha = 1, \cdots, N-1$. Here, $\bar{\mu}$ and $\bar{\lambda}$ are the first and second viscosity coefficients. The last two relations imply an explicit form for the viscous shear stress

$$\boldsymbol{\tau} = \bar{\mu}\left(\nabla\mathbf{u} + \nabla\mathbf{u}^T\right) + \bar{\lambda}\nabla \cdot \mathbf{u}\mathbf{I}. \tag{3.7}$$

3.1 The perfect gas model

I start with the perfect gas model to show that the continuum mechanics framework developed in Chapter 2 incorporates the most classical compressible fluid model, which in turn justifies the modeling approach. Also, the perfect gas model is a good point of departure for discussing sophisticated multiphase fluid models.

The perfect gas law (or the ideal gas law) is a widely used equation of state in aerodynamics studies [7, 44, 126, 178]. It gives a rather accurate approximation of most gases at room temperature and atmospheric pressure. Fundamental postulates of the prefect gas model are that the collisions between molecules are elastic and the intermolecular forces are all negligible at the microscopic level [170]. If the temperature increases beyond a critical value, chemical reactions or even ionization may occur and complex models are needed in these scenarios [6]. On the other hand, under high pressure con-

ditions, intermolecular forces are pronounced, and a new model taking these forces into account will be addressed in Section 3.2. Now let me introduce the perfect gas model by giving its Helmholtz free energy density function

$$\Psi^{pg} = R\theta \log(\rho) - C_v^{pg}\theta \log\left(\frac{\theta}{\theta_{ref}^{pg}}\right) + C_v^{pg}\theta. \tag{3.8}$$

Here R is the universal gas constant, C_v^{pg} is the specific heat at constant volume, and θ_{ref}^{pg} is the reference value of temperature. Since only one component is involved here (i.e., $\mathbf{N} = 1$), the component balance equation is decoupled from the system. The remaining constitutive relations are

$$\boldsymbol{\xi}^{pg} = \mathbf{0}, \tag{3.9}$$

$$\mathbf{T}^{pg} = \boldsymbol{\tau}^{pg} - p^{pg}\mathbf{I}, \tag{3.10}$$

$$\boldsymbol{\tau}^{pg} = \bar{\mu}^{pg}\left(\nabla\mathbf{u} + \nabla\mathbf{u}^T\right) + \bar{\lambda}^{pg}\nabla \cdot \mathbf{u}\mathbf{I}, \tag{3.11}$$

$$p^{pg} = R\rho\theta, \tag{3.12}$$

$$\mathbf{q}^{pg} = -\boldsymbol{\kappa}^{pg}\nabla\theta, \tag{3.13}$$

$$s^{pg} = C_v^{pg}\log\left(\frac{\theta}{\theta_{ref}^{pg}}\right) - R\log(\rho). \tag{3.14}$$

The governing equations can be written as follows.

$$\frac{\partial\rho}{\partial t} + \nabla \cdot (\rho\mathbf{u}) = 0, \tag{3.15}$$

$$\frac{\partial(\rho\mathbf{u})}{\partial t} + \nabla \cdot (\rho\mathbf{u} \otimes \mathbf{u} + p^{pg}\mathbf{I}) = \nabla \cdot \boldsymbol{\tau}^{pg} + \rho\mathbf{b}, \tag{3.16}$$

$$\frac{\partial(\rho E)}{\partial t} + \nabla \cdot (\rho E\mathbf{u} + p^{pg}\mathbf{u}) = \nabla \cdot \left(\boldsymbol{\tau}^{pg}\mathbf{u} - \mathbf{q}^{pg}\right) + \rho\mathbf{b} \cdot \mathbf{u} + \rho r. \tag{3.17}$$
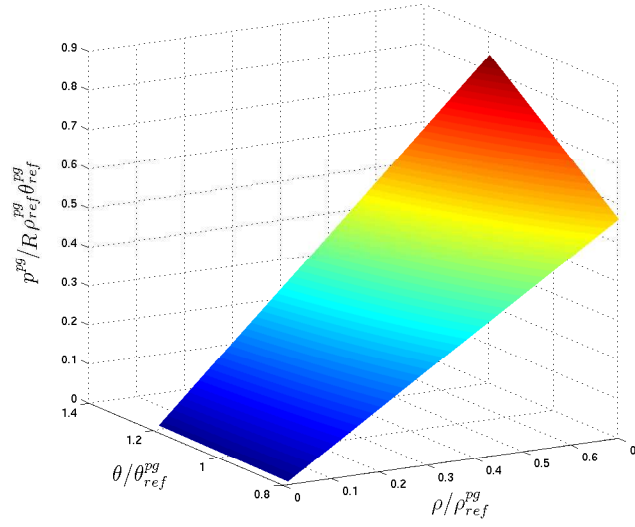
(a)
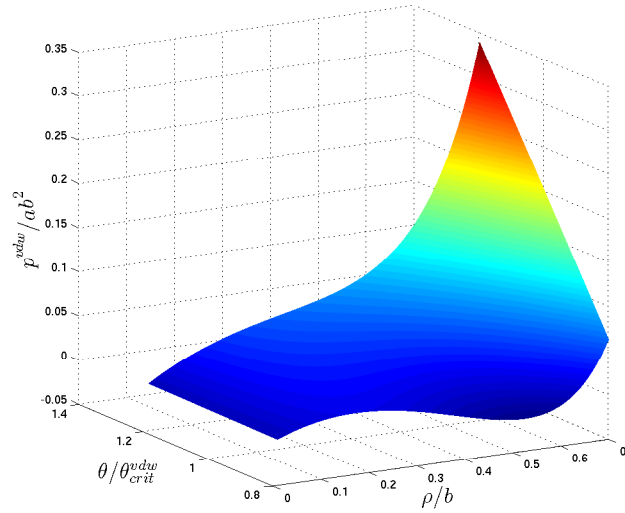
(b)

Figure 3.1: Thermodynamic pressure $p(\rho, \theta)$ as a function of ρ and θ: (a) the perfect gas thermodynamic pressure (3.12), (b) the van der Waals thermodynamic pressure (3.23).

The equations (3.15)-(3.17) give the governing equations for a compressible Newtonian perfect gas [89]. According to Theorem 2.3.1, the dissipation $\mathcal{D}^{pg}$ for this system is

$$\mathcal{D}^{pg} = \frac{1}{\theta}\mathbf{L}^d : \mathbb{D}^{pg}\mathbf{L}^d + \frac{1}{\theta}\mathfrak{B}^{pg}\rho^2\left(\nabla \cdot \mathbf{u}\right)^2 + \frac{1}{\theta^2}\nabla\theta \cdot \boldsymbol{\kappa}^{pg}\nabla\theta \tag{3.18}$$

$$= \frac{2\bar{\mu}^{pg}}{\theta}\mathbf{L}^d : \mathbf{L}^d + \frac{1}{\theta}\left(\bar{\lambda}^{pg} + \frac{2}{3}\bar{\mu}^{pg}\right)\left(\nabla \cdot \mathbf{u}\right)^2 + \frac{1}{\theta^2}\nabla\theta \cdot \boldsymbol{\kappa}^{pg}\nabla\theta. \tag{3.19}$$

It is evident that to ensure the second law of thermodynamics for all admissible processes, it is sufficient to require that

$$\bar{\mu}^{pg} \geq 0, \quad \bar{\lambda}^{pg} + \frac{2}{3}\bar{\mu}^{pg} \geq 0, \quad \boldsymbol{\kappa}^{pg} \text{ is positive semi-definite.} \tag{3.20}$$

A large part of the mathematical analysis of this compressible Newtonian fluid model falls into the category of hyperbolic conservation laws, where the shock wave structure is a focusing topic [55, 131, 138, 147]. Scalar hyperbolic equation in one-dimension has been thoroughly studied [74], however, as for system of hyperbolic equations in multi-dimensions, knowledge about the existence, uniqueness, and admissible criteria is still incomplete, mainly due to the high nonlinearity of the partial differential equations. Endeavors have been made to understand this model theoretically, including the development of proper mathematical entropy conditions to pick the physically admissible solutions [131, 144] and investigating the formal asymptotic equations as the dissipation goes to zero [33]. Meanwhile, numerical techniques have also been extensively studied for the nonlinear hyperbolic equations. A comprehensive report can be found in [139].

The thermodynamic pressure p^{pg} is plotted against ρ and θ in Figure 3.1 (a). It can be seen from the figure that the thermodynamic pressure here is convex with respect to density for all temperatures. This convexity endowed the compressible Navier-Stokes equations (3.15)-(3.17) a desirable property – there exists a set of variables named entropy variables for this system of equations [100, 109, 187]. The second law of thermodynamics is inherently built in the weighted residual formulation in terms of the entropy variables. This property is critical for developing robust numerical schemes since weak solutions of nonlinear hyperbolic problems are often non-unique, and the second law of thermodynamics is believed to be an appropriate admissibility criterion for the compressible Navier-Stokes equations. Successful applications using entropy variable formulation in numerical simulations can be found in [44, 178].

3.2 The van der Waals fluid model

Introduced by and named after the 1910 Nobel Laureate in physics, the van der Waals fluid model [198] is considered as an ideal candidate for modeling liquid-vapor phase transition phenomena. In the van der Waals model, the description of liquid and vapor phases of a single material are unified into one continuous equation of state. This equation of state is regarded as a generalization of the perfect gas law by accounting for molecular interactions and is even believed to be applicable to solid phases [113]. In the setting of continuum mechanics, van der Waals fluid model does not have a classical global convex energy function. Instead, its energy has concave part and

has a multitude of local minima, which represent different stable phases but render instabilities in mathematics. van der Waals studied Gibbs' work on capillarity [81] and proposed a non-local term involving the density gradient to represent capillarity, and this term regularizes the instability induced from the energy function's non-convexity. Later, Korteweg derived the capillarity stress formulation and developed a system of third-order partial differential equations presently known as the Navier-Stokes-Korteweg equations [127]. In this section, I will introduce the van der Waals theory from the thermodynamic perspective and recover the Navier-Stokes-Korteweg equations within the modeling framework. In particular, the recovery procedure of the Navier-Stokes-Korteweg equations will reveal the physical meaning of the mysterious "interstitial working" term [69].

3.2.1 Thermodynamics of the van der Waals fluid

The local free energy density of the van der Waals fluid is

$$
\begin{aligned}
\Psi_{loc}^{vdw}(\rho, \theta) = -a\rho + R\theta \log\left(\frac{\rho}{b - \rho}\right) \\
- C_v^{vdw}\theta \log\left(\frac{\theta}{\theta_{ref}^{vdw}}\right) + C_v^{vdw}\theta,
\end{aligned}
\tag{3.21}
$$

where a, b are associated with fluid properties whose meanings will be revealed in the coming discussion; $\theta_{ref}^{vdw} > 0$ is the temperature reference value for the van der Waals fluid; R is the universal gas constant; C_v^{vdw} is the heat capacity at constant volume for the van der Waals fluid. The total Helmholtz free
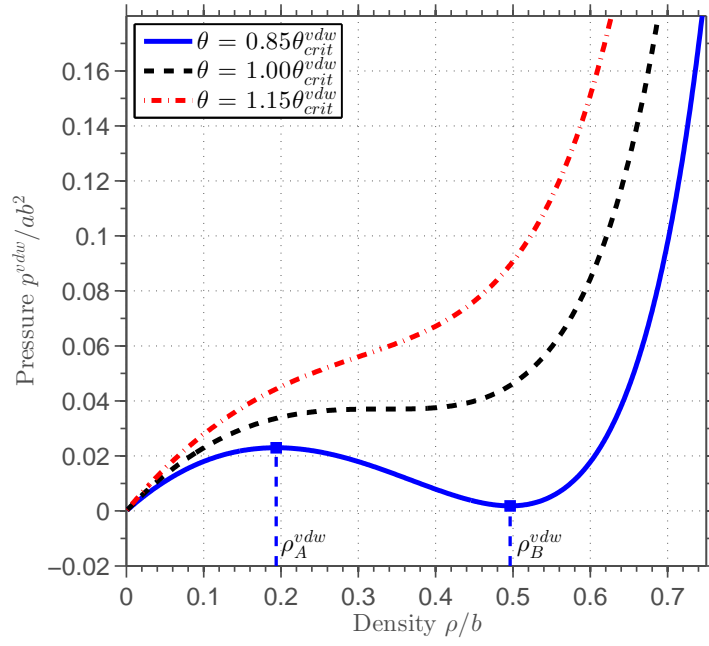
Figure 3.2: The van der Waals thermodynamic pressure p^{vdw} (3.23) at temperatures $\theta = 0.85\theta_{crit}^{vdw}$ (blue), $1.0\theta_{crit}^{vdw}$ (black), $1.15\theta_{crit}^{vdw}$ (red).

energy density is given by the sum of Ψ_{loc}^{vdw} and a non-local term $\lambda|\nabla\rho|^2/2\rho$ as

$$\Psi^{vdw}(\rho,\theta,\nabla\rho) = \Psi_{loc}^{vdw}(\rho,\theta) + \frac{\lambda}{2\rho}|\nabla\rho|^2, \tag{3.22}$$

where λ is the capillarity coefficient. The last term in (3.22) models the surface energy due to molecular attractive forces [198, 206]. To analyze the thermodynamics of the van der Waals fluid, it is helpful to introduce the local thermodynamic pressure p^{vdw} as

$$p^{vdw}(\rho,\theta) := \rho^2 \frac{\partial \Psi_{loc}^{vdw}}{\partial \rho} = Rb\frac{\rho\theta}{b-\rho} - a\rho^2, \tag{3.23}$$

and the local electrochemical potential ν_{loc}^{vdw} as

$$\nu_{loc}^{vdw}(\rho,\theta) := \frac{\partial\left(\rho\Psi_{loc}^{vdw}\right)}{\partial\rho} = -2a\rho + R\theta\log\left(\frac{\rho}{b-\rho}\right)$$
$$+ \frac{R\theta b}{b-\rho} - C_v^{vdw}\theta\log\left(\frac{\theta}{\theta_{ref}^{vdw}}\right) + C_v^{vdw}\theta. \tag{3.24}$$

Relation (3.23) is commonly known as the van der Waals equation of state. Noticing that the binomial expansion gives

$$\left(1-\frac{\rho}{b}\right)^{-1} \approx 1 + \frac{\rho}{b} + \frac{\rho^2}{b^2}, \qquad \text{when } |\frac{\rho}{b}| \ll 1, \tag{3.25}$$

relation (3.23) suggests the van der Waals pressure p^{vdw} can be represented as

$$p^{vdw} \approx R\theta\rho\left(1 + \left(\frac{1}{b} - \frac{a}{R\theta}\right)\rho^2 + \frac{1}{b^2}\rho^3\right). \tag{3.26}$$

This relation hints that the van der Waals equation of state can be viewed as a high-order modification of the perfect gas law. A more intuitive explanation of the van der Waals equation of state can be given from a microscopic

60

perspective. Reorganizing terms in (3.23) leads to

$$\left(p^{vdw} + a\rho^2\right)\left(1 - \frac{\rho}{b}\right) = R\rho\theta. \tag{3.27}$$

Comparing with the perfect gas law (3.12), (3.27) manifests two modifications made in the van der Waals model: (1) $a\rho^2$ is added to the pressure p^{vdw}; (2) $(1 - \rho/b)$ is multiplied in front of the pressure. The first modification represents the pressure contribution from long-range molecular attractive forces, which leads to denser fluid at a given pressure. The second modification indicates that the volume of the fluid cannot be compressed to zero due to short-range molecular repulsive forces. The pressure will go to infinity when the density approaches b. Thus b represents the maximum attainable density of the fluid.

Remark 3.2.1. *It is worth mentioning that the local electrochemical potential does not appear in the derivation of the constitutive relations in Chapter 2. In fact, the definition given in (3.24) can be rewritten as*

$$\nu_{loc}^{vdw}(\rho, \theta) := \Psi_{loc}^{vdw} + \rho\frac{\partial\Psi_{loc}^{vdw}}{\partial\rho} = \Psi_{loc}^{vdw} + \frac{p^{vdw}}{\rho}. \tag{3.28}$$

It is clear that ν_{loc}^{vdw} is the local Gibbs free energy function for the van der Waals fluid. This thermodynamic potential will be useful in the mathematical and numerical analysis of the Navier-Stokes-Korteweg equations. In the following text, ν_{loc}^{vdw} is called the local electrochemical potential, following the terminology in [44].
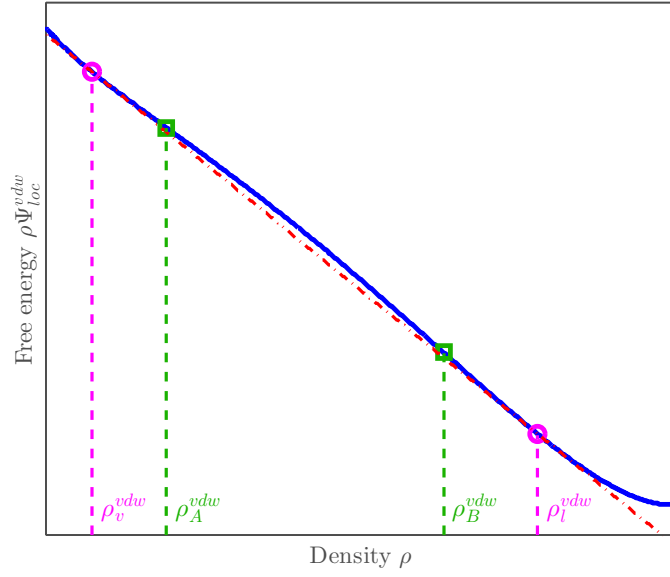
Figure 3.3: The van der Waals free energy $\rho\Psi_{loc}^{vdw}$ at temperature $\theta = 0.8\theta_{crit}^{vdw}$ is plotted as the blue solid line against ρ. The red dash-dot-line is the common tangent line passing through the Maxwell states, which are marked as the magenta circles. The elliptic region is delimited by ρ_A^{vdw} and ρ_B^{vdw}, which are identified by the green squares.

The critical point $(\rho_{crit}^{vdw}, \theta_{crit}^{vdw})$ of the van der Waals fluid is defined to be the point where $\partial p^{vdw}/\partial \rho = 0$ and $\partial^2 p^{vdw}/\partial \rho^2 = 0$. Simple calculations show that

$$\rho_{crit}^{vdw} = \frac{b}{3}, \qquad \theta_{crit}^{vdw} = \frac{8ab}{27R}, \tag{3.29}$$

and the thermodynamic pressure at this critical point is $p_{crit}^{vdw} = ab^2/27$. In Figure 3.1 (b), the van der Waals pressure function (3.23) is plotted over the domain $[0, 0.8\rho_{crit}^{vdw}] \times [0.8\theta_{crit}^{vdw}, 1.2\theta_{crit}^{vdw}]$. Comparing with the perfect gas model (see Figure 3.1 (a)), one distinct feature of the van der Waals pressure function is that it is not globally convex. In Figure 3.2, the non-convexity is illustrated by plotting the pressure as a univariate function of density. It can be observed from the two figures that the pressure is a monotonically increasing function with respect to density when $\theta > \theta_{crit}^{vdw}$. In this case, the fluid is named as supercritical fluid since there are no distinct liquid vapor phases [186]. When the temperature drops below the critical temperature (i.e., $\theta < \theta_{crit}^{vdw}$), the pressure function is no longer monotone, and there exists a region $(\rho_A^{vdw}b, \rho_B^{vdw}b)$ where the pressure function decreases with respect to density, as is shown in Figure 3.2. This region is commonly referred to as the elliptic region, since the system of conservation equations within this region is of first-order elliptic type in the vanishing viscosity-capillarity limit. The elliptic region is physically unstable: the decrease of pressure is accompanied with the increase of density within this region. Additionally, recalling the local sound speed is defined as $\sqrt{dp^{vdw}/d\rho}$, the sound speed within the elliptic region is imaginary. Homogeneous mixture of the van der Waals fluid with density $\rho \in (\rho_A^{vdw}b, \rho_B^{vdw}b)$ will

spontaneously degenerate into a state consisting of liquid and vapor phases, which is commonly known as spinodal decomposition. This process can be better understood from the view of the minimum energy principle. The equilibrium state at a given temperature can be found by constructing a common tangent line passing thorough the free energy curve in below, as is shown in Figure 3.3. I denote the two points through which the common tangent line passes as $(\rho_v^{vdw}, \rho_v^{vdw} \Psi_{loc}^{vdw}(\rho_v^{vdw}))$ and $(\rho_l^{vdw}, \rho_l^{vdw} \Psi_{loc}^{vdw}(\rho_l^{vdw}))$. Then mathematically, the two points have to satisfy the following equations.

$$\frac{\partial(\rho\Psi_{loc}^{vdw})}{\partial\rho}(\rho_v^{vdw}) = \frac{\partial(\rho\Psi_{loc}^{vdw})}{\partial\rho}(\rho_l^{vdw}), \tag{3.30}$$

$$\rho_v^{vdw}\frac{\partial(\rho\Psi_{loc}^{vdw})}{\partial\rho}(\rho_v^{vdw}) - \rho_v^{vdw}\Psi_{loc}^{vdw}(\rho_v^{vdw})$$
$$= \rho_l^{vdw}\frac{\partial(\rho\Psi_{loc}^{vdw})}{\partial\rho}(\rho_l^{vdw}) - \rho_l^{vdw}\Psi_{loc}^{vdw}(\rho_l^{vdw}). \tag{3.31}$$

Notice that the first relation implies that the local electrochemical potentials are equal in both phases, and the second relation implies that the thermodynamic pressures in both phases are the same. Thus, the two-phase system is in mechanical and chemical equilibrium at these two points. From Figure 3.3, it can be observed that the common tangent line lies below the free energy curve. Hence according to the minimum energy principle, the two-phase coexisting state is favored against the homogeneous mixture.

Remark 3.2.2. *Besides the common tangent line method, another way of determining equilibrium states was given by Maxwell. He conjectured a thermodynamic loop $\rho_v^{vdw} \rightarrow \rho_A^{vdw} \rightarrow \rho_e^{vdw} \rightarrow \rho_B^{vdw} \rightarrow \rho_l^{vdw} \rightarrow \rho_v^{vdw}$ in Figure 3.4. Since*

64

this thermodynamic process is an isothermal process, the work done in this loop should be zero, which means the two areas circumscribed by the pressure curve and the straight line passing through $(\rho_v^{vdw}, p^{vdw}(\rho_v^{vdw}))$ and $(\rho_l^{vdw}, p^{vdw}(\rho_l^{vdw}))$ should be equal. By constructing a straight line that encloses two equal areas, thermodynamic equilibrium states can be found directly from the pressure curve. This method is named as the equal area rule [175].

Now let me summarize the thermodynamic properties of the van der Waals fluid by drawing a $\theta-\rho$ phase diagram in Figure 3.5. In this diagram, the values of ρ_A^{vdw}, ρ_B^{vdw}, ρ_v^{vdw} and ρ_l^{vdw} are plotted for temperatures between $0.7\theta_{crit}^{vdw}$ and $1.05\theta_{crit}^{vdw}$. The values of ρ_A^{vdw} at different temperatures are connected by a blue dashed line and the values of ρ_B^{vdw} are connected by a red dashed line. The blue and red dashed lines together are named as the spinodal line. The region enclosed by the spinodal line is the elliptic region. The values of ρ_v^{vdw} and ρ_l^{vdw} at each temperature are connected by a black solid line, which is named as the binodal line. This line indicates the stable liquid and vapor phases at different temperatures. The region between the binodal line and the spinodal line is the metastable region. The metastable state is physically accessible but energetically unstable. With enough energy fluctuations, the concave energy barrier may be overcome and a more stable liquid-vapor two-phase system may form. The binodal line and the spinodal line coincide at the critical point of the van der Waals fluid.

The van der Waals fluid model is the first model that gives a consistent explanation of phase transitions in liquid and vapor phases. Thermodynamic

65
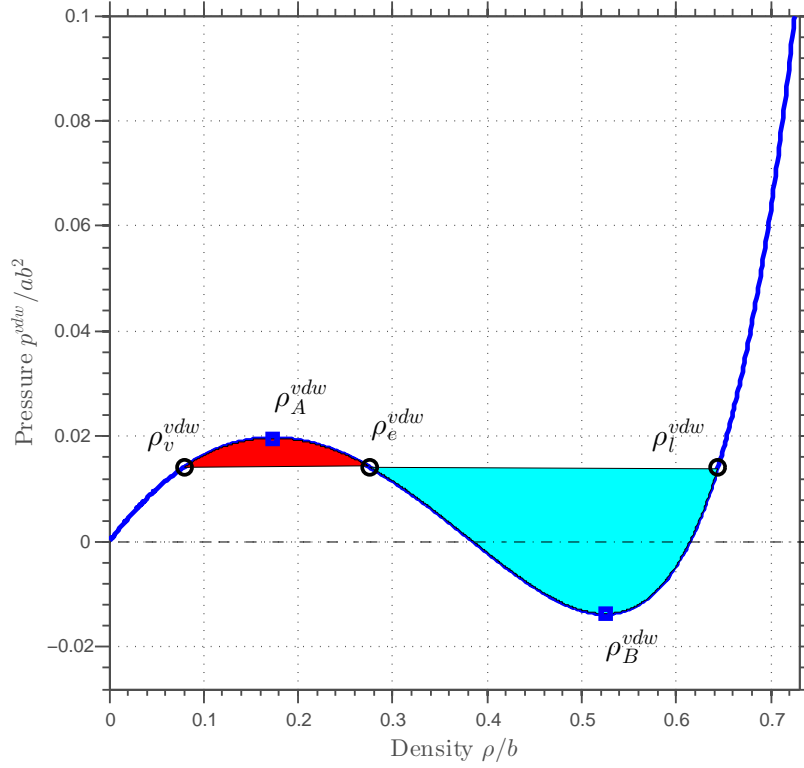
Figure 3.4: Illustration of the equal area rule. The temperature is fixed at $0.80\theta_{crit}^{vdw}$ and the thermodynamic pressure p^{vdw} is plotted as the blue solid line. The area of the red region equals the area of the cyan region. The straight line that encloses the two equal areas intersects with the pressure curve at the stable vapor and liquid states at this temperature. The blue squares $(\rho_A^{vdw}, p^{vdw}(\rho_A^{vdw}))$ and $(\rho_B^{vdw}, p^{vdw}(\rho_B^{vdw}))$ delimits the elliptic region.
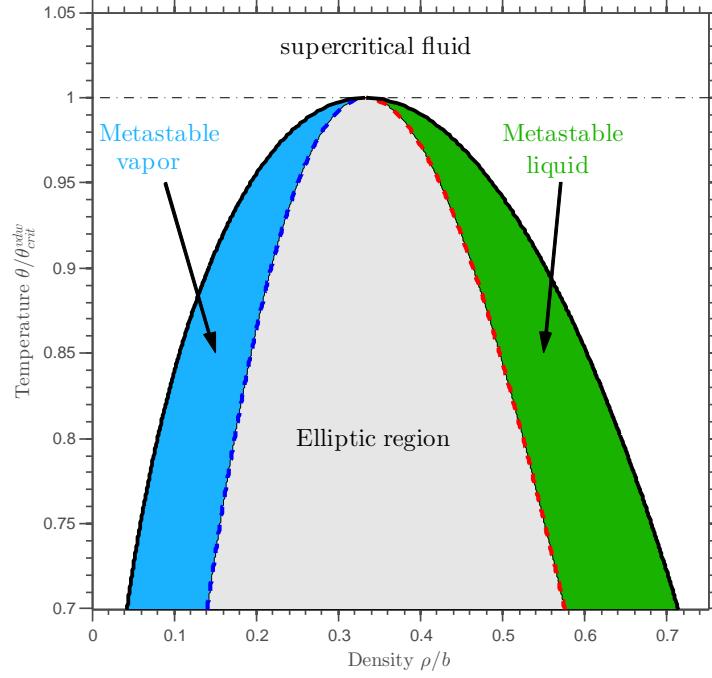
Figure 3.5: Illustration of the elliptic region, the metastable regions, the spinodal line, and the binodal line for the van der Waals fluid model. The elliptic region $(\rho_A^{vdw}, \rho_B^{vdw})$ is colored in grey; the metastable vapor region $(\rho_v^{vdw}, \rho_A^{vdw})$ is colored in blue; the liquid metastable region $(\rho_B^{vdw}, \rho_l^{vdw})$ is colored in green. Above the critical temperature, the fluid becomes supercritical. The solid black line is the binodal line. The dashed line that circumscribes the elliptic region is the spinodal line.
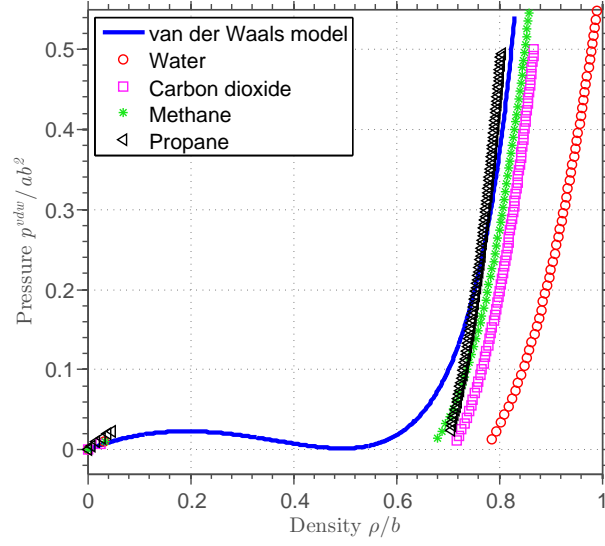
(a)
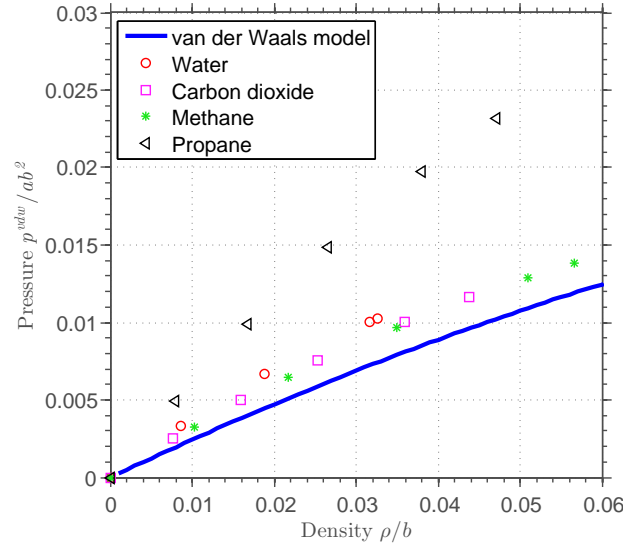
(b)

Figure 3.6: Comparison of the van der Waals equation of state with real fluids at temperature $\theta = 0.85\theta_{crit}$. The data of water, carbon dioxide, methane, and propane are obtained from [157] and scaled to dimensionless form. Figure (b) gives a detailed comparison in the vapor phase.

properties of water, carbon dioxide, methane, and propane are downloaded from the NIST online database [157] and are compared with the van der Waals fluid model in dimensionless quantities. As is depicted in Figure 3.6, the van der Waals fluid model gives a qualitatively accurate description of various fluid materials in both liquid and vapor phases. However, considering the simplicity of the van der Waals fluid model, there are still rooms for improvement. One up-to-date modification was given by Serrin [175], who introduced two more parameters $\hat{r} > 1$ and $\hat{s} < 1$ and a new equation of state

$$p^{serrin} = Rb\frac{\rho\theta}{b - \rho} - a\theta^{\hat{s}}\rho^{\hat{r}}. \tag{3.32}$$

It was claimed that a proper choice of the parameters $a, b, \hat{r}$ and $\hat{s}$ may lead to an accurate pressure curve up to one percent error over large temperature regions [175]. Another modification is inspired by the relation (3.26), and more higher-order terms can be introduced to the equation of state. Examples of this type modification include the Beattie-Bridgeman equation [20] and the Benedict-Webb-Rubin equation [22].

3.2.2 The Navier-Stokes-Korteweg equations
3.2.2.1 The governing equations

Now let me consider the system of governing equations endowed with the Helmholtz free energy (3.21)-(3.22). It is apparent that the free energy density function (3.22) is a special form of the free energy density formulation I considered in (2.80), where the free energy density is independent of mass fractions and their gradients. In other words, only one component is considered

69

here (i.e., $\mathbf{N} = 1$), and thus the component balance equation is identical to the mass balance equation. According to (2.89)-(2.92), the Cauchy stress for this problem can be explicitly written as

$$\mathbf{T}^{vdw} = \boldsymbol{\tau}^{vdw} + \boldsymbol{\varsigma}^{vdw} - p^{vdw}\mathbf{I}, \tag{3.33}$$

$$\boldsymbol{\tau}^{vdw} = \bar{\mu}^{vdw}\left(\nabla\mathbf{u} + \nabla\mathbf{u}^T\right) + \bar{\lambda}^{vdw}\nabla\cdot\mathbf{u}\mathbf{I}, \tag{3.34}$$

$$\boldsymbol{\varsigma}^{vdw} = -\lambda\nabla\rho\otimes\nabla\rho + \left(\lambda\rho\Delta\rho + \frac{\lambda}{2}|\nabla\rho|^2\right)\mathbf{I}, \tag{3.35}$$

$$p^{vdw} = Rb\frac{\rho\theta}{b-\rho} - a\rho^2. \tag{3.36}$$

The stress $\boldsymbol{\varsigma}^{vdw}$ was first derived by Korteweg [127] and is thus named as the Korteweg stress. In addition to the Cauchy stress, the microstress $\boldsymbol{\xi}^{vdw}$, the heat flux $\mathbf{q}^{vdw}$, the entropy density s^{vdw}, and the internal energy density ι^{vdw} can be written explicitly following the general constitutive relations (2.70), (2.77), (2.78), and (2.79).

$$\boldsymbol{\xi}^{vdw} = \lambda\nabla\rho, \tag{3.37}$$

$$\mathbf{q}^{vdw} = -\boldsymbol{\kappa}^{vdw}\nabla\theta, \tag{3.38}$$

$$s^{vdw} = -R\log\left(\frac{\rho}{b-\rho}\right) + C_v^{vdw}\log\left(\frac{\theta}{\theta_{ref}^{vdw}}\right), \tag{3.39}$$

$$\iota^{vdw} = -a\rho + C_v^{vdw}\theta. \tag{3.40}$$

Let me denote the power expenditure of $\boldsymbol{\xi}^{vdw}$ as $\boldsymbol{\Pi}^{vdw}$. Recalling that $\boldsymbol{\Pi}^{vdw} = \rho\nabla\cdot\mathbf{u}\boldsymbol{\xi}^{vdw}$, the power expenditure of the microstress $\boldsymbol{\xi}^{vdw}$ is $\boldsymbol{\Pi}^{vdw} = \lambda\rho\nabla\cdot\mathbf{u}\nabla\rho$. The balance equations can be written in terms of the conservation variables as

70

$$\frac{\partial \rho}{\partial t} + \nabla \cdot (\rho \mathbf{u}) = 0, \tag{3.41}$$

$$\frac{\partial (\rho \mathbf{u})}{\partial t} + \nabla \cdot \left(\rho \mathbf{u} \otimes \mathbf{u} + p^{vdw} \mathbf{I} \right) - \nabla \cdot \boldsymbol{\tau}^{vdw} - \nabla \cdot \boldsymbol{\varsigma}^{vdw} = \rho \mathbf{b}, \tag{3.42}$$

$$\frac{\partial (\rho E)}{\partial t} + \nabla \cdot \left(\left(\rho E + p^{vdw} \right) \mathbf{u} - (\boldsymbol{\tau}^{vdw} + \boldsymbol{\varsigma}^{vdw}) \mathbf{u} \right) + \nabla \cdot \mathbf{q}^{vdw} + \nabla \cdot \boldsymbol{\Pi}^{vdw}$$
$$= \rho \mathbf{b} \cdot \mathbf{u} + \rho r. \tag{3.43}$$

This system of balance equations is the well-known Navier-Stokes-Korteweg equations [69]. According to Theorem 2.3.1, the dissipation $\mathcal{D}^{vdw}$ for this system is

$$\mathcal{D}^{vdw} = \frac{1}{\theta} \mathbf{L}^d : \mathbb{D}^{vdw} \mathbf{L}^d + \frac{1}{\theta} \mathfrak{B}^{vdw} \rho^2 \left(\nabla \cdot \mathbf{u} \right)^2 + \frac{1}{\theta^2} \nabla \theta \cdot \boldsymbol{\kappa}^{vdw} \nabla \theta \tag{3.44}$$

$$= \frac{2\bar{\mu}^{vdw}}{\theta} \mathbf{L}^d : \mathbf{L}^d + \frac{1}{\theta} \left(\bar{\lambda}^{vdw} + \frac{2}{3} \bar{\mu}^{vdw} \right) \left(\nabla \cdot \mathbf{u} \right)^2 + \frac{1}{\theta^2} \nabla \theta \cdot \boldsymbol{\kappa}^{vdw} \nabla \theta. \tag{3.45}$$

To ensure the second law of thermodynamics, it is sufficient to require that

$$\bar{\mu}^{vdw} \geq 0, \quad \bar{\lambda}^{vdw} + \frac{2}{3} \bar{\mu}^{vdw} \geq 0, \quad \boldsymbol{\kappa}^{vdw} \text{ is positive semi-definite.} \tag{3.46}$$

Comparing with the energy equation for the perfect gas (3.17), $\boldsymbol{\Pi}^{vdw}$ is one unfamiliar term entering the energy equation. It was initially devised by Dunn and Serrin to enforce the Clausius-Duhem inequality and named as the "interstitial working flux" [69]. Now it is clear that this term is actually the power expenditure of the microstress $\boldsymbol{\xi}^{vdw}$.

3.2.2.2 The isothermal case

Under the isothermal condition, the Navier-Stokes-Korteweg equations are reduced to

$$\frac{\partial \rho}{\partial t} + \nabla \cdot (\rho \mathbf{u}) = 0, \tag{3.47}$$

$$\frac{\partial(\rho \mathbf{u})}{\partial t} + \nabla \cdot (\rho \mathbf{u} \otimes \mathbf{u}) + \nabla p^{vdw} - \nabla \cdot \boldsymbol{\tau}^{vdw} - \nabla \cdot \boldsymbol{\varsigma}^{vdw} = \rho \mathbf{b}. \tag{3.48}$$

Typical boundary conditions for the isothermal Navier-Stokes-Korteweg equations (3.47)-(3.48) are

$$\nabla \rho \cdot \mathbf{n} = 0, \tag{3.49}$$

$$\mathbf{u} = \mathbf{0}. \tag{3.50}$$

Following Lemma 2.3.1, the isothermal Navier-Stokes-Korteweg equations with boundary conditions (3.49)-(3.50) satisfy

$$\frac{d}{dt} \int_{\Omega_t} \rho \left(\Psi^{vdw} + \frac{|\mathbf{u}|^2}{2} \right) dV_{\mathbf{x}} = \int_{\Omega_t} \rho \mathbf{b} \cdot \mathbf{u} - \theta \mathcal{D}^{vdw} dV_{\mathbf{x}}$$

$$= \int_{\Omega_t} \rho \mathbf{b} \cdot \mathbf{u} - \boldsymbol{\tau}^{vdw} : \nabla \mathbf{u} dV_{\mathbf{x}}. \tag{3.51}$$

Moreover, if the external body force $\mathbf{b}$ is negligible, $\bar{\mu}^{vdw} \geq 0$, and $\bar{\lambda}^{vdw} + \frac{2}{3}\bar{\mu}^{vdw} \geq 0$, the energy dissipates as

$$\frac{d}{dt} \int_{\Omega_t} \rho \left(\Psi^{vdw} + \frac{|\mathbf{u}|^2}{2} \right) dV_{\mathbf{x}} = \int_{\Omega_t} -\boldsymbol{\tau}^{vdw} : \nabla \mathbf{u} dV_{\mathbf{x}} \leq 0. \tag{3.52}$$

72
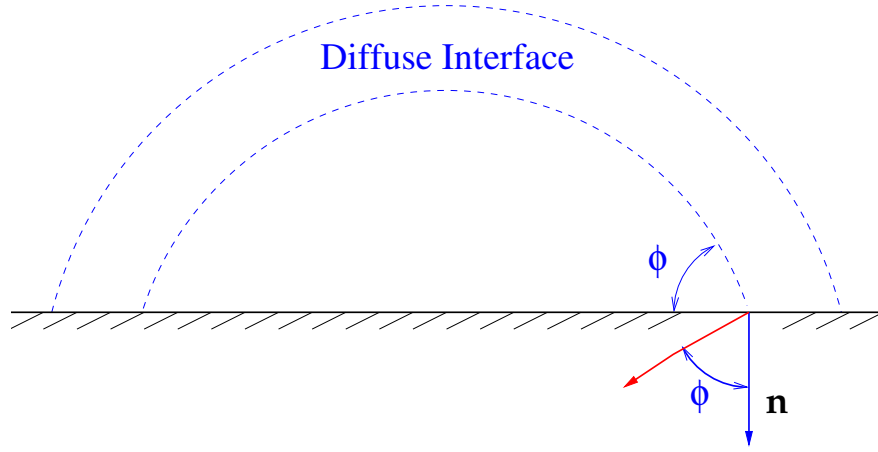
Figure 3.7: Illustration of the contact angle boundary condition (3.53). The red arrow points in the direction $-\nabla\rho/\|\nabla\rho\|$.

Remark 3.2.3. *Periodic boundary conditions for ρ and $\mathbf{u}$ are another simple boundary conditions that can generate the energy dissipation result (3.52).*

Remark 3.2.4. *Boundary condition (3.49) is a special case of the contact-angle boundary condition*

$$-\frac{\nabla\rho}{\|\nabla\rho\|} \cdot \mathbf{n} = cos(\phi), \tag{3.53}$$

wherein

$$\|\nabla\rho\| = \sqrt{\nabla\rho \cdot \nabla\rho}. \tag{3.54}$$

Here ϕ is the contact angle of the diffuse-interface against the wall boundary (see Figure 3.7). Its value depends on the material properties of the fluids as well as the wall.

Remark 3.2.5. *If the interface parameter λ is constant, the capillary force term $\nabla \cdot \boldsymbol{\varsigma}^{vdw}$ can be written in the following non-conservative form.*

$$\nabla \cdot \boldsymbol{\varsigma}^{vdw} = \lambda \rho \nabla \left(\Delta \rho \right). \tag{3.55}$$

3.2.3 A summary of mathematical results

In this section, I discuss some important theoretical results of the van der Waals fluid model. An existence proof for the static equilibrium solutions is first sketched by considering an energy minimization problem. Next, the current mathematical results about the general strong solutions are briefly summarized.

The static equilibrium solutions of the isothermal system (3.47)-(3.48) are defined as the solutions that satisfies the following three conditions:

$$\frac{\partial \rho}{\partial t} = 0, \tag{3.56}$$

$$\frac{\partial (\rho \mathbf{u})}{\partial t} = 0, \tag{3.57}$$

$$\mathbf{u} = 0. \tag{3.58}$$

Based on the above three assumptions, the mass conservation equation (3.47) is automatically satisfied and the momentum conservation equation (3.48) reduces to

$$\nabla p^{vdw} - \nabla \cdot \boldsymbol{\varsigma}^{vdw} = \rho \mathbf{b}. \tag{3.59}$$

Under the isothermal conditions, the pressure p^{vdw} and the local electrochem-

ical potential ν_{loc}^{vdw} reduce to single variable functions of the density,

$$p^{vdw} = \rho^2 \frac{d\Psi_{loc}^{vdw}}{d\rho}, \tag{3.60}$$

$$\nu_{loc}^{vdw} = \frac{d\left(\rho\Psi_{loc}^{vdw}\right)}{d\rho}. \tag{3.61}$$

Straightforward calculations reveal that

$$\frac{dp^{vdw}}{d\rho} = 2\rho\frac{d\Psi^{vdw}}{d\rho} + \rho^2\frac{d^2\Psi^{vdw}}{d\rho^2} = \rho\frac{d\nu_{loc}^{vdw}}{d\rho}. \tag{3.62}$$

Consequently, one has

$$\nabla p^{vdw} = \rho\nabla\nu_{loc}^{vdw}. \tag{3.63}$$

Making use of the relations (3.55) and (3.63) and ignoring the body force $\mathbf{b}$, the relation (3.59) can be rewritten as

$$\rho\nabla\nu_{loc}^{vdw} - \lambda\rho\nabla\Delta\rho = \mathbf{0}. \tag{3.64}$$

One can divide both sides of the above equation by ρ, integrate once, and get an elliptic equation describing the static equilibrium solutions

$$\nu_{loc}^{vdw} - \lambda\Delta\rho = C_{se}^{vdw}, \tag{3.65}$$

where C_{se}^{vdw} is a constant. The above derivation can be summarized as the following lemma.

Lemma 3.2.1. *If the static equilibrium solutions of the isothermal Navier-Stokes-Korteweg equations exist and are sufficiently regular, the density profile will be governed by the nonlinear Poisson equation (3.65).*

Remark 3.2.6. *For the van der Waals fluid, an asymptotic estimate for C_{se}^{vdw} with respect to the surface tension parameter λ has been given in [146].*

If the domain Ω is bounded and connected, one may consider a constrained energy minimization problem: find a density profile $\rho \in H^1(\Omega)$ that satisfies the mass conservation and the natural boundary condition on $\partial\Omega$

$$\int_\Omega \rho dV_{\mathbf{x}} = C_{mass}^{vdw}, \tag{3.66}$$

$$\nabla\rho \cdot \mathbf{n} = 0, \tag{3.67}$$

such that the energy

$$\int_\Omega \rho\Psi^{vdw} dV_{\mathbf{x}} = \int_\Omega \left(\rho\Psi_{loc}^{vdw} + \frac{\lambda}{2}|\nabla\rho|^2\right) dV_{\mathbf{x}} \tag{3.68}$$

is minimized. Then the following lemma connects the nonlinear Poisson equation (3.65) with the minimization problem (3.66)-(3.68).

Lemma 3.2.2. *Given sufficient regularity, the nonlinear Poisson equation (3.65) is the Euler-Lagrange equation of the above constrained energy minimization problem and C_{se}^{vdw} is the corresponding Lagrangian multiplier of the constraint equation (3.66).*

Proof. Let C_{lag}^{vdw} be the Lagrangian multiplier for the mass conservation constraint equation. Consider the Lagrangian function defined as

$$\mathfrak{G} := \int_\Omega \left(\rho\Psi_{loc}^{vdw}(\rho) + \frac{\lambda}{2}|\nabla\rho|^2 - C_{lag}^{vdw}\rho\right) dV_{\mathbf{x}} + C_{mass}^{vdw} C_{lag}^{vdw}. \tag{3.69}$$

76

Its Euler-Lagrange equation can be obtained readily [74] as

$$\frac{d(\rho\Psi_{loc}^{vdw})}{d\rho} - C_{lag}^{vdw} = \lambda\Delta\rho. \tag{3.70}$$

Making use of the thermodynamic relation (3.61) and reorganizing terms, the above equation becomes

$$\nu_{loc}^{vdw} - \lambda\Delta\rho = C_{lag}^{vdw}, \tag{3.71}$$

which completes the proof. $\qquad\square$

Lemma 3.2.2 reveals that the existence of the static equilibrium solutions is equivalent to the existence of the minimizer of the constraint energy minimization problem (3.66)-(3.68). It can be shown that for a sufficiently regular bounded domain, the energy functional (3.68) is weakly lower semi-continuous [97]. Hence, based on the calculus of variation theory, there exists ρ in a Sobolev space that is a global minimizer of (3.68) and satisfies the mass conservation constraint (3.66). Standard regularity theory leads to an estimate of the smoothness of the minimizer. Interested readers are referred to [93, 97] for technical details.

On the other hand, the existence and uniqueness of the general solutions have been investigated by a few researchers. In [128], the author proved that there exists a unique set of strong solutions in a finite time interval for the isothermal Navier-Stokes-Korteweg equations (3.47)-(3.48) with the boundary conditions (3.49)-(3.50). In [59], the authors proved the existence and uniqueness of the strong solutions for the same equations in global time by imposing restrictions on the initial data.

3.3 The Navier-Stokes-Cahn-Hilliard fluid model

3.3.1 Thermodynamics of a binary system

In a series of ground-breaking works [40–42], Cahn and Hilliard proposed a free energy density function Ψ^{ch2} for a binary non-uniform system, which depends on a non-uniform property c_1 and its derivatives. In their theory, the non-uniform property c_1 can be any intensive scalar property of the system except pressure and temperature. This c_1 variable serves as an order parameter which indicates different components. In this way, c_1 plays an analogous role to that of the density variable in the van der Waals single-component multiphase fluid model. In this work, c_1 is one component's mass fraction in the binary system, as was defined in (2.5). The Helmholtz free energy density function Ψ^{ch2} takes the following general format.

$$\Psi^{ch2}(\rho, c_1, \nabla c_1, \theta) = \Psi^{ch2}_{loc}(\rho, c_1, \theta) + \frac{1}{2}\gamma^{ch2}_1 |\nabla c_1|^2. \qquad (3.72)$$

In this free energy formulation, Ψ^{ch2}_{loc} is the local free energy of the binary homogeneous mixture, and the gradient term represents the interface free energy. Parameter γ^{ch2}_1 may depend on the order parameter c_1 and the temperature θ, but is regarded as a constant in this study. Based on the definition, the domain for c_1 should be $[0, 1]$. To simplify the following discussion, Ψ^{ch2}_{loc} is assumed to be at least a C^2-continuous function with respect to c_1. Gibbs pointed out that when $\partial^2 \Psi^{ch2}_{loc}/\partial c_1^2 < 0$ the system is thermodynamically unstable and phase separation will take place spontaneously [82]. This process is called spinodal decomposition [42] and the locus of $\partial^2 \Psi^{ch2}_{loc}/\partial c_1^2 = 0$ is typically referred to as the spinodal line. Consequently, in order to support two

78

distinct phases, the general requirements for the local free energy function are that Ψ_{loc}^{ch2} should be non-convex with respect to the c_1 variable in the spinodal region and have two distinct local minima for $c_1 \in [0,1]$. These requirements infer that Ψ_{loc}^{ch2} has a convex-concave-convex shape. It is up to the modeler to give an analytic expression for the Ψ_{loc}^{ch2} function. In the original work of Cahn and Hilliard [41], the regular solution theory [92] is adopted to construct the local free energy function. Recently, a fourth-order polynomial theory has been widely used [25, 111, 141, 208]. This theory can be viewed as an approximation to the regular solution theory and it is more amenable to mathematical analysis. Both theories will be discussed in the succeeding text.

The regular solution theory stems from a statistical mechanics analysis. For an ideal mixture, the entropy for mixing a two-component fluid is

$$s^{ch2}(c_1) = -R\left(c_1 \log(c_1) + (1 - c_1) \log(1 - c_1)\right), \tag{3.73}$$

where R is the universal gas constant. Assuming the free energy densities of the component 1 and 2 are $\psi_1(\rho, \theta)$ and $\psi_2(\rho, \theta)$ respectively, then the local free energy density of the mixture can be written as

$$\begin{aligned}
\Psi_{loc}^{ch2}(\rho, c_1, \theta) =& c_1 \psi_1(\rho, \theta) + (1 - c_1)\psi_2(\rho, \theta) - \theta s^{ch2}(c_1) \\
=& c_1 \psi_1(\rho, \theta) + (1 - c_1)\psi_2(\rho, \theta) \\
& + R\theta\left(c_1 \log(c_1) + (1 - c_1) \log(1 - c_1)\right).
\end{aligned} \tag{3.74}$$

This free energy density function is globally convex (see Figure 3.8). The global convexity indicates that the equilibrium state will be a homogeneous mixture
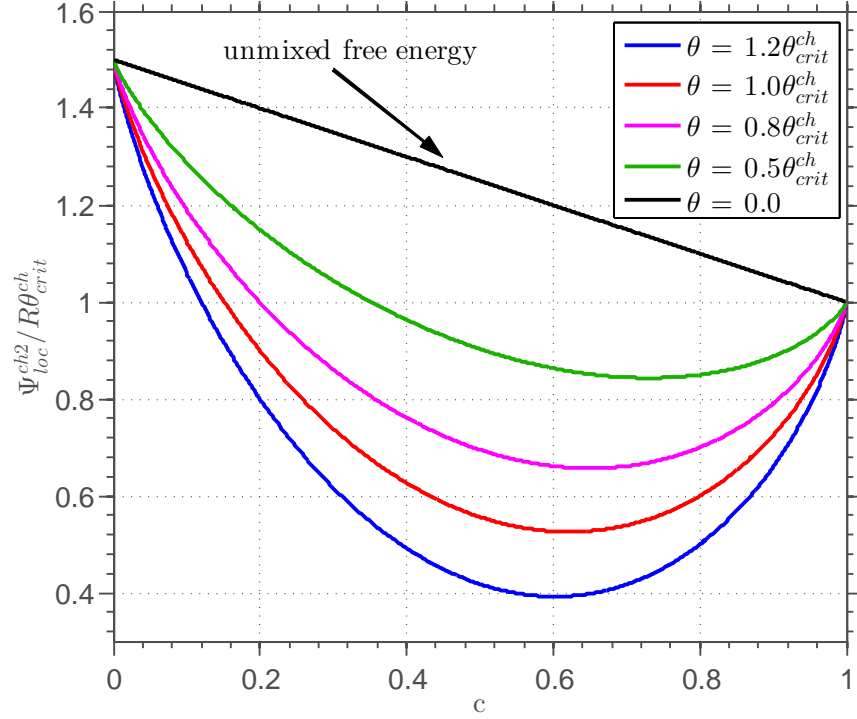
Figure 3.8: Illustration of the local free energy density function Ψ_{loc}^{ch2} of an ideal mixture given by (3.74). The temperatures are set to be $\theta = 1.2\theta_{crit}^{ch2}$ (blue), $1.0\theta_{crit}^{ch2}$ (red), $0.8\theta_{crit}^{ch2}$ (magenta), and $0.5\theta_{cirt}^{ch2}$ (green). The unmixed free energy (equivalent to the free energy at temperature zero) is plotted as the black solid line. Here ψ_1 is chosen to be $R\theta_{crit}^{ch2}$, and ψ_2 is chosen to be $1.5R\theta_{crit}^{ch2}$.
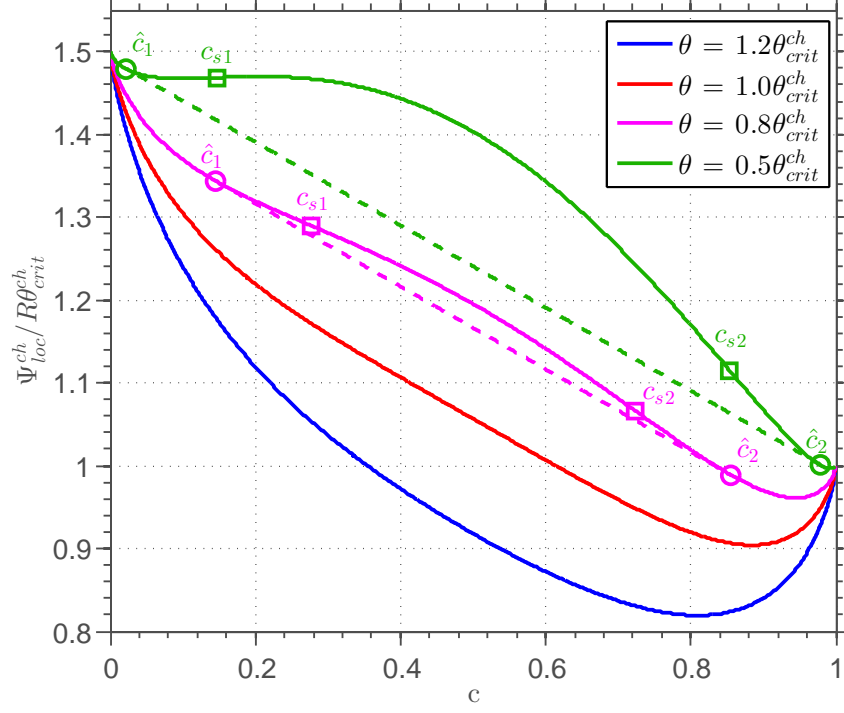
Figure 3.9: Illustration of the local free energy density Ψ_{loc}^{ch2} of the regular solution model given by (3.75). The temperatures are chosen to be $\theta = 1.2\theta_{crit}^{ch2}$ (blue), $1.0\theta_{crit}^{ch2}$ (red), $0.8\theta_{crit}^{ch2}$ (magenta), and $0.5\theta_{cirt}^{ch2}$ (green). Here ψ_1 is chosen to be $R\theta_{crit}^{ch2}$, and ψ_2 is chosen to be $1.5R\theta_{crit}^{ch2}$. At temperatures $0.8\theta_{crit}^{ch2}$ and $0.5\theta_{crit}^{ch2}$, the boundary points of the spinodal region are marked by squares. The thermodynamically stable states are marked by circles. The dashed lines connecting the circles are the common tangent lines representing the free energies at the unmixed states.

of the two components. In the formula derived in (3.73), it is assumed that the molecular force between different type molecules is identical to that between the same type molecules. However, for most materials, molecules of the same type are more likely to attract each other. Assuming molecular interactions are restricted to their nearest neighbors, it can be derived from the statistical mechanics that the energy needed to homogeneously mix the two components is $2R\theta_{crit}^{ch2}c(1-c)$ [43]. Here θ_{crit}^{ch2} represents the critical temperature, whose physical meaning will be revealed in the succeeding text. Accordingly, the free energy function should be modified as

$$\Psi_{loc}^{ch2}(\rho, c_1, \theta) = c_1\psi_1(\rho, \theta) + (1-c_1)\psi_2(\rho, \theta) + R\theta\big(c_1\log(c_1)$$
$$+ (1-c_1)\log(1-c_1)\big) + 2R\theta_{crit}^{ch2}c_1(1-c_1). \qquad (3.75)$$

The local free energy function given by (3.75) leads to the regular solution theory. Figure 3.9 demonstrates the homogeneous free energy Ψ_{loc}^{ch2} at temperatures $\theta = 1.2\theta_{crit}^{ch2}$, $1.0\theta_{crit}^{ch2}$, $0.8\theta_{crit}^{ch2}$, and $0.5\theta_{crit}^{ch2}$. At a given temperature θ, the first and second-order derivatives of Ψ_{loc}^{ch2} with respect to c_1 are

$$\frac{\partial \Psi_{loc}^{ch2}}{\partial c_1} = \psi_1(\rho, \theta) - \psi_2(\rho, \theta) + R\theta\log\left(\frac{c_1}{1-c_1}\right) + 2R\theta_{crit}^{ch2}(1-2c_1), \quad (3.76)$$

$$\frac{\partial^2 \Psi_{loc}^{ch2}}{\partial c_1^2} = \frac{R\theta}{c_1(1-c_1)} - 4R\theta_{crit}^{ch2}. \qquad (3.77)$$

Straightforward calculations may show that when $\theta \geq \theta_{crit}^{ch2}$, Ψ_{loc}^{ch2} is globally convex; when $\theta < \theta_{crit}^{ch2}$, Ψ_{loc}^{ch2} is concave in the spinodal region (c_{s1}, c_{s2}), with $c_{s1} = 1/2 - \sqrt{1-\theta/\theta_{crit}^{ch2}}/2$ and $c_{s2} = 1/2 + \sqrt{1-\theta/\theta_{crit}^{ch2}}/2$. At a given temperature, the stable mass fractions of the component 1 and 2, denoted by $\hat{c}_1$ and

$\hat{c}_2$, can be found by constructing a common tangent line of the homogeneous free energy function:

$$\frac{\partial \Psi_{loc}^{ch2}}{\partial c_1}(\rho, \hat{c}_1, \theta) = \frac{\partial \Psi_{loc}^{ch2}}{\partial c_1}(\rho, \hat{c}_2, \theta), \tag{3.78}$$

$$\frac{\Psi_{loc}^{ch2}(\rho, \hat{c}_1, \theta) - \Psi_{loc}^{ch2}(\rho, \hat{c}_2, \theta)}{\hat{c}_1 - \hat{c}_2} = \frac{\partial \Psi_{loc}}{\partial c_1}(\rho, \hat{c}_1, \theta). \tag{3.79}$$

It is noteworthy that the above two equations inherently imply $\hat{c}_1 + \hat{c}_2 = 1$. Equations (3.78) and (3.79) are nonlinear equations and the solutions can be obtained numerically. The two separate regions $(\hat{c}_1, c_{s1})$ and $(c_{s2}, \hat{c}_2)$ represent the metastable regions. Phases in metastable states will remain stable unless local energy fluctuations are sufficient to overcome the energy barrier.

Remark 3.3.1. *As long as $\theta \neq 0$, $\hat{c}_1$ and $\hat{c}_2$ cannot reach 0 or 1, since $\partial \Psi_{loc}^{ch2}/\partial c_1$ approaches positive infinite as $c_1 \to 0$. In physics, this implies equilibrium states always have some impurities.*

In the literature, an alternative choice for the local free energy function can be constructed by a fourth-order polynomial

$$\Psi_{loc}^{ch2} = c_1 \psi_1(\rho, \theta) + (1 - c_1)\psi_2(\rho, \theta) + C_{p4}^{ch2} c_1^2 (1 - c_1)^2, \tag{3.80}$$

wherein $c_{p4}^{ch2} > 0$ is a constant independent of c_1. Noticing that this polynomial model is essentially an isothermal theory, it can be regarded as an approximation to the regular solution theory (3.75) at a fixed temperature. The second-order derivative of Ψ_{loc}^{ch2} is

$$\frac{\partial^2 \Psi_{loc}^{ch2}}{\partial c_1^2} = 2C_{p4}^{ch2}(6c_1^2 - 6c_1 + 1). \tag{3.81}$$

83

The spinodal region for this model is $(1/2 - \sqrt{3}/6, 1/2 + \sqrt{3}/6)$ by solving $\partial^2 \Psi_{loc}^{ch2}/\partial c_1^2 = 0$. By substituting the fourth-order polynomial model (3.80) into the common tangent line equations (3.78)-(3.79), one may find that the local minima are always achieved at $c_1 = 0$ and 1, regardless of C_{p4}^{ch2}.

Following [41], the interface free energy σ for a planar surface parallel to the y-z plane is defined as

$$\sigma = \int_{-\infty}^{\infty} \left(\Psi_{loc}^{ch2}(\rho, c_1, \theta) + \frac{\gamma_1^{ch2}}{2} \left(\frac{dc_1}{dx} \right)^2 \right. $$
$$\left. - c_1 \psi_1(\rho, \theta) - (1 - c_1)\psi_2(\rho, \theta) \right) dx. \qquad (3.82)$$

Cahn and Hilliard assumed the density remains constant across the interface. Then the planar interface profile is governed by a minimization problem of the interface free energy σ with respect to c_1. The governing equation for the interface profile can be derived from the Euler-Lagrange equation of the minimization problem and it can be written as

$$\frac{\gamma_1^{ch2}}{2} \left(\frac{dc_1}{dx} \right)^2 = \Psi_{loc}^{ch2}(\rho, c_1, \theta) - c_1 \psi_1(\rho, \theta) - (1 - c_1)\psi_2(\rho, \theta). \qquad (3.83)$$

If the local free energy function is given by (3.80), the above equation can be reduced to

$$\frac{\gamma_1^{ch2}}{2} \left(\frac{dc_1}{dx} \right)^2 = C_{p4}^{ch2} c_1^2 (1 - c_1)^2. \qquad (3.84)$$

If one imposes that $c(0) = 1/2$, then the analytic expression of $c(x)$ can be obtained as

$$c(x) = \frac{1}{2} \tanh \left(\sqrt{\frac{C_{p4}^{ch2}}{2\gamma_1^{ch2}}} x \right) + \frac{1}{2}. \qquad (3.85)$$

84

If one defines the interfacial region to be $\{x|0.05 \leq c(x) \leq 0.95\}$, the interface width is $4.16\sqrt{\gamma_1^{ch2}/C_{p4}^{ch2}}$. The value of σ is $\sqrt{2C_{p4}^{ch2}\gamma_1^{ch2}}/6$. If the local free energy function is given by the regular solution theory (3.75), solving the equation (3.83) is not trivial. In [41], the authors derived an estimate of the interface profile by performing a polynomial approximation of the logarithm function near the critical temperature. Their results show that the interface width is proportional to $2\sqrt{\theta_c\gamma_1^{ch2}}/\sqrt{(\theta_c - \theta)R}$ and σ is proportional to $\sqrt{\gamma_1^{ch2}R}\theta_c\left(1 - \theta/\theta_c\right)^{1.5}$ when the temperature is close to the critical temperature.

3.3.2 A two-component fluid model

In this section, I adopt the free energy function (3.72). Since the number of component $\mathbf{N}$ is 2, the system has one component balance equation. Following (2.70)-(2.79), the constitutive relations can be written explicitly as

$$\boldsymbol{\xi}^{ch2} = \mathbf{0}, \tag{3.86}$$

$$\boldsymbol{\zeta}_1^{ch2} = \gamma_1^{ch2}\rho\nabla c_1, \tag{3.87}$$

$$\mu_1^{ch2} = \frac{\partial\Psi_{loc}^{ch2}}{\partial c_1} - \frac{1}{\rho}\nabla\cdot\left(\gamma_1^{ch2}\rho\nabla c_1\right), \tag{3.88}$$

$$\mathbf{h}_1^{ch2} = -\mathbf{M}_1^{ch2}\nabla\mu_1^{ch2}, \tag{3.89}$$

$$\mathbf{T}^{ch2} = \boldsymbol{\tau}^{ch2} + \boldsymbol{\varpi}^{ch2} - p^{ch2}\mathbf{I}, \tag{3.90}$$

$$\boldsymbol{\tau}^{ch2} = \bar{\mu}^{ch2}\left(\nabla\mathbf{u} + \nabla\mathbf{u}^T\right) + \bar{\lambda}^{ch2}\nabla\cdot\mathbf{u}\mathbf{I}, \tag{3.91}$$

$$\boldsymbol{\varpi}^{ch2} = -\gamma_1^{ch2}\rho\nabla c_1 \otimes \nabla c_1, \tag{3.92}$$

$$p^{ch2} = \rho^2\frac{\partial\Psi_{loc}^{ch2}}{\partial\rho}, \tag{3.93}$$

85

$$\mathbf{q}^{ch2} = -\boldsymbol{\kappa}^{ch2}\nabla\theta, \tag{3.94}$$

$$s^{ch2} = -\frac{\partial\Psi_{loc}^{ch2}}{\partial\theta}, \tag{3.95}$$

$$\iota^{ch2} = \Psi + \theta\frac{\partial\Psi_{loc}^{ch2}}{\partial\theta}, \tag{3.96}$$

$$\boldsymbol{\Pi}^{ch2} = \gamma_1^{ch2}\rho\nabla c_1\nabla\cdot\left(\mathbf{M}_1^{ch2}\nabla\mu_1^{ch2}\right) - \mu_1^{ch2}\mathbf{M}_1^{ch2}\nabla\mu_1^{ch2}. \tag{3.97}$$

The governing equations in conservation variables read

$$\frac{\partial\rho}{\partial t} + \nabla\cdot(\rho\mathbf{u}) = 0, \tag{3.98}$$

$$\frac{\partial(\rho c_1)}{\partial t} + \nabla\cdot(\rho c_1\mathbf{u}) = \nabla\cdot\left(\mathbf{M}_1^{ch2}\nabla\mu_1^{ch2}\right), \tag{3.99}$$

$$\frac{\partial(\rho\mathbf{u})}{\partial t} + \nabla\cdot\left(\rho\mathbf{u}\otimes\mathbf{u} + p^{ch2}\mathbf{I}\right) - \nabla\cdot\boldsymbol{\tau}^{ch2} - \nabla\cdot\boldsymbol{\varpi}^{ch2} = \rho\mathbf{b}, \tag{3.100}$$

$$\frac{\partial(\rho E)}{\partial t} + \nabla\cdot\left(\left(\rho E + p^{ch2}\right)\mathbf{u} - (\boldsymbol{\tau}^{ch2} + \boldsymbol{\varpi}^{ch2})\mathbf{u}\right) + \nabla\cdot\mathbf{q}^{ch2} + \nabla\cdot\boldsymbol{\Pi}^{ch2}$$

$$= \rho\mathbf{b}\cdot\mathbf{u} + \rho r. \tag{3.101}$$

Here, $\boldsymbol{\Pi}^{ch2}$ plays an analogous role to the "interstitial working" term in the Navier-Stokes-Korteweg equations (3.41)-(3.43). It represents the work done by the microstress $\boldsymbol{\zeta}_1^{ch2}$ and the energy flux due to the component flux $\mathbf{h}_1^{ch2}$. According to Theorem 2.3.1, the dissipation of this system is

$$\mathcal{D}^{ch2} = \frac{2\bar{\mu}^{ch2}}{\theta}\mathbf{L}^d : \mathbf{L}^d + \frac{1}{\theta}\left(\bar{\lambda}^{ch2} + \frac{2}{3}\bar{\mu}^{ch2}\right)(\nabla\cdot\mathbf{u})^2 + \nabla\mu_1^{ch2}\cdot\mathbf{M}_1^{ch2}\nabla\mu_1^{ch2}$$

$$+ \frac{1}{\theta^2}\nabla\theta\cdot\boldsymbol{\kappa}^{ch2}\nabla\theta. \tag{3.102}$$

Therefore, to ensure dissipation, it is sufficient to require that

$$\bar{\mu}^{ch2} \geq 0, \quad \bar{\lambda}^{ch2} + \frac{2}{3}\bar{\mu}^{ch2} \geq 0,$$

$$\mathbf{M}_1^{ch2} \text{ and } \boldsymbol{\kappa}^{ch2} \text{ are positive semi-definite.} \qquad (3.103)$$

Under the isothermal condition, the energy equation is decoupled from the system, and the governing equations become

$$\frac{\partial \rho}{\partial t} + \nabla \cdot (\rho \mathbf{u}) = 0, \qquad (3.104)$$

$$\frac{\partial (\rho c_1)}{\partial t} + \nabla \cdot (\rho c_1 \mathbf{u}) = \nabla \cdot \left(\mathbf{M}_1^{ch2}\nabla \mu_1^{ch2}\right), \qquad (3.105)$$

$$\frac{\partial (\rho \mathbf{u})}{\partial t} + \nabla \cdot \left(\rho \mathbf{u} \otimes \mathbf{u} + p^{ch2}\mathbf{I}\right) - \nabla \cdot \boldsymbol{\tau}^{ch2} - \nabla \cdot \boldsymbol{\varpi}^{ch2} = \rho\mathbf{b}. \qquad (3.106)$$

This system of equations is exactly the same model derived by Lowengrub and Truskinovsky in [145] based on a Lagrangian mechanics approach. This again confirms the validity of the modeling approach in Chapter 2. Applications and simulations of this isothermal two-phase flow model can be found in [134, 135].

Remark 3.3.2. *As the most popular two-phase flow model, model H was first derived in [106] as an initial attempt of coupling the Cahn-Hilliard equation with hydrodynamics. In 1996, Gurtin recovered this model using the concept of microforce balance [98]. Since then, model H has enjoyed a huge amount*

of popularity due to its simple mathematical structure. Indeed, the governing equations of model H can be viewed as the classical incompressible Navier-Stokes equations supplemented with a capillarity stress. Model H has been used to study capillary waves [111], Rayleigh-Taylor instabilities [67], contact-line dynamics [112], bubble formulation [141], and nematic liquid crystal [208], to name just a few. However, it has been noted by Joseph that the velocity field for multiphase fluid is not necessarily solenoidal [117]. In [145], Lowengrub and Truskinovsky considered the case when both components are incompressible. They derived a new set of balance equations for the so-called quasi-incompressible Cahn-Hilliard fluids. It is evident from their derivation that the velocity field is solenoidal only when densities of the two components are matched. Therefore, model H is not a proper model for problems with large density ratios, such as the Rayleigh-Taylor instability.

Remark 3.3.3. *In the preceding section, the interface profile given by (3.85) is based on the constant-density assumption made by Cahn and Hilliard [41]. However, this assumption is not necessarily true. For the system (3.104)-(3.106), the static equilibrium solutions are governed by*

$$\nabla \cdot \left(\mathbf{M}_1^{ch2} \nabla \mu_1^{ch2} \right) = 0, \tag{3.107}$$

$$\nabla p^{ch2} - \nabla \cdot \boldsymbol{\varpi}^{ch2} = 0, \tag{3.108}$$

which is a set of two differential equations for ρ and c_1. The variation of the density may affect the shape of the static interface. In [145], the authors showed that, if both components are incompressible and the free energy function

is a fourth-order double-well polynomial, the static equilibrium interface still has a hyperbolic-tangent shape, even if the densities of the two components do not match.

3.3.3 An N-component fluid model

The initial study of multicomponent system in the phase-field framework was carried out by Morral and Cahn [154], where the authors analyzed the spinodal decomposition in ternary alloys. Later, simulations of this model were performed by Chen [47]. Recently, the multicomponent Cahn-Hilliard diffusion theory has been applied to topology optimization [210] and four-component spinodal decomposition [133]. A three-component Navier-Stokes-Cahn-Hilliard system was constructed and simulated by Kim and Lowengrub [125]. In that work, the model derivation was similar to that of their previous two-component fluid model [145], and a fourth-order polynomial was employed as the free energy density function (see Figure 3.11). Here I construct an **N**-component Navier-Stokes-Cahn-Hilliard fluid model based on the framework of Chapter 2. The Helmholtz free energy density functional $\Psi^{ch\mathbf{N}}$ takes the form

$$\Psi^{ch\mathbf{N}}(\rho, c_1, \cdots, c_{\mathbf{N}-1}, \nabla c_1, \cdots, \nabla c_{\mathbf{N}-1}, \theta) = \Psi^{ch\mathbf{N}}_{loc}(\rho, c_1, \cdots, c_{\mathbf{N}-1}, \theta)$$
$$+ \sum_{\alpha=1}^{N-1} \frac{\gamma^{ch\mathbf{N}}_{\alpha}}{2} |\nabla c_{\alpha}|^2. \quad (3.109)$$

For a multicomponent system, the mass fractions can be listed in a vector as $\mathbf{c} = (c_1, \cdots, c_N)$, where $c_N = 1 - \sum_{\alpha=1}^{N-1} c_{\alpha}$. This concentration vector has to
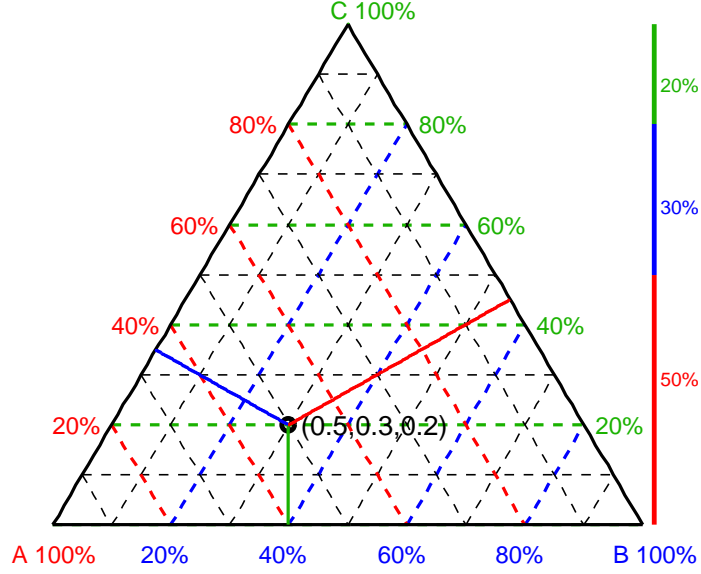
Figure 3.10: A regular 2-simplex. The three corners of this triangle represent pure components. The mixture's composition can be read according to the equidistant parallel dashed lines. For example, the black circle in this figure represents a mixture consisting of fifty percent of component A, thirty percent of component B, and twenty percent of component C.

be restricted within a Gibbs region $\mathcal{G}$:

$$\mathcal{G} := \left\{ \mathbf{c} \in \mathbb{R}^{\mathbf{N}} : 0 \leq c_\alpha \leq 1, \text{ for } 1 \leq \alpha \leq \mathbf{N}, \sum_{\alpha=1}^{\mathbf{N}} c_\alpha = 1 \right\}. \qquad (3.110)$$

This region $\mathcal{G}$ has only $\mathbf{N} - 1$ degrees of freedom and can thus be mapped to the barycentric coordinate of an $\mathbf{N} - 1$ regular simplex. For example, a 2-simplex, which is an equilateral triangle, is demonstrated in Figure 3.10. This 2-simplex can be conveniently used as the domain to define the local Helmholtz free energy density for a ternary system. In [125], a simple polynomial was

proposed as

$$\bar{\Psi}_{loc}^{ch\mathbf{N}}(\rho, c_1, \cdots, c_{\mathbf{N}}, \theta) = \sum_{\alpha=1}^{\mathbf{N}} \sum_{\beta=1, \beta \neq \alpha}^{\mathbf{N}} \chi_{\alpha,\beta}^{ch\mathbf{N}} c_\alpha^2 c_\beta^2 + \sum_{\alpha=1}^{\mathbf{N}} c_\alpha \psi_\alpha(\rho, \theta), \qquad (3.111)$$

$$c_{\mathbf{N}} = 1 - \sum_{\alpha=1}^{\mathbf{N}-1} c_\alpha. \qquad (3.112)$$

Here $\chi_{\alpha,\beta}^{ch\mathbf{N}}$ is a positive constant controlling the concavity of the energy, ψ_α is the free energy density function of the α-th component. Examples of this polynomial for $\mathbf{N} = 3$ are depicted over a 2-simplex in Figure 3.11. It is shown that this free energy density function has local minima at $\mathbf{c} = (1, 0, 0)$, $(0, 1, 0)$, and $(0, 0, 1)$ when $\chi_{\alpha,\beta}^{ch\mathbf{N}} > 0$. This free energy function can be regarded as a generalization to the fourth-order polynomial theory proposed in Section 3.3.2. Similarly, the regular solution theory (3.75) can be generalized to multicomponent systems as well. The local free energy density $\Psi_{loc}^{ch\mathbf{N}}$ is defined as

$$\Psi_{loc}^{ch\mathbf{N}}(\rho, c_1, \cdots, c_{\mathbf{N}}, \theta) = R\theta \sum_{\alpha=1}^{\mathbf{N}} (c_\alpha \log(c_\alpha)) + 2R \sum_{\alpha=1}^{\mathbf{N}} \sum_{\beta=1, \beta \neq \alpha}^{\mathbf{N}} \theta_{crit,\alpha,\beta}^{ch\mathbf{N}} c_\alpha c_\beta$$

$$+ \sum_{\alpha=1}^{\mathbf{N}} c_\alpha \psi_\alpha(\rho, \theta), \qquad (3.113)$$

$$c_{\mathbf{N}} = 1 - \sum_{\alpha=1}^{\mathbf{N}-1} c_\alpha, \qquad (3.114)$$

where R is the universal gas constant, $\theta_{crit,\alpha,\beta}^{ch\mathbf{N}}$ is the critical temperature for the pair of the α-th and the β-th components, and ψ_α is the free energy of the α-th component. In Figure 3.12, the local free energy density for a ternary system is illustrated over a 2-simplex at temperatures $\theta = 0.6\theta_{crit}^{ch\mathbf{N}}$

and $\theta = \theta_{crit}^{chN}$. It can be seen that when the temperature is below the critical temperature, there are three local minima. The local minima of the free energy Ψ_{loc}^{chN} are not located at pure phases, which implies the equilibrium states have impurities. The exact value of the thermodynamic equilibrium state can be found by constructing a common tangent plane to this free energy surface. When the temperature reaches above the critical temperature, the free energy function becomes globally convex, which favors a homogeneous mixture at the equilibrium state.

Remark 3.3.4. *One important generalization of the* **N***-component Navier-Stokes-Cahn-Hilliard fluid model is the multi-species tumour growth model. By adding constituent interaction effects to the free energy function* Ψ*, phase-field models have been systematically introduced to study the interactions among water, tumor cells, and host tissues [9, 57, 103]. One example Helmholtz free energy density function takes the following formulation [57].*

$$\Psi(\rho, c_1, \cdots, c_{N-1}, \nabla c_1, \cdots, \nabla c_{N-1}) = \Psi_{loc}(\rho, c_1, \cdots, c_{N-1}, \nabla c_1, \cdots, \nabla c_{N-1})$$
$$+ \sum_{\alpha=1}^{N-1} c_\alpha \Upsilon_\alpha + \sum_{\alpha=1}^{N-1} \frac{\gamma_\alpha}{2} |\nabla c_\alpha|^2, \quad (3.115)$$

wherein Υ_α *represents the nutrient concentration.*

Following (2.70)-(2.79), the constitutive relations can be written explicitly as

$$\boldsymbol{\xi}^{chN} = \mathbf{0}, \tag{3.116}$$

$$\boldsymbol{\zeta}_\alpha^{chN} = \gamma_\alpha^{chN} \rho \nabla c_\alpha, \qquad \text{for } \alpha = 1, \cdots, \mathbf{N} - 1, \tag{3.117}$$
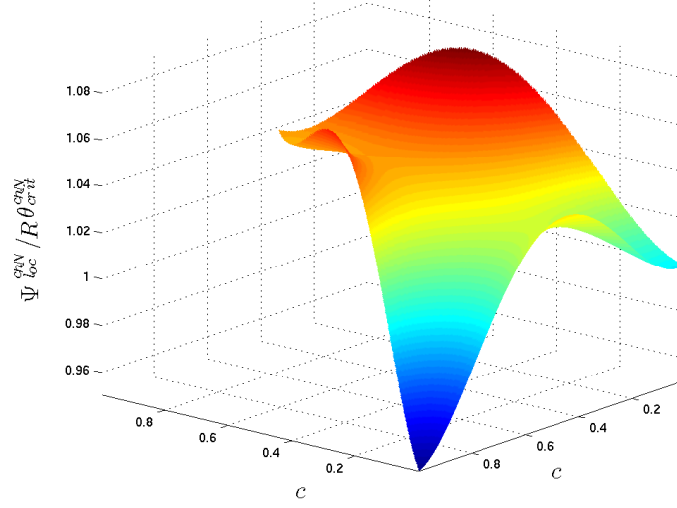
(a)
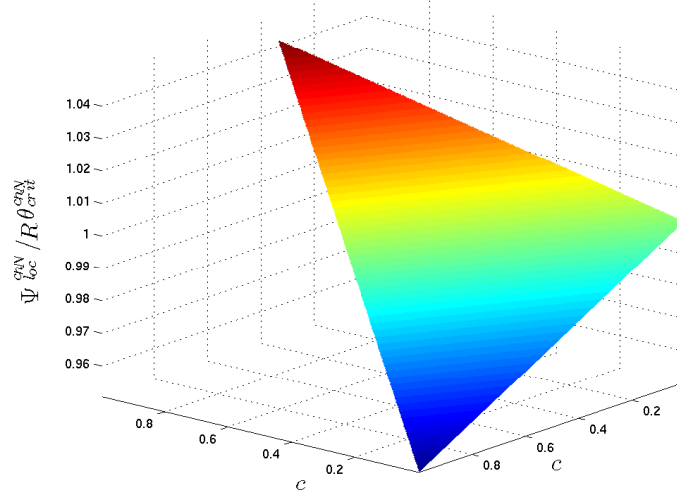
(b)

Figure 3.11: Illustrations of the free energy function $\Psi_{loc}^{ch\mathbf{N}}$ given by (3.111) for $\mathbf{N} = 3$. Here, $\psi_1(\rho, \theta) = 0.95R\theta_{crit}^{ch\mathbf{N}}$, $\psi_2(\rho, \theta) = R\theta_{crit}^{ch\mathbf{N}}$, $\psi_3(\rho, \theta) = 1.05R\theta_{crit}^{ch\mathbf{N}}$. In (a), $\chi_{\alpha,\beta}^{ch\mathbf{N}}$ is 0.5; in (b), $\chi_{\alpha,\beta}^{ch\mathbf{N}} = 0.0$ for $1 \le \alpha, \beta \le 3$.

93
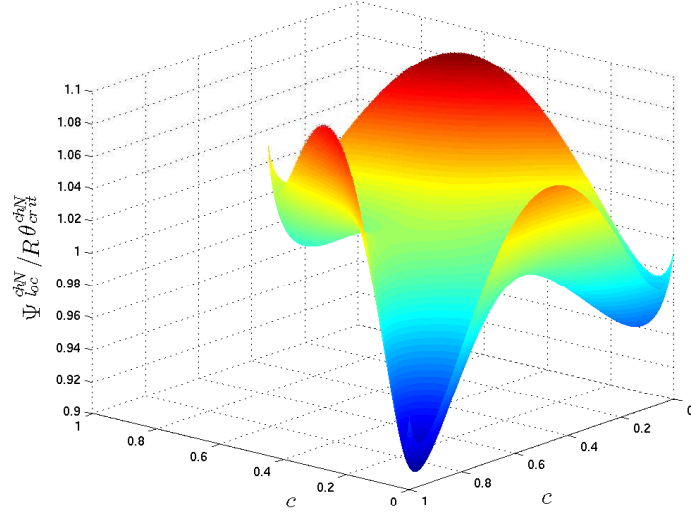
(a)
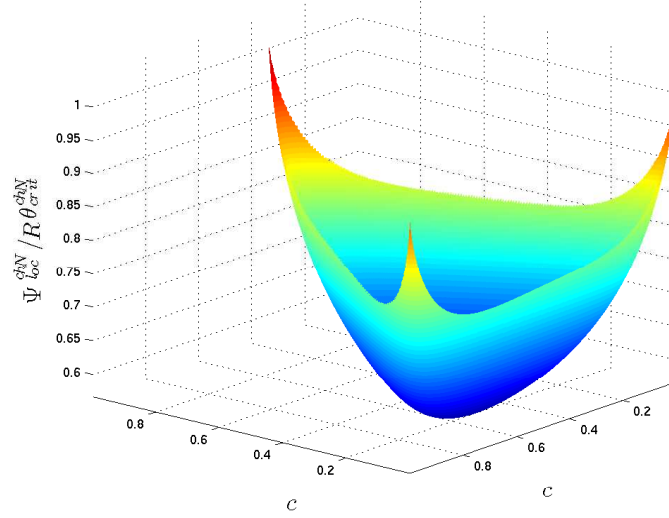
(b)

Figure 3.12: Illustration of the free energy function $\Psi_{loc}^{ch\mathbf{N}}$ given by (3.113) for $\mathbf{N} = 3$. $\psi_1(\rho,\theta) = 0.95R\theta_{crit}^{ch\mathbf{N}}$, $\psi_2(\rho,\theta) = R\theta_{crit}^{ch\mathbf{N}}$, $\psi_3(\rho,\theta) = 1.05R\theta_{crit}^{ch\mathbf{N}}$. Here, $\theta_{crit,\alpha,\beta}^{ch\mathbf{N}} = \theta_{crit}^{ch\mathbf{N}}$ is fixed for $1 \leq \alpha, \beta \leq 3$. In (a), $\theta = 0.6\theta_{crit}^{ch\mathbf{N}}$; in (b), $\theta = 1.0\theta_{crit}^{ch\mathbf{N}}$.

$$\mu_\alpha^{ch\mathbf{N}} = \frac{\partial \Psi_{loc}^{ch\mathbf{N}}}{\partial c_\alpha} - \frac{1}{\rho} \nabla \cdot \left(\rho \gamma_\alpha^{ch\mathbf{N}} \nabla c_\alpha \right), \quad \text{for } \alpha = 1, \cdots, \mathbf{N} - 1, \tag{3.118}$$

$$\mathbf{h}_\alpha^{ch\mathbf{N}} = -\mathbf{M}_\alpha^{ch\mathbf{N}} \nabla \mu_\alpha^{ch\mathbf{N}}, \tag{3.119}$$

$$\mathbf{T}^{ch\mathbf{N}} = \boldsymbol{\tau}^{ch\mathbf{N}} - p^{ch\mathbf{N}} \mathbf{I} + \boldsymbol{\varpi}^{ch\mathbf{N}}, \tag{3.120}$$

$$\boldsymbol{\tau}^{ch\mathbf{N}} = \bar{\mu}^{ch\mathbf{N}} \left(\nabla \mathbf{u} + \nabla \mathbf{u}^T \right) + \bar{\lambda}^{ch\mathbf{N}} \nabla \cdot \mathbf{u} \mathbf{I}, \tag{3.121}$$

$$p^{ch\mathbf{N}} = \rho^2 \frac{\partial \Psi_{loc}^{ch\mathbf{N}}}{\partial \rho}, \tag{3.122}$$

$$\boldsymbol{\varpi}^{ch\mathbf{N}} = -\rho \sum_{\alpha=1}^{\mathbf{N}-1} \left(\gamma_\alpha^{ch\mathbf{N}} \nabla c_\alpha \otimes \nabla c_\alpha \right), \tag{3.123}$$

$$\mathbf{q}^{ch\mathbf{N}} = -\boldsymbol{\kappa}^{ch\mathbf{N}} \nabla \theta, \tag{3.124}$$

$$s^{ch\mathbf{N}} = -\frac{\partial \Psi_{loc}^{ch\mathbf{N}}}{\partial \theta}, \tag{3.125}$$

$$\iota^{ch\mathbf{N}} = \Psi^{ch\mathbf{N}} - \theta \frac{\partial \Psi_{loc}^{ch\mathbf{N}}}{\partial \theta}, \tag{3.126}$$

$$\boldsymbol{\Pi}^{ch\mathbf{N}} = \sum_{\alpha=1}^{\mathbf{N}-1} \left[\gamma_\alpha^{ch\mathbf{N}} \rho \nabla c_\alpha \nabla \cdot \left(\mathbf{M}_\alpha^{ch\mathbf{N}} \nabla \mu_\alpha^{ch\mathbf{N}} \right) - \mu_\alpha^{ch\mathbf{N}} \mathbf{M}_\alpha^{ch\mathbf{N}} \nabla \mu_\alpha^{ch\mathbf{N}} \right]. \tag{3.127}$$

The governing equations for the **N**-component fluid read

$$\frac{\partial \rho}{\partial t} + \nabla \cdot (\rho \mathbf{u}) = 0, \tag{3.128}$$

$$\frac{\partial (\rho c_\alpha)}{\partial t} + \nabla \cdot (\rho c_\alpha \mathbf{u}) = \nabla \cdot \left(\mathbf{M}_\alpha^{ch\mathbf{N}} \nabla \mu_\alpha^{ch\mathbf{N}} \right), \tag{3.129}$$

$$\frac{\partial (\rho \mathbf{u})}{\partial t} + \nabla \cdot \left(\rho \mathbf{u} \otimes \mathbf{u} + p^{ch\mathbf{N}} \mathbf{I} \right) - \nabla \cdot \boldsymbol{\tau}^{ch\mathbf{N}} - \nabla \cdot \boldsymbol{\varpi}^{ch\mathbf{N}} = \rho \mathbf{b}, \tag{3.130}$$

$$\frac{\partial (\rho E)}{\partial t} + \nabla \cdot \left(\left(\rho E + p^{ch\mathbf{N}} \right) \mathbf{u} - (\boldsymbol{\tau}^{ch\mathbf{N}} + \boldsymbol{\varpi}^{ch\mathbf{N}}) \mathbf{u} \right) + \nabla \cdot \mathbf{q}^{ch\mathbf{N}} + \nabla \cdot \boldsymbol{\Pi}^{ch\mathbf{N}}$$

$$= \rho \mathbf{b} \cdot \mathbf{u} + \rho r. \tag{3.131}$$

According to Theorem 2.3.1, the dissipation $\mathcal{D}^{ch\mathbf{N}}$ for this system is

$$
\begin{aligned}
\mathcal{D}^{ch\mathbf{N}} =& \frac{2\bar{\mu}^{ch\mathbf{N}}}{\theta}\mathbf{L}^d : \mathbf{L}^d + \frac{1}{\theta}\left(\bar{\lambda}^{ch\mathbf{N}} + \frac{2}{3}\bar{\mu}^{ch\mathbf{N}}\right)(\nabla \cdot \mathbf{u})^2 \\
& + \frac{1}{\theta}\sum_{\alpha=1}^{\mathbf{N}-1}\nabla\mu_\alpha^{ch\mathbf{N}} \cdot \mathbf{M}_\alpha^{ch\mathbf{N}}\nabla\mu_\alpha^{ch\mathbf{N}} + \frac{1}{\theta^2}\nabla\theta \cdot \boldsymbol{\kappa}^{ch\mathbf{N}}\nabla\theta. \qquad (3.132)
\end{aligned}
$$

Therefore, to ensure dissipation, it is sufficient to require that

$$
\bar{\mu}^{ch\mathbf{N}} \geq 0, \quad \bar{\lambda}^{ch\mathbf{N}} + \frac{2}{3}\bar{\mu}^{ch\mathbf{N}} \geq 0,
$$

$$
\mathbf{M}_\alpha^{ch\mathbf{N}}, \text{ for } 1 \leq \alpha \leq \mathbf{N}-1, \text{ and } \boldsymbol{\kappa}^{ch\mathbf{N}} \text{ are positive semi-definite.} \qquad (3.133)
$$

3.4 A multicomponent multiphase fluid model

Multicomponent multiphase systems have been a research focus in metallurgy. Phase-field models have been applied to investigate many complicated phenomena, such as the dendritic growth of eutectic alloys [25, 119, 204]. In those research models, a conserved field, such as the mass fraction, is often used to identify different material components. This field is typically governed by a Cahn-Hilliard type diffusion equation. Meanwhile, a non-conserved field, such as the entropy density, is used to distinguish between liquid and solid phases, and is governed by an Allen-Cahn type diffusion equation [4]. This modeling approach is physically sound and practically successful [25, 50]. In the following, a multicomponent multiphase model will be built within a more general framework, where different mechanisms other than diffusion can enter into the theory. The object of this model is to describe the interactions among three familiar fluids: air, water and water vapor. At room temperature, air can

96

be viewed as a single uniform material. Hence it can be properly modeled by the perfect gas model. On the other side, water and water vapor are the same material in different phases and can be modeled by the van der Waals fluid model. Therefore, this system can be viewed as a two-component, multiphase flow problem. The interface between the two components is immiscible, which does not allow mass transfer. In contrast, phase transitions may take place across this interface between water and water vapor. Now let me propose the Helmholtz free energy density function Ψ^{awv} for this problem. Let c_1 denote the mass fraction of the van der Waals fluid, then the Helmholtz free energy function of this system can be written as

$$\Psi^{awv}(\rho, \nabla\rho, c_1, \nabla c_1, \theta) = \tilde{\Psi}^{awv}(\rho, \nabla\rho, c_1, \theta) + \frac{\gamma_1^{awv}}{2}|\nabla c_1|^2, \tag{3.134}$$

$$\tilde{\Psi}^{awv}(\rho, \nabla\rho, c_1, \theta) = g(c_1)\Psi^{vdw}(\rho, \nabla\rho, \theta) + (1 - g(c_1))\Psi^{pg}(\rho, \theta)$$
$$+ R\theta\left(c_1 \log(c_1) + (1 - c_1)\log(1 - c_1)\right) + 2R\theta_{crit,i}^{awv}c_1(1 - c_1), \tag{3.135}$$

$$\Psi^{vdw}(\rho, \nabla\rho, \theta) = -a\rho + R\theta \log\left(\frac{\rho}{b - \rho}\right) - C_v^{vdw}\theta \log\left(\frac{\theta}{\theta_{ref}^{vdw}}\right)$$
$$+ C_v^{vdw}\theta + \frac{\lambda^{awv}}{2\rho}|\nabla\rho|^2, \tag{3.136}$$

$$\Psi^{pg}(\rho, \nabla\rho, \theta) = R\theta \log(\rho) - C_v^{pg}\theta \log\left(\frac{\theta}{\theta_{ref}^{pg}}\right) + C_v^{pg}\theta. \tag{3.137}$$

In this model, $g(c_1)$ is a smooth function of c_1 satisfying

$$g(0) = 0, \qquad g(1) = 1, \qquad 0 \leq g(c_1) \leq 1. \tag{3.138}$$

A trivial choice is $g(c_1) = c_1$. Here, a, b, C_v^{vdw}, θ_{ref}^{vdw}, and λ^{awv} characterize the thermodynamic properties of the van der Waals fluid; θ_{ref}^{pg} and C_v^{pg} describe the

97

thermodynamic properties of the perfect gas; γ_1^{awv} and $\theta_{crit,i}^{awv}$ are the interfacial parameter and the critical temperature for the immiscible interface between the perfect gas and the van der Waal fluid. The Helmholtz free energy function given by (3.134)-(3.137) can be rewritten as

$$\Psi^{awv}(\rho, \nabla\rho, c_1, \nabla c_1, \theta) = \Psi_{loc}^{awv}(\rho, c_1, \theta) + g(c_1)\frac{\lambda^{awv}}{2\rho}|\nabla\rho|^2 + \frac{\gamma_1^{awv}}{2}|\nabla c_1|^2,$$

(3.139)

$$\Psi_{loc}^{awv}(\rho, c_1, \theta) = g(c_1)\left(-a\rho + R\theta \log\left(\frac{\rho}{b - \rho}\right) - C_v^{vdw}\theta \log\left(\frac{\theta}{\theta_{ref}^{vdw}}\right) \right.$$

$$\left. + C_v^{vdw}\theta \right) + (1 - g(c_1))\left(R\theta \log(\rho) - C_v^{pg}\theta \log\left(\frac{\theta}{\theta_{ref}^{pg}}\right) + C_v^{pg}\theta \right)$$

$$+ R\theta\left(c_1 \log(c_1) + (1 - c_1)\log(1 - c_1) \right) + 2R\theta_{crit,i}^{awv}c_1(1 - c_1). \qquad (3.140)$$

According to the formulation (3.139)-(3.140), the Helmholtz free energy function Ψ^{awv} can be viewed as an interpolation of the perfect gas model and the van der Waals fluid model by using the regular solution theory. The free energy density function Ψ^{awv} is a special case of the particular formulation given in Section 2.2.4, where $g(c_1)\lambda^{awv}$ is a capillarity coefficient depending on c_1. In this model, there are a number of parameters that need to be carefully calibrated in order to mimic the complex flow reliably. First of all, there are two critical temperatures in this model. One is the minimum temperature for which the perfect gas and the van der Waals fluid can coexist as a homogeneous mixture. This temperature is denoted as $\theta_{crit,i}^{awv}$, where the subscript i represents the immiscible interface. Another critical temperature is the critical temperature for the van der Waals fluid given by the formula (3.29). This
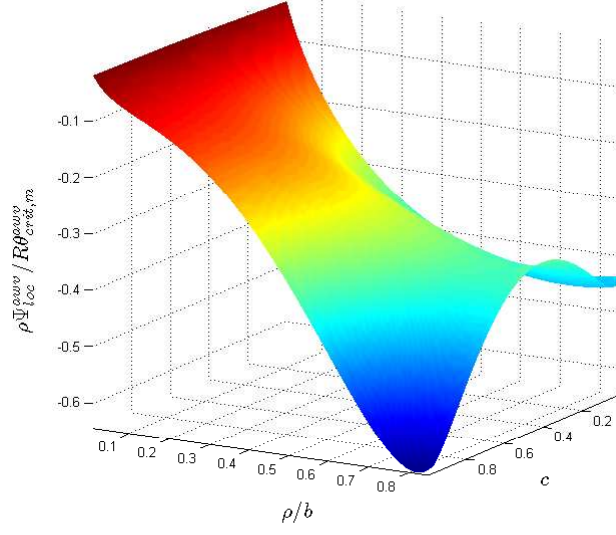
(a)
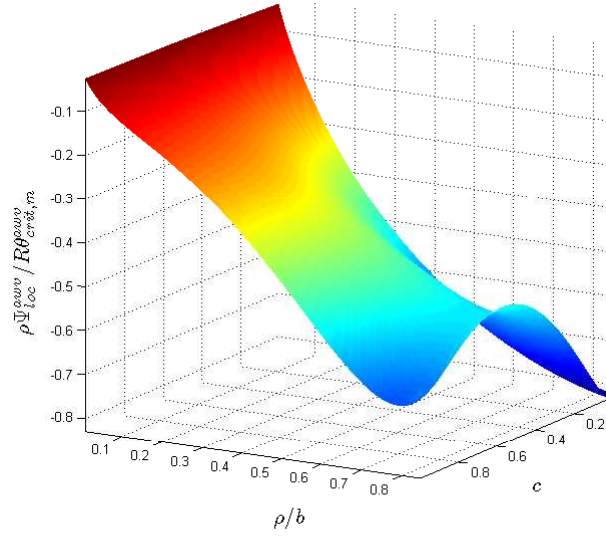
(b)

Figure 3.13: Illustration of the free energy function $\rho\Psi_{loc}^{awv}$ given by (3.140), with $g(c_1) = c_1$: (a) $\theta = 0.65\theta_{crit,m}^{awv}$, (b) $\theta = 0.75\theta_{crit,m}^{awv}$.

critical temperature is denoted as $\theta_{crit,m}^{awv}$, where the subscript m represents the miscible interface. Second, there are two reference values, i.e., θ_{ref}^{vdw} and θ_{ref}^{pg}. In this model, these reference values eventually become weights added to the perfect gas and the van der Waals free energy respectively. These values may affect the relative local minima of the free energy function. Third, there are two heat capacities at constant volume, denoted by C_v^{pg} and C_v^{vdw}. Classical empirical formulas may give rough estimates of these values based on the molecular translation, rotation, and vibration degrees of freedom. It is estimated that for diatomic gases, such as nitrogen and oxygen, the heat capacity at constant volume is approximately $3.5R$; the heat capacity at constant volume for water is about $3R$. Fourth, there are two interfacial parameters and, correspondingly, two interfacial energy terms. One energy term is related to the immiscible interface and is given by $\gamma_1^{awv}|\nabla c_1|^2/2$; another one is used to characterize the miscible interface between water and water vapor and is given by $\lambda^{awv}g(c_1)|\nabla\rho|^2/2\rho$. This interfacial energy will vanish when in pure air, i.e., $c_1 = 0$.

In Figure 3.13, the free energy function $\rho\Psi_{loc}^{awv}$ is depicted at the temperatures $0.65\theta_{crit,m}^{awv}$ and $0.75\theta_{crit,m}^{awv}$. In those figures, the parameters are chosen as $\theta_{crit,m}^{awv} = \theta_{crit,i}^{awv}/2$, $\theta_{ref}^{vdw} = 0.4\theta_{crit,m}$, $\theta_{ref}^{pg} = 0.2\theta_{crit,m}$, $C_v^{pg} = 3.5R$, and $C_v^{vdw} = 3R$. It can be seen from Figure 3.13 that the local free energy function has three local minima when below the critical temperature. These minima correspond to the air, water and water vapor phases respectively. When the temperature raises from $0.65\theta_{crit,m}^{awv}$ to $0.75\theta_{crit,m}^{awv}$, the shape of the local free

100

energy function changes and the position of the local minima moves. These changes correspond to a phase transition process of the multicomponent multiphase fluid.

Now let me give the governing equations for this air, water, water vapor system. According to (2.70)-(2.79), the constitutive relations of this problem read

$$\boldsymbol{\xi}^{awv} = \lambda^{awv} g(c_1) \nabla \rho, \tag{3.141}$$

$$\boldsymbol{\zeta}_1^{awv} = \gamma_1^{awv} \rho \nabla c_1, \tag{3.142}$$

$$\mu_1^{awv} = \frac{\partial \Psi_{loc}^{awv}}{\partial c_1} + g'(c_1) \frac{\lambda^{awv}}{2\rho} |\nabla \rho|^2 - \frac{1}{\rho} \nabla \cdot (\gamma_1^{awv} \rho \nabla c_1), \tag{3.143}$$

$$\mathbf{h}_1^{awv} = -\mathbf{M}_1^{awv} \nabla \mu_1^{awv}, \tag{3.144}$$

$$\mathbf{T}^{awv} = \boldsymbol{\tau}^{awv} + \boldsymbol{\varpi}^{awv} + \boldsymbol{\varsigma}^{awv} - p^{awv} \mathbf{I}, \tag{3.145}$$

$$\boldsymbol{\tau}^{awv} = \bar{\mu}^{awv} \left(\nabla \mathbf{u} + \nabla \mathbf{u}^T \right) + \bar{\lambda}^{awv} \nabla \cdot \mathbf{u} \mathbf{I}, \tag{3.146}$$

$$\boldsymbol{\varpi}^{awv} = -\gamma_1^{awv} \rho \nabla c_1 \otimes \nabla c_1, \tag{3.147}$$

$$\boldsymbol{\varsigma}^{awv} = -\lambda^{awv} g(c_1) \rho \nabla \rho \otimes \nabla \rho + \lambda^{awv} g(c_1) \left(\rho \Delta \rho + \frac{1}{2} |\nabla \rho|^2 \right) \mathbf{I}, \tag{3.148}$$

$$p^{awv} = \rho^2 \frac{\partial \Psi_{loc}^{awv}}{\partial \rho}, \tag{3.149}$$

$$\mathbf{q}^{awv} = -\boldsymbol{\kappa}^{awv} \nabla \theta, \tag{3.150}$$

$$s^{awv} = -\frac{\partial \Psi_{loc}^{awv}}{\partial \theta}, \tag{3.151}$$

$$\iota^{awv} = \Psi^{awv} - \theta \frac{\partial \Psi_{loc}^{awv}}{\partial \theta}, \tag{3.152}$$

$$\boldsymbol{\Pi}^{awv} = \rho \nabla \cdot \mathbf{u} \boldsymbol{\xi}^{awv} + \gamma_1^{awv} \nabla \cdot \mathbf{h}_1^{awv} \nabla c_1 - \mu_1^{awv} \mathbf{M}_1^{awv} \nabla \mu_1^{awv}. \tag{3.153}$$

And the governing equations in conservation variables can be written explicitly as

$$\frac{\partial \rho}{\partial t} + \nabla \cdot (\rho \mathbf{u}) = 0, \tag{3.154}$$

$$\frac{\partial (\rho c_1)}{\partial t} + \nabla \cdot (\rho c_1 \mathbf{u}) = -\nabla \cdot \mathbf{h}_1^{awv}, \tag{3.155}$$

$$\frac{\partial (\rho \mathbf{u})}{\partial t} + \nabla \cdot (\rho \mathbf{u} \otimes \mathbf{u} + p^{awv}\mathbf{I}) = \nabla \cdot \boldsymbol{\tau}^{awv} + \nabla \cdot \boldsymbol{\varpi}^{awv} + \nabla \cdot \boldsymbol{\varsigma}^{awv} + \rho \mathbf{b}, \tag{3.156}$$

$$\frac{\partial (\rho E)}{\partial t} + \nabla \cdot ((\rho E + p^{awv})\mathbf{u}) = \nabla \cdot \left((\boldsymbol{\tau}^{awv} + \boldsymbol{\varpi}^{awv} + \boldsymbol{\varsigma}^{awv}) \mathbf{u} - \boldsymbol{\Pi}^{awv} \right.$$
$$\left. - \mathbf{q}^{awv} \right) + \rho \mathbf{b} \cdot \mathbf{u} + \rho r. \tag{3.157}$$

According to Theorem 2.3.1, the dissipation $\mathcal{D}^{awv}$ of this system is

$$\mathcal{D}^{awv} = \frac{2\bar{\mu}^{awv}}{\theta} \mathbf{L}^d : \mathbf{L}^d + \frac{1}{\theta} \left(\bar{\lambda}^{awv} + \frac{2}{3}\bar{\mu}^{awv} \right) (\nabla \cdot \mathbf{u})^2 + \frac{1}{\theta} \nabla \mu_1^{awv} \cdot \mathbf{M}_1^{awv} \nabla \mu_1^{awv}$$
$$+ \frac{1}{\theta^2} \nabla \theta \cdot \boldsymbol{\kappa}^{awv} \nabla \theta. \tag{3.158}$$

Therefore, to fulfill the second law of thermodynamics, it is sufficient to require that

$$\bar{\mu}^{awv} \geq 0, \quad \bar{\lambda}^{awv} + \frac{2}{3}\bar{\mu}^{awv} \geq 0,$$
$$\mathbf{M}_1^{awv} \text{ and } \boldsymbol{\kappa}^{awv} \text{ are positive semi-definite.} \tag{3.159}$$

Chapter 4

Isogeometric analysis

"Well done is quckly done."

— Caesar Augustus

This chapter first gives a concise introduction to isogeometric analysis, with particular emphasis on the NURBS-based technology [15, 52, 108]. Then the periodic transformation operator is introduced, with the aim of simplifying strong enforcement of periodic boundary conditions within the isogeometric context. After that, the software design of `PERIGEE`, a general-purpose scalable isogeometric analysis code framework, is discussed.

4.1 B-splines and NURBS preliminaries

4.1.1 B-splines

Let n and $\mathfrak{p}$ denote the dimensionality of the basis function space and the polynomial degree respectively. A knot vector Ξ is a one-dimensional non-decreasing coordinate set

$$\Xi = \left\{ \xi_1, \xi_2 \cdots, \xi_{n+\mathfrak{p}+1} \right\}, \tag{4.1}$$

where ξ_i is the i-th knot and satisfies

$$\xi_1 \leq \xi_2 \leq \cdots \leq \xi_{n+\mathfrak{p}+1}. \tag{4.2}$$

Given the knot vector Ξ and the polynomial degree p, B-spline basis functions are defined through the Cox-de Boor recursion formula [26, 56]:

$$N_{i,0}(\xi) = \begin{cases} 1 & \xi_i \leq \xi < \xi_{i+1}, \\ 0 & \text{otherwise}, \end{cases} \tag{4.3}$$

$$N_{i,\mathrm{p}}(\xi) = \frac{\xi - \xi_i}{\xi_{i+\mathrm{p}} - \xi_i} N_{i,\mathrm{p}-1}(\xi) + \frac{\xi_{i+\mathrm{p}+1} - \xi}{\xi_{i+\mathrm{p}+1} - \xi_{i+1}} N_{i+1,\mathrm{p}-1}(\xi). \tag{4.4}$$

B-spline basis functions given by the above definitions are pointwise non-negative and linear independent. The i-th basis function is compactly supported on the interval $[\xi_i, \xi_{i+\mathrm{p}+1}]$, and $\sum_{i=1}^{n} N_{i,\mathrm{p}}(\xi) = 1$. Moreover, if the i-th knot is repeated $\mathfrak{k}$ times, the basis functions are $C^{\mathrm{p}-\mathfrak{k}}$-continuous at ξ_i. An example of quadratic B-spline basis functions built from the knot vector $\Xi = \{0, 0, 0, 1, 2, 2, 3, 4, 5, 5, 5\}$ is demonstrated in Figure 4.1. These basis functions are C^1-continuous except at the knots $\xi = 0$, 2, and 5 due to the knot repetitions.

4.1.2 Non-Uniform Rational B-Splines

The one-dimensional Non-Uniform Rational B-Spline (NURBS) basis functions of degree p are defined by a knot vector $\Xi = \{\xi_1, \xi_2 \cdots, \xi_{n+\mathrm{p}+1}\}$ and a weight vector $\{\mathrm{w}_1, \cdots, \mathrm{w}_n\}$ as

$$R_i^{\mathrm{p}}(\xi) = \frac{\mathrm{w}_i N_i^{\mathrm{p}}(\xi)}{W(\xi)}, \tag{4.5}$$

where $W(\xi)$ is the weight function given by

$$W(\xi) = \sum_{j=1}^{n} \mathrm{w}_j N_j^{\mathrm{p}}(\xi). \tag{4.6}$$

104
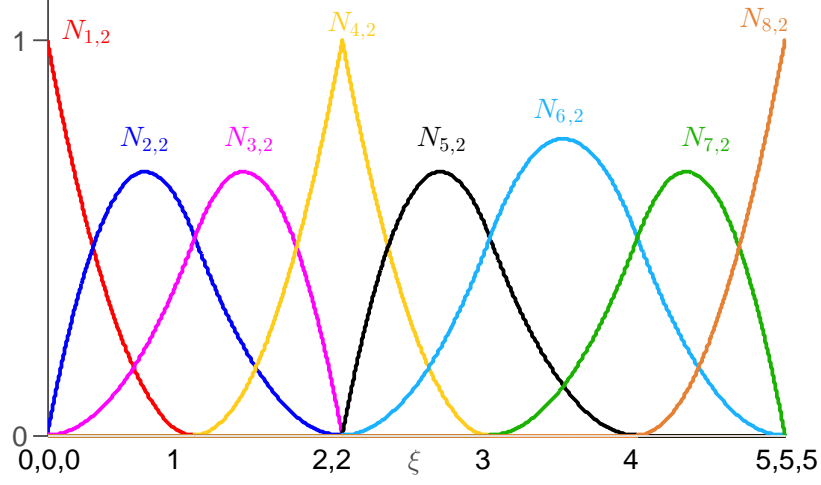
Figure 4.1: Quadratic B-spline basis functions built from the knot vector $\Xi = \{0, 0, 0, 1, 2, 2, 3, 4, 5, 5, 5\}$.

Let $\Xi_1 = \{\xi_1, \cdots, \xi_{n+\mathfrak{p}+1}\}$, $\Xi_2 = \{\eta_1, \cdots, \eta_{m+\mathfrak{q}+1}\}$, and $\Xi_3 = \{\zeta_1, \cdots, \zeta_{l+\mathfrak{r}+1}\}$ be three knot vectors, and $\mathsf{N}_{i,\mathfrak{p}}(\xi)$, $\mathsf{M}_{j,\mathfrak{q}}(\eta)$, and $\mathsf{L}_{k,\mathfrak{r}}(\zeta)$ be the corresponding univariate B-spline basis functions of polynomial degrees $\mathfrak{p}$, $\mathfrak{q}$, and $\mathfrak{r}$ respectively. Then the two and three-dimensional NURBS basis functions are defined as

$$\mathsf{R}_{i,j}^{\mathfrak{p},\mathfrak{q}}(\xi, \eta) = \frac{\mathsf{N}_i^{\mathfrak{p}}(\xi)\mathsf{M}_j^{\mathfrak{q}}(\eta)\mathsf{w}_{i,j}}{\sum_{\hat{i}=1}^{n}\sum_{\hat{j}=1}^{m}\mathsf{N}_{\hat{i}}^{\mathfrak{p}}(\xi)\mathsf{M}_{\hat{j}}^{\mathfrak{q}}(\eta)\mathsf{w}_{\hat{i},\hat{j}}}, \tag{4.7}$$

$$\mathsf{R}_{i,j,k}^{\mathfrak{p},\mathfrak{q},\mathfrak{r}}(\xi, \eta, \zeta) = \frac{\mathsf{N}_i^{\mathfrak{p}}(\xi)\mathsf{M}_j^{\mathfrak{q}}(\eta)\mathsf{L}_k^{\mathfrak{r}}(\zeta)\mathsf{w}_{i,j,k}}{\sum_{\hat{i}=1}^{n}\sum_{\hat{j}=1}^{m}\sum_{\hat{k}=1}^{l}\mathsf{N}_{\hat{i}}^{\mathfrak{p}}(\xi)\mathsf{M}_{\hat{j}}^{\mathfrak{q}}(\eta)\mathsf{L}_{\hat{k}}^{\mathfrak{r}}\mathsf{w}_{\hat{i},\hat{j},\hat{k}}}. \tag{4.8}$$

Let $\mathsf{P} := \{\mathsf{P}_i\}_{i=1}^{n}$ be a set of one-dimensional control points, a NURBS curve is defined as

$$\mathsf{L}(\xi) = \sum_{i=1}^{n} \mathsf{R}_i^{\mathfrak{p}}(\xi)\mathsf{P}_i. \tag{4.9}$$

105
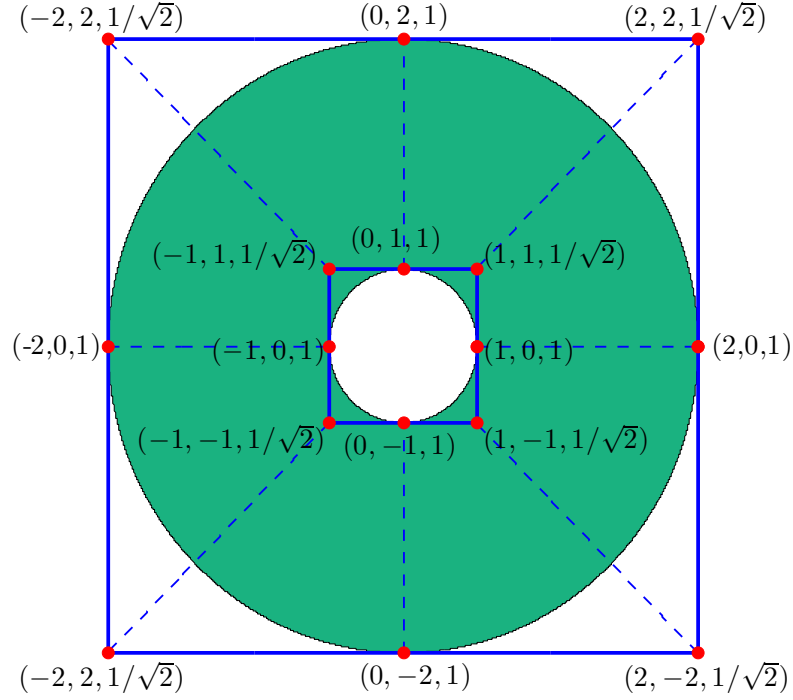
Figure 4.2: Illustration of an annular surface constructed by NURBS basis functions [24]. The NURBS basis functions in the circumferential direction are quadratic and are built from the knot vector $\Xi_1 = \{0, 0, 0, 1, 1, 2, 2, 3, 3, 4, 4, 4\}$; the NURBS basis functions in the radial direction are linear and are built from the knot vector $\Xi_2 = \{0, 0, 1, 1\}$. The red dots represent the control points, and the 3-tuples give the control points' x-coordinates, y-coordinates, and weights.

If $\mathsf{P} := \{\mathsf{P}_{i,j}\}_{i=1,j=1}^{n,m}$ is a set of two-dimensional control points, a NURBS surface is defined as

$$\mathsf{S}(\xi, \eta) = \sum_{i=1,j=1}^{n,m} \mathsf{R}_{i,j}^{\mathfrak{p},\mathfrak{q}}(\xi, \eta)\mathsf{P}_{i,j}. \tag{4.10}$$

Similarly, if $\mathsf{P} := \{\mathsf{P}_{i,j,k}\}_{i=1,j=1,k=1}^{n,m,l}$ denotes a set of three-dimensional control points, a NURBS volume is defined as

$$\mathsf{V}(\xi, \eta, \zeta) = \sum_{i=1,j=1,k=1}^{n,m,l} \mathsf{R}_{i,j,k}^{\mathfrak{p},\mathfrak{q},\mathfrak{r}}(\xi, \eta, \zeta)\mathsf{P}_{i,j,k}. \tag{4.11}$$

The NURBS basis functions inherit all the appealing features of B-splines: they are pointwise non-negative, linear independent, have compact support, form a partition of unity, and have an easy control of continuity. Consequently, an object constructed by NURBS is affine covariant, has convex hull, and is variation diminishing. Moreover, the significance of NURBS geometry is that it is capable of representing conic sections, which are familiar in engineering designs. An example of an annular surface constructed by NURBS is illustrated in Figure 4.2.

NURBS-based isogeometric analysis makes use of NURBS as the basis for representing computational geometry as well as the basis for the solution space in the numerical method. Convergence analysis has been studied for this approach [19], and existing successful applications manifest its practicability [16, 17, 34, 54, 60, 83, 86]. Furthermore, theoretical analysis has shown that splines with high-order continuity have superior approximation properties [73] and robustness [140], compared with traditional finite element methods.

107

Nevertheless, NURBS-based technology has several limitations in both geometry design and isogeometric analysis. First, it is often necessary to create and join multiple NURBS patches for complicated geometry objects. This process requires sophisticated design technology and complicates the whole analysis process. Second, the structure of NURBS basis functions necessitates global refinement when inserting knots, which is a deficiency in both design and analysis. T-spline-based isogeometric analysis, as a recently introduced technology, has been investigated to remedy the above deficiencies. Introduced in [174], T-splines can model complex geometries in a single patch. The topological flexibility of T-splines allows local refinement and local coarsening. These attributes make T-splines a promising technology for isogeometric analysis [171].

4.2 Strong imposition of periodic boundary conditions

Periodic boundary conditions are typically used when the domain and the physical effects are periodic in nature. In isogeometric analysis, most interesting geometries are not represented by periodic NURBS basis functions, which makes the strong imposition of periodic boundary conditions non-trivial. In this section, a new numerical technique will be introduced. This technique can transform a class of open-knot NURBS basis functions to periodic NURBS basis functions, while maintaining the original geometrical representation. This transformation simplifies strong impositions of periodic boundary conditions in implementations.

4.2.1 Periodic boundary conditions

In the rest part of this section, I will restrict my discussion to a univariate NURBS curve for simplicity. Due to the tensor product structure, the results can be generalized to multivariate cases. To define periodic boundary conditions, it is necessary to require the domain to be periodic first.

Definition 4.2.1. *A NURBS curve* $\mathbf{x}(\xi) = \mathsf{L}(\xi)$ *defined on the parametric domain* $\Xi = \{\xi_1, \xi_2 \cdots, \xi_{n+\mathtt{p}+1}\}$ *is* C^q*-periodic if*

$$\frac{d^k \mathbf{x}}{d\xi^k}(\xi_1) = \frac{d^k \mathbf{x}}{d\xi^k}(\xi_{n+\mathtt{p}+1}), \qquad for \ k = 0, \dots, q. \tag{4.12}$$

Definition 4.2.2. $\hat{\mathsf{f}}(\xi) := \mathsf{f}(\mathbf{x}(\xi))$ *satisfies the* C^r*-periodic boundary condition, if it is defined on a* C^q*-periodic NURBS curve* $\mathbf{x}(\xi)$, $q \geq r$, *and*

$$\frac{d^k \hat{\mathsf{f}}}{d\xi^k}(\xi_1) = \frac{d^k \hat{\mathsf{f}}}{d\xi^k}(\xi_{n+\mathtt{p}+1}), \qquad for \ k = 0, \dots, r. \tag{4.13}$$

By invoking the chain rule, it is easy to see that if $\hat{\mathsf{f}}(\xi) = \mathsf{f}(\mathbf{x}(\xi))$ is C^r-periodic, then

$$\frac{d^k \mathsf{f}}{dx^k}(\mathbf{x}(\xi_1)) = \frac{d^k \mathsf{f}}{dx^k}(\mathbf{x}(\xi_{n+\mathtt{p}+1})) \tag{4.14}$$

holds for $k = 0, \dots, q$. Consider a function $\hat{\mathsf{f}}(\xi)$ spanned by the open-knot NURBS basis functions $\mathsf{R}_i^{\mathtt{p}}(\xi)$, i.e., $\hat{\mathsf{f}} = \sum_{i=1}^{n} \hat{\mathsf{f}}_i \mathsf{R}_i^{\mathtt{p}}$, then the C^1-periodic boundary condition leads to the following algebraic equations.

$$\hat{\mathsf{f}}_1 = \hat{\mathsf{f}}_n, \tag{4.15}$$

$$(\hat{\mathsf{f}}_2 - \hat{\mathsf{f}}_1) \frac{\mathsf{w}_2}{\mathsf{w}_1} \frac{d\mathsf{N}_2^{\mathtt{p}}}{d\xi}(\xi_1) = (\hat{\mathsf{f}}_{n-1} - \hat{\mathsf{f}}_n) \frac{\mathsf{w}_{n-1}}{\mathsf{w}_n} \frac{d\mathsf{N}_{n-1}^{\mathtt{p}}}{d\xi}(\xi_{n+\mathtt{p}+1}). \tag{4.16}$$
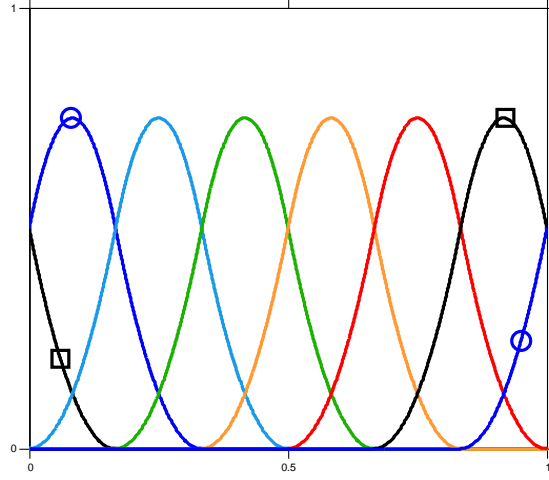
Figure 4.3: One-dimensional quadratic C^1-periodic B-spline basis functions. The squares and the circles indicate the control variables which are set equal to enforce the C^1-periodic boundary condition.

The above constraints need to be explicitly taken into account when assembling the global matrices. From an implementation point of view, this process may require additional data structures and necessitate extra calls for shape function routines. To avoid these procedures in programming, periodic NURBS basis functions are introduced.

Definition 4.2.3. *A NURBS basis $\{\mathsf{R}_i^{per,\mathfrak{p}}\}$ is $C^{\mathfrak{r}}$-periodic, $0 \leq \mathfrak{r} \leq \mathfrak{p} - 1$, if for any function*

$$\hat{\mathsf{f}}(\xi) = \sum_{i=1}^{n} \hat{\mathsf{f}}_i \mathsf{R}_i^{per,\mathfrak{p}},$$

with $\hat{\mathsf{f}}_i = \hat{\mathsf{f}}_{n-(\mathfrak{r}+1)+i}$ for $i = 1, \cdots, \mathfrak{r} + 1$, $\hat{\mathsf{f}}$ is $C^{\mathfrak{r}}$-periodic.

The classical notion of periodic basis as a set of basis functions obtained

110

by recursively replicating a reference basis function no longer holds in the context of NURBS due to the presence of the weights. Hence, the Definition 4.2.3 is a generalization of the traditional concept of periodic basis. The use of a periodic NURBS basis allows us to enforce the periodic boundary conditions simply by modifying the global ID array [107]. In Figure 4.3, a set of periodic quadratic C^1-periodic B-spline basis functions is plotted. By taking the ID array as $\{1, 2, 3, 4, 5, 6, 1, 2\}$, C^1-periodic boundary condition is automatically enforced for any function spanned by such basis functions.

4.2.2 Bézier extraction operator and periodic transformation operator

The Bézier extraction operator is a linear operator that maps the Bernstein polynomials to the B-spline basis functions [27, 172]. In particular, the Bézier extraction operator can be represented locally in each element. Let $\bar{\mathsf{B}}(\xi) = \{\mathsf{B}_1(\xi); \cdots ; \mathsf{B}_{\mathfrak{p}+1}(\xi)\}^T$ denote the Bernstein polynomial vector of degree $\mathfrak{p}$; $\bar{\mathsf{N}}^e(\xi) = \{\mathsf{N}_1^e(\xi); \cdots ; \mathsf{N}_{\mathfrak{p}+1}^e(\xi)\}^T$ denote the B-spline basis function vector in element e. Given the Bézier extraction operator $\mathbb{C}^e \in \mathbb{R}^{(\mathfrak{p}+1)\times(\mathfrak{p}+1)}$ in element e, $\bar{\mathsf{N}}^e(\xi)$ can be written as

$$\bar{\mathsf{N}}^e(\xi) = \mathbb{C}^e \bar{\mathsf{B}}(\xi). \tag{4.17}$$

Let $\bar{\mathsf{N}}(\xi) = \{\mathsf{N}_1^{\mathfrak{p}}(\xi); \cdots ; \mathsf{N}_n^{\mathfrak{p}}(\xi)\}^T$ denote a B-spline basis function vector generated by a knot vector $\Xi = \{\xi_1, \cdots, \xi_{n+\mathfrak{p}+1}\}$; $\bar{\mathsf{B}}(\xi) = \{\mathsf{B}_1(\xi); \cdots ; \mathsf{B}_{n+m}(\xi)\}^T$ denote the C^0 Bézier basis function vector generated by inserting m additional knots into Ξ. According to (4.17), there exists a global extraction operator

$\mathbb{C} \in \mathbb{R}^{n \times (n+m)}$ such that

$$\bar{\mathsf{N}}(\xi) = \mathbb{C}\bar{\mathsf{B}}(\xi). \tag{4.18}$$

$\bar{\mathsf{R}}(\xi) = \{\mathsf{R}_1^{\mathfrak{p}}(\xi); \cdots ; \mathsf{R}_n^{\mathfrak{p}}(\xi)\}^T$ denotes the corresponding NURBS basis function vector. Let $\bar{\mathsf{W}}$ be the diagonal matrix of weights

$$\bar{\mathsf{W}} = \begin{bmatrix} \mathsf{w}_1 & & & \\ & \mathsf{w}_2 & & \\ & & \ddots & \\ & & & \mathsf{w}_n \end{bmatrix}, \tag{4.19}$$

and let $\bar{\mathsf{w}}$ denote the weight vector

$$\bar{\mathsf{w}} = (\mathsf{w}_1; \cdots ; \mathsf{w}_n)^T. \tag{4.20}$$

Then the NURBS basis functions can be represented as

$$\bar{\mathsf{R}}(\xi) = \frac{\bar{\mathsf{W}}\bar{\mathsf{N}}(\xi)}{\mathsf{W}(\xi)} = \frac{\bar{\mathsf{W}}\mathbb{C}\bar{\mathsf{B}}(\xi)}{\mathsf{W}(\xi)}, \tag{4.21}$$

$$\mathsf{W}(\xi) = \bar{\mathsf{w}}^T\bar{\mathsf{N}}(\xi). \tag{4.22}$$

Let $\mathsf{P} = \{\mathsf{P}_1; \cdots ; \mathsf{P}_n\}^T$ be a vector of one-dimensional control points. Then the geometry of a one-dimensional curve $\mathsf{L}(\xi)$ can be represented as

$$\mathsf{L}(\xi) = \mathsf{P}^T\bar{\mathsf{R}}(\xi). \tag{4.23}$$

In summary, the linear operator $\mathbb{C}^e$ in each element defines the NURBS basis functions in the element. This feature enables simple implementation of isogeometric element shape function routine within existing finite element codes. Implementation details, including algorithms for extraction operators, are elaborated in [27, 172].

In [27], the algorithm for computing the Bézier extraction operator is restricted within open knot vectors. Hence, it is often useful to have an algorithm that enables the generation of periodic NURBS basis functions. To achieve the goal, a periodic transformation operator $\mathbb{T} \in \mathbb{R}^{n \times n}$ is introduced. For a globally $C^{\mathfrak{r}}$-continuous NURBS basis function vector $\bar{\mathsf{R}}(\xi)$,

$$\bar{\mathsf{R}}^{per}(\xi) := \mathbb{T}\bar{\mathsf{R}}(\xi) \tag{4.24}$$

is a vector of $C^{\mathfrak{r}}$-periodic NURBS basis functions. The linear transformation operator $\mathbb{T}$ is called suitable if it is invertible and preserves the partition of unity property. It has been shown in [142] that if the original NURBS basis functions $\bar{\mathsf{R}}(\xi)$ satisfies

1. the knot vector $\Xi = \{\xi_1, \cdots, \xi_{n+\mathfrak{p}+1}\}$ is an open uniform knot vector;

2. the number of knot spans $n_{el} = n - \mathfrak{p}$ has to be greater than or equal to $\mathfrak{p} + 1$;

3. the weight vector $\mathbf{w} \in \mathbb{R}^n$ is symmetric with respect to the knot vector Ξ, i.e., $w_i = w_{n-i+1}$ for all $i = \mathsf{g}_n + 1, \ldots, n$, with $\mathsf{g}_n = n/2$ if n is even or $\mathsf{g}_n = (n+1)/2$ if n is odd,

the transformation operator $\mathbb{T}$ is suitable and has local element-wise representations. The periodic NURBS basis function vector $\bar{\mathsf{R}}^{per,e}$ in the e-th element can be given by

$$\bar{\mathsf{R}}^{per,e}(\xi) := \mathbb{T}^e\bar{\mathsf{R}}^e(\xi), \tag{4.25}$$

113

wherein $\bar{\mathsf{R}}^e$ is the original NURBS basis function vector in the e-th element. The value of the $(\mathfrak{p}+1)^2$ components in $\mathbb{T}^e$ can be computed explicitly by solving a system of periodic constraint equations. Here let me give the explicit formulas of $\mathbb{T}^e$ for polynomial degree $\mathfrak{p} = 1, 2$ and 3. When $\mathfrak{p} = 1$, $\mathbb{T}^e = \mathbb{I}_2$, where $\mathbb{I}_2$ is the two-by-two identity matrix. When $\mathfrak{p} = 2$, the local periodic transformation operators $\mathbb{T}^e \in \mathbb{R}^{3\times 3}$ read

$$
\mathbb{T}^e = \begin{cases}
\begin{bmatrix} 1/2 & 0 & 0 \\ 1/2 & 1 & 0 \\ 0 & 0 & 1 \end{bmatrix} & \text{for } e = 1, \\[2mm]
\mathbb{I}_{3\times 3} & \text{for } e = 2, \ldots, n_{el} - 1, \\[2mm]
\begin{bmatrix} 1 & 0 & 0 \\ 0 & 1 & 1/2 \\ 0 & 0 & 1/2 \end{bmatrix} & \text{for } e = n_{el}.
\end{cases}
\tag{4.26}
$$

When $\mathfrak{p} = 3$, the local periodic transformation operators $\mathbb{T}^e \in \mathbb{R}^{4\times 4}$ are

$$
\mathbb{T}^e = \begin{cases}
\begin{bmatrix} 1/6 & 0 & 0 & 0 \\ 2/3 & 2/3 & 0 & 0 \\ 1/6 & 1/3 & 1 & 0 \\ 0 & 0 & 0 & 1 \end{bmatrix} & \text{for } e = 1, \\[4mm]
\begin{bmatrix} 2/3 & 0 & 0 & 0 \\ 1/3 & 1 & 0 & 0 \\ 0 & 0 & 1 & 0 \\ 0 & 0 & 0 & 1 \end{bmatrix} & \text{for } e = 2, \\[4mm]
\mathbb{I}_{4\times 4} & \text{for } e = 3, \ldots, n_{el} - 2, \\[4mm]
\begin{bmatrix} 1 & 0 & 0 & 0 \\ 0 & 1 & 0 & 0 \\ 0 & 0 & 1 & 1/3 \\ 0 & 0 & 0 & 2/3 \end{bmatrix} & \text{for } e = n_{el} - 1, \\[4mm]
\begin{bmatrix} 1 & 0 & 0 & 0 \\ 0 & 1 & 1/3 & 1/6 \\ 0 & 0 & 2/3 & 2/3 \\ 0 & 0 & 0 & 1/6 \end{bmatrix} & \text{for } e = n_{el}.
\end{cases}
\tag{4.27}
$$

To preserve the geometric representation, the control points $\mathsf{P} = \{\mathsf{P}_1, \cdots, \mathsf{P}_n\}$ needs to be updated for the new periodic NURBS basis functions.

Proposition 4.2.1. *The geometry of the curve* $\mathsf{L}(\xi) = \mathsf{P}^T \mathsf{R}(\xi)$ *is preserved with the new control points* $\mathsf{P}^{per} = \{\mathsf{P}_1^{per}, \cdots, \mathsf{P}_n^{per}\}$ *given by*

$$\mathsf{P}^{per} = \mathbb{T}^{-T} \mathsf{P}. \tag{4.28}$$

Proof. The relation (4.28) follows from

$$\mathsf{P}^{per,T} \mathsf{R}^{per}(\xi) = \mathsf{P}^T \mathbb{T}^{-1} \mathbb{T} \mathsf{R}(\xi) = \mathsf{P}^T \mathsf{R}(\xi) = \mathsf{L}(\xi). \tag{4.29}$$

$\square$

In Figure 4.4, the update procedure of control points has been illustrated using a hexagon-based circle [24]. The knot vector for the circular geometry is $\Xi = \{0, 0, 0, 1, 1, 2, 2, 3, 3, 4, 4, 5, 5, 6, 6, 6\}$. The weights for even-indexed (odd-indexed) points are 1 ($\sqrt{3}/2$). According to the expression (4.26) and the formula (4.28),

$$(\mathbb{T}^e)^{-T} = \begin{cases} \begin{bmatrix} 2 & -1 & 0 \\ 0 & 1 & 0 \\ 0 & 0 & 1 \end{bmatrix} & \text{for } e = 1, \\ \mathbb{I}_{3 \times 3} & \text{for } e = 2, \ldots, n_{el} - 1, \\ \begin{bmatrix} 1 & 0 & 0 \\ 0 & 1 & 0 \\ 0 & -1 & 2 \end{bmatrix} & \text{for } e = n_{el}. \end{cases} \tag{4.30}$$

Hence, only the first and the last control points need to be updated for this geometry. In this example, the first and the last control points are moved to

(a)

(b)
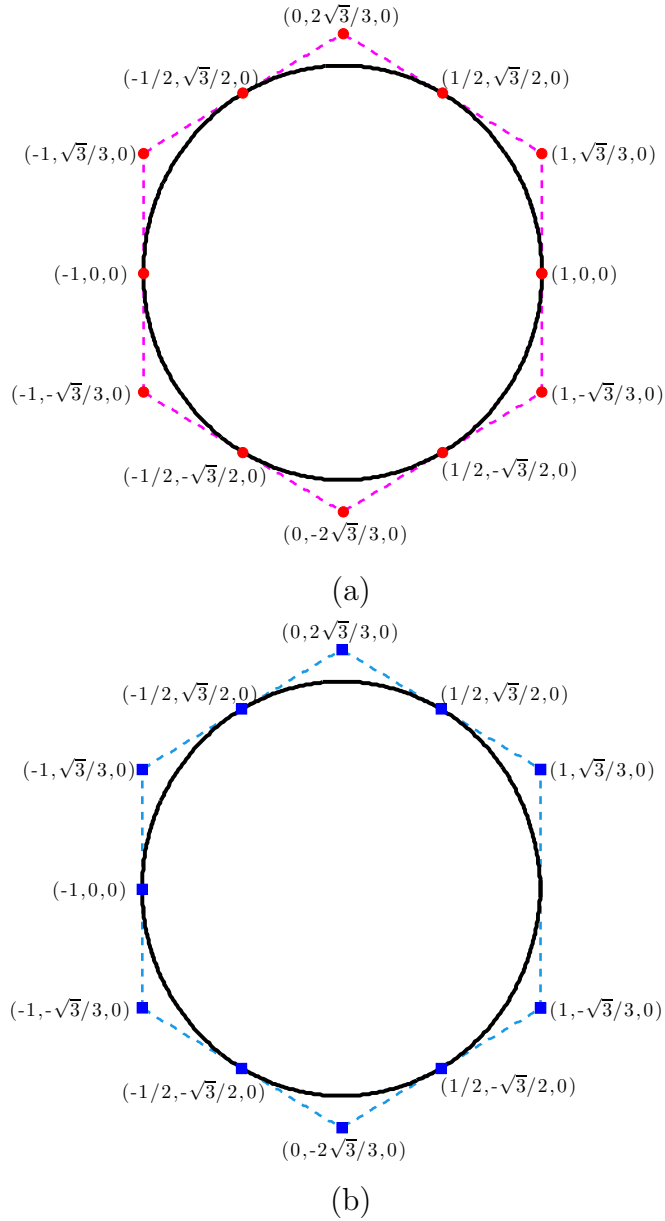
Figure 4.4: Exact representation of a circle by (a) open-knot NURBS basis functions and (b) periodic NURBS basis functions. The control points for open-knot NURBS basis functions are depicted by red circles; the control points for periodic NURBS basis functions are depicted by blue squares.

$(1, -\sqrt{3}/3, 0)$ and $(1, \sqrt{3}/3, 0)$ to maintain the geometry, as is shown in Figure 4.4 (b).

Given the periodic transformation operator $\mathbb{T}$, the periodic NURBS basis functions can be generated by modifying the extraction operator. The new extraction operator for periodic NURBS basis functions is defined as

$$\mathbb{C}^{per} = \bar{\mathsf{W}}^{-1} \mathbb{T} \bar{\mathsf{W}} \mathbb{C}. \tag{4.31}$$

Proposition 4.2.2. *The periodic NURBS basis functions* $\bar{\mathsf{R}}^{per}(\xi)$ *given by a suitable transformation operator* $\mathbb{T}$ *can be written as*

$$\bar{\mathsf{R}}^{per}(\xi) = \frac{\bar{\mathsf{W}} \bar{\mathsf{N}}^{per}(\xi)}{\mathsf{W}(\xi)}, \tag{4.32}$$

$$\mathsf{W}(\xi) = \bar{\mathsf{w}}^T \bar{\mathsf{N}}^{per}(\xi), \tag{4.33}$$

$$\bar{\mathsf{N}}^{per}(\xi) = \mathbb{C}^{per} \bar{\mathsf{B}}(\xi). \tag{4.34}$$

Proof. According to (4.21) and (4.24), $\bar{\mathsf{R}}^{per}(\xi)$ is defined as

$$\bar{\mathsf{R}}^{per}(\xi) = \mathbb{T}\bar{\mathsf{R}}(\xi) = \frac{\mathbb{T}\bar{\mathsf{W}}\bar{\mathsf{N}}(\xi)}{\mathsf{W}(\xi)} = \frac{\mathbb{T}\bar{\mathsf{W}}\mathbb{C}\bar{\mathsf{B}}(\xi)}{\mathsf{W}(\xi)}, \tag{4.35}$$

$$\mathsf{W}(\xi) = \bar{\mathsf{w}}^T \bar{\mathsf{N}}(\xi). \tag{4.36}$$

According to the definition of $\mathbb{C}^{per}$, it can be shown that

$$\bar{\mathsf{W}}\bar{\mathsf{N}}^{per}(\xi) = \bar{\mathsf{W}}\mathbb{C}^{per}\bar{\mathsf{B}}(\xi) = \bar{\mathsf{W}}\bar{\mathsf{W}}^{-1}\mathbb{T}\bar{\mathsf{W}}\mathbb{C}\bar{\mathsf{B}}(\xi) = \mathbb{T}\bar{\mathsf{W}}\mathbb{C}\bar{\mathsf{B}}(\xi). \tag{4.37}$$

Since the transformation operator $\mathbb{T}$ is assumed to preserve the partition of unity, it can be shown that

$$\bar{\mathsf{w}}^T \bar{\mathsf{N}}^{per}(\xi) = \bar{\mathsf{w}}^T \mathbb{C}^{per} \bar{\mathsf{B}}(\xi) = \bar{\mathsf{w}}^T \bar{\mathsf{W}}^{-1} \mathbb{T}\bar{\mathsf{W}}\mathbb{C}\bar{\mathsf{B}}(\xi) = \mathbf{1}^T \mathbb{T}\bar{\mathsf{W}}\mathbb{C}\bar{\mathsf{B}}(\xi)$$

$$= \mathbf{1}^T \bar{\mathsf{W}}\mathbb{C}\bar{\mathsf{B}}(\xi) = \bar{\mathsf{w}}^T \mathbb{C}\bar{\mathsf{B}}(\xi) = \mathsf{W}(\xi). \tag{4.38}$$

117

Thus, (4.32)-(4.34) coincides with the definition of $\bar{\mathsf{R}}^{per}(\xi)$ given by (4.21). $\quad\square$

The above proposition reveals that the periodic NURBS basis functions can be generated by simply updating the extraction operator. Since both $\mathbb{C}$ and $\mathbb{T}$ have local element-wise representations, this update procedure can be performed within each element. In fact, $\mathbb{T}^e$ is not an identity matrix only in the first and last $\mathfrak{p} - 1$ elements for $\mathfrak{p} \geq 2$. Hence, the local extraction operators only needs to be updated in these $2\mathfrak{p} - 2$ elements. Interested readers are referred to [142] for more details.

4.3 Parallel implementation

4.3.1 Software design

In this section, I briefly describe `PERIGEE`, an object-oriented parallel nonlinear dynamic `C++` framework for isogeometric analysis. The basic idea is to make the implementation of different problems (i.e., different variational formulation, boundary conditions, material properties, shape function routine, etc.) in a simple, unified way, while keeping the computational efficiency as high as possible. This object is achieved by making abstract object-oriented software design and utilizing existing high-performance scientific computing libraries. An overview of the software structure is illustrated in Figure 4.5. It can be seen that `PERIGEE` depends on several external packages – METIS [120], PETSc [13], HDF5 [91], and VTK [1]. It also contains a number of independent routines, each of which contains several classes encapsulating routine

objects. Pure abstract classes are used as interfaces for different detailed implementations. This object-oriented design makes it easier to add additional capabilities by simply inserting new derived classes without touching the main body for the code. This design strategy enhanced the code reusability and provide a generic support for a wide range of problems. Core features of PERIGEE include:

- Generation of NURBS basis functions using the Bézier extraction operators [27];

- Mesh partition based on METIS [120];

- Parallel data structures for matrices and vectors;

- Parallel system assembly;

- Parallel Krylov subspace iterative methods;

- Parallel preconditioners for Krylov subspace iterative methods;

- Nonlinear solver and time stepping frameworks;

- Mesh and solution input/output in standard PETSc format [13] and HDF5 format [91]

- Parallel post-processor [1, 104].

Parallelism has been a key factor in the design of PERIGEE. Particularly, the following aspects are taken into account for the parallel implementation.

119
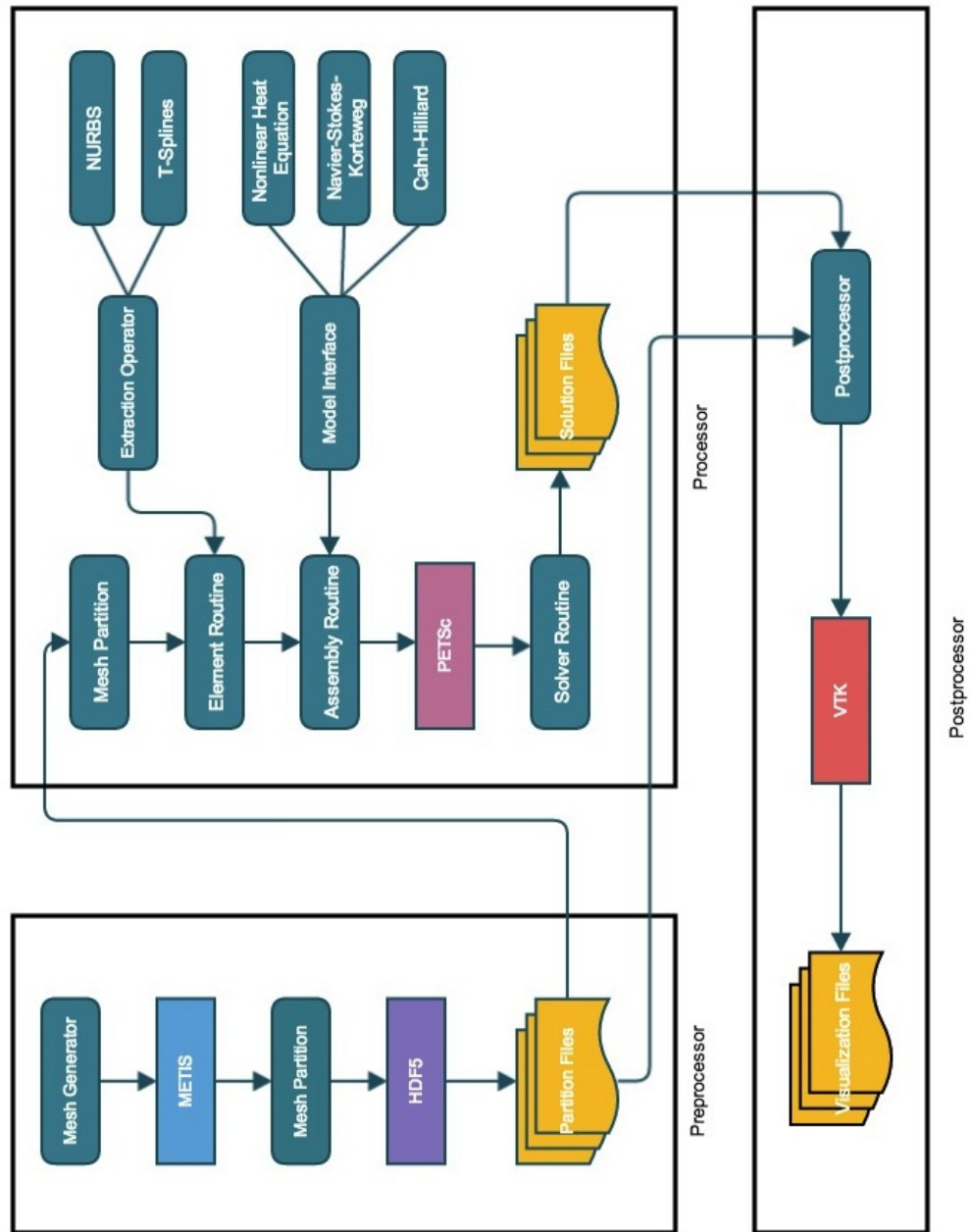
Figure 4.5: Software structure of `PERIGEE`.
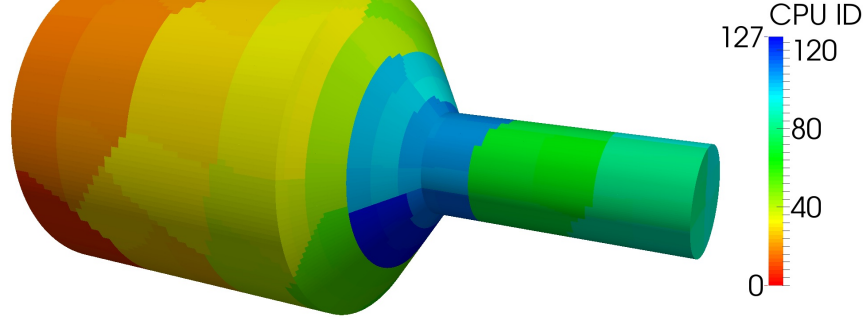
Figure 4.6: Domain decomposition of a three-dimensional converging tube. The three-dimensional physical domain is decomposed into 128 subdomains using METIS [120].

Mesh partition

In PERIGEE, the elements and degrees of freedom are assigned to a particular subdomain, which is owned by a processor. Quadrature informations and IEN arrays [107] of these elements are stored in the memory associated with the processor. Besides, "ghost" elements and "ghost" degrees of freedom on neighbouring processors are recorded and synchronized in each parallel operation. Hence, the communication cost of these ghost values should not dominate the computation time. This requires the number of edge-cuts to be minimized. In the meantime, the load of each subdomain should be balanced to reduce synchronizing times. To obtain a high-quality mesh partition, METIS [120] is employed to generate the partition in the preprocessor of PERIGEE. Based on the partition results,

121

the `PERIGEE` preprocessor will write HDF5 partition files for each sub-domain, containing all necessary information. In the analysis code, each processor will read its own HDF5 file to perform parallel computing. For most applications, post-processors are less intensive in computing. Hence, it is advisable to run the mesh partition again for post-processors with less subdomains. An index mapping function is designed to carefully manage different nodal indices for different mesh partitions.

Parallel data structure

The structure of parallel vectors and matrices follows from the mesh partition straightforwardly. Specifically, parallel vectors use the format of `Vec` in PETSc with ghost entries; parallel matrices use the Yale sparse matrix format [70] given by the `Mat` data structure in PETSc. Specific data structures can be easily added within the framework. The output data of the `PERIGEE` analysis routine can be written in the PETSc binary format or the HDF5 format. The visualization files are written in the parallel VTK format [1]. Users can easily visualize the results in ParaView [104] on modern parallel visualization systems.

Parallel linear solver

In modern finite element programs, a dynamic nonlinear problem eventually reduces to a series of linear algebraic equations. Therefore, the parallel performance of a linear solver fundamentally impacts the overall performance of the dynamic nonlinear solver. The `KSP` object, as a core

122

component of PETSc, provides a unified access to most existing solvers for linear algebraic equations; the `PC` object offers various preconditioner options for the Krylov subspace iterative methods. In PETSc, various different linear algebraic solvers are provided [13]. Users are responsible for choosing the linear solver based on their specific research problems. The default linear solver in `PERIGEE` is the Generalized Minimal Residual method [166]; the default preconditioner is the overlapping additive Schwarz parallel preconditioner with incomplete LU factorization in each block.

4.3.2 Scalability

In this section, I report the parallel performance test of `PERIGEE` by solving the thermal Navier-Stokes-Korteweg equations. The detailed numerical scheme is reported in Chapter 7. Three strong scalability tests have been performed on the Dell Linux cluster Stampede at the Texas Advanced Computing Center (TACC). I list the computing times in seconds and the speedup ratios in Table 4.1. The speedup curves are illustrated in Figure 4.7. The results demonstrate the parallel scalability of `PERIGEE`.

Table 4.1: Computing times, speedup ratios, and parallel efficiencies of PERIGEE. Three group of tests are performed for the thermal Navier-Stokes-Korteweg equations with five hundred time integrations. The spatial meshes are comprised of 1.50 million, 13.55 million, and 96.14 million degree of freedoms (DoFs), respectively.

	1.231M DoFs on Stampede		
Number of processors	CPU Time(sec)	Speedup ratio	Efficiency
1	1.073×10^4	-	-
2	5.910×10^3	1.82	90.8%
4	3.000×10^3	3.58	89.4%
8	1.572×10^3	6.83	85.3%
16	7.801×10^2	13.75	86.0%
32	4.461×10^2	24.05	75.2%
64	2.168×10^2	49.49	77.3%
128	1.348×10^2	79.60	62.2%

	13.55M DoFs on Stampede		
Number of processors	CPU Time(sec)	Speedup ratio	Efficiency
64	2.265×10^3	-	-
128	1.118×10^3	2.03	101.3%
256	6.251×10^2	3.62	90.5 %
512	3.441×10^2	6.58	82.3 %

	96.14M DoFs on Stampede		
Number of processors	CPU Time(sec)	Speedup ratio	Efficiency
512	2.483×10^3	-	-
1024	1.174×10^3	2.12	105.8%
2048	6.765×10^2	3.67	91.8 %
4096	3.655×10^2	6.79	84.9 %
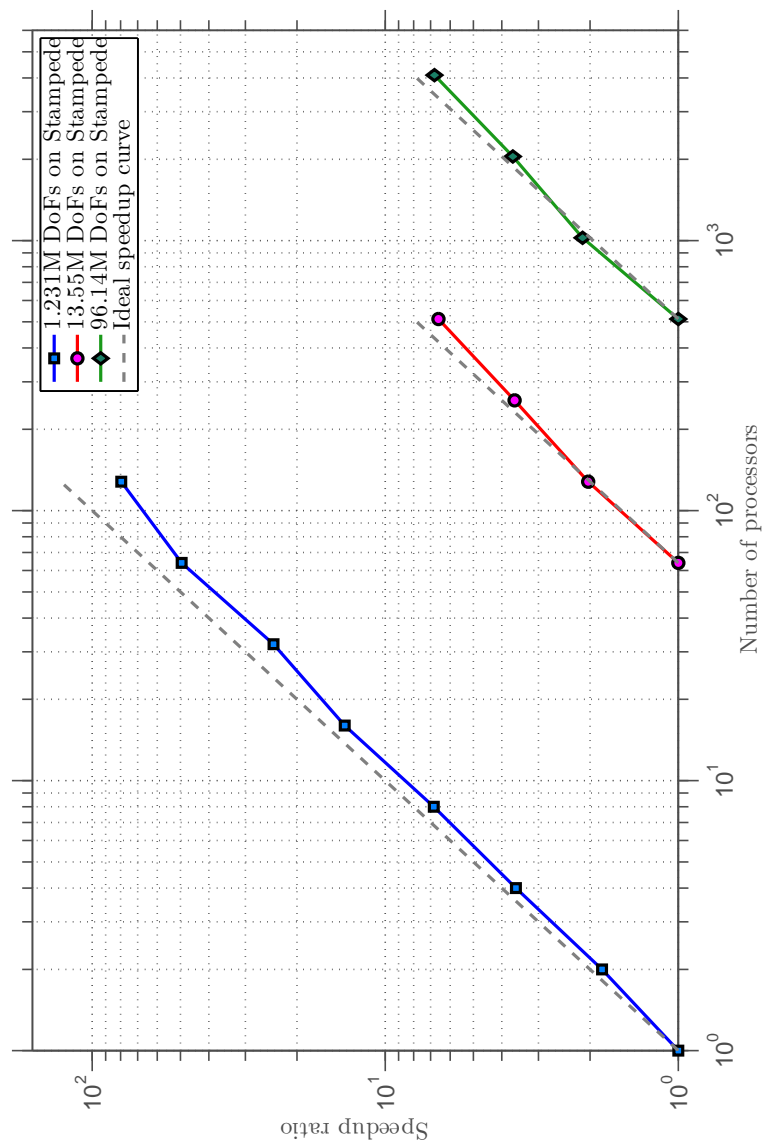
Figure 4.7: Speedup curves of `PERIGEE`.

Chapter 5

Numerical analysis of the advective Cahn-Hilliard equation

"Things should be as simple as possible, but not simpler."

— Albert Einstein

In this chapter, I numerically investigate the advective Cahn-Hilliard equation, which is a simplification of the two-component Navier-Stokes-Cahn-Hilliard equations[1]. This model represents a passive two-component fluid model in which the velocity field is externally applied. It can be applied to studying spinodal decomposition under shear flow. This problem is of fundamental importance in understanding metallic alloys [183], binary liquid mixtures [45], and polymer blends [101]. Of particular interests are the possible existence of steady states and the dependence of the steady state morphology on shear rate and geometry. In this chapter, numerical experiments are designed and carried out. The advective Cahn-Hilliard equation is directly discretized using the Galerkin method. Due to the presence of a fourth-order differential operator, basis functions of high-order continuity are employed. A

---

[1]Part of this chapter has been published as a journal paper [142] and is reproduced by permission of Elsevier. The dissertation author is the first author of this paper. Luca Dedè implemented part of the numerical code and produced Figures 5.1, 5.6, and 5.9. The rest of the authors supervised the numerical experiments and revised the paper.

C^1-periodic boundary condition is applied at the inflow and outflow boundaries of the computational domain in order to mimic the periodic structure of shear flows. In view of the strong enforcement of these boundary conditions, the periodic transformation operator developed in Section 4.2.2 is utilized. This technology is proven to be critical for discrete mass conservation in curved geometries. As for the time integration, the fully implicit generalized-α method is applied. To accommodate for the disparity of temporal scales, an adaptive time stepping scheme is introduced to efficiently achieve the steady state solutions.

The rest of this chapter is organized as follows. In Section 5.1, the strong problem of the advective Cahn-Hilliard equation is derived based on the two-component Navier-Stokes-Cahn-Hilliard model. In Section 5.2, a dimensional analysis of this strong problem is performed. Following that, the numerical formulation is presented in Section 5.3. In Section 5.4, several two and three-dimensional examples are simulated and discussed.

5.1   The advective Cahn-Hilliard equation

Recall that the binary two-component fluid in a connected, bounded domain $\Omega \subset \mathbb{R}^d$ is governed by the Navier-Stokes-Cahn-Hilliard equations (3.104)-(3.106). Since my discussion in this chapter is restricted to the two-component fluid model, the superscript $ch2$ will be omitted and c_1 will be

replaced with c in the following text. The balance equations read as follows.

$$\frac{\partial \rho}{\partial t} + \nabla \cdot (\rho \mathbf{u}) = 0, \tag{5.1}$$

$$\frac{\partial (\rho c_1)}{\partial t} + \nabla \cdot (\rho c \mathbf{u}) = \nabla \cdot (\mathbf{M} \nabla \mu), \tag{5.2}$$

$$\frac{\partial (\rho \mathbf{u})}{\partial t} + \nabla \cdot (\rho \mathbf{u} \otimes \mathbf{u} + p \mathbf{I}) - \nabla \cdot \boldsymbol{\tau} - \nabla \cdot \boldsymbol{\varpi} = \rho \mathbf{b}. \tag{5.3}$$

The advective Cahn-Hilliard equation can be derived by decoupling the component balance equation (5.2) from the hydrodynamic system by imposing a given velocity field $\mathbf{u}$. Furthermore, I assume that the externally applied velocity field is divergence-free ($\nabla \cdot \mathbf{u} = 0$) and the fluid density is constant (i.e., $\rho = \rho_c$). With the above assumptions, the component balance equation (5.2) can be rewritten as

$$\rho_c \frac{\partial c}{\partial t} + \rho_c \mathbf{u} \cdot \nabla c = \nabla \cdot (\mathbf{M} \nabla \mu). \tag{5.4}$$

The constitutive relations for the chemical potential μ given in (3.88) can be simplified using the constant-density assumption.

$$\mu = \mu_{loc} - \frac{1}{\rho_c} \nabla \cdot (\gamma \rho_c \nabla c) \tag{5.5}$$

$$= \mu_{loc} - \nabla \cdot (\gamma \nabla c) \tag{5.6}$$

$$= \mu_{loc} - \gamma \Delta c, \tag{5.7}$$

wherein

$$\mu_{loc} := \frac{\partial \Psi_{loc}}{\partial c}. \tag{5.8}$$

Assuming there is no contribution to the free energy from pure materials (i.e., $\psi_1 = \psi_2 = 0$), the local free energy of the non-uniform system can be written as

$$\Psi_{loc} = R\theta \left(c \log c + (1-c) \log(1-c)\right) + 2R\theta_{crit}c(1-c).$$ (5.9)

Hence, one has

$$\mu_{loc} = \frac{d\Psi_{loc}}{dc} = R\theta \log \left(\frac{c}{1-c}\right) + 2R\theta_{crit}\left(1-2c\right).$$ (5.10)

The mobility tensor $\mathbf{M}$ is assumed to be isotropic and takes the following specific form

$$\mathbf{M}_{ij} = M_0 c(1-c)\delta_{ij}.$$ (5.11)

This choice of mobility tensor enhances diffusion processes within the interface region, which has been validated by experiments. I consider the initial condition

$$c(\mathbf{x}, 0) = c_0(\mathbf{x}), \quad \forall \mathbf{x} \in \Omega,$$ (5.12)

which, by dropping the explicit dependence on the space variable $\mathbf{x}$, reads $c(0) = c_0$, with $c_0 : \Omega \rightarrow \mathbb{R}$. The boundary of Ω is denoted as Γ and is assumed to be at least Lipschitz continuous. The boundary Γ is partitioned into three non-overlapping subdivisions:

$$\Gamma_s := \{\mathbf{x} \in \Gamma \mid \mathbf{u}(\mathbf{x}) \cdot \mathbf{n}(\mathbf{x}) = 0\},$$ (5.13)

$$\Gamma_{in} := \{\mathbf{x} \in \Gamma \mid \mathbf{u}(\mathbf{x}) \cdot \mathbf{n}(\mathbf{x}) < 0\},$$ (5.14)

$$\Gamma_{out} := \{\mathbf{x} \in \Gamma \mid \mathbf{u}(\mathbf{x}) \cdot \mathbf{n}(\mathbf{x}) > 0\},$$ (5.15)

depending on the advective flow field $\mathbf{u}$ and the outward normal vector $\mathbf{n}$. On Γ_s, the essential no-flux boundary condition $\nabla c \cdot \mathbf{n} = 0$ as well as the natural boundary condition $\mathbf{M}\nabla\nu \cdot \mathbf{n} = 0$ are imposed to mimic the presence of a rigid wall. On Γ_{in} and Γ_{out}, periodic boundary conditions are imposed in order to simulate a periodic structure along the flow direction. With the above conditions, the initial-boundary value problem of the advective Cahn-Hilliard equation can be stated as follows.

$$\rho_c \frac{\partial c}{\partial t} + \rho_c \mathbf{u} \cdot \nabla c = \nabla \cdot \big(\mathbf{M}\nabla(\mu_{loc} - \gamma\Delta c)\big), \quad \text{in } \Omega \times (0, T), \tag{5.16}$$

$$\mathbf{M}\nabla\mu_{loc} \cdot \mathbf{n} = 0, \quad \text{on } \Gamma_s \times (0, T), \tag{5.17}$$

$$\mathbf{M}\gamma\nabla c \cdot \mathbf{n} = 0, \quad \text{on } \Gamma_s \times (0, T), \tag{5.18}$$

$$c \mid_{\Gamma_{in}} = c \mid_{\Gamma_{out}}, \quad \text{on } \Gamma_{in} \cup \Gamma_{out} \times [0, T), \tag{5.19}$$

$$\nabla c \cdot \mathbf{n} \mid_{\Gamma_{in}} = -\nabla c \cdot \mathbf{n} \mid_{\Gamma_{out}}, \quad \text{on } \Gamma_{in} \cup \Gamma_{out} \times [0, T), \tag{5.20}$$

$$c(0) = c_0, \quad \text{in } \Omega. \tag{5.21}$$

5.2 The dimensionless formulation

Let me introduce the following dimensionless quantities, which are denoted with a superscript $*$:

$$x = L_0 x^*, \quad t = T_0 t^*, \quad \mathbf{M} = M_0 \mathbf{M}^*, \quad \mathbf{u} = U_0 \mathbf{u}^*, \quad \theta = \theta_{crit}\theta^*. \tag{5.22}$$

The mass fraction c is a non-dimensional quantity already, and the local chemical potential can be rescaled as

$$\mu_{loc} = 2R\theta_{crit}\mu_{loc}^*, \tag{5.23}$$

$$\mu_{loc}^* = \frac{\theta^*}{2} \log \left(\frac{c}{1-c} \right) + (1 - 2c). \tag{5.24}$$

Then the dimensionless form of the advective Cahn-Hilliard equation (5.16) can be written as

$$\mathbb{N}_1 \frac{\partial c^*}{\partial t^*} + \mathbb{N}_3 \mathbf{u}^* \cdot \nabla^* c^* = \nabla^* \cdot (\mathbf{M}^* \nabla^* (\mathbb{N}_2 \mu_{loc}^* - \Delta^* c^*)), \tag{5.25}$$

where the dimensionless parameters $\mathbb{N}_i$, for $i = 1, 2, 3$, are defined as

$$\mathbb{N}_1 = \frac{\rho_c L_0^4}{M_0 \gamma T_0}, \quad \mathbb{N}_2 = \frac{2R\theta_{crit} L_0^2}{\gamma}, \quad \mathbb{N}_3 = \frac{\rho_c L_0^3 U_0}{M_0 \gamma}. \tag{5.26}$$

The characteristic time scale can be chosen as $T_0 = \rho_c L_0^4 / M_0 \gamma$, so that $\mathbb{N}_1 = 1$. By recalling the definition of the Péclet number, one has

$$\mathrm{Pe} = \frac{\rho_c L_0 U_0}{2R\theta_{crit} M_0}, \tag{5.27}$$

and the non-dimensional number $\mathbb{N}_3$ can be represented as

$$\mathbb{N}_3 = \mathrm{Pe}\, \mathbb{N}_2. \tag{5.28}$$

For simplicity, the superscript $*$ will be dropped for the dimensionless equation and the governing equation takes the following form,

$$\frac{\partial c}{\partial t} + \mathbb{N}_2 \,\mathrm{Pe}\, \mathbf{u} \cdot \nabla c = \nabla \cdot (\mathbf{M} \nabla (\mathbb{N}_2 \mu_{loc} - \Delta c)). \tag{5.29}$$

In the remainder of the discussion, the dimensionless temperature θ is fixed to be $2/3$, and the local chemical potential μ_{loc} is consequently fixed as

$$\mu_{loc} = \frac{1}{3} \log \left(\frac{c}{1-c} \right) + (1 - 2c). \tag{5.30}$$

Then the advective Cahn-Hilliard equation (5.29) is completely characterized by a set of two dimensionless numbers: $\mathbb{N}_2$ and Pe.

5.3   Numerical formulation

In this section, I construct the numerical scheme for the advective Cahn-Hilliard equation using NURBS-based isogeometric analysis [108]. This approach is quite similar to the one utilized in [60, 83]. Standard notations are used to denote the Sobolev spaces and norms [2].

5.3.1   The weak problem

Let $\mathcal{V}$ denote the trial solution and test function spaces, which are assumed to be identical for this problem. Due to the presence of the fourth-order operator in (5.29), the space $\mathcal{V}$ is chosen as

$$\mathcal{V} = \left\{ v \in H^2(\Omega) : \begin{array}{c} v|_{\Gamma_{in}} = v|_{\Gamma_{out}}, \nabla v \cdot \mathbf{n}|_{\Gamma_{in}} = -\nabla v \cdot \mathbf{n}|_{\Gamma_{out}}, \\ \nabla v \cdot \mathbf{n}|_{\Gamma_s} = 0 \end{array} \right\}. \qquad (5.31)$$

The weak formulation reads

$$\text{find } c(t) \in L^2\left(0, T; \mathcal{V}\right) \cap H^1\left(0, T; L^2(\Omega)\right) \text{ such that}$$

$$\mathbf{B}(w; \dot{c}(t), c(t)) = 0 \quad \forall w \in \mathcal{V}, \; t \in [0, T), \qquad (5.32)$$

$$\text{with } c(0) = c_0 \quad \text{in } \Omega,$$

wherein,

$$\mathbf{B}(w; \dot{c}, c) := (w, \dot{c})_\Omega + (w, \mathbb{N}_2 \operatorname{Pe} \mathbf{u} \cdot \nabla c)_\Omega$$

$$+ (\nabla w, \mathbb{N}_2 \mathbf{M} \nabla \mu_{loc} + \nabla \mathbf{M} \Delta c)_\Omega + (\Delta w, \mathbf{M} \Delta c)_\Omega. \qquad (5.33)$$

In the above weak formulation, $(\cdot, \cdot)_\Omega$ indicates the L^2 inner product over the domain Ω and $\dot{c} := \partial c / \partial t$. Standard integration by parts leads to the Euler-Lagrange form of the weak problem (5.32):

$$\left(w, \frac{\partial c}{\partial t} + \mathbb{N}_2 \operatorname{Pe} \mathbf{u} \cdot \nabla c - \nabla \cdot (\mathbf{M} \nabla (\mathbb{N}_2 \mu_{loc} - \Delta c)) \right)_\Omega = 0. \qquad (5.34)$$

5.3.2   The semi-discrete formulation

The weak problem (5.32) is spatially discretized by using NURBS basis functions [108]. Since the NURBS basis functions of degree $\mathfrak{p} \geq 2$ can achieve global $C^{\mathfrak{p}-1}$-continuity, the weak problem (5.32) can be directly discretized by means of the Galerkin method. Let $\mathcal{V}^h \subset \mathcal{V}$ denote the finite dimensional function space spanned by such NURBS basis functions in two or three-dimensions and satisfying the essential boundary conditions. The semi-discrete formulation reads as

$$\text{find } c^h(t) \in L^2\left(0, T; \mathcal{V}^h\right) \cap H^1\left(0, T; L^2(\Omega)\right) \text{ such that}$$

$$\mathbf{B}(w^h; \dot{c}^h(t), c^h(t)) = 0 \quad \forall w^h \in \mathcal{V}^h, \ t \in [0, T), \tag{5.35}$$

$$\text{with } c^h(0) = c_0^h \quad \text{in } \Omega,$$

where c_0^h is the L^2 projection of the function c_0 onto $\mathcal{V}^h$. The weighting function w^h and trial solution c^h can be explicitly written as

$$w^h = \sum_{A=1}^{n_{bf}} w_A \mathsf{R}_A, \tag{5.36}$$

$$c^h = \sum_{A=1}^{n_{bf}} c_A \mathsf{R}_A. \tag{5.37}$$

The R_A's represent the NURBS basis functions spanning the discrete space $\mathcal{V}^h$ of dimension n_{bf} and the coefficients c_A represent the control variables.

5.3.3   The fully discrete scheme

Several time marching schemes have been developed for the Cahn-Hilliard equation, including the backward Euler method [163], the Crank-Nicolson method [203], and the high-order implicit Runge-Kutta methods

[205]. It is noteworthy that a perturbed mid-point rule [85] has recently been developed based on a mixed formulation of the Cahn-Hilliard equation [151]. This scheme is provably unconditionally stable-in-energy and second-order accurate in time. More details about this method will be discussed in the subsequent chapters. In this chapter, the generalized-α method [49, 116] is applied to the advective Cahn-Hilliard equation. This method is characterized as a fully implicit time discretization scheme with controllable numerical dissipation on high frequency modes.

Let me first divide the time interval $\mathcal{I} = (0, T)$ into a set of N_{ts} time intervals of size $\Delta t_n = t_{n+1} - t_n$. I denote by $\mathbf{C}_n = \mathbf{C}(t_n) = \{c_A(t_n)\}_{A=1}^{n_{bf}}$ and $\dot{\mathbf{C}}_n = \dot{\mathbf{C}}(t_n) = \{\dot{c}_A(t_n)\}_{A=1}^{n_{bf}}$ the vectors of control variables and their corresponding time derivatives evaluated at the time step t_n. The residual vector is defined as

$$\mathbf{Q}(\dot{\mathbf{C}}_n, \mathbf{C}_n) := \{Q_A(\mathbf{C}_n, \dot{\mathbf{C}}_n)\}, \tag{5.38}$$

$$Q_A(\dot{\mathbf{C}}_n, \mathbf{C}_n) := \mathbf{B}(\mathsf{R}_A; \dot{c}^h(t_n), c^h(t_n)). \tag{5.39}$$

The generalized-α method can be stated as follows: at the time step t_n, given $\dot{\mathbf{C}}_n$, $\mathbf{C}_n$, the time step $\Delta t_n = t_{n+1} - t_n$, and the parameters α_m, α_f and $\bar{\delta}$,

find $\dot{\mathbf{C}}_{n+1}$, $\mathbf{C}_{n+1}$, $\dot{\mathbf{C}}_{n+\alpha_m}$, and $\mathbf{C}_{n+\alpha_f}$ such that

$$\mathbf{Q}(\dot{\mathbf{C}}_{n+\alpha_m}, \mathbf{C}_{n+\alpha_f}) = 0,$$
$$\mathbf{C}_{n+1} = \mathbf{C}_n + \Delta t_n \dot{\mathbf{C}}_n + \bar{\delta}\Delta t_n(\dot{\mathbf{C}}_{n+1} - \dot{\mathbf{C}}_n), \tag{5.40}$$
$$\dot{\mathbf{C}}_{n+\alpha_m} = \dot{\mathbf{C}}_n + \alpha_m(\dot{\mathbf{C}}_{n+1} - \dot{\mathbf{C}}_n),$$
$$\mathbf{C}_{n+\alpha_f} = \mathbf{C}_n + \alpha_f(\mathbf{C}_{n+1} - \mathbf{C}_n).$$

134

The parameters α_m, α_f and $\bar{\delta}$ are chosen based on the considerations of accuracy, stability, and robustness. It has been shown in [116] that, for linear problems, an unconditionally stable, second-order accurate scheme is attained for:

$$\bar{\delta} = \frac{1}{2} + \alpha_m - \alpha_f, \qquad \alpha_m \geq \alpha_f \geq \frac{1}{2}. \tag{5.41}$$

The parameters α_m and α_f can be parametrized in terms of ρ_∞, the spectral radius of the amplification matrix when $\Delta t \rightarrow \infty$, as

$$\alpha_m = \frac{1}{2}\left(\frac{3 - \rho_\infty}{1 + \rho_\infty}\right), \qquad \alpha_f = \frac{1}{1 + \rho_\infty}. \tag{5.42}$$

With the above parametrization given, a family of second-order accurate and unconditionally stable time integration schemes is defined in terms of the parameter $\rho_\infty \in [0, 1]$. It has been demonstrated that the high-frequency behavior of the time marching scheme is controlled by ρ_∞ [107, 116]. For linear problems, if ρ_∞ is chosen to be zero, the method annihilates the high frequency modes in one step; if ρ_∞ is chosen to be one, the high frequency modes are preserved. It is in general advisable to select ρ_∞ strictly less than one so that the high-frequency modes do not spoil long-time simulations. The choice of $\rho_\infty = 0.5$ has been shown to be effective for turbulence computations [16, 116] as well as for the phase-field models [83, 84, 86, 87]. Hence this value is adopted in the following numerical simulations. The nonlinear system of equations (5.40) is solved by the Newton-Raphson method [52].

Remark 5.3.1. *If one chooses $\alpha_f = \alpha_m = \bar{\delta} = 1$, the generalized-$\alpha$ method*

coincides with the backward Euler method, which is unconditionally stable but only first-order accurate.

5.3.4 Time step adaptivity

In practical computations, the generalized-α method is coupled with an adaptive time step strategy [58, 83] to accommodate for the many time scales in the advective Cahn-Hilliard equation. This methodology allows time-step size adjustment, by several orders of magnitude, to efficiently compute long-time phase separation dynamics. This is particularly important for multiphase flows due to the intermittent nature of the phase separation process.

I will adopt the adaptive scheme proposed in [58, 83]. The time-step size criterion is based on the comparison of the solutions obtained with the second-order accurate generalized-α method and the first-order accurate backward Euler method. With this idea in mind, the algorithm can be stated as follows. At each time step t_n, given $\dot{\mathbf{C}}_n$, $\mathbf{C}_n$ and time step Δt_{n-1}, the following steps are repeated for $\mathfrak{l} = 1, \ldots, \mathfrak{l}_{max}$, with $\Delta t_{n,(0)} = \Delta t_{n-1}$:

1. Compute $\mathbf{C}^{BE}_{n+1,(\mathfrak{l}-1)}$ using the backward Euler method and $\Delta t_{n,(\mathfrak{l}-1)}$,

2. Compute $\mathbf{C}^{\alpha}_{n+1,(\mathfrak{l}-1)}$ using the generalized-α method and $\Delta t_{n,(\mathfrak{l}-1)}$,

3. Calculate the relative error

$$\mathfrak{e}_{n+1,(\mathfrak{l}-1)} := \frac{\|\mathbf{C}^{BE}_{n+1,(\mathfrak{l}-1)} - \mathbf{C}^{\alpha}_{n+1,(\mathfrak{l}-1)}\|}{\|\mathbf{C}^{\alpha}_{n+1,(\mathfrak{l}-1)}\|}, \tag{5.43}$$

4. Update the time step size according to the following formula

$$\Delta t_{n,(l)} = \mathfrak{c} \left(\frac{TOL}{e_{n+1,(l-1)}} \right)^{1/2} \Delta t_{n,(l-1)}, \tag{5.44}$$

with TOL a prescribed tolerance and $\mathfrak{c}$ a suitable safety coefficient,

5. If $\mathfrak{e}_{n+1,(l-1)} \geq TOL$, return to step 1; otherwise, set $\dot{\mathbf{C}}_{n+1} = \dot{\mathbf{C}}_{n+1,(l-1)}$, $\mathbf{C}_{n+1} = \mathbf{C}_{n+1,(l-1)}$, and $\Delta t_n = \Delta t_{n,(l)}$.

In all the reported simulations, the parameters are chosen as $\mathfrak{c} = 0.85$, and $TOL = 10^{-3}$.

5.4 Numerical results

In this section, the numerical methodology outlined in the preceding section is applied to studying the spinodal decomposition under shear flow. Most of the existing numerical studies of the shear-driven spinodal decomposition are restricted to the two-dimensional cases [30, 155, 201], and only a few of them have obtained steady state solutions [191]. In this work, the steady state solutions are achieved in both two and three-dimensions. In particular, the periodic transformation operator developed in Section 4.2.2 is utilized to study the spinodal decomposition in a Taylor-Couette cell. The original hexagon-based NURBS representation of the geometry is transformed into the periodic NURBS representation in the circumferential direction. Then the C^1-periodic boundary condition at the inflow and outflow boundaries are strongly enforced. Numerical experiments indicate that the exact satisfaction

137

of periodic boundary conditions in this curved geometry is critical for mass conservation, which is essential for obtaining correct steady state solutions.

In the numerical simulations reported in this section, the initial condition c_0 is always chosen as

$$c_0 = \bar{c}_0 + \delta_c, \tag{5.45}$$

where $\bar{c}_0 \in (0, 1)$ is a constant, and $\delta_c = \delta_c(\mathbf{x}) : \Omega \to \mathbb{R}$ is scalar function with uniform random distribution such that $\delta_c(\mathbf{x}) \in [-0.05, 0.05]$. In this chapter, all two-dimensional simulations are performed with uniform quadratic 512^2 meshes and all three-dimensional simulations are performed with uniform quadratic 80^3 meshes. All simulations are integrated in time up to $T = 1.0 \times 10^4$ to obtain steady state solutions. The initial time step is fixed to $\Delta t_0 = 1.0 \times 10^{-12}$.

5.4.1 Two-dimensional results in a square domain

In the first example, I consider the shear-driven spinodal decomposition in a square domain $\Omega = (0, 1)^2$, which is depicted in Figure 5.1. The divergence-free advection field $\mathbf{u}$ is given by

$$\mathbf{u} = \mathfrak{s} y \mathbf{e_x}, \tag{5.46}$$

wherein $\mathfrak{s}$ is the shear rate and $\mathbf{e_x}$ is the unit vector pointing in the positive x-direction. The C^1-periodic boundary conditions are imposed on the left and right boundaries of the domain. The top and bottom of the square boundaries
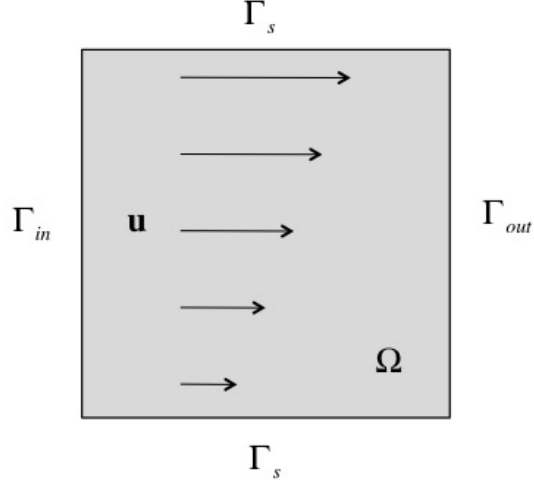
Figure 5.1: Shear-driven spinodal decomposition in the square domain $\Omega = (0,1)^2$: Problem setup.

are modeled as solid walls and the wall boundary conditions (5.17)-(5.18) are imposed. The averaged mass fraction is $\bar{c}_0 = 0.5$, and the dimensionless parameter $\mathbb{N}_2$ is taken as 1.05×10^5.

In Figures 5.2-5.3, the evolutions of the phase separation for $\text{Pe} = 1$ and $\text{Pe} = 10$ are illustrated. It can be observed that at the early stage, the evolution of the solutions is mainly driven by the minimization of the double-well local chemical free energy Ψ_{loc}. After that, the coarsening is mainly driven by the interplay between the shear flow and the minimization of the surface energy. At the steady state, 6 bands are formed for $\text{Pe} = 1$, and 13 bands are formed for $\text{Pe} = 10$.

In Figure 5.4 the steady state solutions for the Péclet numbers $\text{Pe} = 0.01, 0.1, 1, 5, 10$, and 100 are illustrated. There are $2, 3, 6, 9, 13$, and 20 bands

(a) $t = 3.262 \times 10^{-7}$

(b) $t = 6.677 \times 10^{-6}$

(c) $t = 1.675 \times 10^{-5}$

(d) $t = 4.379 \times 10^{-5}$

(e) $t = 1.061 \times 10^{-4}$
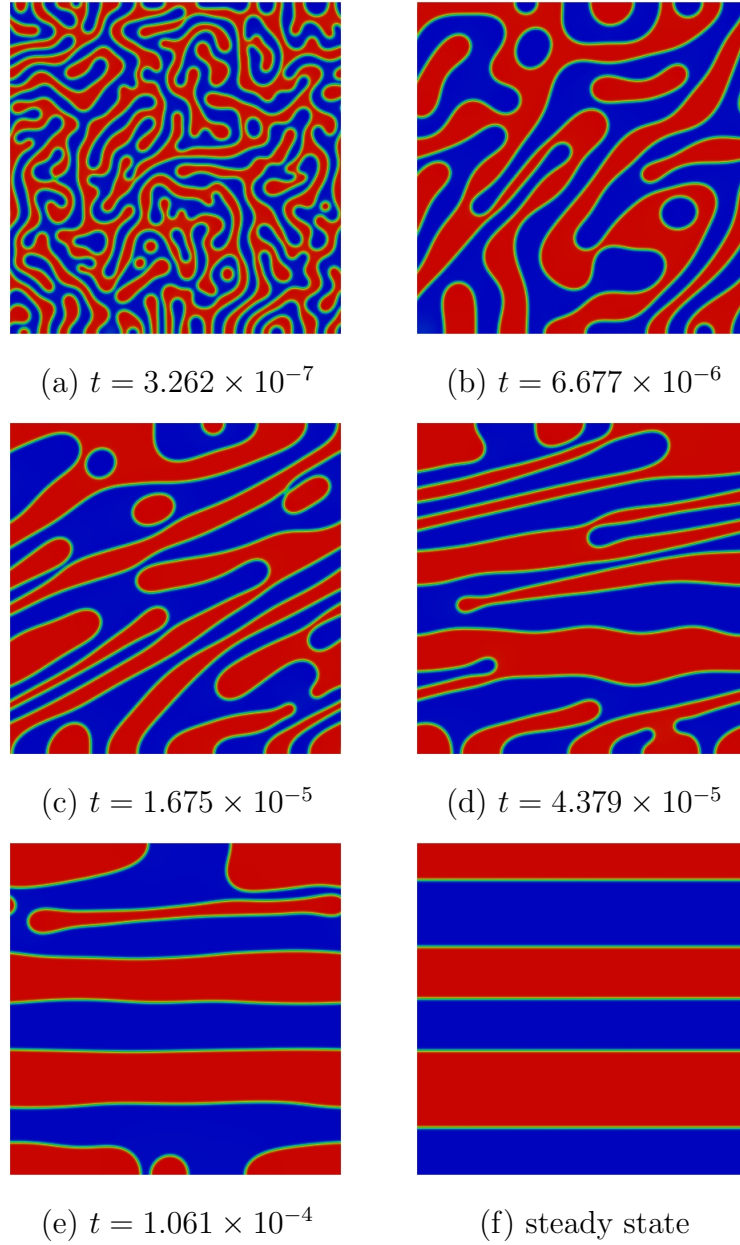
(f) steady state

Figure 5.2: Shear-driven spinodal decomposition in the square domain: Evolution of mass fraction c from a randomly perturbed initial condition to the steady state for $\text{Pe} = 1$.

(a) $t = 6.594 \times 10^{-7}$ (b) $t = 2.421 \times 10^{-6}$

(c) $t = 9.535 \times 10^{-6}$ (d) $t = 1.145 \times 10^{-5}$

(e) $t = 2.817 \times 10^{-5}$ (f) steady state
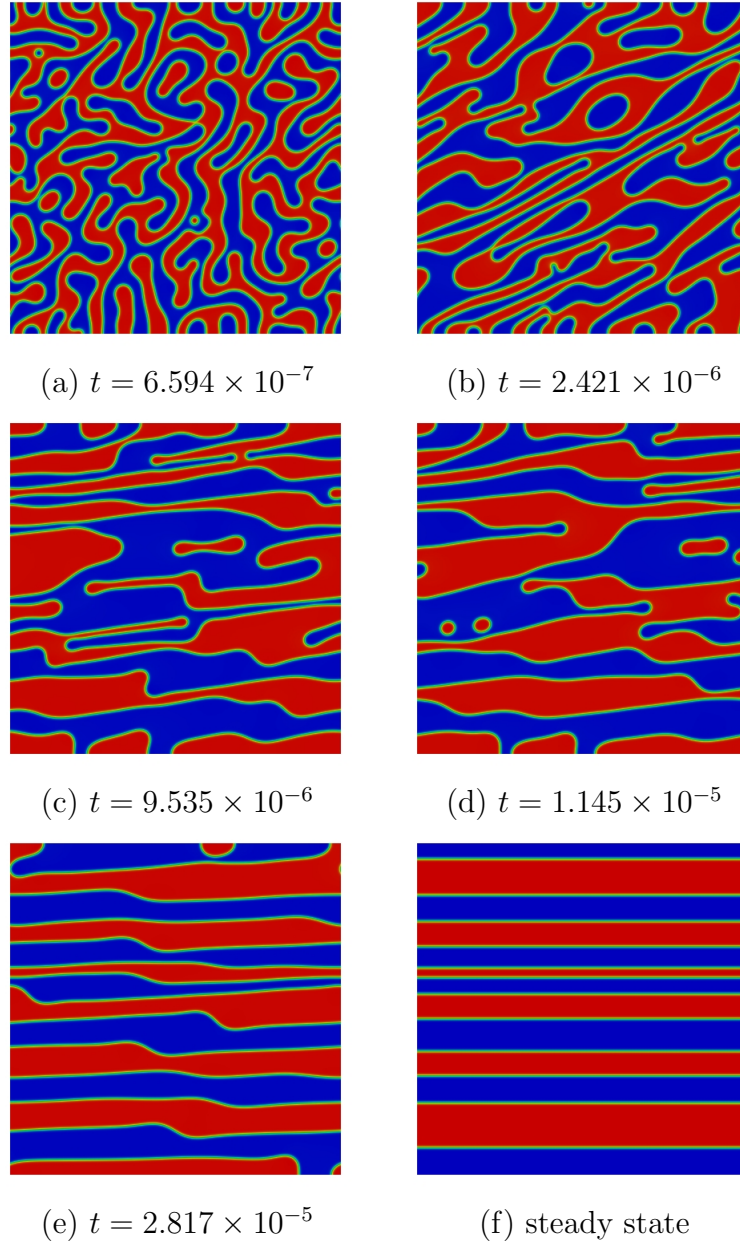
Figure 5.3: Shear-driven spinodal decomposition in the square domain: Evolution of mass fraction c from a randomly perturbed initial condition to the steady state for $\mathrm{Pe} = 10$.

(a) Pe = 0.01

(b) Pe = 0.1

(c) Pe = 1

(d) Pe = 5

(e) Pe = 10

(f) Pe = 100
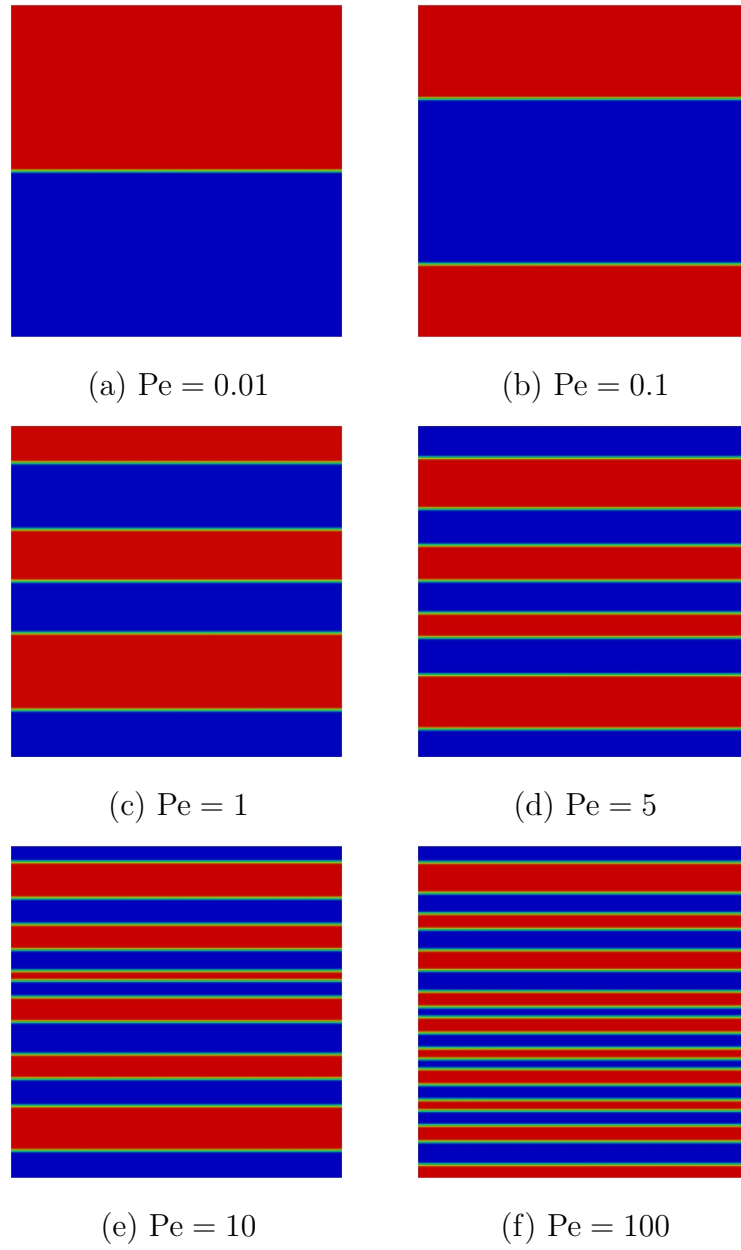
Figure 5.4: Shear-driven spinodal decomposition in the square domain: Solutions at steady state for the Péclet numbers Pe = 0.01, 0.1, 1, 5, 10, and 100.

formed respectively at the steady states. The width of the formed bands decreases with the increasing of the Péclet number. Using a least square fitting method, the averaged band width is proportional to $\mathfrak{s}^{-0.26}$. A similar power law relation between the Péclet number and the average band width has been proposed in [101].

In Figure 5.5, the evolution of the time step size is plotted against the the time step. It is observed that the time step varies enormously over the whole simulation processes. In particular, the time step experiences frequent local reductions, which corresponds to topological changes of the morphology. In Figure 5.5 (d), a comparison shows that for a larger Péclet number, the time step size is typically smaller than that of a smaller Péclet number. This implies the advective mechanism imposes stronger restrictions on Δt_n. The adaptive time stepping method requires 10589, 20051, and 65404 time steps for Pe $= 0.1, 1$, and 10 respectively.

5.4.2   Two-dimensional results in a Taylor-Couette cell

In this example, the spinodal decomposition is simulated in a Taylor-Couette cell. The physical geometry is delimited by two concentric cylinders. It is assumed that the shear flow is driven by the rotating inner cylinder with the outer cylinder fixed. Let me denote the radius of the inner cylinder as $\mathfrak{r}_{in}$ and that of the outer cylinder as $\mathfrak{r}_{out}$. The advection flow field assumes the

143
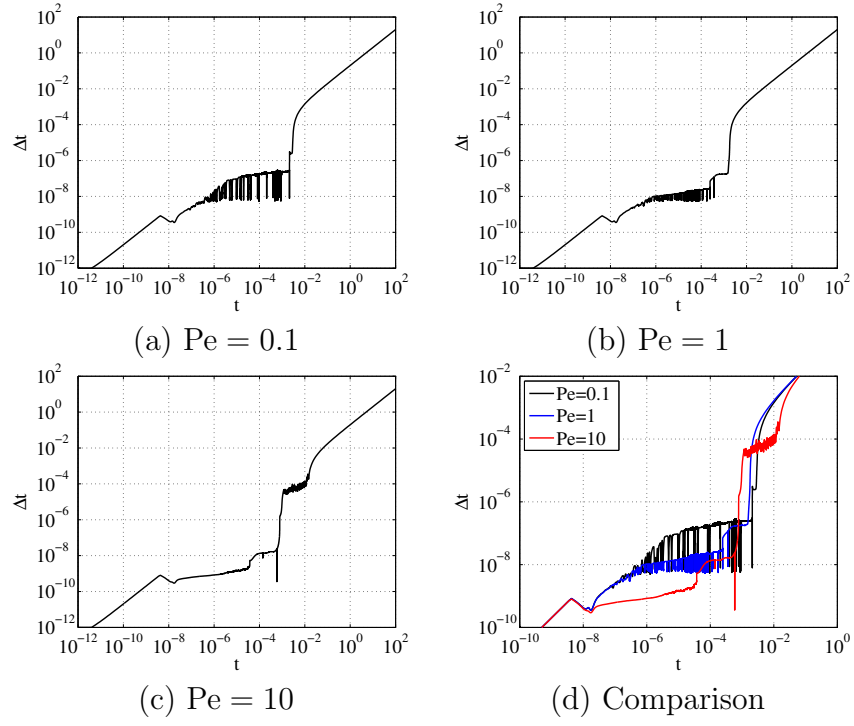
Figure 5.5: Shear-driven spinodal decomposition in the square domain: Evolution of the time step size Δt_n versus time t_n for Pe = 0.1, 1, and 10.

form:

$$\mathbf{u} = \mathbf{u}(\mathfrak{r}) = \mathfrak{v}\mathfrak{r}\frac{\left(\frac{\mathfrak{r}_{in}}{\mathfrak{r}}\right)^2 - \mathfrak{m}^2}{1 - \mathfrak{m}^2}\mathbf{e}_\theta, \tag{5.47}$$

$$\mathfrak{m} := \frac{\mathfrak{r}_{in}}{\mathfrak{r}_{out}}, \tag{5.48}$$

wherein $\mathfrak{r}$ is the distance from the origin, $\mathfrak{v}$ is the angular velocity of the inner cylinder, and $\mathbf{e}_\theta$ is a unit vector aligned in the circumferential direction. It should be noticed that $\mathbf{u}(\mathfrak{r}_{in}) = \mathfrak{v}\mathfrak{r}_{in}\mathbf{e}_\theta$ and $\mathbf{u}(\mathfrak{r}_{out}) = \mathbf{0}$.

The geometrical description of the Taylor-Couette cell is based on the hexagon-based quadratic NURBS parametrization [24], as is depicted in Figure 4.4 (a). To enforce the C^1-periodic boundary condition, the control points in the circumferential direction are updated based on the periodic transformation operator technique introduced in Section 4.2. The updated control points have been illustrated in Figure 4.4 (b). In the numerical simulations, the problem is solved in a restricted domain representing 1/6 of the full Taylor-Couette cell, as is shown in Figure 5.6. Specifically, the parameters are chosen as $\mathfrak{r}_{in} = 1$, $\mathfrak{r}_{out} = 2$, $\bar{c}_0 = 0.5$, $\mathbb{N}_2 = 1.05 \times 10^5$.

The shear-driven spinodal decomposition in the Taylor-Couette cell is simulated for $\mathrm{Pe} = 1$ and $\mathrm{Pe} = 10$. The evolutions of the solutions are illustrated in Figures 5.7 and 5.8 respectively. It can be observed that the phase separation processes in this example can be categorized into three stages: the phase separation is initially driven by the minimization of the chemical free energy; coarsening due to the shear flow plays a dominant role at latter times; as soon as multiple bands are formed along the flow direction, one additional
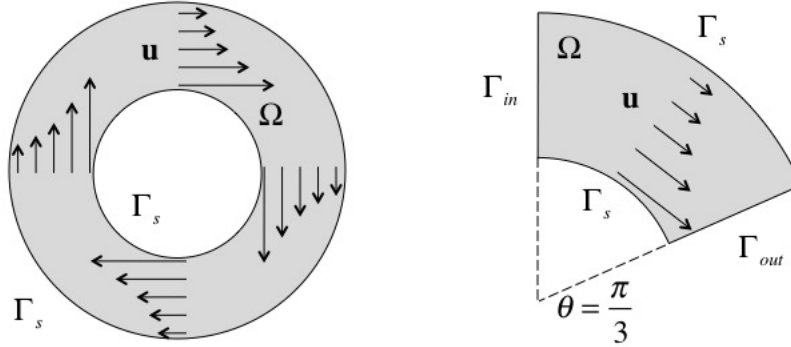
Figure 5.6: Shear-driven spinodal decomposition in the Taylor-Couette cell: Problem setup.

coarsening process takes place between these bands. Eventually only two bands are formed at the steady state. The additional coarsening process occurs regardless of the Péclet number. In fact, this two banded steady state solution is expected. Once the solution evolves toward a banded structure where all bands are aligned along the flow direction, the advection term $\mathbf{u} \cdot \nabla c$ vanishes. Therefore, the advective Cahn-Hilliard equation reduces to the standard Cahn-Hilliard equation. Then the excess amount of the surface energy between bands will drive the evolution. In the square domain setting, each band interface has the same length. Hence, the surface tensions are balanced and the multi-band solution is metastable. In the Taylor-Couette case, the interface near the outer cylinder wall is endowed with more surface energy than the interface close to the inner cylinder. Consequently, the instability in the surface energy drives the solution towards the two-banded structure, which is a minimizer of the surface energy.

146

(a) $t = 3.261 \times 10^{-6}$

(b) $t = 9.592 \times 10^{-5}$

(c) $t = 1.464 \times 10^{-4}$

(d) $t = 3.235 \times 10^{-4}$

(e) $t = 2.729 \times 10^{-3}$

(f) steady state
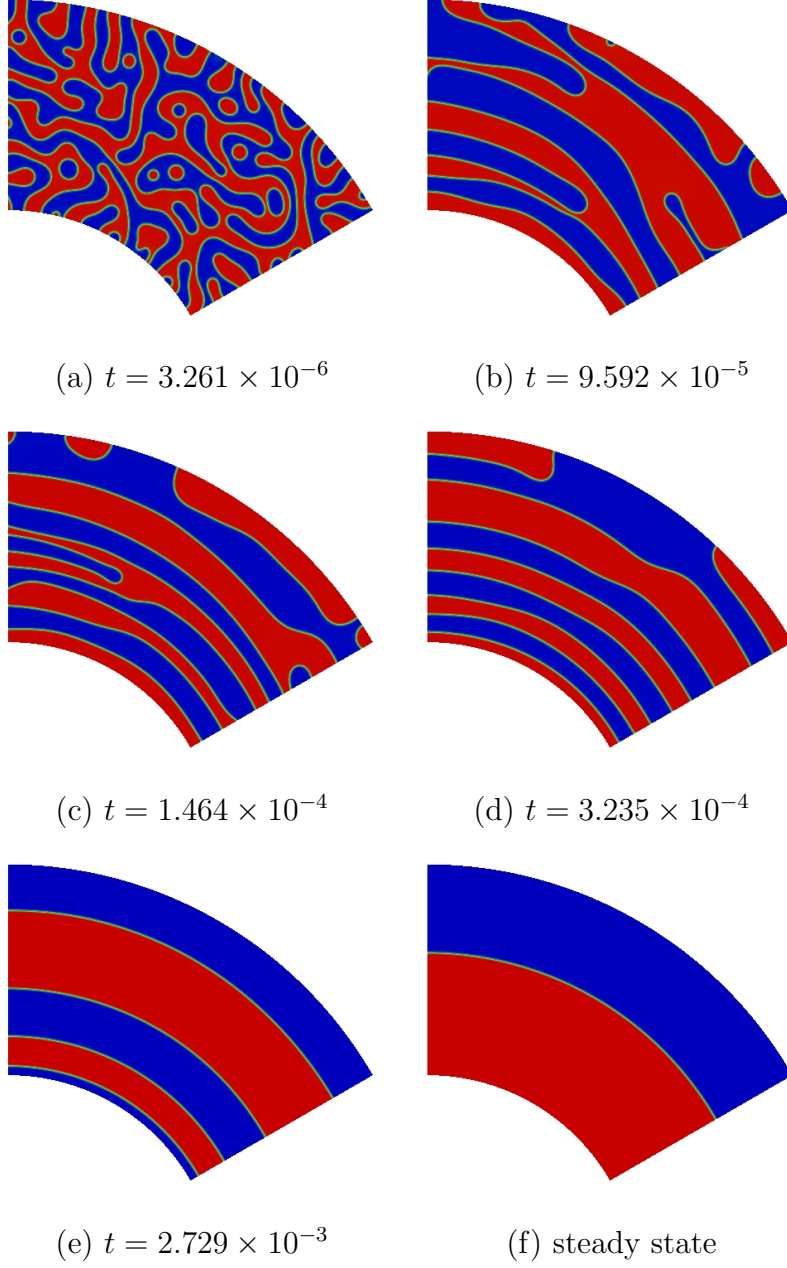
Figure 5.7: Phase separation in the Taylor-Couette cell: Pe = 1.

(a) $t = 3.038 \times 10^{-7}$ (b) $t = 2.223 \times 10^{-6}$

(c) $t = 1.762 \times 10^{-5}$ (d) $t = 5.303 \times 10^{-5}$

(e) $t = 1.675 \times 10^{-3}$ (f) steady state
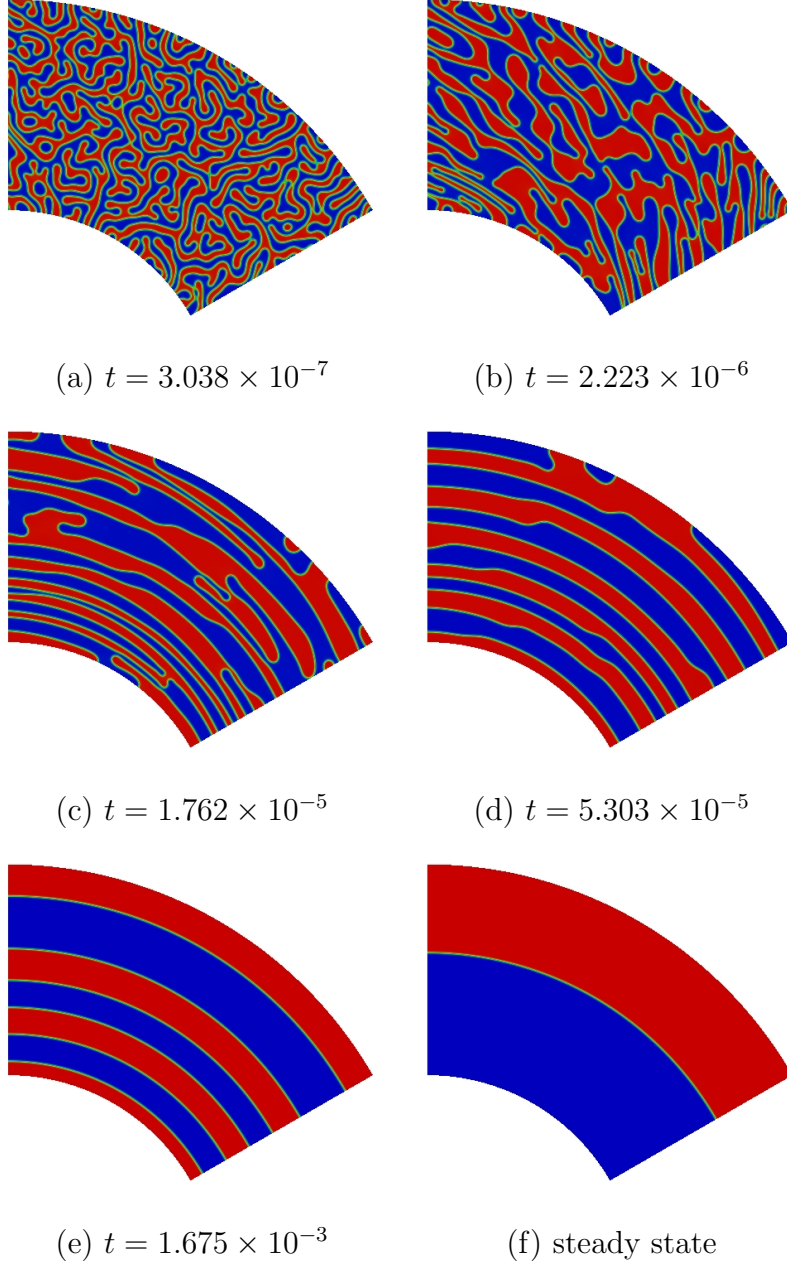
Figure 5.8: Phase separation in the Taylor-Couette cell: Pe = 10.
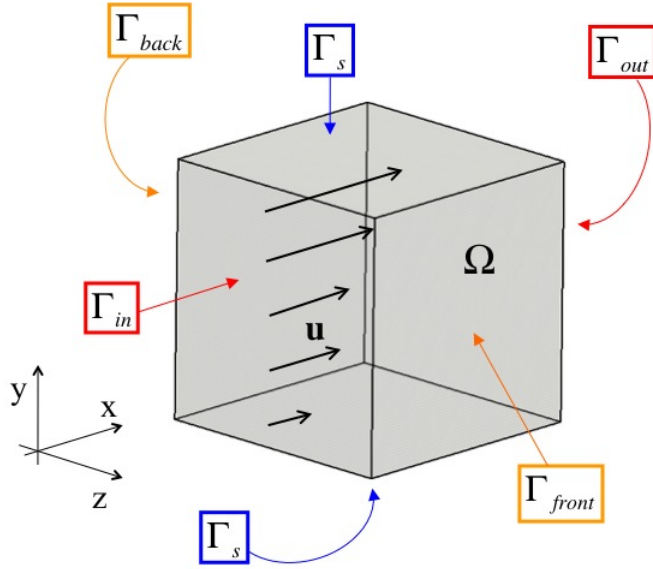
Figure 5.9: Shear-driven spinodal decomposition in the three-dimensional cube $\Omega = (0,1)^3$: Problem setup.

5.4.3 Three-dimensional results in a cube

As a third example, two simulations are performed within a three-dimensional cube $\Omega = (0,1)^3$. The problem setting is illustrated in Figure 5.9. Periodic boundary conditions are imposed on two pairs of boundaries: Γ_{in}/Γ_{out} and $\Gamma_{front}/\Gamma_{back}$. The top and bottom faces are modeled as rigid wall boundaries. The advective velocity field is taken as

$$\mathbf{u} = \mathfrak{s}y\mathbf{e_x}. \tag{5.49}$$

The dimensionless numbers $\mathbb{N}_2$ and Pe are fixed to be 6.4×10^3 and 1.0×10^2 respectively. Figures 5.10 and 5.11 illustrate the evolution of phase separation with the averaged mass fraction $\bar{c}_0 = 0.50$ and $\bar{c}_0 = 0.30$ respectively. The

three-dimensional solutions are visualized by means of the isosurfaces corresponding to $c = 0.35$, 0.5, and 0.65. In Figure 5.10, it is observed that the solution evolves toward a four-banded structure at the steady state. This evolution process is very similar to that of the square domain case. In Figure 5.11, the solution evolution is very similar to that of the Taylor-Couette cell problem. At $t = 2.168 \times 10^{-3}$, four tubular structures with different diameters are formed along the shear flow direction. Similar results have been obtained in [11] using an active Cahn-Hilliard multi-component fluid model. After that intermediate state, the imbalance of the surface tension breaks down the tubular structure. At the steady state, a single tabular structure is obtained after taking $22,543$ time steps.
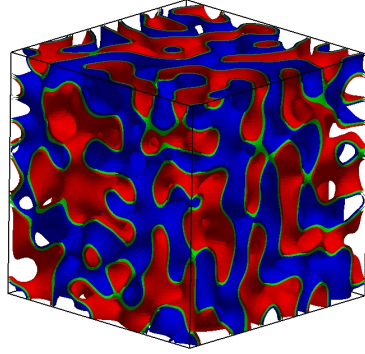
(a) $t = 1.566 \times 10^{-5}$
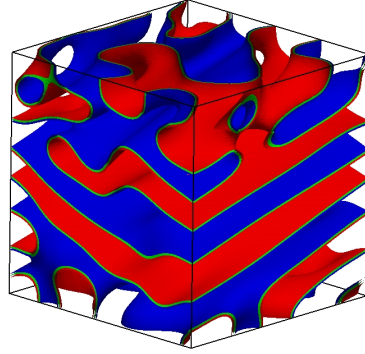
(b) $t = 1.425 \times 10^{-4}$
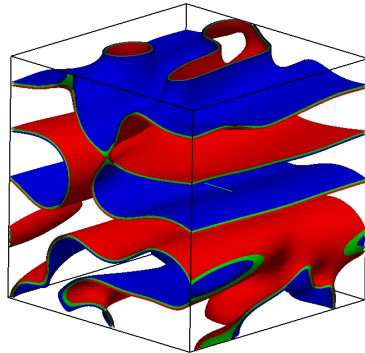
(c) $t = 3.982 \times 10^{-4}$
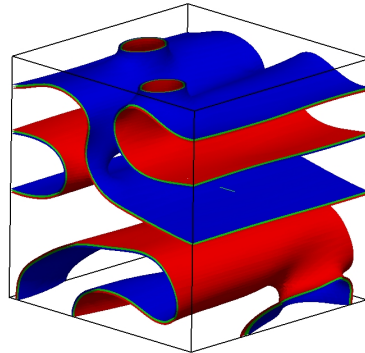
(d) $t = 7.359 \times 10^{-4}$
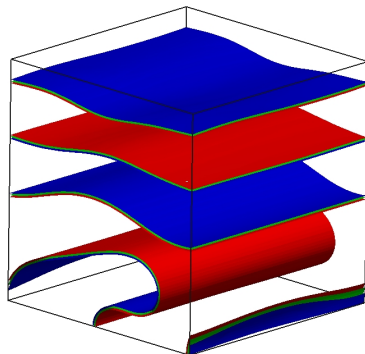
(e) $t = 1.215 \times 10^{-3}$
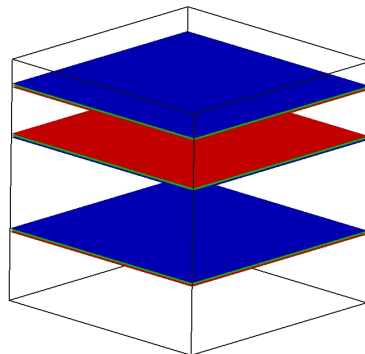
(f) steady state

Figure 5.10: Phase separation in the three-dimensional cube: $\bar{c}_0 = 0.5$.

151
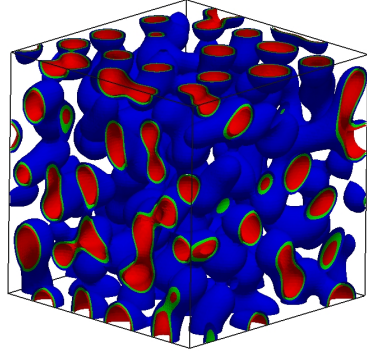
(a) $t = 2.135 \times 10^{-5}$
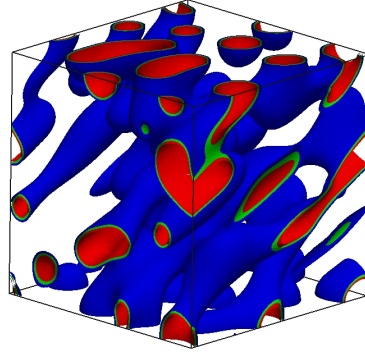
(b) $t = 7.275 \times 10^{-5}$
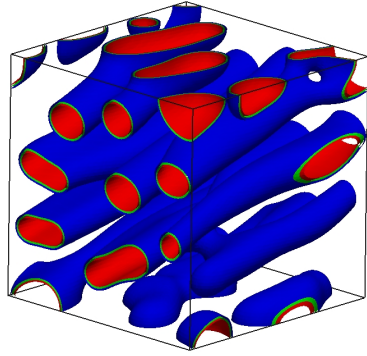
(c) $t = 1.407 \times 10^{-4}$
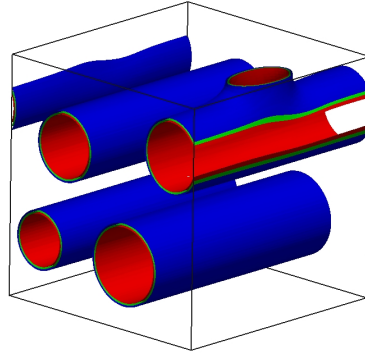
(d) $t = 1.214 \times 10^{-3}$
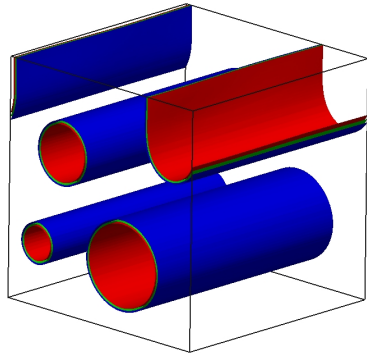
(e) $t = 2.168 \times 10^{-3}$
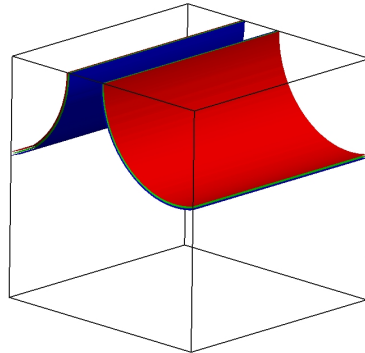
(f) steady state

Figure 5.11: Phase separation in the three-dimensional cube: $\bar{c}_0 = 0.3$.

Chapter 6

Numerical analysis of the isothermal Navier-Stokes-Korteweg equations

"Every mathematician knows it is impossible to understand an elementary course in thermodynamics."

— Vladimir I. Arnold, 1990

In this chapter, an entropy-dissipative, second-order accurate-in-time numerical scheme for the isothermal Navier-Stokes-Korteweg equations is presented[1]. Despite the constant temperature assumption, the isothermal Navier-Stokes-Korteweg equations present considerable difficulty in both theoretical and numerical analysis. Under the critical temperature, in the limit of vanishing viscosity and capillarity, the problem is a mixed hyperbolic-elliptic differential system. Mathematical knowledge about this kind of problem is still very limited [136]. In numerical analysis, the discrete energy dissipation has been demonstrated to be critical for obtaining physically admissible solutions [115]. The new spatial discretization developed in this work can be viewed as a generalization of the classical entropy variable formulation developed for the compressible Euler and Navier-Stokes equations [110]. For the temporal

---

[1]Part of this chapter has been published as a journal paper [143] and is reproduced by permission of Elsevier. The dissertation author is the first author of this paper. The rest of the authors supervised the numerical experiments and revised the paper.

discretization, a family of time marching schemes based on new quadrature rules is devised as a generalization of the Eyre's method [75].

An outline of this chapter is as follows. In Section 6.1, the initial-boundary value problem of the isothermal Navier-Stokes-Korteweg equations is introduced and its non-dimensional form is presented in Section 6.2. Following that, the concept of functional entropy variables is introduced and an alternative strong form of the Navier-Stokes-Korteweg problem is derived in Section 6.3. The corresponding weak problem is given in Section 6.4 and the semi-discrete formulation is given in Section 6.5. A family of special quadrature rules is developed in Section 6.6. Then, one pair of these quadrature rules is applied to constructing a fully discrete scheme. A detailed numerical analysis is elaborated in Section 6.7. A comprehensive set of numerical examples are numerically studied in Section 6.8 to verify the aforesaid properties. In Section 6.9, this chapter is finished by considering four application examples.

6.1 The initial-boundary value problem

Let $\Omega \subset \mathbb{R}^d$ be an arbitrary open, connected, and bounded domain, where d is the number of spatial dimensions. The isothermal Navier-Stokes-Korteweg equations (3.47)-(3.48) are considered in $\Omega \times (0, T)$. For notational simplicity, the superscript vdw is omitted in the subsequent discussion. The boundary of Ω is denoted as $\partial\Omega$ and assumed to be sufficiently smooth (e.g. Lipschitz). A pure material (e.g. water) is contained in Ω. $\rho : \bar{\Omega} \times (0, T) \to (0, b)$ and $\mathbf{u} : \bar{\Omega} \times (0, T) \to \mathbb{R}^d$ denote the density and velocity fields of the

material. The initial-boundary value problem of interest can be stated as follows: find the density ρ and velocity $\mathbf{u}$ such that

$$\frac{\partial \rho}{\partial t} + \nabla \cdot (\rho \mathbf{u}) = 0 \qquad\qquad \text{in } \Omega \times (0, T), \quad (6.1)$$

$$\frac{\partial (\rho \mathbf{u})}{\partial t} + \nabla \cdot (\rho \mathbf{u} \otimes \mathbf{u} + p\mathbf{I}) - \nabla \cdot \boldsymbol{\tau} - \nabla \cdot \boldsymbol{\varsigma} = \rho \mathbf{b} \qquad \text{in } \Omega \times (0, T), \quad (6.2)$$

$$\nabla \rho \cdot \mathbf{n} = 0 \qquad\qquad \text{on } \partial\Omega \times (0, T), \quad (6.3)$$

$$\mathbf{u} = \mathbf{0} \qquad\qquad \text{on } \partial\Omega \times (0, T), \quad (6.4)$$

$$\rho(\mathbf{x}, 0) = \rho_0(\mathbf{x}) \qquad\qquad \text{in } \bar{\Omega}, \quad (6.5)$$

$$\mathbf{u}(\mathbf{x}, 0) = \mathbf{u}_0(\mathbf{x}) \qquad\qquad \text{in } \bar{\Omega}. \quad (6.6)$$

Above, $\rho_0 : \bar{\Omega} \to (0, b)$ and $\mathbf{u}_0 : \bar{\Omega} \to \mathbb{R}^d$ are given functions which represent the initial density and velocity fields. Recall that $\boldsymbol{\tau}$ is the viscous stress tensor, $\boldsymbol{\varsigma}$ is the Korteweg stress tensor defined as

$$\boldsymbol{\varsigma} = \lambda \left(\rho \Delta \rho + \frac{1}{2} |\nabla \rho|^2 \right) \mathbf{I} - \lambda \nabla \rho \otimes \nabla \rho, \qquad (6.7)$$

where λ is the capillary coefficient, $\mathbf{b}$ is the body force per unit mass, and p is the thermodynamic pressure:

$$p = Rb \frac{\rho \theta}{b - \rho} - a \rho^2. \qquad (6.8)$$

Remember that the critical temperature, density, and pressure are given by

$$\theta_{crit} = \frac{8ab}{27R}, \quad \rho_{crit} = \frac{b}{3}, \quad p_{crit} = \frac{ab^2}{27}. \qquad (6.9)$$

Moreover, let me introduce the following energy terms,

$$\mathcal{E}(\rho, \rho\mathbf{u}) := \int_\Omega \mathcal{H} dV_\mathbf{x}, \qquad (6.10)$$

155

$$\mathcal{H}(\rho, \rho\mathbf{u}) := \int_{\Omega} W(\rho) + \frac{\lambda}{2}|\nabla\rho|^2 + \frac{1}{2}\rho|\mathbf{u}|^2 dV_{\mathbf{x}}, \qquad (6.11)$$

$$W(\rho) := \rho\Psi_{loc}^{vdw}(\rho). \qquad (6.12)$$

According to (3.51)-(3.52), the isothermal Navier-Stokes-Korteweg equations have the following energy dissipation property.

Theorem 6.1.1. *Let $(\rho, \rho\mathbf{u})$ be a sufficiently smooth solution of the isothermal Navier-Stokes-Korteweg equations (6.1)-(6.6). Then the energy $\mathcal{E}$ satisfies the relation*

$$\frac{d}{dt}\mathcal{E}(\rho(\cdot,t), \rho\mathbf{u}(\cdot,t)) = \int_{\Omega_t} \rho\mathbf{b}\cdot\mathbf{u} - \theta\mathcal{D}dV_{\mathbf{x}} = \int_{\Omega_t} \rho\mathbf{b}\cdot\mathbf{u} - \boldsymbol{\tau}:\nabla\mathbf{u}dV_{\mathbf{x}}. \quad (6.13)$$

Moreover, if there is no body force (i.e., $\mathbf{b} = \mathbf{0}$) and that the viscosity coefficients $\bar{\mu}$, $\bar{\lambda}$ satisfy

$$\bar{\mu} \geq 0, \quad \bar{\lambda} + \frac{2}{3}\bar{\mu} \geq 0, \qquad (6.14)$$

then the energy $\mathcal{E}$ satisfies the dissipation relation

$$\frac{d}{dt}\mathcal{E}(\rho(\cdot,t), \rho\mathbf{u}(\cdot,t)) = -\int_{\Omega_t} \boldsymbol{\tau}:\nabla\mathbf{u}dV_{\mathbf{x}} \leq 0. \qquad (6.15)$$

Remark 6.1.1. *In the following discussion, the Stokes's assumption is always satisfied, i.e.,*

$$\bar{\lambda} = -\frac{2}{3}\bar{\mu}. \qquad (6.16)$$

The following proposition gives another interesting and significant observation for the free energy function W.

156

Proposition 6.1.1. *The free energy function $W(\rho)$ has positive fourth order derivative, i.e., $W''''(\rho) > 0$, for $\rho \in (0, b)$.*

Proof. Direct computations reveal that

$$W''''(\rho) = \frac{2Rb^2\theta(6\rho^2 - 4b\rho + b^2)}{\rho^3(b-\rho)^4}. \tag{6.17}$$

The temperature and universal gas constant are positive, i.e., $\theta > 0$, $R > 0$. Furthermore, a direct calculation shows that the minimum of the quadratic polynomial $6\rho^2 - 4b\rho + b^2$ is $b^2/3 > 0$. Combining all of these facts with the expression given by (6.17) leads to the conclusion that $W'''' > 0$. □

Remark 6.1.2. *Free energy functions characterized by a positive fourth-order derivative prevail in the area of phase-field modeling. This is a consequence of the fact that free energy functions arising in phase-field models have convex-concave-convex structures. I call functions with a positive fourth derivative as* **super-convex functions** *and functions with a negative fourth derivative as* **super-concave functions**.

6.2   The dimensionless formulation

The system is rescaled using the $MLT\Theta$ system. Let me denote the reference scale of mass by M_0, length by L_0, time by T_0, and temperature by θ_0. Then I have the following non-dimensional quantities denoted with a superscript $*$:

$$x = L_0 x^*, \qquad t = T_0 t^*, \qquad \rho = \frac{M_0}{L_0^3}\rho^*, \qquad \mathbf{u} = \frac{L_0}{T_0}\mathbf{u}^*, \qquad \mathbf{b} = \frac{L_0}{T_0^2}\mathbf{b}^*,$$

$$\theta = \theta_0\theta^*, \quad p = \frac{M_0}{L_0T_0^2}p^*, \quad \lambda = \frac{L_0^7}{M_0T_0^2}\lambda^*, \quad \mathcal{H} = \frac{M_0}{L_0T_0^2}\mathcal{H}^*. \tag{6.18}$$

Using the above scaling relations, the dimensionless mass balance equation reads

$$\frac{M_0}{T_0L_0^3}\left(\frac{\partial\rho^*}{\partial t^*} + \nabla^* \cdot (\rho^*\mathbf{u}^*)\right) = 0. \tag{6.19}$$

The momentum balance equations are rescaled as

$$\frac{M_0}{T_0^2L_0^2}\left(\frac{\partial(\rho^*\mathbf{u}^*)}{\partial t^*} + \nabla^* \cdot (\rho^*\mathbf{u}^* \otimes \mathbf{u}^*) + \nabla^*p^* - \nabla^* \cdot \boldsymbol{\tau}^* - \nabla^* \cdot \boldsymbol{\varsigma}^* - \rho^*\mathbf{b}^*\right) = 0, \tag{6.20}$$

where the dimensionless viscous stress tensor and Korteweg stress tensor read

$$\boldsymbol{\tau}^* = \bar{\mu}^*\left(\nabla^*\mathbf{u}^* + \nabla^{*T}\mathbf{u} - \frac{2}{3}\nabla^* \cdot \mathbf{u}^*\mathbf{I}\right), \tag{6.21}$$

$$\boldsymbol{\varsigma}^* = \lambda^*\left(\rho^*\Delta^*\rho^* + \frac{1}{2}|\nabla^*\rho^*|^2\right)\mathbf{I} - \lambda^*\nabla^*\rho^*\nabla^{*T}\rho^*. \tag{6.22}$$

The equation of state is nondimensionalized as

$$\frac{M_0}{L_0T_0^2}p^* = Rb\theta_0\frac{\rho^*M_0\theta^*}{bL_0^3 - \rho^*M_0} - a\rho^{*2}\frac{M_0^2}{L_0^6}, \tag{6.23}$$

and the energy density is rescaled as

$$\mathcal{H}^* = W^*(\rho^*) + \frac{1}{2}\rho^*|\mathbf{u}^*| + \frac{1}{2}\lambda^*|\nabla^*\rho^*|^2, \tag{6.24}$$

where

$$W^*(\rho^*) = R\theta_0\frac{T_0^2}{L_0^2}\theta^*\rho^* \log\left(\frac{M_0\rho^*}{bL_0^3 - M_0\rho^*}\right) - a\frac{M_0T_0^2}{L_0^5}\rho^{*2}. \tag{6.25}$$

Notice that the dimensionless viscosity coefficient $\bar{\mu}^* = L_0T_0\bar{\mu}/M_0$ measures the ratio of the viscous force to the inertial force while the dimensionless

capillarity coefficient $\lambda^* = M_0 T_0^2 \lambda / L_0^7$ measures the ratio of the surface tension to the inertia. Consequently, I denote these two coefficients as

$$\bar{\mu}^* = \frac{1}{\text{Re}}, \qquad \lambda^* = \frac{1}{\text{We}}, \tag{6.26}$$

where Re is the Reynolds number and We is the Weber number.

Remark 6.2.1. *There are two other important dimensionless numbers associated with the problem. The capillarity number* Ca, *which measures the relative effect of the viscous force against the surface tension force, is defined to be*

$$\text{Ca} = \frac{\text{We}}{\text{Re}}. \tag{6.27}$$

The Bond number Bo, *which measures the importance of the body force compared with the surface tension, is defined to be*

$$\text{Bo} = |\mathbf{b}^*| \, \text{We}. \tag{6.28}$$

If I choose reference scales such that

$$\frac{M_0}{L_0^3} = b, \tag{6.29}$$

$$\frac{M_0}{L_0 T_0^2} = ab^2, \tag{6.30}$$

$$\theta_0 = \theta_{crit} = \frac{8ab}{27R}, \tag{6.31}$$

the dimensionless Navier-Stokes-Korteweg equations read

$$\frac{\partial \rho^*}{\partial t^*} + \nabla^* \cdot (\rho^* \mathbf{u}^*) = 0, \tag{6.32}$$

$$\frac{\partial (\rho^* \mathbf{u}^*)}{\partial t^*} + \nabla^* \cdot (\rho^* \mathbf{u}^* \otimes \mathbf{u}^*) + \nabla^* p^* - \nabla^* \cdot \boldsymbol{\tau}^* - \nabla^* \cdot \boldsymbol{\varsigma}^* - \rho^* \mathbf{b}^* = 0, \tag{6.33}$$

where

$$p^* = \frac{8}{27}\frac{\theta^*\rho^*}{1-\rho^*} - \rho^{*2}, \tag{6.34}$$

$$W^*(\rho^*) = \frac{8}{27}\theta^*\rho^* \log\left(\frac{\rho^*}{1-\rho^*}\right) - \rho^{*2}, \tag{6.35}$$

$$\boldsymbol{\tau}^* = \frac{1}{\text{Re}}\left(\nabla^*\mathbf{u}^* + \nabla^{*T}\mathbf{u}^* - \frac{2}{3}\nabla^* \cdot \mathbf{u}^*\boldsymbol{I}\right), \tag{6.36}$$

$$\boldsymbol{\varsigma}^* = \frac{1}{\text{We}}\left(\left(\rho^*\Delta^*\rho^* + \frac{1}{2}|\nabla^*\rho^*|^2\right)\mathbf{I} - \nabla^*\rho^*\nabla^{*T}\rho^*\right), \tag{6.37}$$

$$\text{Re} = \frac{L_0 b\sqrt{ab}}{\bar{\mu}}, \tag{6.38}$$

$$\text{We} = \frac{aL_0^2}{\lambda}. \tag{6.39}$$

Likewise, $\mathcal{E}$ is rescaled as

$$\mathcal{E}^*(\rho^*, \rho^*\mathbf{u}^*) = \int_\Omega \left(W^*(\rho^*) + \frac{1}{2\,\text{We}}|\nabla^*\rho^*|^2 + \frac{1}{2}\rho^*|\mathbf{u}^*|^2\right) d\mathbf{x}^*. \tag{6.40}$$

From (6.29) and (6.30), it can be found that the reference time scale $T_0 = L_0/\sqrt{ab}$, which can be regarded as an inertial time scale. Among many other choices of time scales, $\sqrt{\lambda/(a^2b)}$ is one associated with capillarity. Accordingly, one may define the dimensionless time $\hat{t}$ scaled by the capillarity time scale as

$$t = T_0 t^* = \sqrt{\frac{\lambda}{a^2b}}\hat{t}. \tag{6.41}$$

Then, the two dimensionless times are related by

$$\hat{t} = \sqrt{\frac{a^2b}{\lambda}}T_0 t^* = L_0\sqrt{\frac{a}{\lambda}}t^* = \text{We}^{\frac{1}{2}} t^*. \tag{6.42}$$

The relation (6.42) will be useful when designing the numerical algorithm in Section 6.7. I will henceforth use only the dimensionless form of the Navier-

160

Stokes-Korteweg equations and, for the sake of notational simplicity, I will omit the superscript $*$ for the dimensionless quantities.

6.3 An alternative statement of the isothermal Navier-Stokes-Korteweg equations

For systems of conservation laws, stability with respect to a mathematical entropy function $\mathcal{H}$ is considered as a suitable notion for nonlinear stability and as an admissibility criterion for selecting physically relevant weak solutions. In the context of the isothermal Navier-Stokes-Korteweg equations, such a stability condition is represented by the energy dissipation relation. In [100, 187], it was shown that systems of conservation laws which are endowed with a convex flux vector are symmetrizable if and only if there exists a mathematical entropy function. Given a set of conservation variables $\mathcal{U}$, the entropy variables are defined as the derivatives of the mathematical entropy function with respect to $\mathcal{U}$. In [109], the authors extended these ideas to the compressible Navier-Stokes equations. There, it was shown that the mathematical entropy must be an affine function of the physical entropy function and that semi-discrete solutions obtained from a weighted residual formulation based on entropy variables will respect the Clausius-Duhem inequality. Hence, entropy variables are a critical ingredient in the design of numerical schemes exhibiting nonlinear stability. To date, the entropy variable formulations have been successfully applied to various problems including gas dynamics [177], the shallow water equations [29], and magnetohydrodynamics [137].

Unfortunately, for the van der Waals fluid model, the standard methodology for constructing an entropy-dissipative semi-discrete formulation cannot be directly applied. Notably, the entropy variables which are normally associated with the isothermal Navier-Stokes equations do not comprise a viable variable set in the context of the van der Waals model. This is a consequence of the fact that the free energy function associated with the van der Waals model is non-convex within the elliptic region, as is shown in the following proposition.

Proposition 6.3.1. *Let* $\hat{\mathcal{H}} = W(\rho) + \dfrac{1}{2}\rho|\mathbf{u}|^2$ *denote the mathematical entropy function associated with the isothermal Navier-Stokes equations. Furthermore, recall that* $\mathcal{U} = (\rho, \rho\mathbf{u})^T$ *denote the conservation variables associated with the isothermal Navier-Stokes equations. If* W *is given by the van der Waals model, the entropy variables* $\hat{\mathfrak{V}}^T = \partial\hat{\mathcal{H}}/\partial\mathcal{U}$ *do not comprise a viable variable set when* $\theta \leq 1$ *in the sense that the mapping from* $\mathcal{U}$ *to* $\hat{\mathfrak{V}}$ *is not invertible within the elliptic region.*

Proof. The Hessian matrix $\dfrac{\partial\hat{\mathfrak{V}}}{\partial\mathcal{U}}$ can be written explicitly as

$$\frac{\partial\hat{\mathfrak{V}}}{\partial\mathcal{U}} = \frac{\partial^2\hat{\mathcal{H}}}{\partial\mathcal{U}^2} = \begin{pmatrix} W''(\rho) + \frac{|\mathbf{u}|^2}{\rho} & -\frac{u_1}{\rho} & -\frac{u_2}{\rho} & -\frac{u_3}{\rho} \\ -\frac{u_1}{\rho} & \frac{1}{\rho} & 0 & 0 \\ -\frac{u_2}{\rho} & 0 & \frac{1}{\rho} & 0 \\ -\frac{u_3}{\rho} & 0 & 0 & \frac{1}{\rho} \end{pmatrix}. \tag{6.43}$$

The determinant of the Hessian matrix is

$$\det\left(\frac{\partial^2\hat{\mathcal{H}}}{\partial\mathcal{U}^2}\right) = \frac{dp}{d\rho}\frac{1}{\rho^4}. \tag{6.44}$$

162

It has been shown that below (at) the critical temperature there exist two (one) stationary points where $dp/d\rho = 0$. Hence, the Hessian matrix is not invertible everywhere and likewise neither is the change-of-variables mapping from $\mathcal{U}$ to $\hat{\mathfrak{V}}$. □

Remark 6.3.1. *While the entropy variables $\hat{\mathfrak{V}}$ do not comprise a viable variable set when $\theta \leq 1$, the Navier-Stokes-Korteweg equations can be formally symmetrized in terms of $\hat{\mathfrak{V}}$, and the inner product of $\hat{\mathfrak{V}}$ with the Navier-Stokes-Korteweg equations does result in the Clausius-Duhem inequality. This implies that entropy variables $\hat{\mathfrak{V}}$ still can be used for the Navier-Stokes-Korteweg equations when above the critical temperature, but that is not the focus of this work.*

Remark 6.3.2. *Primitive variables (velocity and pressure) also do not comprise a viable variable set in the context of the van der Waals fluid model, because one cannot uniquely solve for the density field given the pressure field within the elliptic region.*

Proposition 6.3.1 prohibits the use of entropy variables obtained from the entropy function $\hat{\mathcal{H}}$ since the change-of-variables mapping is degenerate within the elliptic region. However, there exists a high-order capillarity term in the Navier-Stokes-Korteweg equations which regularizes the singularity in the elliptic region. Indeed, this term can also assist regularizing the entropy function $\hat{\mathcal{H}}$ in such a way that one can obtain well-defined entropy variables. In this direction, let me consider the following new mathematical entropy

163

function,

$$\mathcal{H} = \hat{\mathcal{H}} + \frac{1}{2\,\text{We}}|\nabla\rho|^2 = W(\rho) + \frac{1}{2}\rho|\mathbf{u}|^2 + \frac{1}{2\,\text{We}}|\nabla\rho|^2. \qquad (6.45)$$

This mathematical entropy function coincides with the total energy density given by (6.40) and is no longer just a function but rather a functional of the conservation variables $\mathcal{U}$. Therefore, to define the entropy variables associated with the new mathematical entropy function, one needs to take the variational derivatives of $\mathcal{H}$ with respect to $\mathcal{U}$ to define $\mathfrak{V}$. Under appropriate boundary conditions (e.g. $\nabla\rho \cdot \mathbf{n} = 0$ on $\partial\Omega$), this yields

$$\frac{\delta\mathcal{H}}{\delta\rho} = W'(\rho) - \frac{1}{2}|\mathbf{u}|^2 - \frac{1}{\text{We}}\Delta\rho, \qquad (6.46)$$

$$\frac{\delta\mathcal{H}}{\delta(\rho\mathbf{u})} = \mathbf{u}^T. \qquad (6.47)$$

Notice that the capillarity regularization term results in a Laplace operator appearing in $\delta\mathcal{H}/\delta\rho$. The presence of this Laplace operator dictates that the change-of-variables back from entropy variables to conservation variables is non-local and involves the solution operator of the Laplace problem. To avoid the difficulties associated with such an operator, let me introduce $\delta\mathcal{H}/\delta\rho$ as a new unknown v to the system,

$$v = W'(\rho) - \frac{1}{\text{We}}\Delta\rho - \frac{|\mathbf{u}|^2}{2}. \qquad (6.48)$$

By rearranging terms in (6.48) and taking the gradient of both sides, one can obtain an interesting relationship between v and the pressure and capillarity terms appearing in the momentum equations:

$$\nabla v + \nabla\frac{|\mathbf{u}|^2}{2} = W''(\rho)\nabla\rho - \frac{1}{\text{We}}\nabla\Delta\rho$$

$$= \frac{p_{,\rho}}{\rho} \nabla \rho - \frac{1}{\mathrm{We}} \nabla \Delta \rho$$

$$= \frac{1}{\rho} \left(\nabla p - \nabla \cdot \boldsymbol{\varsigma} \right). \tag{6.49}$$

The above relationship implies that the pressure and capillarity terms in the momentum balance equations can be replaced by terms involving v as

$$\nabla p - \nabla \cdot \boldsymbol{\varsigma} = \rho \nabla v + \rho \nabla \frac{|\mathbf{u}|^2}{2}. \tag{6.50}$$

This inspires the following alternate strong form of the isothermal Navier-Stokes-Korteweg equations in terms of ρ, $\mathbf{u}$, and v:

$$\frac{\partial \rho}{\partial t} + \nabla \cdot (\rho \mathbf{u}) = 0, \tag{6.51}$$

$$\frac{\partial (\rho \mathbf{u})}{\partial t} + \nabla \cdot (\rho \mathbf{u} \otimes \mathbf{u}) - \nabla \cdot \boldsymbol{\tau} + \rho \nabla v + \rho \nabla \frac{|\mathbf{u}|^2}{2} = \rho \mathbf{b}, \tag{6.52}$$

$$v = W'(\rho) - \frac{1}{\mathrm{We}} \Delta \rho - \frac{|\mathbf{u}|^2}{2}. \tag{6.53}$$

Equation (6.53) can be understood as a new differential equation-of-state. Although some terms have been rewritten, (6.52) still provides a consistent momentum balance law when coupled with (6.53).

6.4 The weak formulation

Let $L^2(\Omega)$ be the space of square integrable functions over the domain Ω. Let $(\cdot, \cdot)_\Omega$ represent the L^2 inner product over the domain Ω and $(\cdot, \cdot)_{\partial\Omega}$ represent the L^2 inner product over the boundary $\partial\Omega$. Let $H^1(\Omega)$ denote the space of functions in $L^2(\Omega)$ with square integrable first-order derivatives. Finally, let $L^2(0, T; \mathfrak{U})$ denote the space which consists of all strongly measurable

165

functions $u : [0, T] \rightarrow \mathfrak{U}$ with

$$\|u\|_{L^2(0,T;\mathfrak{U})} := \left(\int_0^T \|u(t)\|_{\mathfrak{U}}^2 \right)^{1/2} < \infty. \tag{6.54}$$

The numerical scheme is based on the alternate statement of the strong formulation (6.51)-(6.53). Let $\mathcal{V}_1$ denote the trial solution space for ρ, and let $\mathcal{V}_2$ denote the trial solution space for u_i such that $u_i \in \mathcal{V}_2$ implies $u_i = 0$ on $\partial\Omega$ for each $i = 1, 2, 3$. The space $\mathcal{V}_1$ is also used as a trial solution space for v. It is assumed that the test function spaces coincide with the trial solution spaces. With these assumptions, the variational formulation for the isothermal Navier-Stokes-Korteweg system given by (6.51)-(6.53) is stated as follows.

Find $\rho(t) \in L^2\left(0, T; \mathcal{V}_1\right) \cap H^1\left(0, T; L^2(\Omega)\right)$, $\mathbf{u}(t) = (u_1(t), u_2(t), u_3(t))^T \in \left(L^2\left(0, T; \mathcal{V}_2\right)\right)^3 \cap \left(H^1\left(0, T; L^2(\Omega)\right)\right)^3$, and $v(t) \in L^2\left(0, T; \mathcal{V}_1\right)$, such that

$$\left(w_1, \frac{\partial\rho}{\partial t}\right)_\Omega - (\nabla w_1, \rho\mathbf{u})_\Omega = 0 \qquad \forall w_1 \in \mathcal{V}_1, \tag{6.55}$$

$$\left(\mathbf{w}, \mathbf{u}\frac{\partial\rho}{\partial t} + \rho\frac{\partial\mathbf{u}}{\partial t}\right)_\Omega - (\nabla\mathbf{w}, \rho\mathbf{u} \otimes \mathbf{u})_\Omega + (\mathbf{w}, \rho\nabla v)_\Omega + \left(\mathbf{w}, \rho\nabla\frac{|\mathbf{u}|^2}{2}\right)_\Omega$$
$$+ (\nabla\mathbf{w}, \boldsymbol{\tau})_\Omega = (\mathbf{w}, \rho\mathbf{b})_\Omega \qquad \forall\mathbf{w} = (w_2, w_3, w_4)^T \in (\mathcal{V}_2)^3, \tag{6.56}$$

$$(w_5, v)_\Omega = \left(w_5, W'(\rho) - \frac{|\mathbf{u}|^2}{2}\right)_\Omega + \frac{1}{\text{We}}(\nabla w_5, \nabla\rho)_\Omega \qquad \forall w_5 \in \mathcal{V}_1, \tag{6.57}$$

with $\rho(0) = \rho_0$ and $\mathbf{u}(0) = \mathbf{u}_0$ in Ω.

Assuming sufficiently regular $\mathcal{V}_1$ and $\mathcal{V}_2$, integrating (6.55)-(6.57) by parts yields the Euler-Lagrange form of the variational problem:

$$\left(w_1, \frac{\partial\rho}{\partial t}\right)_\Omega + (w_1, \nabla \cdot (\rho\mathbf{u}))_\Omega - (w_1, \rho\mathbf{u} \cdot \mathbf{n})_{\partial\Omega} = 0, \tag{6.58}$$

166

$$\left(\mathbf{w}, \mathbf{u}\frac{\partial\rho}{\partial t} + \rho\frac{\partial\mathbf{u}}{\partial t}\right)_\Omega + (\mathbf{w}, \nabla(\rho\mathbf{u}\otimes\mathbf{u}))_\Omega + (\mathbf{w}, \rho\nabla v)_\Omega + \left(\mathbf{w}, \rho\nabla\frac{|\mathbf{u}|^2}{2}\right)_\Omega$$

$$- (\mathbf{w}, \nabla\cdot\boldsymbol{\tau})_\Omega - (\mathbf{w}, \rho\mathbf{u}\otimes\mathbf{u}\cdot\mathbf{n})_{\partial\Omega} - (\mathbf{w}, \boldsymbol{\tau}\cdot\mathbf{n})_{\partial\Omega} - (\mathbf{w}, \rho\mathbf{b})_\Omega = 0, \qquad (6.59)$$

$$(w_5, v)_\Omega - \left(w_5, W'(\rho) + \frac{|\mathbf{u}|^2}{2}\right)_\Omega + \frac{1}{\text{We}}(w_5, \Delta\rho)_\Omega - \frac{1}{\text{We}}(w_5, \nabla\rho\cdot\mathbf{n})_{\partial\Omega} = 0.$$

$$(6.60)$$

Equations (6.58)-(6.60) enforce weak satisfaction of the differential equations given by (6.51)-(6.53) and the boundary conditions given by (6.3). The following theorem reveals that solutions of the weak problem given by (6.55)-(6.57) satisfy the energy dissipation relation of the isothermal Navier-Stokes-Korteweg equations.

Theorem 6.4.1. *Sufficiently smooth weak solutions of the variational problem given by (6.55)-(6.57) verify the energy dissipation condition (6.13).*

Proof. Since ρ and v share the same trial solution and test function spaces, one can take $w_1 = v$ in (6.55), $w_5 = \dfrac{\partial\rho}{\partial t}$ in (6.57), and perform integration by parts. This results in

$$\left(v, \frac{\partial\rho}{\partial t}\right)_\Omega - (\nabla v, \rho\mathbf{u})_\Omega = 0, \qquad (6.61)$$

$$\left(\frac{\partial\rho}{\partial t}, v\right)_\Omega = (\frac{\partial\rho}{\partial t}, W'(\rho) - \frac{|\mathbf{u}|^2}{2})_\Omega - \left(\frac{\partial\rho}{\partial t}, \frac{1}{\text{We}}\Delta\rho\right)_\Omega. \qquad (6.62)$$

Subtracting the first equation above from the second gives

$$\left(\frac{\partial\rho}{\partial t}, W'(\rho) - \frac{|\mathbf{u}|^2}{2} - \frac{1}{\text{We}}\Delta\rho\right)_\Omega = (\nabla v, \rho\mathbf{u})_\Omega. \qquad (6.63)$$

Noting that $\frac{\delta\mathcal{H}}{\delta\rho} = W'(\rho) - \frac{|\mathbf{u}|^2}{2} - \frac{1}{\text{We}}\Delta\rho$, one arrives at the following relation,

$$\frac{\delta\mathcal{E}}{\delta\rho}[\frac{\partial\rho}{\partial t}] := \left(\frac{\partial\rho}{\partial t}, \frac{\delta\mathcal{H}}{\delta\rho}\right)_\Omega = (\nabla v, \rho\mathbf{u})_\Omega. \tag{6.64}$$

Next, taking $\mathbf{w} = \mathbf{u}$ in (6.56) results in

$$\left(\mathbf{u}, \frac{\partial(\rho\mathbf{u})}{\partial t}\right)_\Omega - (\nabla\mathbf{u}, \rho\mathbf{u}\otimes\mathbf{u})_\Omega + (\mathbf{u}, \rho\nabla v)_\Omega + \left(\mathbf{u}, \rho\nabla\frac{|\mathbf{u}|^2}{2}\right)_\Omega + (\nabla\mathbf{u}, \boldsymbol{\tau})_\Omega$$
$$= (\mathbf{u}, \rho\mathbf{b})_\Omega. \tag{6.65}$$

Noting that $\frac{\delta\mathcal{H}}{\delta(\rho\mathbf{u})} = \mathbf{u}^T$, the above equation implies that

$$\frac{\delta\mathcal{E}}{\delta(\rho\mathbf{u})}[\frac{\partial(\rho\mathbf{u})}{\partial t}] := \left(\frac{\partial(\rho\mathbf{u})}{\partial t}, \frac{\delta\mathcal{H}}{\delta(\rho\mathbf{u})}\right)_\Omega$$
$$= (\nabla\mathbf{u}, \rho\mathbf{u}\otimes\mathbf{u})_\Omega - (\mathbf{u}, \rho\nabla v)_\Omega - \left(\mathbf{u}, \rho\nabla\frac{|\mathbf{u}|^2}{2}\right)_\Omega - (\nabla\mathbf{u}, \boldsymbol{\tau})_\Omega + (\mathbf{u}, \rho\mathbf{b})_\Omega. \tag{6.66}$$

The chain rule and equations (6.64) and (6.66) lead to the following expression for the time derivative of the free energy $\mathcal{E}$.

$$\frac{d\mathcal{E}}{dt} = \frac{\delta\mathcal{E}}{\delta\rho}[\frac{\partial\rho}{\partial t}] + \frac{\delta\mathcal{E}}{\delta(\rho\mathbf{u})}[\frac{\partial(\rho\mathbf{u})}{\partial t}]$$
$$= (\nabla v, \rho\mathbf{u})_\Omega + (\nabla\mathbf{u}, \rho\mathbf{u}\otimes\mathbf{u})_\Omega - (\mathbf{u}, \rho\nabla v)_\Omega - \left(\mathbf{u}, \rho\nabla\frac{|\mathbf{u}|^2}{2}\right)_\Omega - (\nabla\mathbf{u}, \boldsymbol{\tau})_\Omega$$
$$\quad + (\mathbf{u}, \rho\mathbf{b})_\Omega$$
$$= (\nabla\mathbf{u}, \rho\mathbf{u}\otimes\mathbf{u})_\Omega - \left(\mathbf{u}, \rho\nabla\frac{|\mathbf{u}|^2}{2}\right)_\Omega - (\nabla\mathbf{u}, \boldsymbol{\tau})_\Omega + (\mathbf{u}, \rho\mathbf{b})_\Omega. \tag{6.67}$$

Simple calculation shows that

$$(\nabla\mathbf{u}, \rho\mathbf{u}\otimes\mathbf{u})_\Omega - \left(\mathbf{u}, \rho\nabla\frac{|\mathbf{u}|^2}{2}\right)_\Omega = 0. \tag{6.68}$$

Then (6.67) becomes

$$\frac{d\mathcal{E}}{dt} = -\left(\nabla \mathbf{u}, \boldsymbol{\tau}\right)_\Omega + \left(\mathbf{u}, \rho \mathbf{b}\right)_\Omega. \tag{6.69}$$

In particular, when $\mathbf{b} = \mathbf{0}$, one has the dissipation inequality

$$\frac{d\mathcal{E}}{dt} = -\left(\nabla \mathbf{u}, \boldsymbol{\tau}\right)_\Omega \leq 0. \tag{6.70}$$

$\square$

Remark 6.4.1. *Theorem 6.4.1 together with Proposition 6.3.1 shows that the non-convexity is regularized by the non-local differential operator. The v variable is the non-local entropy variable for density. Here I do not directly perform the change-of-variable from ρ to v; instead, I weakly define the entropy variable v in terms of ρ and $\mathbf{u}$. Indeed, by resorting to such a "weak" way of defining the entropy variable, I avoid the prohibitive computational cost associated with inverting a differential operator.*

6.5 The semi-discrete formulation

The Galerkin method [107] is used to perform spatial discretization of (6.55)-(6.57). Let $\mathcal{V}_1^h \subset \mathcal{V}_1$ and $\mathcal{V}_2^h \subset \mathcal{V}_2$ be finite dimensional function spaces spanned by finite element basis functions, where the h-superscript denotes a mesh parameter. Equations (6.55)-(6.57) are approximated in space as follows. Find $\rho^h(t) \in L^2\left(0, T; \mathcal{V}_1^h\right) \cap H^1\left(0, T; L^2(\Omega)\right)$, $\mathbf{u}^h(t) = (u_1(t), u_2(t), u_3(t))^T \in$

$\left(L^2 \left(0, T; \mathcal{V}_2^h \right) \right)^3 \cap \left(H^1 \left(0, T; L^2(\Omega) \right) \right)^3$, and $v^h(t) \in L^2 \left(0, T; \mathcal{V}_1^h \right)$, such that

$$\left(w_1^h, \frac{\partial \rho^h}{\partial t} \right)_\Omega - \left(\nabla w_1^h, \rho^h \mathbf{u}^h \right)_\Omega = 0, \qquad \forall w_1^h \in \mathcal{V}_1^h, \tag{6.71}$$

$$\left(\mathbf{w}^h, \mathbf{u}^h \frac{\partial \rho^h}{\partial t} + \rho^h \frac{\partial \mathbf{u}^h}{\partial t} \right)_\Omega - \left(\nabla \mathbf{w}^h, \rho^h \mathbf{u}^h \otimes \mathbf{u}^h \right)_\Omega + \left(\mathbf{w}^h, \rho^h \nabla v^h \right)_\Omega$$
$$+ \left(\mathbf{w}^h, \rho^h \nabla \frac{|\mathbf{u}^h|^2}{2} \right)_\Omega + \left(\nabla \mathbf{w}^h, \boldsymbol{\tau}(\mathbf{u}^h) \right)_\Omega = \left(\mathbf{w}^h, \rho \mathbf{b} \right)_\Omega,$$
$$\forall \mathbf{w}^h = (w_2^h, w_3^h, w_4^h)^T \in \left(\mathcal{V}_2^h \right)^3, \tag{6.72}$$

$$\left(w_5^h, v^h \right)_\Omega = \left(w_5^h, W'(\rho^h) - \frac{|\mathbf{u}^h|^2}{2} \right)_\Omega + \frac{1}{\text{We}} \left(\nabla w_5^h, \nabla \rho^h \right)_\Omega,$$
$$\forall w_5^h \in \mathcal{V}_1^h, \tag{6.73}$$

with $\rho^h(0) = \rho_0^h$ and $\mathbf{u}^h(0) = \mathbf{u}_0^h$ in Ω.

Above, ρ_0^h and $\mathbf{u}_0^h$ are L^2-projections of $\rho_0(\mathbf{x})$, $\mathbf{u}_0(\mathbf{x})$ onto $\mathcal{V}_1^h$ and $(\mathcal{V}_2^h)^3$ respectively. By employing the same method as was used to prove Theorem 6.4.1, it can be shown that the semi-discrete problem inherits the energy dissipation property of the isothermal Navier-Stokes-Korteweg equations.

Theorem 6.5.1. *Solutions of the semi-discrete variational problem given by (6.71)-(6.73) verify the energy dissipation condition (6.13).*

Remark 6.5.1. *Henceforth, I use the same discrete space (up to prescription of boundary conditions) for ρ^h, u_i^h, $i = 1, 2, 3$, and v^h, i.e., I assume that $\mathcal{V}_1^h = \mathcal{V}_2^h = \mathcal{V}^h$.*

Remark 6.5.2. *I utilize NURBS basis functions to define the discrete spaces. Making use of NURBS basis functions and the isoparametric concept has led to the concept of isogeometric analysis.*

6.6 A family of quadrature rules

Before introducing the time integration scheme for the semi-discrete problem (6.71)-(6.73), three pairs of quadrature formulas are presented and proved. As a common feature, each pair has different signs in the asymptotic error terms, which will be critical in the development of stable time discretizations of general nonlinear terms. Let me start by introducing the well-known rectangular quadrature rules.

Lemma 6.6.1. *(Rectangular quadrature rules) For a function $f \in C^1([m,n])$, $m, n \in \mathbb{R}$, there exist $\xi_1, \xi_2 \in (m,n)$ such that the following quadrature rules hold true.*

$$\int_m^n f(x)dx = (n-m)f(m) + \frac{(n-m)^2}{2}f'(\xi_1), \tag{6.74}$$

$$\int_m^n f(x)dx = (n-m)f(n) - \frac{(n-m)^2}{2}f'(\xi_2). \tag{6.75}$$

Proof. Consider functions $F(x)$ and $G(x)$ defined as follows:

$$F(x) = \int_m^x f(s)ds, \tag{6.76}$$

$$G(x) = \int_n^x f(s)ds. \tag{6.77}$$

Taylor expansions of $F(x)$ at m and $G(x)$ at n lead to

$$
\begin{aligned}
F(x) &= F(m) + (x-m)f(m) + \frac{(x-m)^2}{2}f'(\hat{\xi}_1) \\
&= (x-m)f(m) + \frac{(x-m)^2}{2}f'(\hat{\xi}_1), \qquad \hat{\xi}_1 \in (m,n);
\end{aligned} \tag{6.78}
$$

$$
\begin{aligned}
G(x) &= G(n) + (x-n)f(n) + \frac{(x-n)^2}{2}f'(\hat{\xi}_2) \\
&= (x-n)f(n) + \frac{(x-n)^2}{2}f'(\hat{\xi}_2), \qquad \hat{\xi}_2 \in (m,n),
\end{aligned} \tag{6.79}
$$

171

where $\hat{\xi}_1$ and $\hat{\xi}_2$ depend on x. Specifically, by taking $x = n$ for $F(x)$, and $x = m$ for $G(x)$, one has

$$\int_m^n f(x)dx = F(n)$$

$$= (n-m)f(m) + \frac{(n-m)^2}{2}f'(\xi_1), \quad \xi_1 \in (m,n), \qquad (6.80)$$

$$\int_m^n f(x)dx = -G(m)$$

$$= (n-m)f(n) - \frac{(n-m)^2}{2}f'(\xi_2), \quad \xi_2 \in (m,n), \qquad (6.81)$$

which completes the proof. $\qquad\qquad\qquad\qquad\qquad\qquad\qquad\qquad\qquad\qquad\square$

Despite its low accuracy, the rectangular quadrature rules are useful for constructing nonlinearly stable, first-order accurate time integration schemes. It has been found that the time integration scheme generated by this pair of quadrature rules is closely related to the Eyre's method [75, 143], a widespread time integration scheme in the phase-field community. Next, let me briefly review a pair perturbed trapezoidal rules developed in [85] for the Cahn-Hilliard equation.

Lemma 6.6.2. *(Perturbed trapezoidal rules) For a function* $f \in C^3([m,n])$, *where* $m, n \in \mathbb{R}$, *there exist* $\xi_1, \xi_2 \in (m,n)$ *such that the following quadrature formulas hold true.*

$$\int_m^n f(x)dx = \frac{n-m}{2}\left(f(m) + f(n)\right) - \frac{(n-m)^3}{12}f''(m)$$

$$- \frac{(n-m)^4}{24}f'''(\xi_1), \qquad (6.82)$$

$$\int_m^n f(x)dx = \frac{n-m}{2}(f(m)+f(n)) - \frac{(n-m)^3}{12}f''(n)$$
$$+ \frac{(n-m)^4}{24}f'''(\xi_2). \tag{6.83}$$

Proof. The proof can be found in the appendix of [85]. □

In the last, a pair of perturbed mid-point rules is introduced. Similar to the perturbed trapezoidal rules, this pair of quadrature formulas can also generate an energy-stable second-order accurate temporal scheme [143]. Interestingly, the asymptotic error of the perturbed mid-point rules is smaller than that of the perturbed trapezoidal rules. This fact suggests that the fully discrete scheme based on the perturbed mid-point rules is less dissipative than the scheme based on the perturbed trapezoidal rules.

Lemma 6.6.3. *(Perturbed mid-point rules) For a function $f \in C^3([m,n])$, $m, n \in \mathbb{R}$, there exist $\xi_1, \xi_2 \in (m,n)$ such that the following quadrature rules hold true.*

$$\int_m^n f(x)dx = (n-m)f(\frac{m+n}{2}) + \frac{(n-m)^3}{24}f''(m)$$
$$+ \frac{(n-m)^4}{48}f'''(\xi_1), \tag{6.84}$$
$$\int_m^n f(x)dx = (n-m)f(\frac{m+n}{2}) + \frac{(n-m)^3}{24}f''(n)$$
$$- \frac{(n-m)^4}{48}f'''(\xi_2). \tag{6.85}$$

Proof. Let $P(x)$ be a quadratic polynomial satisfying

$$P(\frac{m+n}{2}) = f(\frac{m+n}{2}), \quad P'(\frac{m+n}{2}) = f'(\frac{m+n}{2}), \quad P'' = f''(m). \tag{6.86}$$

173

Denote $R(x)$ as $R(x) = f(x) - P(x)$, and $R(x)$ may be rewritten as

$$R(x) = w(x)S(x), \tag{6.87}$$

$$w(x) = (x - \frac{m+n}{2})^2(x - 2m + n). \tag{6.88}$$

According to l'Hôspital's rule,

$$\lim_{x \to \frac{m+n}{2}} S(x) = \frac{R''(\frac{m+n}{2})}{3(n-m)} = \frac{f''(\frac{m+n}{2}) - P''}{3(n-m)}$$

$$= \frac{f''(\frac{m+n}{2}) - f''(m)}{3(n-m)} = \frac{f'''(m + \zeta)}{6}, \tag{6.89}$$

for $\zeta \in (0, (n-m)/2)$. Therefore, $S(x)$ is well-defined in (m, n). Consider a function $F(z) = f(z) - P(z) - w(z)S(x)$, with $x \in (m, n), x \ne \frac{m+n}{2}$ fixed. Apparently, $F(z)$ satisfies

$$F(\frac{m+n}{2}) = F'(\frac{m+n}{2}) = F''(m) = F(x) = 0. \tag{6.90}$$

Applying Rolle's rule three times, one may obtain $\vartheta \in (m, n)$ such that $F'''(\vartheta) = 0$. Therefore, one has

$$f'''(\vartheta) - P'''(\vartheta) - w'''(\vartheta)S(x) = 0 \tag{6.91}$$

$$\Rightarrow S(x) = \frac{f'''(\vartheta)}{w'''(\vartheta)} = \frac{f'''(\vartheta)}{6}. \tag{6.92}$$

Relations (6.89) and (6.92) imply that there exist $\vartheta \in (m, n)$ such that $S(x) = f'''(\vartheta)/6$ for $\forall x \in (m, n)$. Considering the integration of $f(x)$ over (m, n), one has

$$\int_m^n f(x)dx = \int_m^n P(x)dx + \int_m^n w(x)S(x)dx. \tag{6.93}$$

It is easy to verify that $w(x)$ does not change its sign in (m, n), therefore, the mean value theorem implies

$$\int_m^n w(x)S(x)dx = \int_m^n w(x)\frac{f'''(\vartheta)}{6}dx = \frac{f'''(\xi_1)}{6}\int_m^n w(x)dx$$
$$= \frac{f'''(\xi_1)}{48}(n-m)^4. \qquad (6.94)$$

Also, an explicit form of $P(x)$ can be obtained by solving the equations (6.86), and one has

$$\int_m^n P(x)dx = (n-m)f(\frac{m+n}{2}) + \frac{(n-m)^3}{24}f''(m). \qquad (6.95)$$

Combing the results (6.94) and (6.95) yields

$$\int_m^n f(x)dx = (n-m)f(\frac{m+n}{2}) + \frac{(n-m)^3}{24}f''(m)$$
$$+ \frac{(n-m)^4}{48}f'''(\xi_1), \qquad (6.96)$$

which proved the first quadrature formula (6.84). The proof for the second formula (6.85) follows the same manner by choosing $P(x)$ satisfying

$$P(\frac{m+n}{2}) = f(\frac{m+n}{2}), \quad P'(\frac{m+n}{2}) = f'(\frac{m+n}{2}), \quad P'' = f''(n), \quad (6.97)$$

and

$$w(x) = (x - \frac{m+n}{2})^2(x - 2n + m). \qquad (6.98)$$

$\square$

175

6.7 The fully discrete scheme

As was mentioned in Section 1.1.3, the weighted residual form of the symmetrized Navier-Stokes equations in terms of classical entropy variables in conjunction with a space-time formulation constitutes a fully discrete scheme which is provably unconditionally stable-in-energy [178]. Unfortunately, classical entropy variables do not comprise a viable variable set in the context of the van der Waals fluid. Moreover, the stability of the space-time formulation in the context of the symmetrized Navier-Stokes equations is contingent upon the fact that the Jacobian matrix describing the mapping from conservation variables to classical entropy variables is positive definite. In the context of the van der Waals fluid model, the Jacobian matrix can be singular or even negative definite within the elliptic region. This is due to the non-convexity of the classical mathematical entropy function within the elliptic region.

Perhaps the simplest second-order time-marching scheme for time dependent systems is the mid-point rule. In fact, for some nonlinear systems such as the incompressible Navier-Stokes equations, the application of the mid-point rule to a provably energy-stable semi-discrete formulation will lead to a provably energy-stable fully discrete formulation. Unfortunately, this is not true for the isothermal Navier-Stokes-Korteweg system studied here. The primary issue in deriving a finite-difference time-discretization scheme for this system lies with approximating the chemical potential at a particular time step. A simple evaluation of the chemical potential using the mid-point rule is generally unstable. An alternative and somewhat appealing methodology

176

is inspired by the fact that the chemical potential is precisely the derivative of the free energy function with respect to the density field. Hence, one may approximate the chemical potential at time $t_{n+1/2} = \frac{1}{2}(t_{n+1} + t_n)$ using the finite difference formula

$$\mu(t_{n+1/2}) \approx \frac{W(\rho_{n+1}^h) - W(\rho_n^h)}{\rho_{n+1}^h - \rho_n^h}, \qquad (6.99)$$

where ρ_n^h and ρ_{n+1}^h are discrete approximations of the density field at time-steps t_n and t_{n+1}, respectively. Indeed, one can show that a time-marching scheme in which the above formula is used to approximate the chemical potential while all other terms are approximated using a variant of the mid-point rule is energy-stable and in fact energy-conservative in the inviscid setting. Unfortunately, the finite difference approximation given by (6.99) is ill-defined when $\rho_{n+1} = \rho_n$ and numerical tests have revealed it is unstable when $\rho_{n+1} \approx \rho_n$. When the free energy function is a polynomial, an equivalent and numerically stable representation of (6.99) can be recovered using a truncated Taylor expansion of the form

$$\frac{W(\rho_{n+1}^h) - W(\rho_n^h)}{\rho_{n+1}^h - \rho_n^h} = \sum_{i=0}^{n} \frac{1}{2^{2i}(2i+1)!} \frac{d^{2i}\mu\left(\rho_{n+1/2}^h\right)}{d\rho^{2i}} [\![\rho_n^h]\!]^{2i}, \qquad (6.100)$$

where

$$[\![\rho_n^h]\!] = \rho_{n+1}^h - \rho_n^h \text{ and } \rho_{n+1/2}^h = \frac{1}{2}\left(\rho_n^h + \rho_{n+1}^h\right). \qquad (6.101)$$

But in the non-polynomial setting, such an expansion results in fully discrete schemes which are no longer provably energy-stable. Hence, one is left with the

question: how can one approximate the finite difference approximation given by (6.99) in such a manner that energy stability is not upset? It turns out that one can do so by employing the specialized quadrature formulas introduced in Section 6.6 to develop an energy-stable fully discrete scheme. Using Lemma 6.6.2, one has

$$
\begin{aligned}
\frac{W(\rho_{n+1}^h) - W(\rho_n^h)}{\rho_{n+1}^h - \rho_n^h} &= \frac{1}{\rho_{n+1}^h - \rho_n^h} \int_{\rho_n^h}^{\rho_{n+1}^h} W'(\rho) d\rho \\
&= \frac{1}{\rho_{n+1}^h - \rho_n^h} \int_{\rho_n^h}^{\rho_{n+1}^h} \mu(\rho) d\rho \\
&= \frac{1}{2}(\mu(\rho_n^h) + \mu(\rho_{n+1}^h)) \\
&\quad - \frac{[\![\rho_n^h]\!]^2}{12} \mu''(\rho_n^h) - \frac{[\![\rho_n^h]\!]^3}{24} \mu'''(\rho_{n+\xi}^h),
\end{aligned}
\tag{6.102}
$$

for some $\xi \in (0, 1)$ where $\rho_{n+\xi}^h = (1 - \xi)\rho_n^h + \xi \rho_{n+1}^h$. This inspires the following approximation of the chemical potential at time $t_{n+1/2} = \frac{1}{2}(t_{n+1} + t_n)$,

$$
\mu(t_{n+1/2}) \approx \frac{1}{2}(\mu(\rho_n^h) + \mu(\rho_{n+1}^h)) - \frac{[\![\rho_n^h]\!]^2}{12} \mu''(\rho_n^h).
\tag{6.103}
$$

It can be seen that the above approximation is a perturbation of the stable approximation given in (6.99) by a factor of $-\frac{[\![\rho_n^h]\!]^3}{24} \mu'''(\rho_{n+\xi}^h)$, and this in turn is a stable perturbation as the free energy function for a van der Waal's fluid is super-convex.

With the approximation given by (6.103), it is ready to describe in full the proposed time integration scheme. Let me assume that the time interval $\mathcal{I} = (0, T)$ is divided into N_{ts} subintervals $\mathcal{I}_n = (t_n, t_{n+1})$, $n = 0, \cdots, N_{ts} - 1$. I use the notation ρ_{n+1}^h, $\mathbf{u}_{n+1}^h = (u_{1,n+1}^h, u_{2,n+1}^h, u_{3,n+1}^h)^T$, and v_{n+1}^h to represent

178

the fully discrete solutions at time level $n+1$. In each time step, given ρ_n^h, $\mathbf{u}_n^h$ and v_n^h, one needs to find ρ_{n+1}^h, $\mathbf{u}_{n+1}^h$ and v_{n+1}^h such that for all w_1^h, $w_5^h \in \mathcal{V}^h$, and $\mathbf{w}^h = (w_1^h, w_2^h, w_3^h) \in (\mathcal{V}^h)^3$,

$$\mathbf{B}^M(w_1^h; \rho_{n+1}^h, \mathbf{u}_{n+1}^h, v_{n+1}^h) := \left(w_1^h, \frac{[\![\rho_n^h]\!]}{\Delta t_n}\right)_\Omega - \left(\nabla w_1^h, \rho_{n+\frac{1}{2}}^h \mathbf{u}_{n+\frac{1}{2}}^h\right)_\Omega = 0,$$

$$(6.104)$$

$$\mathbf{B}^{\mathbf{U}}(\mathbf{w}^h; \rho_{n+1}^h, \mathbf{u}_{n+1}^h, v_{n+1}^h) := \left(\mathbf{w}^h, \mathbf{u}_{n+\frac{1}{2}}^h \frac{[\![\rho_n^h]\!]}{\Delta t_n} + \rho_{n+\frac{1}{2}}^h \frac{[\![\mathbf{u}_n^h]\!]}{\Delta t_n}\right)_\Omega$$
$$- \left(\nabla \mathbf{w}^h, \rho_{n+\frac{1}{2}}^h \mathbf{u}_{n+\frac{1}{2}}^h \otimes \mathbf{u}_{n+\frac{1}{2}}^h\right)_\Omega + \left(\nabla \mathbf{w}^h, \boldsymbol{\tau}(\mathbf{u}_{n+\frac{1}{2}}^h)\right)_\Omega$$
$$+ \left(\mathbf{w}^h, \rho_{n+\frac{1}{2}}^h \nabla v_{n+1}^h + \rho_{n+\frac{1}{2}}^h \nabla\left(\frac{|\mathbf{u}_{n+\frac{1}{2}}^h|^2}{2}\right)\right)_\Omega = 0, \qquad (6.105)$$

$$\mathbf{B}^E(w_5^h; \rho_{n+1}^h, \mathbf{u}_{n+1}^h, v_{n+1}^h) := \left(w_5^h, v_{n+1}^h\right)_\Omega$$
$$- \left(w_5^h, \frac{1}{2}(\mu(\rho_n^h) + \mu(\rho_{n+1}^h)) - \frac{[\![\rho_n^h]\!]^2}{12}\mu''(\rho_n^h)\right)_\Omega$$
$$+ \left(w_5^h, \frac{2|\mathbf{u}_{n+\frac{1}{2}}^h|^2 - |\mathbf{u}^h|_{n+\frac{1}{2}}^2}{2}\right)_\Omega - \left(\nabla w_5^h, \frac{1}{\mathrm{We}}\nabla \rho_{n+\epsilon}^h\right)_\Omega = 0, \quad (6.106)$$

where

$$\Delta t_n = t_{n+1} - t_n, \tag{6.107}$$

$$\rho_{n+\epsilon}^h = \rho_n^h + \epsilon[\![\rho_n^h]\!], \tag{6.108}$$

$$\epsilon = 1/2 + \eta, \tag{6.109}$$

$$\eta = \frac{1}{2}\tanh\left(\frac{\Delta t_n \mathrm{We}^{\frac{1}{2}}}{\mathcal{C}}\right). \tag{6.110}$$

As will become evident later, the parameter $\mathcal{C}$ appearing above is a non-dimensional constant that can be used to adjust the dissipation of the proposed time integration scheme. The quantity $\mathrm{We}^{1/2}$ in (6.110) will ensure that the dissipation varies according to the choices of length scale L_0.

Theorem 6.7.1. *The fully discrete variational formulation (6.104)-(6.110) satisfies the following properties:*

(1) The scheme is mass-conservative, i.e.,

$$\int_\Omega \rho_n^h d\mathbf{x} = \int_\Omega \rho_0^h d\mathbf{x}, \qquad \forall n = 1, \cdots, N_{ts}. \tag{6.111}$$

(2) The scheme verifies the discrete energy dissipation condition, that is,

$$\mathcal{E}(\rho_n^h, \rho_n^h \mathbf{u}_n^h) \leq \mathcal{E}(\rho_{n-1}^h, \rho_{n-1}^h \mathbf{u}_{n-1}^h), \qquad \forall n = 1, \cdots, N_{ts}. \tag{6.112}$$

(3) The local truncation error in time $\tau(t)$ can be bounded by $|\tau(t_n)| \leq K \Delta t_n^2$ for all $0 \leq n \leq N_{ts} - 1$, where K is a constant independent of Δt_n.

Proof. (1) Taking $w_1^h = 1$ in equation (6.104) gives

$$\left(1, \frac{[\![\rho_n^h]\!]}{\Delta t_n} \right)_\Omega = \frac{1}{\Delta t} \left(\int_\Omega \rho_{n+1}^h d\mathbf{x} - \int_\Omega \rho_n^h d\mathbf{x} \right)_\Omega = 0. \tag{6.113}$$

By induction, one has

$$\int_\Omega \rho_n^h d\mathbf{x} = \int_\Omega \rho_0^h d\mathbf{x}. \tag{6.114}$$

(2) As a result of (6.102), it is straightforward to have

$$\frac{[\![W(\rho_n^h)]\!]}{[\![\rho_n^h]\!]} + \frac{[\![\rho_n^h]\!]^3}{24} \mu'''(\rho_{n+\xi}^h) = \frac{1}{2}(\mu(\rho_n^h) + \mu(\rho_{n+1}^h)) - \frac{[\![\rho_n^h]\!]^2}{12} \mu''(\rho_n^h), \tag{6.115}$$

for $\xi \in (0, 1)$. By taking $w_1^h = v_{n+1}^h$ in equation (6.104) and $w_5^h = [\![\rho_n^h]\!]/\Delta t_n$ in equation (6.106), one has

$$\left(v_{n+1}^h, \frac{[\![\rho_n^h]\!]}{\Delta t_n} \right)_\Omega - \left(\nabla v_{n+1}^h, \rho_{n+\frac{1}{2}}^h \mathbf{u}_{n+\frac{1}{2}}^h \right)_\Omega = 0, \tag{6.116}$$

180

and

$$\left(\frac{[\![\rho_n^h]\!]}{\Delta t_n}, v_{n+1}^h\right)_\Omega - \left(\frac{[\![\rho_n^h]\!]}{\Delta t_n}, \frac{1}{2}(\mu(\rho_n^h) + \mu(\rho_{n+1}^h)) - \frac{[\![\rho_n^h]\!]^2}{12}\mu''(\rho_n^h)\right)_\Omega$$
$$+ \left(\frac{[\![\rho_n^h]\!]}{\Delta t_n}, \frac{2|\mathbf{u}_{n+\frac{1}{2}}^h|^2 - |\mathbf{u}^h|_{n+\frac{1}{2}}^2}{2}\right)_\Omega - \left(\nabla\frac{[\![\rho_n^h]\!]}{\Delta t_n}, \frac{1}{\text{We}}\nabla\rho_{n+\epsilon}^h\right)_\Omega = 0. \qquad (6.117)$$

Combining equations (6.116) and (6.117) by canceling the term $\left(v_{n+1}^h, \frac{[\![\rho_n^h]\!]}{\Delta t_n}\right)_\Omega$

yields

$$\left(\nabla v_{n+1}^h, \rho_{n+\frac{1}{2}}^h \mathbf{u}_{n+\frac{1}{2}}^h\right)_\Omega - \left(\frac{[\![\rho_n^h]\!]}{\Delta t_n}, \frac{1}{2}(\mu(\rho_n^h) + \mu(\rho_{n+1}^h)) - \frac{[\![\rho_n^h]\!]^2}{12}\mu''(\rho_n^h)\right)_\Omega$$
$$+ \left(\frac{[\![\rho_n^h]\!]}{\Delta t_n}, \frac{2|\mathbf{u}_{n+\frac{1}{2}}^h|^2 - |\mathbf{u}^h|_{n+\frac{1}{2}}^2}{2}\right)_\Omega - \left(\nabla\frac{[\![\rho_n^h]\!]}{\Delta t_n}, \frac{1}{\text{We}}\nabla\rho_{n+\epsilon}^h\right)_\Omega = 0. \qquad (6.118)$$

Due to the relation given by (6.115), the second term in (6.118) can be written

as

$$\left(\frac{[\![\rho_n^h]\!]}{\Delta t_n}, \frac{1}{2}(\mu(\rho_n^h) + \mu(\rho_{n+1}^h)) - \frac{[\![\rho_n^h]\!]^2}{12}\mu''(\rho_n^h)\right)_\Omega$$
$$= \left(\frac{[\![\rho_n^h]\!]}{\Delta t_n}, \frac{[\![W(\rho_n^h)]\!]}{[\![\rho_n^h]\!]} + \frac{[\![\rho_n^h]\!]^3}{24}\mu'''(\rho_{n+\xi}^h)\right)_\Omega$$
$$= \int_\Omega \frac{[\![W(\rho_n^h)]\!]}{\Delta t_n}d\mathbf{x} + \left(\frac{[\![\rho_n^h]\!]}{\Delta t_n}, \frac{[\![\rho_n^h]\!]^3}{24}\mu'''(\rho_{n+\xi}^h)\right)_\Omega, \qquad (6.119)$$

and the last term in (6.118) can be rewritten as

$$\left(\nabla\frac{[\![\rho_n^h]\!]}{\Delta t_n}, \frac{1}{\text{We}}\nabla\rho_{n+\epsilon}^h\right)_\Omega = \left(\nabla[\![\rho_n^h]\!], \frac{\nabla\rho_{n+\frac{1}{2}}^h}{\text{We}\,\Delta t_n}\right)_\Omega + \left(\nabla[\![\rho_n^h]\!], \frac{\eta}{\text{We}\,\Delta t_n}\nabla[\![\rho_n^h]\!]\right)_\Omega$$
$$= \int_\Omega \frac{[\![|\nabla\rho^h|_n^2]\!]}{2\,\text{We}\,\Delta t_n}d\mathbf{x} + \left(\nabla[\![\rho_n^h]\!], \frac{\eta\nabla[\![\rho_n^h]\!]}{\text{We}\,\Delta t_n}\right)_\Omega. \qquad (6.120)$$

Therefore, equation (6.118) can be rewritten as

$$
(\nabla v_{n+1}^h, \rho_{n+\frac{1}{2}}^h \mathbf{u}_{n+\frac{1}{2}}^h)_\Omega - \left(\frac{[\![\rho_n^h]\!]}{\Delta t_n}, \frac{[\![\rho_n^h]\!]^3}{24} \mu'''(\rho_{n+\xi}^h) \right)_\Omega
$$
$$
+ \left(\frac{[\![\rho_n^h]\!]}{\Delta t_n}, \frac{2|\mathbf{u}_{n+\frac{1}{2}}^h|^2 - |\mathbf{u}^h|_{n+\frac{1}{2}}^2}{2} \right)_\Omega - \int_\Omega \frac{[\![W(\rho_n^h)]\!]}{\Delta t_n} d\mathbf{x}
$$
$$
- \int_\Omega \frac{1}{2\,\mathrm{We}\,\Delta t_n} [\![|\nabla \rho^h|_n^2]\!] d\mathbf{x} - \left(\nabla[\![\rho_n^h]\!], \frac{\eta}{\mathrm{We}\,\Delta t_n} \nabla[\![\rho_n^h]\!] \right)_\Omega = 0. \qquad (6.121)
$$

Next, taking $\mathbf{w}^h = \mathbf{u}_{n+\frac{1}{2}}^h$ in equation (6.105) leads to

$$
\left(\mathbf{u}_{n+\frac{1}{2}}^h, \mathbf{u}_{n+\frac{1}{2}}^h \frac{[\![\rho_n^h]\!]}{\Delta t_n} + \rho_{n+\frac{1}{2}} \frac{[\![\mathbf{u}_n^h]\!]}{\Delta t_n} \right)_\Omega - (\nabla \mathbf{u}_{n+\frac{1}{2}}^h, \rho_{n+\frac{1}{2}} \mathbf{u}_{n+\frac{1}{2}} \otimes \mathbf{u}_{n+\frac{1}{2}})_\Omega
$$
$$
+ (\nabla \mathbf{u}_{n+\frac{1}{2}}^h, \boldsymbol{\tau}(\mathbf{u}_{n+\frac{1}{2}}^h))_\Omega
$$
$$
+ \left(\mathbf{u}_{n+\frac{1}{2}}^h, \rho_{n+\frac{1}{2}} \nabla v_{n+1}^h + \rho_{n+\frac{1}{2}} \nabla(\frac{|\mathbf{u}_{n+\frac{1}{2}}^h|^2}{2}) \right)_\Omega = 0. \qquad (6.122)
$$

Subtracting (6.121) from (6.122) yields

$$
- (\nabla v_{n+1}^h, \rho_{n+\frac{1}{2}}^h \mathbf{u}_{n+\frac{1}{2}}^h)_\Omega + \left(\frac{[\![\rho_n^h]\!]}{\Delta t_n}, \frac{[\![\rho_n^h]\!]^3}{24} \mu'''(\rho_{n+\xi}^h) \right)_\Omega
$$
$$
- \left(\frac{[\![\rho_n^h]\!]}{\Delta t_n}, \frac{2|\mathbf{u}_{n+\frac{1}{2}}^h|^2 - |\mathbf{u}^h|_{n+\frac{1}{2}}^2}{2} \right)_\Omega + \int_\Omega \frac{[\![W(\rho_n^h)]\!]}{\Delta t_n} d\mathbf{x}
$$
$$
+ \int_\Omega \frac{1}{2\,\mathrm{We}\,\Delta t_n} [\![|\nabla \rho^h|_n^2]\!] d\mathbf{x} + \left(\nabla[\![\rho_n^h]\!], \frac{\eta}{\mathrm{We}\,\Delta t_n} \nabla[\![\rho_n^h]\!] \right)_\Omega
$$
$$
+ \left(\mathbf{u}_{n+\frac{1}{2}}^h, \mathbf{u}_{n+\frac{1}{2}}^h \frac{[\![\rho_n^h]\!]}{\Delta t_n} + \rho_{n+\frac{1}{2}} \frac{[\![\mathbf{u}_n^h]\!]}{\Delta t_n} \right)_\Omega - (\nabla \mathbf{u}_{n+\frac{1}{2}}^h, \rho_{n+\frac{1}{2}} \mathbf{u}_{n+\frac{1}{2}} \otimes \mathbf{u}_{n+\frac{1}{2}})_\Omega
$$
$$
+ (\nabla \mathbf{u}_{n+\frac{1}{2}}^h, \boldsymbol{\tau}(\mathbf{u}_{n+\frac{1}{2}}^h))_\Omega + \left(\mathbf{u}_{n+\frac{1}{2}}^h, \rho_{n+\frac{1}{2}} \nabla v_{n+1}^h + \rho_{n+\frac{1}{2}} \nabla(\frac{|\mathbf{u}_{n+\frac{1}{2}}^h|^2}{2}) \right)_\Omega
$$
$$
= 0. \qquad (6.123)
$$

Noticing that

$$-\left(\frac{[\![\rho_n^h]\!]}{\Delta t_n}, \frac{2|\mathbf{u}_{n+\frac{1}{2}}^h|^2 - |\mathbf{u}^h|_{n+\frac{1}{2}}^2}{2}\right)_\Omega + \left(\mathbf{u}_{n+\frac{1}{2}}^h, \mathbf{u}_{n+\frac{1}{2}}^h \frac{[\![\rho_n^h]\!]}{\Delta t_n} + \rho_{n+\frac{1}{2}} \frac{[\![\mathbf{u}_n^h]\!]}{\Delta t_n}\right)_\Omega$$

$$= \int_\Omega \frac{[\![\rho_n^h]\!]|\mathbf{u}^h|_{n+\frac{1}{2}}^2}{2\Delta t_n} + \frac{\rho_{n+\frac{1}{2}}^h [\![|\mathbf{u}^h|_n^2]\!]}{2\Delta t_n} d\mathbf{x}$$

$$= \int_\Omega \frac{1}{\Delta t_n} [\![\rho_n^h \frac{|\mathbf{u}^h|_n^2}{2}]\!] d\mathbf{x}, \tag{6.124}$$

and

$$(\nabla \mathbf{u}_{n+\frac{1}{2}}^h, \rho_{n+\frac{1}{2}} \mathbf{u}_{n+\frac{1}{2}} \otimes \mathbf{u}_{n+\frac{1}{2}})_\Omega - \left(\mathbf{u}_{n+\frac{1}{2}}^h, \rho_{n+\frac{1}{2}} \nabla(\frac{|\mathbf{u}_{n+\frac{1}{2}}^h|^2}{2})\right)_\Omega = 0 \tag{6.125}$$

$$- (\nabla v_{n+1}^h, \rho_{n+\frac{1}{2}}^h \mathbf{u}_{n+\frac{1}{2}}^h)_\Omega + (\mathbf{u}_{n+\frac{1}{2}}^h, \rho_{n+\frac{1}{2}} \nabla v_{n+1}^h)_\Omega = 0, \tag{6.126}$$

the equation (6.123) implies

$$\frac{[\![\mathcal{E}(\rho_n^h, \rho_n^h \mathbf{u}_n^h)]\!]}{\Delta t_n} = \frac{1}{\Delta t_n} \int_\Omega [\![\rho_n^h \frac{|\mathbf{u}^h|_n^2}{2}]\!] + [\![W(\rho_n^h)]\!] + \frac{1}{2\,\mathrm{We}} [\![|\nabla \rho^h|_n^2]\!] d\mathbf{x}$$

$$= -(\nabla \mathbf{u}_{n+\frac{1}{2}}^h, \boldsymbol{\tau}(\mathbf{u}_{n+\frac{1}{2}}^h))_\Omega - \left(\frac{[\![\rho_n^h]\!]}{\Delta t_n}, \frac{[\![\rho_n^h]\!]^3}{24} \mu'''(\rho_{n+\xi}^h)\right)_\Omega$$

$$- \left(\nabla[\![\rho_n^h]\!], \frac{\eta}{\mathrm{We}\,\Delta t_n} \nabla[\![\rho_n^h]\!]\right)_\Omega$$

$$\leq 0. \tag{6.127}$$

The last inequality is due to Proposition 6.1.1 and super-convexity, that is, $\mu''' = W'''' > 0$.

(3) Consider the mid-point rule applied to the semi-discrete formulation (6.55)-(6.57):

$$\left(w_1^h, \frac{[\![\rho_n^h]\!]}{\Delta t}\right)_\Omega - \left(\nabla w_1^h, \rho_{n+\frac{1}{2}}^h \mathbf{u}_{n+\frac{1}{2}}^h\right)_\Omega = 0, \tag{6.128}$$

183

$$\left(\mathbf{w}^h, \mathbf{u}^h_{n+\frac{1}{2}}\frac{[\![\rho^h_n]\!]}{\Delta t_n} + \rho_{n+\frac{1}{2}}\frac{[\![\mathbf{u}^h_n]\!]}{\Delta t_n}\right)_\Omega - \left(\nabla\mathbf{w}^h, \rho_{n+\frac{1}{2}}\mathbf{u}_{n+\frac{1}{2}}\otimes\mathbf{u}_{n+\frac{1}{2}}\right)_\Omega$$

$$+\left(\nabla\mathbf{w}^h, \boldsymbol{\tau}(\mathbf{u}^h_{n+\frac{1}{2}})\right)_\Omega + \left(\mathbf{w}^h, \rho_{n+\frac{1}{2}}\nabla v^h_{mid} + \rho_{n+\frac{1}{2}}\nabla(\frac{|\mathbf{u}^h_{n+\frac{1}{2}}|^2}{2})\right)_\Omega = 0, \quad (6.129)$$

$$\left(w^h_5, v^h_{mid}\right)_\Omega - \left(w^h_5, \mu(\rho^h_{n+\frac{1}{2}})\right)_\Omega + \left(w^h_5, \frac{|\mathbf{u}^h_{n+\frac{1}{2}}|^2}{2}\right)_\Omega$$

$$- \left(\nabla w^h_5, \frac{1}{\mathrm{We}}\nabla\rho^h_{n+\frac{1}{2}}\right)_\Omega = 0. \quad (6.130)$$

The local truncation error associated with the mid-point rule can be obtained by replacing the time discrete solution $\rho^h_n, \mathbf{u}^h_n$ with the corresponding exact time continuous solution $\rho^h(t_n), \mathbf{u}^h(t_n)$ in the above equations and performing Taylor expansions:

$$\left(w^h_1, \frac{[\![\rho^h(t_n)]\!]}{\Delta t}\right)_\Omega - \left(\nabla w^h_1, \rho^h(t_{n+\frac{1}{2}})\mathbf{u}^h(t_{n+\frac{1}{2}})\right)_\Omega = \left(w^h_1, \Theta^{mid}_\rho\right)_\Omega, \quad (6.131)$$

$$\left(\mathbf{w}^h, \mathbf{u}^h(t_{n+\frac{1}{2}})\frac{[\![\rho^h(t_n)]\!]}{\Delta t_n} + \rho^h(t_{n+\frac{1}{2}})\frac{[\![\mathbf{u}^h(t_n)]\!]}{\Delta t_n}\right)_\Omega$$

$$- \left(\nabla\mathbf{w}^h, \rho^h(t_{n+\frac{1}{2}})\mathbf{u}^h(t_{n+\frac{1}{2}})\otimes\mathbf{u}^h(t_{n+\frac{1}{2}})\right)_\Omega + \left(\nabla\mathbf{w}^h, \boldsymbol{\tau}(\mathbf{u}^h(t_{n+\frac{1}{2}}))\right)_\Omega$$

$$+ \left(\mathbf{w}^h, \rho^h(t_{n+\frac{1}{2}})\nabla\tilde{v}^h_{mid} + \rho^h(t_{n+\frac{1}{2}})\nabla(\frac{|\mathbf{u}^h(t_{n+\frac{1}{2}})|^2}{2})\right)_\Omega = \left(\mathbf{w}^h, \boldsymbol{\Theta}^{mid}_\mathbf{u}\right)_\Omega,$$

$$(6.132)$$

$$\left(w^h_5, \tilde{v}^h_{mid}\right)_\Omega - \left(w^h_5, \mu(\rho^h(t_{n+\frac{1}{2}}))\right)_\Omega + \left(q^h_5, \frac{|\mathbf{u}^h(t_{n+\frac{1}{2}})|^2}{2}\right)_\Omega$$

$$- \left(\nabla w^h_5, \frac{1}{\mathrm{We}}\nabla\rho^h(t_{n+\frac{1}{2}})\right)_\Omega = 0, \quad (6.133)$$

where Θ^{mid}_ρ and $\boldsymbol{\Theta}^{mid}_\mathbf{u}$ are the local truncation errors. Assuming sufficient smoothness, Taylor expansions of the time continuous solutions lead to

$$\Theta^{mid}_\rho = \mathcal{O}(\Delta t_n^2), \quad \boldsymbol{\Theta}^{mid}_\mathbf{u} = \mathcal{O}(\Delta t_n^2)\mathbf{1}. \quad (6.134)$$

This calculation verifies the second-order accuracy of the mid-point rule. Now one may consider the time discrete scheme (6.104)-(6.106). Replacing the time discrete solution with the time continuous solution, it can be obtained that

$$\left(w_1^h, \frac{[\![\rho^h(t_n)]\!]}{\Delta t}\right)_\Omega - \left(\nabla w_1^h, \rho^h(t_{n+\frac{1}{2}})\mathbf{u}^h(t_{n+\frac{1}{2}})\right)_\Omega = \left(w_1^h, \Theta_\rho\right)_\Omega, \qquad (6.135)$$

$$\left(\mathbf{w}^h, \mathbf{u}^h(t_{n+\frac{1}{2}})\frac{[\![\rho^h(t_n)]\!]}{\Delta t_n} + \rho^h(t_{n+\frac{1}{2}})\frac{[\![\mathbf{u}^h(t_n)]\!]}{\Delta t_n}\right)_\Omega$$

$$- \left(\nabla \mathbf{w}^h, \rho^h(t_{n+\frac{1}{2}})\mathbf{u}^h(t_{n+\frac{1}{2}}) \otimes \mathbf{u}^h(t_{n+\frac{1}{2}})\right)_\Omega + \left(\nabla \mathbf{w}^h, \boldsymbol{\tau}(\mathbf{u}^h(t_{n+\frac{1}{2}}))\right)_\Omega$$

$$+ \left(\mathbf{w}^h, \rho^h(t_{n+\frac{1}{2}})\nabla\tilde{v}^h + \rho^h(t_{n+\frac{1}{2}})\nabla(\frac{|\mathbf{u}^h(t_{n+\frac{1}{2}})|^2}{2})\right)_\Omega = \left(\mathbf{w}^h, \Theta_\mathbf{u}\right)_\Omega, \quad (6.136)$$

$$\left(w_5^h, \tilde{v}^h\right)_\Omega - \left(w_5^h, \frac{1}{2}\left(\mu(\rho^h(t_n)) + \mu(\rho^h(t_{n+1}))\right) - \frac{[\![\rho^h(t_n)]\!]^2}{12}\mu''(\rho^h(t_n))\right)_\Omega$$

$$+ \left(w_5^h, \nabla\frac{2|\mathbf{u}^h(t_{n+\frac{1}{2}})|^2 - \frac{1}{2}(|\mathbf{u}^h(t_n)|^2 + |\mathbf{u}^h(t_{n+1})|^2)}{2}\right)_\Omega$$

$$- \left(\nabla w_5^h, \frac{1}{\mathrm{We}}\nabla\rho^h(t_{n+\epsilon})\right)_\Omega = 0. \qquad (6.137)$$

Assuming sufficient smoothness in time, Taylor series can be utilized to prove

$$\frac{1}{2}\left(\mu(\rho^h(t_n)) + \mu(\rho^h(t_{n+1}))\right) = \mu(\rho^h(t_{n+\frac{1}{2}})) + \mathcal{O}(\Delta t_n^2), \quad (6.138)$$

$$\frac{[\![\rho^h(t_n)]\!]^2}{12}\mu''(\rho^h(t_n)) = \mathcal{O}(\Delta t_n^2), \qquad (6.139)$$

$$2|\mathbf{u}^h(t_{n+\frac{1}{2}})|^2 - \frac{1}{2}(|\mathbf{u}^h(t_n)|^2 + |\mathbf{u}^h(t_{n+1})|^2) = |\mathbf{u}^h(t_{n+\frac{1}{2}})|^2 + \mathcal{O}(\Delta t_n^2), \quad (6.140)$$

$$\rho^h(t_{n+\epsilon}) = \rho^h(t_{n+\frac{1}{2}}) + \mathcal{O}(\eta\Delta t). \qquad (6.141)$$

Considering that

$$\eta = \frac{1}{2}\tanh\left(\frac{\Delta t\, \mathrm{We}^{\frac{1}{2}}}{\mathcal{C}}\right) \le \frac{\Delta t\, \mathrm{We}^{\frac{1}{2}}}{2\mathcal{C}}, \qquad (6.142)$$

185

it can be concluded that

$$\rho^h(t_{n+\epsilon}) = \rho^h(t_{n+\frac{1}{2}}) + \mathcal{O}(\Delta t_n^2). \qquad (6.143)$$

Combining the above results, it follows that

$$\left(w_1^h, \Theta_\rho\right)_\Omega = \left(w_1^h, \Theta_\rho^{mid}\right)_\Omega + \mathcal{O}(\Delta t_n^2), \qquad (6.144)$$

$$\left(\mathbf{w}^h, \boldsymbol{\Theta}_\mathbf{u}\right)_\Omega = \left(\mathbf{w}^h, \boldsymbol{\Theta}_\mathbf{u}^{mid}\right)_\Omega + \mathcal{O}(\Delta t_n^2)\mathbf{1}. \qquad (6.145)$$

Therefore, one has

$$\left(w_1^h, \Theta_\rho\right)_\Omega = \mathcal{O}(\Delta t_n^2), \qquad (6.146)$$

$$\left(\mathbf{w}^h, \boldsymbol{\Theta}_\mathbf{u}\right)_\Omega = \mathcal{O}(\Delta t_n^2), \qquad (6.147)$$

which complete the proof. $\qquad\square$

Remark 6.7.1. *According to the relations (6.144) and (6.145), this scheme may be viewed as a second-order perturbation of the mid-point rule which achieves energy dissipation.*

Remark 6.7.2. *From the relation (6.127), it can be seen that the energy dissipation associated with the time integration scheme actually consists of two parts: physical dissipation and numerical dissipation. The numerical dissipation will vanish if the time step approaches zero. When the time step is large, the numerical dissipation terms will enhance the stability of the scheme. Such a property makes the scheme very robust.*

Remark 6.7.3. *If I temporarily denote $\widehat{\Delta t_n}$ and $\overline{\Delta t_n}$ as the dimensionless time step scaled with capillarity time scale $\sqrt{\lambda/(a^2 b)}$ and the dimensional time step,*

186

respectively, then the meaning of the term $\Delta t_n \, \mathrm{We}^{\frac{1}{2}} \, / \mathcal{C}$ in (6.110) is revealed in the following relations by recalling (6.42) in Section 6.2,

$$\frac{\Delta t_n \, \mathrm{We}^{\frac{1}{2}}}{\mathcal{C}} = \frac{\widehat{\Delta t_n}}{\mathcal{C}} = \frac{\overline{\Delta t_n}}{\mathcal{C} \sqrt{\frac{\lambda}{a^2 b}}}. \tag{6.148}$$

Thus, in terms of the dimensional time step $\overline{\Delta t_n}$, it can be seen that the dimensionless expression $\Delta t_n \, \mathrm{We}^{\frac{1}{2}} \, / \mathcal{C}$ in fact does not depend on arbitrary scaling introduced by the non-dimensionalization. This relation also indicates that the numerical dissipation introduced by the last term in (6.106) is actually dictated by $\widehat{\Delta t_n}$, which is analogous to the design of the numerical dissipation in [85].

Remark 6.7.4. *Note that the other two pairs of quadrature rules can also be used to generate different energy-stable time integration schemes. For more details, see the appendices of [143] for details.*

6.8   Benchmark problems

In this section, a selection of numerical examples are presented to verify the theoretical estimates.

6.8.1   Manufactured solution

For the first numerical example, a one-dimensional manufactured solution is constructed to verify my code as well as the time accuracy of the time integration scheme. In particular, I consider the manufactured solution

$$\rho = 0.6 + 0.1 \sin(5\pi t) \cos(3\pi x), \tag{6.149}$$

$$\mathbf{u} = \sin(3\pi t)\sin(2\pi x). \tag{6.150}$$

Restricting my computations to the domain $\Omega = (0, 1)$, I observe that the manufactured solution satisfies the boundary conditions given by (6.4) and (6.3). The force vector $\mathbf{b}$ is obtained by substituting the above manufactured solution into equations (6.32)-(6.33). The dimensionless parameters are fixed to be Re $= 2.0 \times 10^1$ and We $= 1.0 \times 10^2$. First, I compute the problem with mesh sizes $\Delta x = 1/16, 1/32, 1/64, 1/128$, and $1/256$ for a fixed time step size of $\Delta t = 1.0 \times 10^{-5}$ for polynomial degrees $\mathfrak{p} = 1, 2$, and 3. The L^2-errors of ρ and $\mathbf{u}$, together with the corresponding convergence rates of the errors at $t = 0.1$, are listed in Table 6.1. Notice that the L^2-norm of the density and velocity errors optimally converges like $\mathcal{O}(\Delta x^{(\mathfrak{p}+1)})$. The deteriorated convergence rate for $\mathfrak{p} = 3$ at $\Delta x = 1/256$ is expected since the numerical errors are driven close to the machine precision at these spatial resolutions. Next, to analyze the behavior of the temporal discretization, I fix the spatial mesh to consist of 10^4 linear, quadratic, and cubic elements and calculate the discrete solutions up to $t = 1.0$ with $20, 100, 200, 1000$, and 2000 time steps. The solution errors at $t = 1.0$ versus the number of time steps are listed in Table 6.2. It can be seen that the numerical scheme exhibits second-order accuracy in time for all three polynomial degrees.

6.8.2 Coalescence of two bubbles in the absence of gravity

In this example, I consider a problem with zero body force (i.e., $\mathbf{b} = \mathbf{0}$) for the purpose of examining the mass conservation and energy dissipation

188

Table 6.1: Manufactured solution in 1-D for the isothermal Navier-Stokes-Korteweg equations: Spatial convergence rates at $t = 0.1$ with time-step size $\Delta t = 1.0 \times 10^{-5}$.

Polynomial degree $\mathfrak{p} = 1$

Δx	1/16	1/32	1/64	1/128	1/256
$\|\rho - \rho^h\|_{L^2(\Omega)}$	9.94×10^{-4}	2.41×10^{-4}	5.97×10^{-5}	1.49×10^{-5}	3.72×10^{-6}
order	-	2.04	2.01	2.00	2.00
$\|\mathbf{u} - \mathbf{u}^h\|_{L^2(\Omega)}$	3.74×10^{-3}	9.26×10^{-4}	2.31×10^{-4}	5.77×10^{-5}	1.44×10^{-5}
order	-	2.01	2.00	2.00	2.00

Polynomial degree $\mathfrak{p} = 2$

Δx	1/16	1/32	1/64	1/128	1/256
$\|\rho - \rho^h\|_{L^2(\Omega)}$	1.00×10^{-4}	1.19×10^{-5}	1.46×10^{-6}	1.82×10^{-7}	2.28×10^{-8}
order	-	3.07	3.03	3.00	3.00
$\|\mathbf{u} - \mathbf{u}^h\|_{L^2(\Omega)}$	2.36×10^{-4}	2.82×10^{-5}	3.47×10^{-6}	4.31×10^{-7}	5.37×10^{-8}
order	-	3.07	3.02	3.01	3.00

Polynomial degree $\mathfrak{p} = 3$

Δx	1/16	1/32	1/64	1/128	1/256
$\|\rho - \rho^h\|_{L^2(\Omega)}$	8.75×10^{-6}	4.94×10^{-7}	3.02×10^{-8}	1.92×10^{-9}	3.94×10^{-10}
order	-	4.15	4.03	3.98	2.28
$\|\mathbf{u} - \mathbf{u}^h\|_{L^2(\Omega)}$	1.38×10^{-5}	7.94×10^{-7}	4.87×10^{-8}	3.31×10^{-9}	1.35×10^{-9}
order	-	4.12	4.03	3.88	1.29

Table 6.2: Manufactured solution in 1-D for the isothermal Navier-Stokes-Korteweg equations: Temporal convergence rates at $t = 1.0$ with $\Delta x = 1.0 \times 10^{-4}$.

Polynomial degree $\mathfrak{p} = 1$

Δt	5.0×10^{-2}	1.0×10^{-2}	5.0×10^{-3}	1.0×10^{-3}	5.0×10^{-4}
$\|\rho - \rho^h\|_{L^2(\Omega)}$	7.35×10^{-3}	2.77×10^{-4}	6.90×10^{-5}	2.76×10^{-6}	6.93×10^{-7}
order	-	2.04	2.00	2.00	1.99
$\|\mathbf{u} - \mathbf{u}^h\|_{L^2(\Omega)}$	1.74×10^{-2}	6.75×10^{-4}	1.68×10^{-4}	6.72×10^{-6}	1.67×10^{-6}
order	-	2.02	2.01	2.00	2.01

Polynomial degree $\mathfrak{p} = 2$

Δt	5.0×10^{-2}	1.0×10^{-2}	5.0×10^{-3}	1.0×10^{-3}	5.0×10^{-4}
$\|\rho - \rho^h\|_{L^2(\Omega)}$	7.35×10^{-3}	2.77×10^{-4}	6.90×10^{-5}	2.76×10^{-6}	6.90×10^{-7}
order	-	2.04	2.00	2.00	2.00
$\|\mathbf{u} - \mathbf{u}^h\|_{L^2(\Omega)}$	1.74×10^{-2}	6.75×10^{-4}	1.68×10^{-4}	6.73×10^{-6}	1.68×10^{-6}
order	-	2.02	2.00	2.00	2.00

Polynomial degree $\mathfrak{p} = 3$

Δt	5.0×10^{-2}	1.0×10^{-2}	5.0×10^{-3}	1.0×10^{-3}	5.0×10^{-4}
$\|\rho - \rho^h\|_{L^2(\Omega)}$	7.35×10^{-3}	2.77×10^{-4}	6.90×10^{-5}	2.76×10^{-6}	6.90×10^{-7}
order	-	2.04	2.00	2.00	2.00
$\|\mathbf{u} - \mathbf{u}^h\|_{L^2(\Omega)}$	1.74×10^{-2}	6.75×10^{-4}	1.68×10^{-4}	6.73×10^{-6}	1.68×10^{-6}
order	-	2.02	2.00	2.00	2.00

properties. Specifically, I consider a bubble coalescence problem that was originally studied in [86, 114]. In this example, two vapor bubbles of different radii are originally placed close to each other. Capillarity and pressure forces then drive the two bubbles to merge together and form a single vapor bubble in equilibrium. For this example, the computational domain is set to be $\Omega = (0,1)^2$, and 256^2 quadratic NURBS elements are used to discretize in space. The centers of the bubbles are originally located at points $C_1 = (0.40, 0.50)$ and $C_2 = (0.78, 0.50)$. The radii of the bubbles are set to be $R_1 = 0.25$ and $R_2 = 0.10$. I specify the interface between the vapor and liquid phases via a hyperbolic tangent regularization

$$
\rho_0(\mathbf{x}) = 0.10 + 0.25 \left[\tanh\left(\frac{d_1(\mathbf{x}) - R_1}{2} \sqrt{\text{We}} \right) \right.
$$
$$
\left. + \tanh\left(\frac{d_2(\mathbf{x}) - R_2}{2} \sqrt{\text{We}} \right) \right], \tag{6.151}
$$

where $d_i(\mathbf{x})$ is the Euclidean distance between $\mathbf{x}$ and C_i, $i = 1, 2$. The initial velocities are set to be zero, i.e., $\mathbf{u} = \mathbf{0}$, and I simulate the coalescence process up to the final time of $T = 5.0$. In my simulation, the dimensionless parameters are fixed to be $\text{Re} = 5.12 \times 10^2$ and $\text{We} = 6.55 \times 10^4$. To verify the time accuracy of the scheme, a set overkill solutions is calculated to compare the numerical solutions.

6.8.2.1 Mass conservation

Let me denote the discrete mass at time step t_n as

$$
m_n := \int_\Omega \rho_n^h d\mathbf{x}, \tag{6.152}
$$

191

and the initial mass as

$$m_0 := \int_\Omega \rho_0^h d\mathbf{x} = \int_\Omega \rho_0(\mathbf{x})d\mathbf{x}. \qquad (6.153)$$

I have computed the coalescence problem with time step sizes of $\Delta t = 2.50 \times 10^{-2}, 1.25 \times 10^{-2}, 6.25 \times 10^{-3}, 5.00 \times 10^{-3}, 2.50 \times 10^{-3}$, and 1.25×10^{-3}. The corresponding maximum norms of relative mass errors are listed in Table 6.3. Note that the maximum mass errors are on the order of 10^{-12}, which may be attributed to quadrature errors, the nonlinear solver tolerance, and round-off errors.

Table 6.3: Coalescence of two bubbles in the absence of gravity: Relative mass errors.

Δt	1.25×10^{-2}	6.25×10^{-3}	5.00×10^{-3}	2.50×10^{-3}	1.25×10^{-3}
$\|\frac{m_n - m_0}{m_0}\|_{l_\infty}$	1.97×10^{-12}	1.89×10^{-12}	1.96×10^{-12}	2.02×10^{-12}	2.06×10^{-12}

6.8.2.2 Energy dissipation

To verify the energy dissipation property, I have calculated the discrete energy associated with the numerical solutions corresponding to time step sizes of $\Delta t = 2.50 \times 10^{-2}, 1.25 \times 10^{-2}, 6.25 \times 10^{-3}$, and 2.50×10^{-3}. I have also computed the discrete energy associated with a set of overkill solutions corresponding to a time step size of $\Delta t = 2.5 \times 10^{-5}$. These discrete energies $\mathcal{E}(\rho_n^h, \rho_n^h \mathbf{u}_n^h)$ are plotted against time in Figure 6.1. From the figure, it can be observed that the energy monotonically decreases with time for each time step size. Additionally, there is no visual difference between the different discrete

192

energies. In Figure 6.2, a detailed view of the discrete energies is plotted near $t = 0.1$. From this figure, it can be seen that the difference between the numerical solution and the overkill solution decreases with a reduction of the time step size.
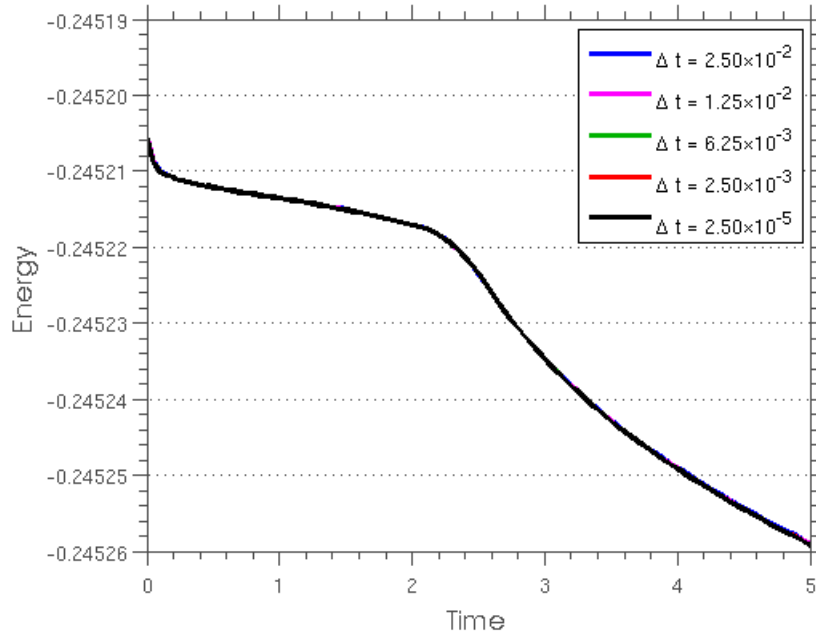
Figure 6.1: Coalescence of two bubbles in the absence of gravity: Evolution of the free energy calculated using the provably stable algorithm with different time steps.

6.8.2.3 Time accuracy

I calculate overkill solutions with $\Delta t = 2.50 \times 10^{-5}$. Then I repeat the computations with larger time steps $\Delta t = 2.50 \times 10^{-2}, 1.25 \times 10^{-2}, 6.25 \times 10^{-3}$, 2.50×10^{-3}, and 1.25×10^{-3}. The errors at $t = 1.0, 2.0, 3.0, 4.0$ and 5.0 are
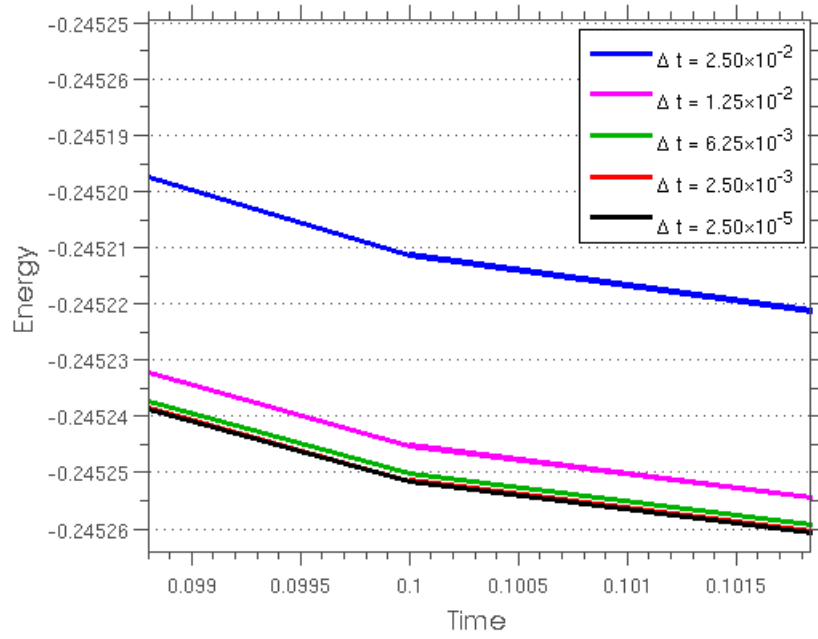
Figure 6.2: Coalescence of two bubbles in the absence of gravity: Evolution of the free energy calculated using the provably stable algorithm with different time steps. Detailed view in the vicinity of $t = 0.1$.

listed in Tables 6.4 - 6.5. In these tables, one may observe that the time accuracy for both density and velocity are second-order, which confirms the theoretical estimate. In Figures 6.3-6.5, I visualize the density profiles and the velocity fields at times $t = 1.0$, 3.0, and 5.0.

Table 6.4: Coalescence of two bubbles in the absence of gravity: Temporal convergence rates at times $t = 1.0$ and 2.0.

Time $t = 1.0$

Δt	2.50×10^{-2}	1.25×10^{-2}	6.25×10^{-3}	2.50×10^{-3}	1.25×10^{-3}
$\|\rho - \rho^h\|_{L^2(\Omega)}$	1.81×10^{-4}	4.57×10^{-5}	1.14×10^{-5}	1.83×10^{-6}	4.57×10^{-7}
order	-	1.99	2.00	1.99	2.00
$\|\mathbf{u} - \mathbf{u}^h\|_{L^2(\Omega)}$	3.56×10^{-5}	8.81×10^{-6}	2.20×10^{-6}	3.52×10^{-7}	8.79×10^{-8}
order	-	2.02	2.00	2.00	2.00

Time $t = 2.0$

Δt	2.50×10^{-2}	1.25×10^{-2}	6.25×10^{-3}	2.50×10^{-3}	1.25×10^{-3}
$\|\rho - \rho^h\|_{L^2(\Omega)}$	5.75×10^{-4}	1.45×10^{-4}	3.65×10^{-5}	5.83×10^{-6}	1.46×10^{-6}
order	-	1.99	1.99	2.00	2.00
$\|\mathbf{u} - \mathbf{u}^h\|_{L^2(\Omega)}$	4.79×10^{-5}	1.21×10^{-5}	3.04×10^{-6}	4.86×10^{-7}	1.21×10^{-7}
order	-	1.98	2.00	2.00	2.00

6.9 Applications

In this section, I simulate four different benchmark problems to investigate the effectiveness of my method as well as the validity of the Navier-Stokes-Korteweg model.

Table 6.5: Coalescence of two bubbles in the absence of gravity: Temporal convergence rates at times $t = 3.0$, 4.0 and 5.0.

Time $t = 3.0$

Δt	2.50×10^{-2}	1.25×10^{-2}	6.25×10^{-3}	2.50×10^{-3}	1.25×10^{-3}
$\|\rho - \rho^h\|_{L^2(\Omega)}$	8.21×10^{-4}	2.08×10^{-4}	5.21×10^{-5}	8.34×10^{-6}	2.09×10^{-6}
order	-	1.98	2.00	2.00	2.00
$\|\mathbf{u} - \mathbf{u}^h\|_{L^2(\Omega)}$	5.20×10^{-5}	1.33×10^{-5}	3.33×10^{-6}	5.33×10^{-7}	1.33×10^{-7}
order	-	1.97	1.99	2.00	2.00

Time $t = 4.0$

Δt	2.50×10^{-2}	1.25×10^{-2}	6.25×10^{-3}	2.50×10^{-3}	1.25×10^{-3}
$\|\rho - \rho^h\|_{L^2(\Omega)}$	9.00×10^{-4}	2.28×10^{-4}	5.70×10^{-5}	9.12×10^{-6}	2.28×10^{-6}
order	-	1.98	2.00	2.00	2.00
$\|\mathbf{u} - \mathbf{u}^h\|_{L^2(\Omega)}$	3.54×10^{-5}	8.49×10^{-6}	2.24×10^{-6}	3.58×10^{-7}	8.95×10^{-8}
order	-	2.06	1.92	2.00	2.00

Time $t = 5.0$

Δt	2.50×10^{-2}	1.25×10^{-2}	6.25×10^{-3}	2.50×10^{-3}	1.25×10^{-3}
$\|\rho - \rho^h\|_{L^2(\Omega)}$	1.10×10^{-3}	2.77×10^{-4}	6.92×10^{-5}	1.11×10^{-5}	2.76×10^{-6}
order	-	1.99	2.00	2.00	2.00
$\|\mathbf{u} - \mathbf{u}^h\|_{L^2(\Omega)}$	3.56×10^{-5}	8.98×10^{-6}	2.25×10^{-6}	3.59×10^{-7}	8.96×10^{-8}
order	-	1.99	2.00	2.00	2.00
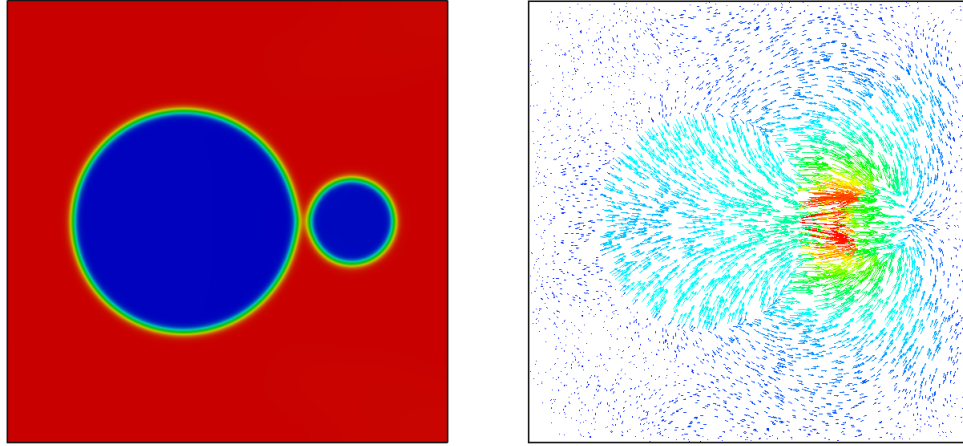
Figure 6.3: Coalescence of two bubbles in the absence of gravity: (left) density profile, (right) velocity field at time $t = 1.0$.
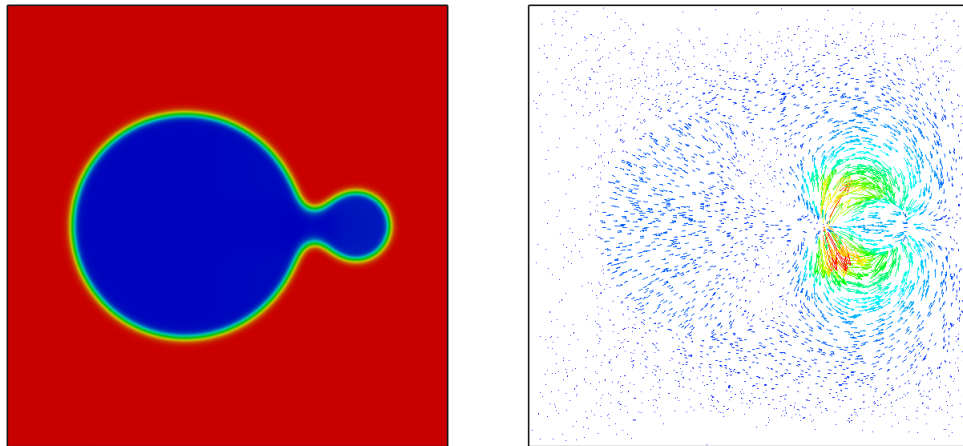
Figure 6.4: Coalescence of two bubbles in the absence of gravity: (left) density profile, (right) velocity field at time $t = 3.0$.
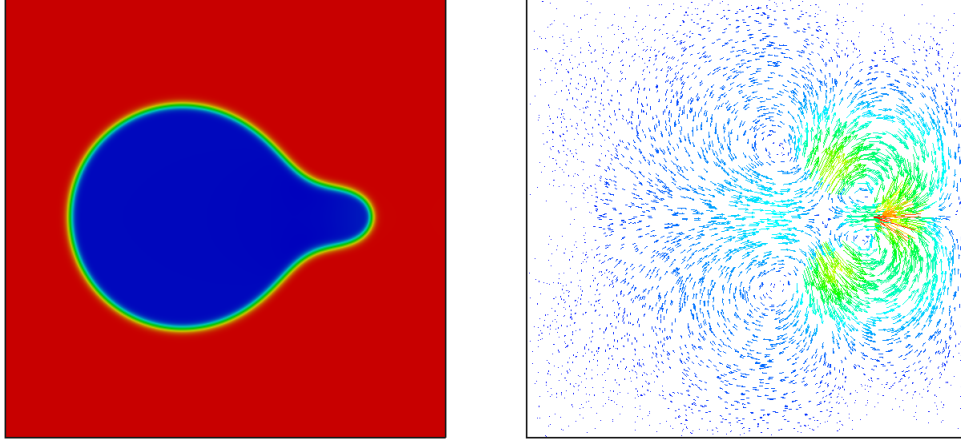
Figure 6.5: Coalescence of two bubbles in the absence of gravity: (left) density profile, (right) velocity field at time $t = 5.0$.

6.9.1 Traveling wave problem

The traveling wave problem is one of the few benchmark problems that possess a firm mathematical foundation [23]. It is frequently used to assess the accuracy and robustness of numerical schemes for conservation laws. As is well-known, poorly-designed numerical schemes will result in approximate solutions characterized by overshoots, undershoots, and incorrect propagation speeds of waves in the presence of sharp layers or discontinuities. Here, I consider travelling wave solutions to the one-dimensional Navier-Stokes-Korteweg equations. I restrict the simulation to the domain $\Omega = (0, 1)$ and set the initial conditions as

$$\rho_0(x) = \frac{\rho^{right} + \rho^{left}}{2} + \frac{\rho^{right} - \rho^{left}}{2} \tanh\left(\frac{x - 0.5}{2}\sqrt{We}\right), \qquad (6.154)$$

$$u_0(x) = \frac{u^{right} + u^{left}}{2} + \frac{u^{right} - u^{left}}{2} \tanh\left(\frac{x - 0.5}{2}\sqrt{We}\right). \qquad (6.155)$$

Periodic boundary conditions are imposed on an extended region $(-1, 1)$.
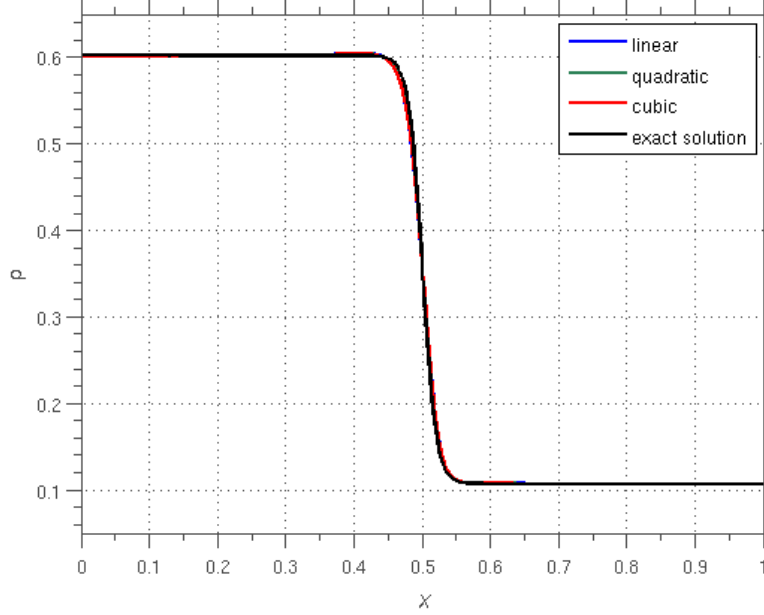
Figure 6.6: Stationary wave problem: Density profiles at $t = 0.1$ for $\mathfrak{p} = 1$, 2, and 3, when $\Delta x = 1.0 \times 10^{-2}$, $\Delta t = 1.0 \times 10^{-6}$, Re $= 2.0 \times 10^2$, and We $= 1.0 \times 10^4$.

6.9.1.1 Stationary wave problem

Let me begin by considering a stationary wave problem. By applying the initial conditions

$$(\rho^{right}, u^{right}) = (0.602, 0.0), \qquad (\rho^{left}, u^{left}) = (0.107, 0.0), \qquad (6.156)$$

a stationary wave is obtained centered at $x = 0.5$. This is due to the fact that the initial velocity field is zero and the initial density profile satisfies the Maxwell states (3.30)-(3.31) as well as the Rankine-Hugoniot conditions [74]. The Reynolds number and the Weber number are fixed as $\mathrm{Re} = 2.0 \times 10^2$ and $\mathrm{We} = 1.0 \times 10^4$. The problem is simulated using linear, quadratic, and cubic NURBS for $\Delta x = 1.0 \times 10^{-2}$ up to the final time of $T = 0.1$ using a time step size of $\Delta t = 1.0 \times 10^{-6}$. The resulting density profiles are illustrated in Figure 6.6. It can be seen from the figure that the differences between the numerical solutions and the exact solution are indistinguishable for all three polynomial degrees. Another important feature is that all three numerical solutions are smooth without oscillations.

Next, let me compare the effect of capillarity on my approximation of the stationary wave problem. In [66], the author gives a rough formula for the dimensionless interface width, which is $5.4\theta^2 \, \mathrm{We}^{-\frac{1}{2}}$. This formula provides an empirical estimate for the computational mesh size. Too coarse mesh may fail to capture the interface and may trigger numerical instability. In this example, I try to illustrate the importance of the mesh size criterion. I discretize in space using quadratic NURBS basis functions and fix the spatial mesh size to be $\Delta x = 1.0 \times 10^{-2}$. The temporal integration is performed up to $T = 0.1$ with a step size of $\Delta t = 1.0 \times 10^{-6}$. The Reynolds number is fixed to be 2.0×10^2. In Figure 6.7, I have plotted the numerical solution for the Weber numbers 1.0×10^2, 1.0×10^4, and 1.0×10^6 respectively. For $\mathrm{We} = 1.0 \times 10^2$ and 1.0×10^4, the obtained numerical solutions are smooth and without oscillations. It may
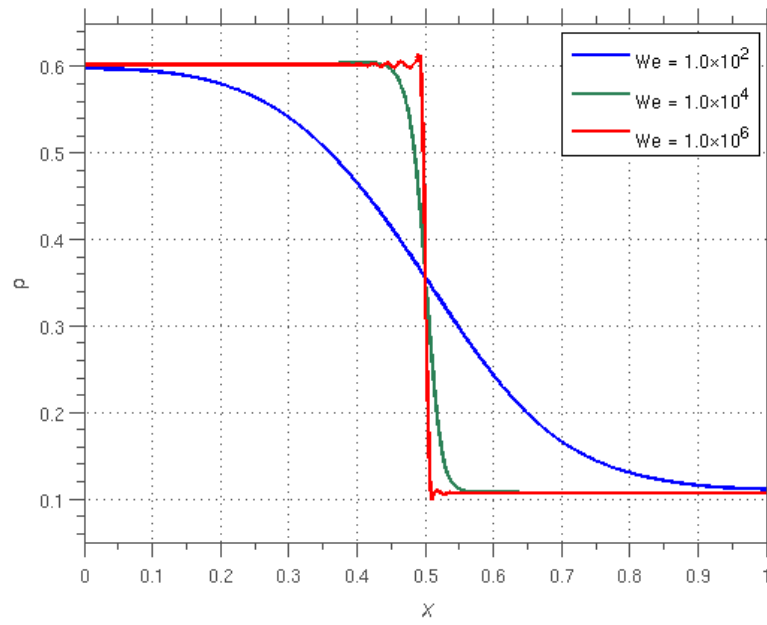
Figure 6.7: Stationary wave problem: Density profiles at $t = 0.1$ for We $= 1.0 \times 10^2$, 1.0×10^4, and 1.0×10^6, when $\Delta x = 1.0 \times 10^{-2}$, $\Delta t = 1.0 \times 10^{-6}$, and Re $= 2.0 \times 10^2$.

be also observed that the interface width for We $= 1.0 \times 10^2$ is of the order $\mathcal{O}(1)$, while that for We $= 1.0 \times 10^4$ is of the order $\mathcal{O}(0.1)$. These observations match well with the interface width estimate made in [66]. For We $= 1.0 \times 10^6$, the mesh size criterion is upset. Spikes and oscillations are observed near a very sharp phase boundary, which is harmful for long time simulations. This example indicates that a proper mesh size choice for a given Weber number is necessary for providing non-oscillatory results.

6.9.1.2 Propagating wave problem

A propagating wave problem is considered next. The initial conditions are set to be

$$(\rho^{right}, u^{right}) = (0.602, 1.0), \qquad (\rho^{left}, u^{left}) = (0.107, 1.0). \qquad (6.157)$$

In this setting, a propagating travelling solution will form, moving in the positive x direction at speed 1.0. The spatial discretization consists of quadratic NURBS basis functions with $\Delta x = 1.0 \times 10^{-2}$. The dimensionless quantities are taken as Re $= 2.0 \times 10^2$ and We $= 1.0 \times 10^4$. I perform temporal integrations up to $T = 0.2$ with time step sizes of $\Delta t = 5.0 \times 10^{-3}$, $\Delta t = 1.0 \times 10^{-2}$, and $\Delta t = 2.0 \times 10^{-2}$. Notice that the characteristic speeds of this problem are $u \pm \sqrt{dp/d\rho}$. The CFL number Cf is defined as

$$\text{Cf} = \max_{\rho \in [0.602, 0.107]} \left\{ u \pm \sqrt{\frac{dp}{d\rho}} \right\} \frac{\Delta t}{\Delta x} = 162.1 \Delta t. \qquad (6.158)$$

Thus, the corresponding CFL numbers are 0.81, 1.62, and 3.24. It can be observed that correct traveling waves are captured at all three CFL numbers.

Oscillations are seen for Cf $\geq$ 1. For even larger time steps, there is the counterbalancing effect of even more numerical dissipation being introduced and the computed solution becomes more diffusive, as can be seen in Figure 6.8.
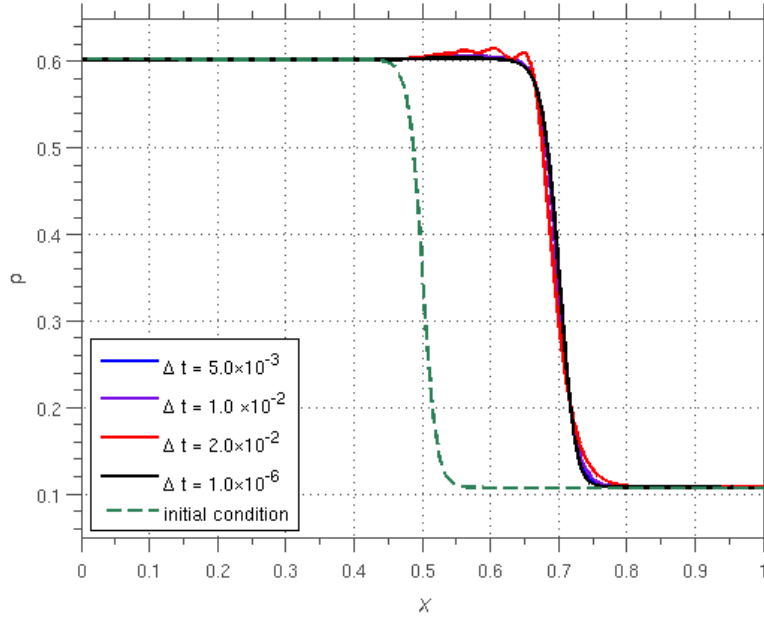
Figure 6.8: Propagating wave problem: Density profiles at $t = 0.2$ for time step sizes of $\Delta t = 5.0 \times 10^{-3}$, $\Delta t = 1.0 \times 10^{-2}$, $\Delta t = 2.0 \times 10^{-2}$, and $\Delta t = 1.0 \times 10^{-6}$ (reference solution) when $\Delta x = 1.0 \times 10^{-2}$, Re $= 2.0 \times 10^2$, and We $= 1.0 \times 10^4$.

6.9.2 Bubble dynamics on an annular surface

As a second benchmark problem, I solve the Navier-Stokes-Korteweg equations on an annular surface to study vapor bubble dynamics on a curved geometry. There are several objectives of this study. First of all, I want to re-
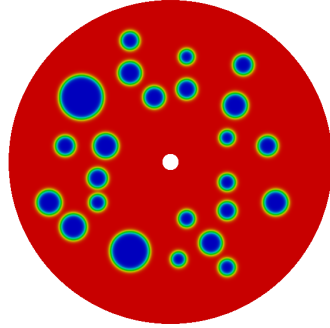
(a) Initial condition
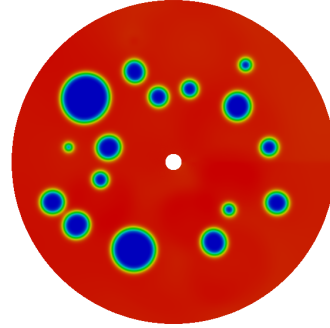
(b) $t = 3.0$
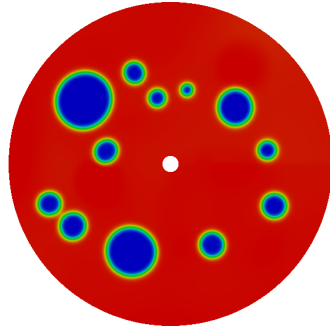
(c) $t = 5.0$
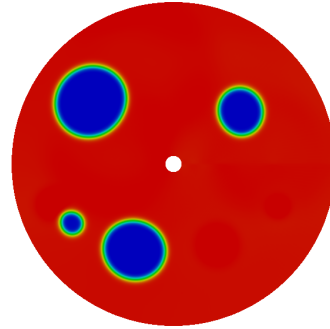
(d) $t = 10.0$
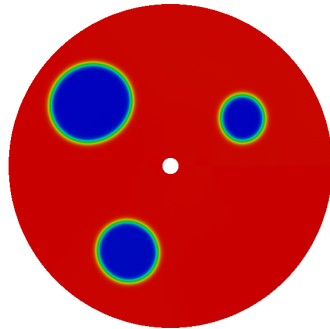
(e) $t = 20.0$
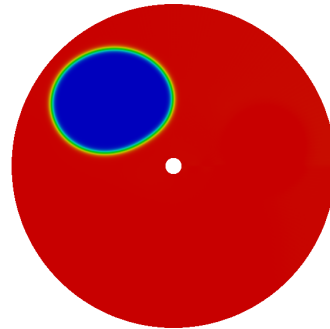
(f) $t = 55.0$

Figure 6.9: Bubble dynamics on an annular surface: Density profiles at times $t = 0.0, 3.0, 5.0, 10.0, 20.0,$ and 55.0.

search the effects of the capillarity and the pressure force on bubble dynamics. According to thermodynamics [79], inward-pointing pressure gradients exist at the surface of smaller bubbles due to capillarity effects. These pressure gradients cause smaller bubbles to disappear in favor of larger ones. Therefore, small bubbles are considered to be thermodynamically unstable. A closely related phenomenon is known as Ostwald's ripening [164]. Using the van der Waals model, I endeavor to obtain insights on such an important phenomenon. My second objective is to show the geometrical and topological flexibility of isogeometric analysis. The annular surface is a common engineering geometry, yet it is hard to represent exactly within traditional numerical frameworks such as finite differences or finite elements. Specifically finite difference or finite element methods usually approximate annular geometries using polyhedral grids or elements, inevitably introducing approximation errors due to the geometry. This geometric approximation error may introduce erroneous numerical mass sources, which in turn may deteriorate the conservation properties of a given numerical scheme. By employing NURBS-based isogeometric analysis, one is able to exactly represent the geometry of the annular surface. Such an exact representation will play a critical role in retaining the nonlinear stability and mass conservation properties of the fully discrete scheme.

The interior radius of the annular surface is taken to be $r_{in} = 0.1$, while the exterior radius is taken as $r_{ex} = 2.0$. To parametrize the annular surface using NURBS, I employ the square-based NURBS construction of degree two outlined in [24, 52] (see Figure 4.2). In the circumferential direction,

513 uniform quadratic NURBS are used for spatial discretization, and in the radial direction, 120 uniform quadratic NURBS are used. In the circumferential direction, periodic boundary conditions are imposed for all variables. On the interior and exterior circular boundaries, the boundary condition (6.3) is imposed weakly as a natural boundary condition while the no-slip boundary condition (6.4) is imposed strongly on the velocity field. The initial bubble distribution is chosen randomly. That is, for n_{bub} bubbles at the initial stage, the bubble centers C_i, $i = 1, \cdots, n_{bub}$ are generated randomly within the annular surface. The bubble radii R_i, $i = 1, \cdots, n_{bub}$ are also generated randomly in such a manner that each bubble does not overlap with any other bubble nor cross the annular boundary. I take $n_{bub} = 24$ in this case. If I define $d_j(\mathbf{x})$ as the Euclidean distance between $\mathbf{x}$ and C_j, the initial density profile reads

$$\rho_0(\mathbf{x}) = 0.25 \sum_{j=1}^{n_{bub}} \tanh\left(\frac{d_j(\mathbf{x}) - R_j}{2}\sqrt{\text{We}}\right) - 0.25 n_{bub} + 0.6. \qquad (6.159)$$

The initial velocity field is set to be zero. The dimensionless parameters are fixed as $\text{Re} = 1.372 \times 10^2$ and $\text{We} = 4.705 \times 10^3$. A fixed time step size of $\Delta t = 1.0 \times 10^{-4}$ is used for time integration. In Figure 6.9, snapshots of the density profile are presented at different times. The physical process simulated here is similar to the two-bubble dynamics problem I studied in Section 6.8.2. Small bubbles merge into large bubbles. After enough time has passed, all 24 bubbles merge together and form one large vapor bubble. In Figure 6.10, I plot the evolution of the total energy over time. This figure shows the total energy is monotonically decreasing with respect to time, again verifying

206

the energy dissipation property of the fully discrete algorithm. Following the notation defined in (6.152) and (6.153), the relative mass error is $\left\|\frac{m_n-m_0}{m_0}\right\|_{l_\infty} = 7.707 \times 10^{-9}$.
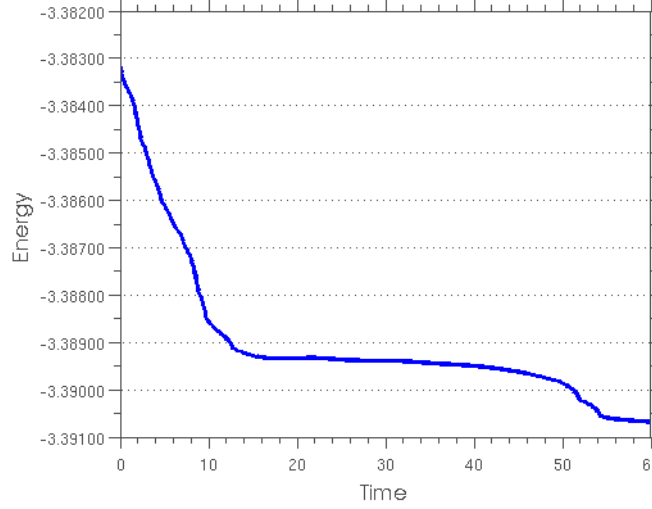
Figure 6.10: Bubble dynamics on an annular surface: Evolution of the Lyapunov functional $\mathcal{E}$.

6.9.3 Liquid droplet on a solid substrate

In this benchmark problem, I study the wetting phenomenon, which describes the shape of a liquid droplet on a solid substrate. It is a challenging problem in fluid mechanics, since this problem involves the interaction between three interfaces: the liquid-vapor interface, the liquid-solid interface, and the vapor-solid interface. The shape of the liquid droplet is primarily determined by two factors: (1) the contact angle of the droplet with the solid substrate, and (2) the Bond number Bo. The size of the contact angle varies depending

207

on whether the surface is hydrophilic or hydrophobic to the fluid. In my model, this contact angle is enforced as a wall boundary condition

$$-\frac{\nabla\rho}{\|\nabla\rho\|} \cdot \mathbf{n} = \cos\phi, \tag{6.160}$$

at the wetted surface, where ϕ is the contact angle. On the other hand, the Bond number assesses the relative importance of the gravity force against the surface tension. If the Bond number is small, the surface tension dominates and the droplet will contract like a sphere. If the Bond number is larger, the gravity force, being the dominant effecting force, will flatten the droplet like a pancake. The wetting phenomenon for two immiscible fluids, e.g. water and air, has been studied in depth both theoretically [79] and numerically [112, 209]. However, the wetting phenomenon of a single material on a solid substrate has not been the focus of as much study. In [66], the author considered the effects of different contact angle boundary conditions on the shape of the droplet. In this work, I will focus on the effect of the Bond number by fixing the contact angle to be $\pi/2$.

For this problem, the computational domain is restricted to be the unit square $\Omega = (0,1)^2$. The spatial discretization is comprised of 300^2 quadratic NURBS basis functions. The dimensionless quantities are fixed to be Re $=$ 848.53 and We $= 1.80 \times 10^5$. The initial density profile is set as

$$\rho_0(\mathbf{x}) = 0.35 - 0.25\tanh\left(\frac{d(\mathbf{x}) - 0.2}{2}\sqrt{We}\right), \tag{6.161}$$

$$d(\mathbf{x}) = \sqrt{(x_1 - 0.5)^2 + x_2^2}. \tag{6.162}$$
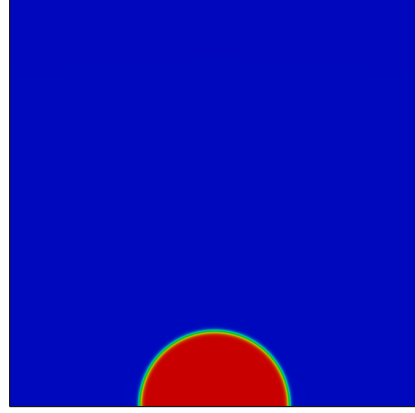
(a) $|\mathbf{b}| = \mathrm{Bo} \,/\, \mathrm{We} = 1.0 \times 10^{-3}$
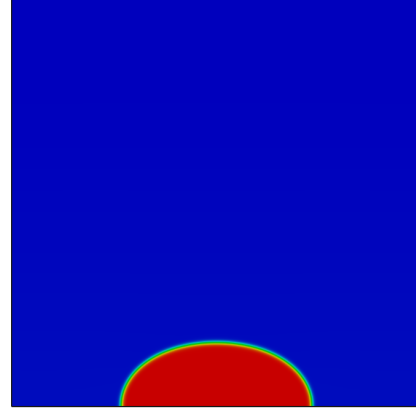
(b) $|\mathbf{b}| = \mathrm{Bo} \,/\, \mathrm{We} = 1.0 \times 10^{-2}$
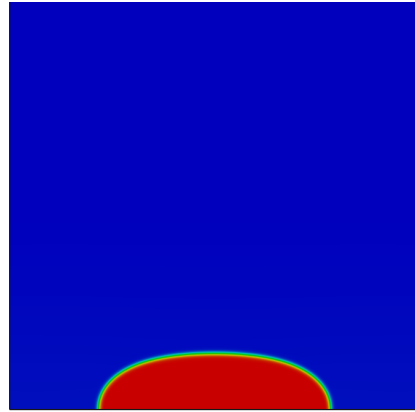
(c) $|\mathbf{b}| = \mathrm{Bo} \,/\, \mathrm{We} = 2.0 \times 10^{-2}$
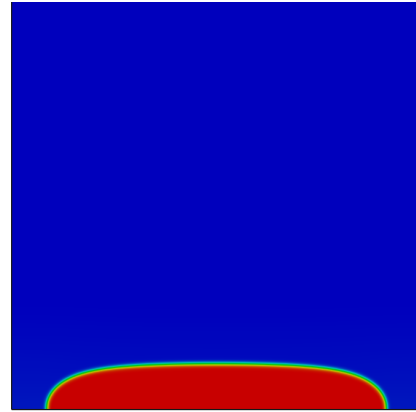
(d) $|\mathbf{b}| = \mathrm{Bo} \,/\, \mathrm{We} = 5.0 \times 10^{-2}$

Figure 6.11: Liquid droplet on a solid surface: Density profiles at $t = 20.0$ for $\mathrm{Bo} = 1.8 \times 10^2$, 1.8×10^3, 3.6×10^3 and 9.0×10^3.

I set the volumetric force $\mathbf{b}$ to point in the negative y direction with magnitude $|\mathbf{b}| = 1.0 \times 10^{-3}$, 1.0×10^{-2}, 2.0×10^{-2}, and 5.0×10^{-2}. Recalling the relation (6.28), this means the corresponding Bond numbers Bo are 1.8×10^2, 1.8×10^3, 3.6×10^3, and 9.0×10^3 respectively. I simulate the wetting problem up to the final time of $T = 20.0$ with a fixed time step size of $\Delta t = 4.0 \times 10^{-5}$. The corresponding density profiles at $t = 20.0$ are plotted in Figure 6.11. It can be observed from the four figures that the magnitude of Bond number has a significant impact on the shape of the droplet. In Figure 6.11 (a), the Bond number is relatively small and hence capillarity dominates. The strong surface tension tries to maintain curvature and makes the droplet almost a spherical cap. In contrast, in Figure 6.11 (d), the Bond number is 50 times larger, and the gravitational force has a significant impact on the droplet. Consequently, the droplet is flattened as is expected. Intermediate shapes are obtained for Bo $= 1.8 \times 10^3$ and 3.6×10^3.

6.9.4 Bubble dynamics in a three-dimensional cylinder

In this problem, the isothermal Navier-Stokes-Korteweg equations are solved in a three-dimensional cylinder $\Omega = \{(x, y, z) | x^2 + y^2 \leq 0.25, z \in [0, 1]\}$. The initial condition is set to be three static vapor bubbles with centers at $C_1 = (-0.20, 0.00, 0.50)$, $C_2 = (0.10, -0.30, 0.40)$, and $C_3 = (0.20, 0.20, 0.60)$. The radii of the three bubbles are $R_1 = 0.20$, $R_2 = 0.15$, and $R_3 = 0.10$. The
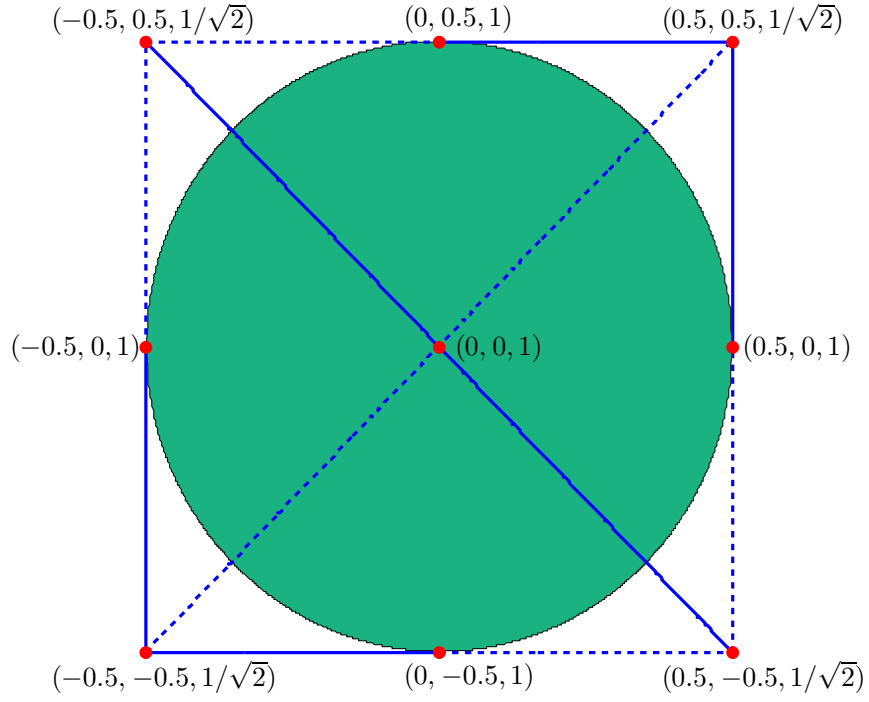
Figure 6.12: Illustration of a circular domain constructed by square-based NURBS of degree two [188]. The NURBS basis functions in the circumferential and radial direction are quadratic and are built from the knot vectors $\Xi_1 = \Xi_2 = \{0, 0, 0, 1, 1, 1\}$. The red dots are the control points, and the 3-tuples give the control points' x-coordinates, y-coordinates, and weights.

initial density and velocity functions are set as

$$\rho_0(\mathbf{x}) = -0.15 + 0.25 \sum_{i=1}^{3} \tanh\left(\frac{d_i(\mathbf{x}) - R_i}{2}\sqrt{We}\right), \tag{6.163}$$

$$\mathbf{u}_0(\mathbf{x}) = \mathbf{0}. \tag{6.164}$$

The three-dimensional cylinder is discretized by 100^3 NURBS functions, which are quadratic in the x and y-directions and linear in the z-direction. The NURBS representation of the circular region in the x-y plane is illustrated in Figure 6.12. In this representation, there are four singular points on the circular boundary. I impose no-slip boundary conditions for the velocity and boundary condition (6.3) for density. Both imposition does not require boundary integrals, which avoids boundary integration at the singular points. In the simulation, the Reynolds number Re and the Weber number We are fixed to be 2.31×10^2 and 1.33×10^4 respectively. The problem is integrated in time up to $T = 7.5$ with a fixed time-step size $\Delta t = 2.5 \times 10^{-5}$. In Figures 6.13-6.14, the dynamics is visualized from $t = 0.0$ to 7.5. It can be seen from the figures that the small bubbles are compressed due to the pressure imposed by the largest bubble. At $t = 7.5$, all three bubbles merge together and form one single vapor bubble. In Figure 6.15, the Lyapunov functional $\mathcal{E}$ of this problem is plotted against time. It can be seen that the Lyapunov functional of the discrete solution is a monotonically decreasing function with respect to time, which manifests the dissipation property of the numerical scheme.

212

(a) Initial condition   (b) $t = 1.00$

(c) $t = 2.00$ (d) $t = 3.00$
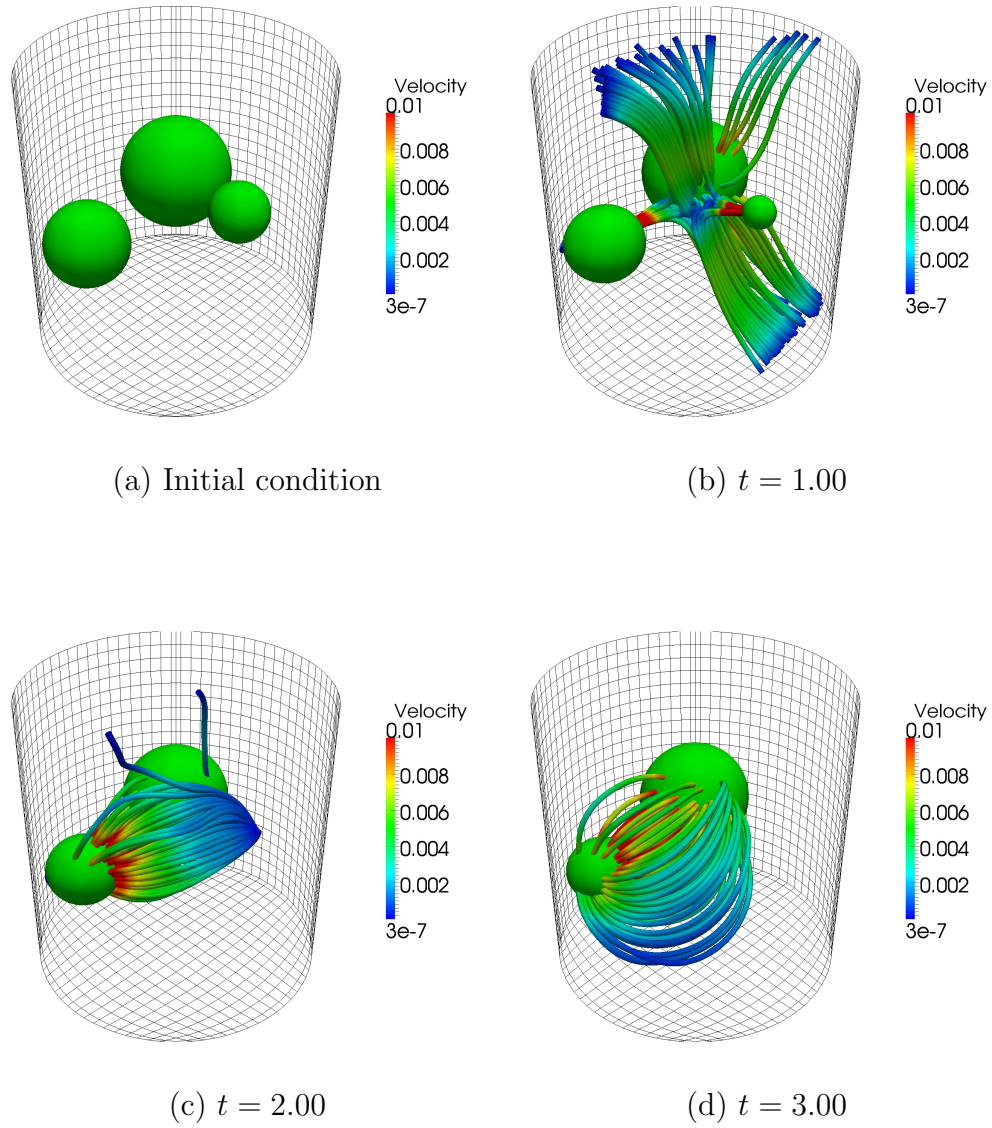
Figure 6.13: Bubble dynamics in a three-dimensional cylinder: Density isosurfaces and velocity streamlines at times $t = 0.0$, 1.0, 2.0, and 3.0.

(a) $t = 4.00$ (b) $t = 5.00$

(c) $t = 6.00$ (d) $t = 7.5$
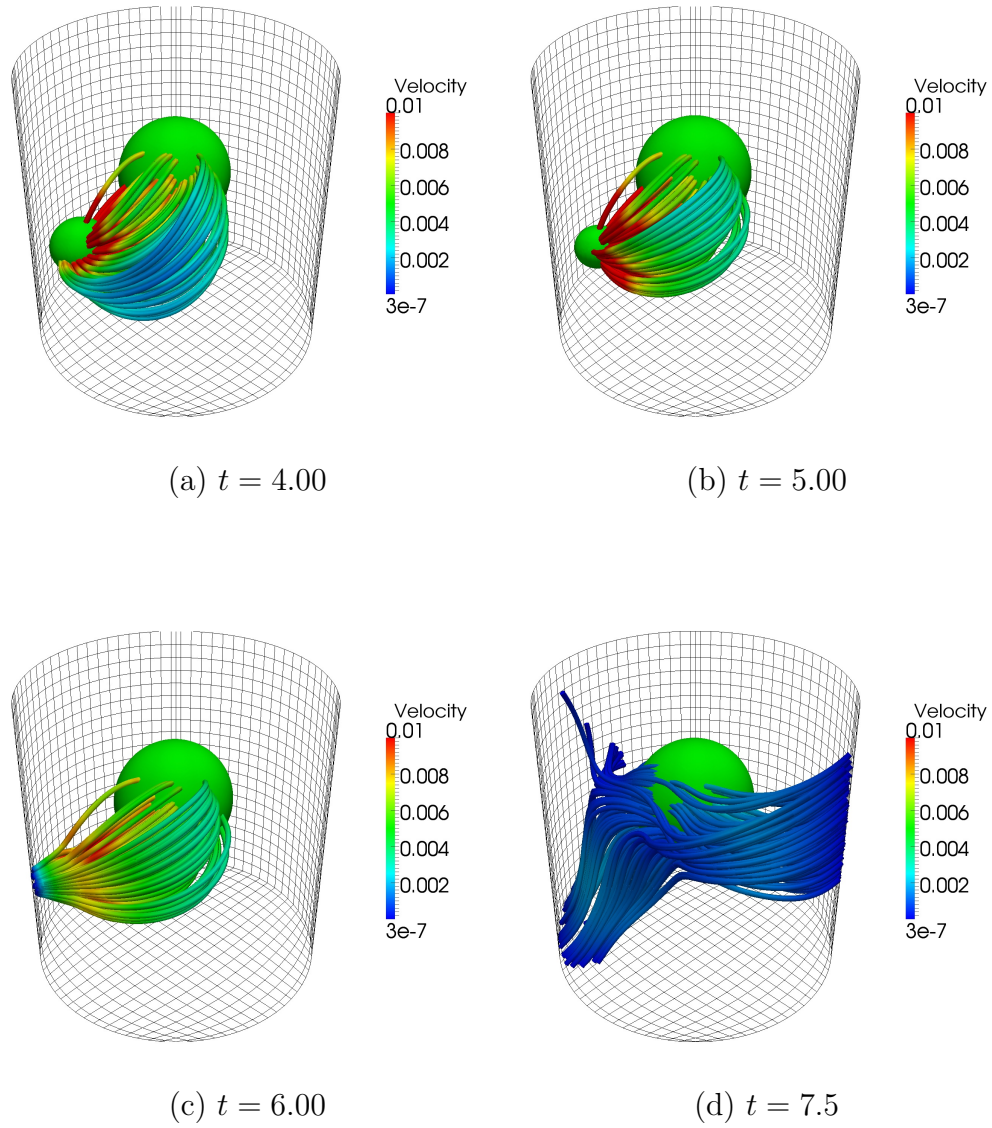
Figure 6.14: Bubble dynamics in a three-dimensional cylinder: Density isosurfaces and velocity streamlines at times $t = 4.0$, 5.0, 6.0, and 7.5.
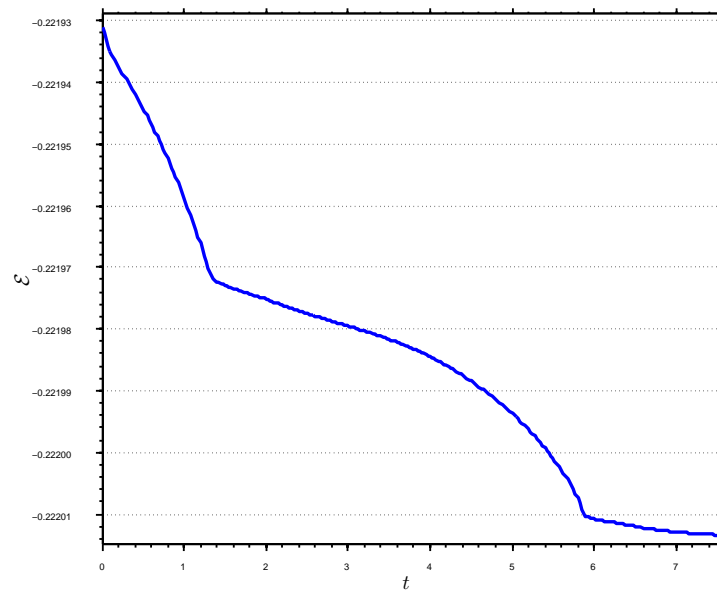
Figure 6.15: Bubble dynamics in a three-dimensional cylinder: Evolution of the Lyapunov functional $\mathcal{E}$.

Chapter 7

Numerical analysis of the thermal Navier-Stokes-Korteweg equations

> *"Thermodynamics is a funny subject. The first time you go through it, you don't understand it at all. The second time you go through it, you think you understand it, except for one or two small points. The third time you go through it, you know you don't understand it, but by that time you are so used to it, it doesn't bother you any more."*
>
> — Arnold J.W. Sommerfeld, 1950

In the preceding chapter, numerical strategies for the isothermal Navier-Stokes-Korteweg equations have been developed. Although that system models a wide variety of fluid flows, thermal effects sometimes may have a significant impact on flow patterns (e.g., the Rayleigh-Bénard convection [150]). Typically, an energy equation or a simplified heat equation [37] has to be coupled with the hydrodynamic system to mimic thermal effects. In this chapter, the full Navier-Stokes-Korteweg equations derived in Chapter 3 are considered. In this model, a highly nonlinear energy equation is coupled with the isothermal system, which introduces additional difficulties for numerical analysis. The benefit of this fully coupled approach is that the model is thermodynamically consistent. This very feature allows one to simulate very complex physical phenomena without introducing unnecessary modeling or numerical artifacts.

The functional entropy variable technique is generalized to the thermal Navier-Stokes-Korteweg equations in this chapter. Interestingly, the entropy variables are formally identical to those of the compressible Euler and Navier-Stokes equations. The difference is that the functional entropy variables are linear operators and live in the dual spaces. As for the temporal discretization, the approximation of the energy time derivative becomes a challenging task. The special quadrature formulas introduced in Chapter 6 are again utilized to construct a temporal scheme for the energy equation. Eventually, the above techniques lead to a fully discrete scheme that is provably entropy dissipative and second-order accurate. The effectiveness of this method is validated by simulating a variety of benchmark problems. In particular, boiling flows are numerically studied in this work, which demonstrates the ability of this modeling approach for solving complex flows.

The rest of this chapter is organized as follows. In Section 7.1, the initial-boundary value problem of the thermal Navier-Stokes-Korteweg equations is presented. A dimensional analysis is performed in Section 7.2. In Section 7.3, the entropy variables for the system are derived by invoking the calculus of variations technique. An auxiliary variable is introduced to construct an alternative statement for the strong problem in Section 7.4. The corresponding weak formulation is proved to be entropy dissipative in Section 7.5. The semi-discrete formulation is then presented in Section 7.6. In Section 7.7, the fully discrete scheme is introduced. In Section 7.8, two benchmark problems are simulated to verify the theoretical estimates. Following that,

three application examples are studied in Section 7.9.

7.1   The initial-boundary value problem

Let $\Omega \subset \mathbb{R}^d$ be an arbitrary open, connected, and bounded domain, where d is the number of spatial dimensions. The thermal Navier-Stokes-Korteweg equations (3.41)-(3.43) are considered in $\Omega \times (0, T)$. For notational simplicity, the superscript vdw is omitted in the subsequent discussion. The boundary of Ω is denoted as $\partial \Omega$ and assumed to be sufficiently smooth (e.g. Lipschitz). $\rho : \bar{\Omega} \times (0, T) \to (0, b)$, $\rho \mathbf{u} : \bar{\Omega} \times (0, T) \to \mathbb{R}^d$, and $\rho E : \bar{\Omega} \times (0, T) \to \mathbb{R}$ denote the density, linear momentum, and total energy of the fluid system. The governing equations can be stated as follows.

$$\frac{\partial \rho}{\partial t} + \nabla \cdot (\rho \mathbf{u}) = 0 \quad \text{in } \Omega \times (0, T), \tag{7.1}$$

$$\frac{\partial (\rho \mathbf{u})}{\partial t} + \nabla \cdot (\rho \mathbf{u} \otimes \mathbf{u} + p\mathbf{I}) - \nabla \cdot \boldsymbol{\tau} - \nabla \cdot \boldsymbol{\varsigma} = \rho \mathbf{b} \quad \text{in } \Omega \times (0, T), \tag{7.2}$$

$$\frac{\partial (\rho E)}{\partial t} + \nabla \cdot ((\rho E + p) \mathbf{u} - (\boldsymbol{\tau} + \boldsymbol{\varsigma}) \mathbf{u}) + \nabla \cdot \mathbf{q} + \nabla \cdot \boldsymbol{\Pi}$$
$$= \rho \mathbf{b} \cdot \mathbf{u} + \rho r \quad \text{in } \Omega \times (0, T). \tag{7.3}$$

Above, $\boldsymbol{\tau}$ is the viscous stress, $\boldsymbol{\varsigma}$ is the Korteweg stress, p is the thermodynamic pressure, $\mathbf{q}$ is the heat flux, and $\boldsymbol{\Pi}$ is the interstitial working flux. They are defined by the constitutive relations given in Chapter 3:

$$\boldsymbol{\tau} = \bar{\mu} \left(\nabla \mathbf{u} + \nabla \mathbf{u}^T \right) + \bar{\lambda} \nabla \cdot \mathbf{u} \mathbf{I}, \tag{7.4}$$

$$\boldsymbol{\varsigma} = \left(\lambda \rho \Delta \rho + \frac{\lambda}{2} |\nabla \rho|^2 \right) \mathbf{I} - \lambda \nabla \rho \otimes \nabla \rho, \tag{7.5}$$

$$p = Rb\theta \frac{\rho}{b - \rho} - a\rho^2, \tag{7.6}$$

$$\mathbf{q} = -\boldsymbol{\kappa}\nabla\theta, \tag{7.7}$$

$$\boldsymbol{\Pi} = \lambda\rho\nabla \cdot \mathbf{u}\nabla\rho. \tag{7.8}$$

In this chapter, unless otherwise specified, periodic boundary conditions for ρ, $\rho\mathbf{u}$, and ρE are considered in all directions. Given $\rho_0 : \bar{\Omega} \to (0, b)$, $\mathbf{u}_0 : \bar{\Omega} \to \mathbb{R}^d$, and $\theta_0 : \bar{\Omega} \to \mathbb{R}$ as the initial density, velocity, and temperature fields, the initial conditions for the system are

$$\rho(\mathbf{x}, 0) = \rho_0(\mathbf{x}), \tag{7.9}$$

$$\mathbf{u}(\mathbf{x}, 0) = \mathbf{u}_0(\mathbf{x}), \tag{7.10}$$

$$\theta(\mathbf{x}, 0) = \theta_0(\mathbf{x}). \tag{7.11}$$

Recalling the results given in Chapter 3, the dissipation $\mathcal{D}$ for the system (7.1)-(7.3) is

$$\begin{aligned}
\mathcal{D} :=& \frac{\partial(\rho s)}{\partial t} + \nabla \cdot (\rho s) + \nabla \cdot \left(\frac{\mathbf{q}}{\theta}\right) - \frac{\rho r}{\theta} \\
=& \frac{2\bar{\mu}}{\theta}\mathbf{L}^d : \mathbf{L}^d + \frac{1}{\theta}\left(\bar{\lambda} + \frac{2}{3}\bar{\mu}\right)(\nabla \cdot \mathbf{u})^2 + \frac{1}{\theta^2}\nabla\theta \cdot \boldsymbol{\kappa}\nabla\theta \\
=& \frac{1}{\theta}\boldsymbol{\tau} : \nabla\mathbf{u} + \frac{1}{\theta^2}\nabla\theta \cdot \boldsymbol{\kappa}\nabla\theta. \tag{7.12}
\end{aligned}$$

To make this chapter self-consistent, let me recollect some thermodynamic state variables given in Section 3.2. The Helmholtz free energy density Ψ, the local Helmholtz free energy density Ψ_{loc}, the local internal energy density ι_{loc}, the internal energy density ι, the local electrochemical potential ν_{loc}, and the entropy density s for the van der Waals fluid are defined as

$$\Psi(\rho, \theta, \nabla\rho) = \Psi_{loc}(\rho, \theta) + \frac{\lambda}{2\rho}|\nabla\rho|^2, \tag{7.13}$$

$$\Psi_{loc}(\rho,\theta) = -a\rho + R\theta \log\left(\frac{\rho}{b-\rho}\right) - C_v\theta \log\left(\frac{\theta}{\theta_{ref}}\right) + C_v\theta, \qquad (7.14)$$

$$\iota_{loc} = -a\rho + C_v\theta, \qquad (7.15)$$

$$\iota = \iota_{loc} + \frac{\lambda}{2\rho}|\nabla\rho|^2, \qquad (7.16)$$

$$\nu_{loc} = -2a\rho + R\theta \log\left(\frac{\rho}{b-\rho}\right) + \frac{R\theta b}{b-\rho}$$
$$- C_v\theta \log\left(\frac{\theta}{\theta_{ref}}\right) + C_v\theta, \qquad (7.17)$$

$$s = -R\log\left(\frac{\rho}{b-\rho}\right) + C_v \log\left(\frac{\theta}{\theta_{ref}}\right). \qquad (7.18)$$

Remark 7.1.1. *According to the dissipation relation (7.12), positive entropy production is guaranteed if the material moduli satisfy that*

$$\bar{\mu} \geq 0, \qquad \bar{\lambda} + \frac{2}{3}\bar{\mu} \geq 0, \qquad (7.19)$$

and $\boldsymbol{\kappa}$ is positive semi-definite.

Remark 7.1.2. *In the remainder of this chapter, the Stokes's assumption is satisfied, i.e.,*

$$\bar{\lambda} = -\frac{2}{3}\bar{\mu}. \qquad (7.20)$$

7.2 The dimensionless formulation

In this section, the dimensionless form of the Navier-Stokes-Korteweg equations is derived. The Navier-Stokes-Korteweg equations are rescaled using the $MLT\Theta$ system. The reference scales of mass, length, time, and temperature are denoted as M_0, L_0, T_0, and θ_0. Then one may directly obtain the

following dimensionless quantities denoted with a superscript $*$:

$$x = L_0 x^*, \quad t = T_0 t^*, \quad \rho = \frac{M_0}{L_0^3} \rho^*, \quad \theta = \theta_0 \theta^*, \quad \mathbf{u} = \frac{L_0}{T_0} \mathbf{u}^*,$$

$$p = \frac{M_0}{L_0 T_0^2} p^*, \quad \lambda = \frac{L_0^7}{M_0 T_0^2} \lambda^*, \quad \bar{\mu} = \frac{M_0}{L_0 T_0} \bar{\mu}^*, \quad \boldsymbol{\tau} = \frac{M_0}{T_0^2 L_0} \boldsymbol{\tau}^*,$$

$$\boldsymbol{\varsigma} = \frac{M_0}{T_0^2 L_0} \boldsymbol{\varsigma}^*, \quad \mathbf{b} = \frac{L_0}{T_0^2} \mathbf{b}^*, \quad \boldsymbol{\kappa} = \frac{M_0 L_0}{\theta_0 T_0^3} \boldsymbol{\kappa}^*, \quad E = \frac{L_0^2}{T_0^2} E^*,$$

$$\mathbf{q} = \frac{M_0}{T_0^3} \mathbf{q}^*, \quad \boldsymbol{\Pi} = \frac{M_0}{T_0^3} \boldsymbol{\Pi}^*, \quad r = \frac{L_0^2}{T_0^3} r^*, \quad s = \frac{L_0^2}{T_0^2 \theta_0} s^*. \tag{7.21}$$

The above relations directly lead to the dimensionless balance equations:

$$\frac{M_0}{T_0 L_0^3} \left(\frac{\partial \rho^*}{\partial t^*} + \nabla^* \cdot \left(\rho^* \mathbf{u}^* \right) \right) = 0, \tag{7.22}$$

$$\frac{M_0}{T_0^2 L_0^2} \left(\frac{\partial (\rho^* \mathbf{u}^*)}{\partial t^*} + \nabla^* \cdot (\rho^* \mathbf{u}^* \otimes \mathbf{u}^*) + \nabla^* p^* - \nabla^* \cdot \boldsymbol{\tau}^* - \nabla^* \cdot \boldsymbol{\varsigma}^* \right.$$
$$\left. - \rho^* \mathbf{b}^* \right) = \mathbf{0}, \tag{7.23}$$

$$\frac{M_0}{T_0^3 L_0} \left(\frac{\partial (\rho^* E^*)}{\partial t^*} + \nabla^* \cdot ((\rho^* E^* + p^*) \mathbf{u}^* - (\boldsymbol{\tau}^* + \boldsymbol{\varsigma}^*) \mathbf{u}^*) + \nabla^* \cdot \mathbf{q}^* \right.$$
$$\left. + \nabla^* \cdot \boldsymbol{\Pi}^* - \rho^* \mathbf{b}^* \mathbf{u}^* - \rho^* r^* \right) = 0. \tag{7.24}$$

And the constitutive relations are rescaled as

$$p^* = Rb \frac{L_0 T_0^2 \theta_0 \rho^* \theta^*}{b L_0^3 - M_0 \rho^*} - a \frac{M_0 T_0^2}{L_0^5} \rho^{*2}, \tag{7.25}$$

$$\boldsymbol{\tau}^* = \bar{\mu}^* \left(\nabla^* \mathbf{u}^* + \nabla^* \mathbf{u}^{*T} \right) + \bar{\lambda}^* \nabla^* \cdot \mathbf{u}^* \mathbf{I}, \tag{7.26}$$

$$\boldsymbol{\varsigma}^* = -\lambda^* \nabla^* \rho^* \otimes \nabla^* \rho^* + \left(\lambda^* \rho^* \Delta^* \rho^* + \frac{\lambda^*}{2} |\nabla^* \rho^*|^2 \right) \mathbf{I}, \tag{7.27}$$

$$\mathbf{q}^* = -\boldsymbol{\kappa}^* \nabla^* \theta^*, \tag{7.28}$$

$$s^* = -\frac{R T_0^2 \theta_0}{L_0^2} \log \left(\frac{M_0 \rho^*}{L_0^3 b - M_0 \rho^*} \right) + \frac{C_v T_0^2 \theta_0}{L_0^2} \log \left(\frac{\theta_0 \theta^*}{\theta_{crit}} \right), \tag{7.29}$$

$$\mathbf{\Pi}^* = \lambda^* \rho^* \nabla^* \cdot \mathbf{u}^* \nabla^* \rho^*. \tag{7.30}$$

Similarly to the isothermal case, the dimensionless viscosity coefficient $\bar{\mu}^* = L_0 T_0 \bar{\mu}/M_0$ and the dimensionless capillarity coefficient $\lambda^* = M_0 T_0^2 \lambda / L_0^7$ can be represented in terms of the Reynolds number and the Weber number as

$$\bar{\mu}^* = \frac{1}{\mathrm{Re}}, \qquad \lambda^* = \frac{1}{\mathrm{We}}. \tag{7.31}$$

The capillarity number Ca and the Bond number Bo are defined as

$$\mathrm{Ca} = \frac{\mathrm{We}}{\mathrm{Re}}, \tag{7.32}$$

$$\mathrm{Bo} = |\mathbf{b}^*| \, \mathrm{We} . \tag{7.33}$$

There is one standard thermodynamic relation relating the heat capacity at constant volume C_v and the universal gas constant R:

$$C_v = \frac{R}{\gamma - 1}, \tag{7.34}$$

wherein γ is the heat capacity ratio. Therefore, one has

$$\frac{C_v}{R} = \frac{1}{\gamma - 1}. \tag{7.35}$$

Remark 7.2.1. *The value of γ is always greater than 1 and is related to the molecular translation, vibration, and rotation degrees of freedom. For example, γ for water vapor is about* 1.33. *Interested readers are referred to [170] for more details.*

If the reference scales are chosen such that

$$\frac{M_0}{L_0^3} = b, \tag{7.36}$$

$$\frac{M_0}{L_0 T_0^2} = ab^2, \tag{7.37}$$

$$\theta_0 = \theta_{crit} = \frac{8ab}{27R}, \tag{7.38}$$

and if the temperature reference value is picked as the critical temperature,

$$\theta_{ref} = \theta_{crit}, \tag{7.39}$$

the dimensionless Navier-Stokes-Korteweg equations can be written as

$$\frac{\partial \rho^*}{\partial t^*} + \nabla^* \cdot (\rho^* \mathbf{u}^*) = 0, \tag{7.40}$$

$$\frac{\partial (\rho^* \mathbf{u}^*)}{\partial t^*} + \nabla^* \cdot (\rho^* \mathbf{u}^* \otimes \mathbf{u}^*) + \nabla^* p^* - \nabla^* \cdot \boldsymbol{\tau}^* - \nabla^* \cdot \boldsymbol{\varsigma}^* - \rho^* \mathbf{b}^* = \mathbf{0}, \tag{7.41}$$

$$\frac{\partial (\rho^* E^*)}{\partial t^*} + \nabla^* \cdot ((\rho^* E^* + p^*)\mathbf{u}^* - (\boldsymbol{\tau}^* + \boldsymbol{\varsigma}^*)\mathbf{u}^*) + \nabla^* \cdot \mathbf{q}^*$$
$$+ \nabla^* \cdot \boldsymbol{\Pi}^* - \rho^* \mathbf{b}^* \mathbf{u}^* - \rho^* r^* = 0, \tag{7.42}$$

wherein

$$p^* = \frac{8\theta^* \rho^*}{27(1 - \rho^*)} - \rho^{*2}, \tag{7.43}$$

$$\boldsymbol{\tau}^* = \frac{1}{\mathrm{Re}} \left(\nabla^* \mathbf{u}^* + \nabla^* \mathbf{u}^{*T} - \frac{2}{3} \nabla^* \cdot \mathbf{u}^* \mathbf{I} \right), \tag{7.44}$$

$$\boldsymbol{\varsigma}^* = \frac{1}{\mathrm{We}} \left(\left(\rho^* \Delta^* \rho^* + \frac{1}{2} |\nabla^* \rho^*|^2 \right) \mathbf{I} - \nabla^* \rho^* \otimes \nabla^* \rho^* \right), \tag{7.45}$$

$$\mathbf{q}^* = -\boldsymbol{\kappa}^* \nabla^* \theta^*, \tag{7.46}$$

$$\boldsymbol{\Pi}^* = \frac{1}{\mathrm{We}} \rho^* \nabla^* \cdot \mathbf{u}^* \nabla^* \rho^*, \tag{7.47}$$

$$\mathrm{Re} = \frac{L_0 b \sqrt{ab}}{\bar{\mu}}, \tag{7.48}$$

$$\mathrm{We} = \frac{a L_0^2}{\lambda}. \tag{7.49}$$

Likewise, the Helmholtz free energy density, the local Helmholtz free energy density, the local internal energy density, the internal energy density, the local electrochemical potential, and the entropy density are rescaled as

$$\Psi^* = \Psi^*_{loc}(\rho, \theta) + \frac{1}{\text{We}} \frac{1}{2\rho^*} |\nabla^* \rho^*|^2, \tag{7.50}$$

$$\Psi^*_{loc}(\rho, \theta) = -\rho^* + \frac{8}{27} \theta^* \log \left(\frac{\rho^*}{1 - \rho^*} \right)$$
$$- \frac{8}{27(\gamma - 1)} \theta^* \log(\theta^*) + \frac{8}{27(\gamma - 1)} \theta^*, \tag{7.51}$$

$$\iota^*_{loc} = -\rho^* + \frac{8}{27(\gamma - 1)} \theta^*, \tag{7.52}$$

$$\iota^* = \iota^*_{loc} + \frac{1}{2 \, \text{We} \, \rho^*} |\nabla^* \rho^*|^2, \tag{7.53}$$

$$\nu^*_{loc} = -2\rho^* + \frac{8\theta^*}{27(1 - \rho^*)} + \frac{8}{27} \theta^* \log \left(\frac{\rho^*}{1 - \rho^*} \right)$$
$$- \frac{8}{27(\gamma - 1)} \theta^* \log(\theta^*) + \frac{8}{27(\gamma - 1)} \theta^*, \tag{7.54}$$

$$s^* = -\frac{8}{27} \log \left(\frac{\rho^*}{1 - \rho^*} \right) + \frac{8}{27(\gamma - 1)} \log(\theta). \tag{7.55}$$

Henceforth, I will restrict my discussion to the dimensionless form (7.40)-(7.55). The superscript $*$ will be omitted for notational simplicity in the following sections.

7.3   Functional entropy variables

In this section, functional derivatives are taken to the mathematical entropy function $\mathfrak{H}$ with respect the the conservation variables to define the functional entropy variables. The mathematical entropy for the thermal Navier-

224

Stokes-Korteweg equations is defined as

$$\mathfrak{H} := -\rho s = \frac{8}{27} \rho \log \left(\frac{\rho}{1 - \rho} \right) - \frac{8}{27(1 - \gamma)} \rho \log (\theta). \qquad (7.56)$$

With this definition, the dissipation relation can be rewritten in terms of $\mathfrak{H}$ as

$$\frac{\partial \mathfrak{H}}{\partial t} + \nabla \cdot (\mathfrak{H} \mathbf{u}) - \nabla \cdot \left(\frac{\mathbf{q}}{\theta} \right) + \frac{\rho r}{\theta} = -\frac{1}{\theta} \boldsymbol{\tau} : \nabla \mathbf{u} - \frac{1}{\theta^2} \nabla \theta \cdot \boldsymbol{\kappa} \nabla \theta \leq 0. \qquad (7.57)$$

In three dimensions, the conservation variables for the thermal Navier-Stokes-Korteweg equations are

$$\mathcal{U} = \begin{bmatrix} U_1 \\ U_2 \\ U_3 \\ U_4 \\ U_5 \end{bmatrix} = \rho \begin{bmatrix} 1 \\ u_2 \\ u_3 \\ u_4 \\ E \end{bmatrix}.$$

Following the definition of the entropy variables [109] and invoking the techniques of calculus of variations, the entropy variables $\mathbf{V}$ for the Navier-Stokes-Korteweg equations are defined as the functional derivatives of $\mathfrak{H}$ with respect to $\mathcal{U}$, i.e.,

$$\mathbf{V} = \frac{\delta \mathfrak{H}}{\delta \mathcal{U}} = \begin{bmatrix} V_1 \\ V_2 \\ V_3 \\ V_4 \\ V_5 \end{bmatrix} = \begin{bmatrix} \delta \mathfrak{H} / \delta U_1 \\ \delta \mathfrak{H} / \delta U_2 \\ \delta \mathfrak{H} / \delta U_3 \\ \delta \mathfrak{H} / \delta U_4 \\ \delta \mathfrak{H} / \delta U_5 \end{bmatrix} = \begin{bmatrix} \delta \mathfrak{H} / \delta \rho \\ \delta \mathfrak{H} / \delta (\rho u_1) \\ \delta \mathfrak{H} / \delta (\rho u_2) \\ \delta \mathfrak{H} / \delta (\rho u_3) \\ \delta \mathfrak{H} / \delta (\rho E) \end{bmatrix}. \qquad (7.58)$$

Given the test functions $\delta\mathbf{v} = [\delta v_1, \delta v_2, \delta v_3, \delta v_4, \delta v_5]^T$, the entropy variables $\mathbf{V}$ can be represented explicitly as linear operators acting on $\delta\mathbf{v}$:

$$V_1[\delta v_1] = \frac{1}{\theta}\left(-2\rho + \frac{8}{27}\theta\log\left(\frac{\rho}{1-\rho}\right) - \frac{8}{27(\gamma-1)}\theta\log(\theta) + \frac{8}{27(\gamma-1)}\theta\right.$$
$$\left. + \frac{8\theta}{27(1-\rho)} - \frac{|\mathbf{u}|^2}{2}\right)\delta v_1 + \frac{1}{\text{We}}\frac{1}{\theta}\nabla\rho \cdot \nabla\delta v_1, \tag{7.59}$$

$$V_2[\delta v_2] = \frac{u_1}{\theta}\delta v_2, \tag{7.60}$$

$$V_3[\delta v_3] = \frac{u_2}{\theta}\delta v_3, \tag{7.61}$$

$$V_4[\delta v_4] = \frac{u_3}{\theta}\delta v_4, \tag{7.62}$$

$$V_5[\delta v_5] = -\frac{1}{\theta}\delta v_5. \tag{7.63}$$

Remark 7.3.1. *If $\rho\Psi_{loc}$ is regarded as a function of density ρ and temperature θ, straightforward calculations show that*

$$\mathfrak{H} = \frac{\partial(\rho\Psi_{loc})}{\partial\theta}, \tag{7.64}$$

$$\nu_{loc} = \frac{\partial(\rho\Psi_{loc})}{\partial\rho}. \tag{7.65}$$

Remark 7.3.2. *In classical thermodynamics, the electrochemical potential is defined as $\Psi + \rho\partial\Psi/\partial\rho$. Here, I generalize this definition to the functional setting and define the global electrochemical potential ν as*

$$\nu[\delta v_1] := \Psi[\delta v_1] + \rho\frac{\delta\Psi}{\delta\rho}[\delta v_1]$$
$$= \left(-2\rho + \frac{8}{27}\theta\log\left(\frac{\rho}{1-\rho}\right) - \frac{8}{27(\gamma-1)}\theta\log(\theta) + \frac{8}{27(\gamma-1)}\theta\right.$$
$$\left. + \frac{8\theta}{27(1-\rho)}\right)\delta v_1 + \frac{1}{\text{We}}\nabla\rho \cdot \nabla\delta v_1, \tag{7.66}$$

$$= \nu_{loc}\delta v_1 + \frac{1}{\text{We}}\nabla\rho \cdot \nabla\delta v_1. \tag{7.67}$$

226

With this definition, the first component of $\mathbf{V}$ can be written compactly as

$$V_1[\delta v_1] = \frac{1}{\theta}\left(\nu - \frac{|\mathbf{u}|^2}{2}\right)[\delta v_1]. \qquad (7.68)$$

Consequently, the entropy variables (7.59)-(7.63) can be formally written as

$$\mathbf{V} = \frac{1}{\theta}\begin{bmatrix} \nu - \dfrac{|\mathbf{u}|^2}{2} \\ u_1 \\ u_2 \\ u_3 \\ -1 \end{bmatrix}, \qquad (7.69)$$

which symbolically coincides with the definition of the entropy variables for the compressible Navier-Stokes equations [109, 178]. The global electrochemical potential ν here should be understood as a linear operator acting on a Banach space rather than a local function. Intriguingly, this fact also suggests that the definition of the functional entropy variables is formally invariant under different choices of the Helmholtz free energy function.

Theorem 7.3.1. *The entropy variables $\mathbf{V}$ acting on the thermal Navier-Stokes-Korteweg equations recovers the Clausius-Duhem inequality.*

Proof. Direct calculations will show that

$$\mathbf{V}\left[\frac{\partial \mathcal{U}}{\partial t}\right] = \frac{\delta H}{\delta \mathcal{U}}\left[\frac{\partial \mathcal{U}}{\partial t}\right] = \frac{\partial \mathfrak{H}}{\partial t}. \qquad (7.70)$$

227

Taking the test functions as the advective fluxes leads to

$$
\mathbf{V}
\begin{bmatrix}
\nabla \cdot (\rho \mathbf{u}) \\
\nabla \cdot (\rho \mathbf{u} \otimes \mathbf{u}) + \nabla p \\
\nabla \cdot (\rho E \mathbf{u} + p \mathbf{u})
\end{bmatrix}
= \nabla \cdot (\mathfrak{H} \mathbf{u})
$$
$$
+ \frac{1}{\mathrm{We}\,\theta} \left(\nabla \mathbf{u} : \nabla \rho \otimes \nabla \rho + \frac{1}{2} |\nabla \rho|^2 \nabla \cdot \mathbf{u} + \rho \nabla \rho \cdot \nabla (\nabla \cdot \mathbf{u}) \right). \quad (7.71)
$$

Testing the entropy variables with the capillarity terms results in

$$
\mathbf{V}
\begin{bmatrix}
0 \\
-\nabla \cdot \varsigma \\
-\nabla \cdot (\varsigma \mathbf{u}) + \nabla \cdot \boldsymbol{\Pi}
\end{bmatrix}
$$
$$
= -\frac{1}{\mathrm{We}\,\theta} \left(\nabla \mathbf{u} : \nabla \rho \otimes \nabla \rho + \frac{1}{2} |\nabla \rho|^2 \nabla \cdot \mathbf{u} + \rho \nabla \rho \cdot \nabla (\nabla \cdot \mathbf{u}) \right). \quad (7.72)
$$

Combing (7.71)-(7.72) yields

$$
\mathbf{V}
\begin{bmatrix}
\nabla \cdot (\rho \mathbf{u}) \\
\nabla \cdot (\rho \mathbf{u} \otimes \mathbf{u}) + \nabla p - \nabla \cdot \varsigma \\
\nabla \cdot (\rho E \mathbf{u} + p \mathbf{u}) - \nabla \cdot (\varsigma \mathbf{u}) + \nabla \cdot \boldsymbol{\Pi}
\end{bmatrix}
= \nabla \cdot (\mathfrak{H} \mathbf{u}). \qquad (7.73)
$$

Testing the entropy variables against the viscous flux gives

$$
\mathbf{V}
\begin{bmatrix}
0 \\
-\nabla \cdot \boldsymbol{\tau} \\
-\nabla \cdot (\boldsymbol{\tau} \mathbf{u})
\end{bmatrix}
= \frac{1}{\theta} \boldsymbol{\tau} : \nabla \mathbf{u}. \qquad (7.74)
$$

Testing the entropy variable with the heat flux, the heat source, and the body force terms results in

$$\mathbf{V} \begin{bmatrix} 0 \\ -\rho \mathbf{b} \\ \nabla \cdot \mathbf{q} - \rho \mathbf{u} \cdot \mathbf{b} - \rho r \end{bmatrix} = -\nabla \cdot \left(\frac{\mathbf{q}}{\theta} \right) + \frac{\rho r}{\theta} + \frac{\nabla \theta \cdot \boldsymbol{\kappa} \nabla \theta}{\theta^2}. \qquad (7.75)$$

The relations (7.70), (7.73), (7.74), and (7.75) can be combined to get

$$\frac{\partial \mathfrak{H}}{\partial t} + \nabla \cdot (\mathfrak{H} \mathbf{u}) + \nabla \cdot \left(\frac{\mathbf{q}}{\theta} \right) - \frac{\rho r}{\theta} = -\frac{\nabla \theta \cdot \boldsymbol{\kappa} \nabla \theta}{\theta^2} - \frac{1}{\theta} \boldsymbol{\tau} : \nabla \mathbf{u}, \qquad (7.76)$$

or equivalently,

$$\frac{\partial (\rho s)}{\partial t} + \nabla \cdot (\rho s \mathbf{u}) - \nabla \cdot \left(\frac{\mathbf{q}}{\theta} \right) + \frac{\rho r}{\theta} = \frac{\nabla \theta \cdot \boldsymbol{\kappa} \nabla \theta}{\theta^2} + \frac{1}{\theta} \boldsymbol{\tau} : \nabla \mathbf{u}. \qquad (7.77)$$

This is exactly the dissipation relation given by (2.25) and (3.45). □

    This theorem suggests that a weak formulation may inherently satisfy the Clausius-Duhem inequality as long as the entropy variables $\mathbf{V}$ can be chosen as the test functions. However, this job is non-trivial since the definitions of $\mathbf{V}$ are nonlinear and include a Laplace operator in the definition of V_1. One should be clever enough to engineer a function space satisfying the nonlinear differential relation in (7.59). Alternatively, one may introduce an auxiliary equation in a similar fashion to that was done for the isothermal Navier-Stokes-Korteweg equations in Section 6.3. This equation may weakly enforce V_1 to be in the test function space for the mass equation. For the momentum equations and the energy equation, the working variables are taken as u_i/θ, $i = 1, 2, 3$ and $-1/\theta$ by performing algebraic transformations. In doing so, the entropy variables $\mathbf{V}$ will be guaranteed to be in the test function spaces.

7.4 An alternative statement of the thermal Navier-Stokes-Korteweg equations

Let me introduce an auxiliary variable V for the thermal Navier-Stokes-Korteweg equations as

$$V := \frac{1}{\theta}\left(\nu_{loc} - \frac{|\mathbf{u}|^2}{2}\right) - \frac{1}{\text{We}}\nabla \cdot \left(\frac{\nabla\rho}{\theta}\right). \tag{7.78}$$

Recalling the thermodynamic relation

$$\nu_{loc} = \frac{p}{\rho} + \Psi_{loc}, \tag{7.79}$$

the auxiliary variable can be rewritten as

$$V = \frac{1}{\theta}\left(\frac{p}{\rho} + \Psi_{loc} - \frac{|\mathbf{u}|^2}{2}\right) - \frac{1}{\text{We}}\nabla \cdot \left(\frac{\nabla\rho}{\theta}\right). \tag{7.80}$$

Timing $\rho\theta$ at both sides of the above equation, one has

$$p = \rho V\theta - \rho\Psi_{loc} + \frac{\rho|\mathbf{u}|^2}{2} + \frac{1}{\text{We}}\rho\theta\nabla \cdot \left(\frac{\nabla\rho}{\theta}\right). \tag{7.81}$$

The equation (7.81) can be viewed as an equivalent statement of the equation-of-state (7.43) in terms of the newly introduced the auxiliary variable V. Consequently, the pressure gradient term ∇p in the momentum balance equation (7.41) can be rewritten as

$$
\begin{aligned}
\nabla p &= \nabla\left(\rho V\theta + \frac{\rho|\mathbf{u}|^2}{2} + \frac{1}{\text{We}}\rho\theta\nabla \cdot \left(\frac{\nabla\rho}{\theta}\right)\right) - \nabla\left(\rho\Psi_{loc}\right) \\
&= \nabla\left(\rho V\theta + \frac{\rho|\mathbf{u}|^2}{2} + \frac{1}{\text{We}}\rho\theta\nabla \cdot \left(\frac{\nabla\rho}{\theta}\right)\right) - \frac{\partial\left(\rho\Psi_{loc}\right)}{\partial\rho}\nabla\rho - \frac{\partial\left(\rho\Psi_{loc}\right)}{\partial\theta}\nabla\theta \\
&= \nabla\left(\rho V\theta + \frac{\rho|\mathbf{u}|^2}{2} + \frac{1}{\text{We}}\rho\theta\nabla \cdot \left(\frac{\nabla\rho}{\theta}\right)\right) - \nu_{loc}\nabla\rho - \mathfrak{H}\nabla\theta
\end{aligned}
$$

230

$$= \nabla \left(\rho V \theta + \frac{\rho |\mathbf{u}|^2}{2} + \frac{1}{\mathrm{We}} \rho \theta \nabla \cdot \left(\frac{\nabla \rho}{\theta} \right) \right)$$
$$- \left(V \theta + \frac{|\mathbf{u}|^2}{2} + \frac{1}{\mathrm{We}} \theta \nabla \cdot \left(\frac{\nabla \rho}{\theta} \right) \right) \nabla \rho - \mathfrak{H} \nabla \theta. \qquad (7.82)$$

The term $\rho E + p$ appearing in the energy equation can be written as

$$\rho E + p = \rho \Psi_{loc} - \theta \mathfrak{H} + \frac{1}{2 \, \mathrm{We}} |\nabla \rho|^2 + \frac{1}{2} \rho |\mathbf{u}|^2$$
$$+ \rho V \theta + \frac{1}{2} \rho |\mathbf{u}|^2 - \rho \Psi_{loc} + \frac{1}{\mathrm{We}} \rho \theta \nabla \cdot \left(\frac{\nabla \rho}{\theta} \right)$$
$$= \rho V \theta - \theta \mathfrak{H} + \frac{1}{2 \, \mathrm{We}} |\nabla \rho|^2 + \rho |\mathbf{u}|^2 + \frac{1}{\mathrm{We}} \rho \theta \nabla \cdot \left(\frac{\nabla \rho}{\theta} \right). \qquad (7.83)$$

Therefore, the thermal Navier-Stokes-Korteweg equations can be equivalently stated as

$$\frac{\partial \rho}{\partial t} + \nabla \cdot (\rho \mathbf{u}) = 0, \qquad (7.84)$$

$$\frac{\partial (\rho \mathbf{u})}{\partial t} + \nabla \cdot (\rho \mathbf{u} \otimes \mathbf{u}) + \nabla \left(\rho V \theta + \frac{\rho |\mathbf{u}|^2}{2} + \frac{1}{\mathrm{We}} \rho \theta \nabla \cdot \left(\frac{\nabla \rho}{\theta} \right) \right)$$
$$- \left(V \theta + \frac{|\mathbf{u}|^2}{2} + \frac{1}{\mathrm{We}} \theta \nabla \cdot \left(\frac{\nabla \rho}{\theta} \right) \right) \nabla \rho - \mathfrak{H} \nabla \theta - \nabla \cdot \boldsymbol{\tau} - \nabla \cdot \boldsymbol{\varsigma} = \rho \mathbf{b}, \quad (7.85)$$

$$\frac{\partial (\rho E)}{\partial t} + \nabla \cdot \left(\left(\rho V \theta - \theta \mathfrak{H} + \frac{1}{2 \, \mathrm{We}} |\nabla \rho|^2 + \rho |\mathbf{u}|^2 + \frac{1}{\mathrm{We}} \rho \theta \nabla \cdot \left(\frac{\nabla \rho}{\theta} \right) \right) \mathbf{u} \right)$$
$$- \nabla \cdot ((\boldsymbol{\tau} + \boldsymbol{\varsigma}) \mathbf{u}) + \nabla \cdot \mathbf{q} + \nabla \cdot \boldsymbol{\Pi} = \rho \mathbf{b} \cdot \mathbf{u} + \rho r, \qquad (7.86)$$

$$V = \frac{1}{\theta} \left(\nu_{loc} - \frac{|\mathbf{u}|^2}{2} \right) - \frac{1}{\mathrm{We}} \nabla \cdot \left(\frac{\nabla \rho}{\theta} \right), \qquad (7.87)$$

wherein,

$$\mathfrak{H} = -\rho s, \qquad (7.88)$$
$$s = -\frac{8}{27} \log \left(\frac{\rho}{1 - \rho} \right) + \frac{8}{27(\gamma - 1)} \log(\theta), \qquad (7.89)$$

231

$$\nu_{loc} = -2\rho + \frac{8\theta}{27(1-\rho)} + \frac{8}{27}\theta \log\left(\frac{\rho}{1-\rho}\right)$$
$$- \frac{8}{27(\gamma-1)}\theta \log(\theta) + \frac{8}{27(\gamma-1)}\theta. \tag{7.90}$$

In the linear momentum balance equations (7.85) and the energy balance equation (7.86), the pressure force ∇p and the power of the pressure $\nabla \cdot (p\mathbf{u})$ are replaced using the relations (7.82) and (7.83). The relations (7.82) and (7.83) together with the differential equation for the auxiliary variable (7.87) make the new strong problem (7.84)-(7.90) consistent with the original Navier-Stokes-Korteweg equations (7.40)-(7.42). The following numerical analysis will be based on this alternative strong problem.

7.5 The weak formulation

In this section, the weak formulation is built based on the alternative strong problem (7.84)-(7.87). Let me first introduce a new set of variables for the system of equations (7.84)-(7.87):

$$\mathbf{Y} := \begin{bmatrix} Y_1 \\ Y_2 \\ Y_3 \\ Y_4 \\ Y_5 \\ Y_6 \end{bmatrix} = \begin{bmatrix} \rho \\ \dfrac{u_1}{\theta} \\ \dfrac{u_2}{\theta} \\ \dfrac{u_3}{\theta} \\ -\dfrac{1}{\theta} \\ V \end{bmatrix}. \tag{7.91}$$

Let $\mathcal{V}_1$ be the trial solution space for $Y_1 = \rho$ and $Y_6 = V$; $\mathcal{V}_2$ be the trial solution space for $Y_{i+1} = u_i/\theta$, $i = 1, 2, 3$; $\mathcal{V}_3$ be the trial solution space for $Y_5 = -1/\theta$. The test function spaces are assumed to be identical to the corresponding trial solution spaces. With the definitions of the function spaces, the weak formulation for the thermal Navier-Stokes-Korteweg equations can be stated as follows.

Find $Y_1(t) = \rho(t) \in L^2(0, T; \mathcal{V}_1) \cap H^1(0, T; L^2(\Omega))$, $Y_{i+1}(t) = u_i(t)/\theta(t) \in L^2(0, T; \mathcal{V}_2) \cap H^1(0, T; L^2(\Omega))$ for $i = 1, 2, 3$, $Y_4(t) = -1/\theta(t) \in L^2(0, T; \mathcal{V}_3) \cap H^1(0, T; L^2(\Omega))$, and $Y_6(t) = V \in L^2(0, T; \mathcal{V}_1)$, such that

$$\left(w_1, \frac{\partial \rho}{\partial t}\right)_\Omega - (\nabla w_1, \rho \mathbf{u})_\Omega = 0, \qquad \forall w_1 \in \mathcal{V}_1, \tag{7.92}$$

$$\left(\mathbf{w}, \frac{\partial(\rho \mathbf{u})}{\partial t}\right)_\Omega - (\nabla \mathbf{w}, \rho \mathbf{u} \otimes \mathbf{u})_\Omega - \left(\nabla \cdot \mathbf{w}, \rho V \theta + \frac{1}{2}\rho|\mathbf{u}|^2\right.$$
$$\left.+ \frac{1}{\mathrm{We}}\rho\theta\nabla \cdot \left(\frac{\nabla \rho}{\theta}\right)\right)_\Omega - \left(\mathbf{w}, \left(V\theta + \frac{|\mathbf{u}|^2}{2} + \frac{1}{\mathrm{We}}\theta\nabla \cdot \left(\frac{\nabla \rho}{\theta}\right)\right)\nabla\rho\right)_\Omega$$
$$- (\mathbf{w}, \mathfrak{H}\nabla\theta)_\Omega + (\nabla \mathbf{w}, \boldsymbol{\tau})_\Omega + (\nabla \mathbf{w}, \boldsymbol{\varsigma})_\Omega = (\mathbf{w}, \rho\mathbf{b})_\Omega,$$

$$\forall \mathbf{w} = (w_2; w_3; w_4)^T \in (\mathcal{V}_2)^3, \quad (7.93)$$

$$\left(w_5, \frac{\partial(\rho E)}{\partial t}\right)_\Omega - \left(\nabla w_5, \left(\rho V \theta - \theta\mathfrak{H} + \frac{1}{2\,\mathrm{We}}|\nabla\rho|^2 + \rho|\mathbf{u}|^2\right.\right.$$
$$\left.\left.+ \frac{1}{\mathrm{We}}\rho\theta\nabla \cdot \left(\frac{\nabla \rho}{\theta}\right)\right)\mathbf{u}\right)_\Omega + (\nabla w_5, \boldsymbol{\tau}\mathbf{u})_\Omega + (\nabla w_5, \boldsymbol{\varsigma}\mathbf{u})_\Omega - (\nabla w_5, \mathbf{q})_\Omega$$
$$- (\nabla w_5, \boldsymbol{\Pi})_\Omega = (w_5, \rho\mathbf{b} \cdot \mathbf{u})_\Omega + (w_5, \rho r)_\Omega, \quad \forall w_5 \in \mathcal{V}_3, \tag{7.94}$$

$$(w_6, V)_\Omega = \left(w_6, \frac{1}{\theta}\left(\nu_{loc} - \frac{|\mathbf{u}|^2}{2}\right)\right)_\Omega + \left(\nabla w_6, \frac{1}{\mathrm{We}\,\theta}\nabla\rho\right)_\Omega, \forall w_6 \in \mathcal{V}_1, \tag{7.95}$$

with $\rho(0) = \rho_0$, $\mathbf{u}(0)/\theta(0) = \mathbf{u}_0/\theta_0$, and $-1/\theta(0) = -1/\theta_0$ in Ω.

233

It is noteworthy that the equation (7.95) is in fact identical to the definition of the entropy variable V_1 in (7.59). By choosing the test function and the trial solution spaces for the equations (7.92) and (7.95) as the same function space $\mathcal{V}_1$, the entropy variable V_1 is weakly enforced to be in the test function space for the weak mass equation (7.92). This is a key ingredient for proving the dissipative structure of the weak formulation. In the following theorem, the dissipation property of this weak formulation is revealed.

Theorem 7.5.1. *Sufficiently smooth weak solutions of the problem (7.92)-(7.95) verify the second law of thermodynamics, i.e.,*

$$\int_\Omega \left(\frac{\partial \mathfrak{H}}{\partial t} + \nabla \cdot (\mathfrak{H}\mathbf{u}) - \nabla \cdot \left(\frac{\mathbf{q}}{\theta} \right) + \frac{\rho r}{\theta} \right) d\mathbf{x}$$

$$= -\int_\Omega \frac{1}{\theta} \boldsymbol{\tau} : \nabla \mathbf{u} d\mathbf{x} - \int_\Omega \frac{\nabla \theta \cdot \boldsymbol{\kappa} \nabla \theta}{\theta^2} d\mathbf{x}. \qquad (7.96)$$

Proof. Taking $w_1 = V$ in (7.92) and $w_6 = \partial \rho / \partial t$ in (7.95) leads to

$$\left(V, \frac{\partial \rho}{\partial t} \right)_\Omega - (\nabla V, \rho \mathbf{u})_\Omega = 0, \qquad (7.97)$$

$$\left(\frac{\partial \rho}{\partial t}, V \right)_\Omega = \left(\frac{\partial \rho}{\partial t}, \frac{1}{\theta} \left(\nu_{loc} - \frac{|\mathbf{u}|^2}{2} \right) \right)_\Omega + \left(\nabla \left(\frac{\partial \rho}{\partial t} \right), \frac{1}{\mathrm{We}\,\theta} \nabla \rho \right)_\Omega. \qquad (7.98)$$

Combing the above two equations, one can get

$$\int_\Omega \frac{\delta \mathfrak{H}}{\delta \rho} \left[\frac{\partial \rho}{\partial t} \right] d\mathbf{x} = \left(\frac{\partial \rho}{\partial t}, \frac{1}{\theta} \left(\nu_{loc} - \frac{|\mathbf{u}|^2}{2} \right) \right)_\Omega + \left(\nabla \left(\frac{\partial \rho}{\partial t} \right), \frac{1}{\mathrm{We}\,\theta} \nabla \rho \right)_\Omega$$

$$= (\nabla V, \rho \mathbf{u})_\Omega. \qquad (7.99)$$

Choosing $\mathbf{w} = \mathbf{u}/\theta$ in (7.93) results in

$$\int_\Omega \frac{\delta \mathfrak{H}}{\delta(\rho \mathbf{u})} \left[\frac{\partial (\rho \mathbf{u})}{\partial t} \right] d\mathbf{x} = \left(\frac{\mathbf{u}}{\theta}, \frac{\partial (\rho \mathbf{u})}{\partial t} \right)_\Omega = \left(\nabla \left(\frac{\mathbf{u}}{\theta} \right), \rho \mathbf{u} \otimes \mathbf{u} \right)_\Omega$$

234

$$+ \left(\nabla \cdot \left(\frac{\mathbf{u}}{\theta} \right), \rho V \theta + \frac{1}{2} \rho |\mathbf{u}|^2 + \frac{1}{\mathrm{We}} \rho \theta \nabla \cdot \left(\frac{\nabla \rho}{\theta} \right) \right)_\Omega$$

$$+ \left(\frac{\mathbf{u}}{\theta}, \left(V \theta + \frac{|\mathbf{u}|^2}{2} + \frac{1}{\mathrm{We}} \theta \nabla \cdot \left(\frac{\nabla \rho}{\theta} \right) \right) \nabla \rho \right)_\Omega$$

$$+ \left(\frac{\mathbf{u}}{\theta}, \mathfrak{H} \nabla \theta \right)_\Omega - \left(\nabla \left(\frac{\mathbf{u}}{\theta} \right), \boldsymbol{\tau} \right)_\Omega - \left(\nabla \left(\frac{\mathbf{u}}{\theta} \right), \varsigma \right)_\Omega$$

$$+ \left(\frac{\mathbf{u}}{\theta}, \rho \mathbf{b} \right)_\Omega. \tag{7.100}$$

Taking $w_5 = -1/\theta$ in (7.94) yields

$$\int_\Omega \frac{\delta \mathfrak{H}}{\delta(\rho E)} \left[\frac{\partial(\rho E)}{\partial t} \right] d\mathbf{x} = \left(-\frac{1}{\theta}, \frac{\partial(\rho E)}{\partial t} \right)_\Omega = - \left(\nabla \left(\frac{1}{\theta} \right), \left(\rho V \theta - \theta \mathfrak{H} \right. \right.$$

$$\left. \left. + \frac{1}{2\mathrm{We}} |\nabla \rho|^2 + \rho |\mathbf{u}|^2 + \frac{1}{\mathrm{We}} \rho \theta \nabla \cdot \left(\frac{\nabla \rho}{\theta} \right) \right) \mathbf{u} \right)_\Omega$$

$$+ \left(\nabla \left(\frac{1}{\theta} \right), \boldsymbol{\tau} \mathbf{u} \right)_\Omega + \left(\nabla \left(\frac{1}{\theta} \right), \varsigma \mathbf{u} \right)_\Omega$$

$$+ \left(\frac{1}{\theta}, \nabla \cdot \mathbf{q} \right)_\Omega - \left(\nabla \left(\frac{1}{\theta} \right), \boldsymbol{\Pi} \right)_\Omega - \left(\frac{1}{\theta}, \rho \mathbf{b} \cdot \mathbf{u} \right)_\Omega$$

$$- \left(\frac{1}{\theta}, \rho r \right)_\Omega. \tag{7.101}$$

Collecting all terms in (7.99)-(7.101) involving V, one has

$$(\nabla V, \rho \mathbf{u})_\Omega + \left(\nabla \cdot \left(\frac{\mathbf{u}}{\theta} \right), \rho V \theta \right)_\Omega + \left(\frac{\mathbf{u}}{\theta}, V \theta \nabla \rho \right)_\Omega - \left(\nabla \left(\frac{1}{\theta} \right), V \theta \rho \mathbf{u} \right)_\Omega$$

$$= \int_\Omega \nabla \cdot (\rho V \mathbf{u}) \, d\mathbf{x} = \int_{\partial \Omega} \rho V \mathbf{u} \cdot \mathbf{n} ds = 0. \tag{7.102}$$

Summing all terms in (7.99)-(7.101) involving $\mathfrak{H}$ leads to

$$\left(\frac{\mathbf{u}}{\theta}, \mathfrak{H} \nabla \theta \right)_\Omega + \left(\nabla \left(\frac{1}{\theta} \right), \theta \mathfrak{H} \mathbf{u} \right)_\Omega = \left(\frac{\mathbf{u}}{\theta}, \mathfrak{H} \nabla \theta \right)_\Omega - \left(\frac{1}{\theta}, \nabla (\theta \mathfrak{H} \mathbf{u}) \right)_\Omega$$

$$= - \int_\Omega \nabla \cdot (\mathfrak{H} \mathbf{u}) \, d\mathbf{x}. \tag{7.103}$$

Grouping the following terms and making use of the velocity boundary conditions result in

$$\left(\nabla\left(\frac{\mathbf{u}}{\theta}\right), \rho\mathbf{u}\otimes\mathbf{u}\right)_{\Omega} + \left(\nabla\cdot\left(\frac{\mathbf{u}}{\theta}\right), \frac{1}{2}\rho|\mathbf{u}|^2\right)_{\Omega} + \left(\frac{\mathbf{u}}{\theta}, \frac{|\mathbf{u}|^2}{2}\nabla\rho\right)_{\Omega}$$

$$-\left(\nabla\left(\frac{1}{\theta}\right), \rho|\mathbf{u}|^2\mathbf{u}\right)_{\Omega}$$

$$=\int_{\Omega}\nabla\cdot\left(\frac{1}{2\theta}\rho|\mathbf{u}|^2\mathbf{u}\right)d\mathbf{x} = \int_{\partial\Omega}\frac{1}{2\theta}\rho|\mathbf{u}|^2\mathbf{u}\cdot\mathbf{n}ds = 0. \qquad (7.104)$$

Again, grouping all terms in (7.99)-(7.101) explicitly involving We, one has

$$\left(\nabla\cdot\left(\frac{\mathbf{u}}{\theta}\right), \frac{1}{\mathrm{We}}\rho\theta\nabla\cdot\left(\frac{\nabla\rho}{\theta}\right)\right)_{\Omega} + \left(\frac{\mathbf{u}}{\theta}, \frac{1}{\mathrm{We}}\theta\nabla\cdot\left(\frac{\nabla\rho}{\theta}\right)\nabla\rho\right)_{\Omega}$$

$$-\left(\nabla\left(\frac{1}{\theta}\right), \frac{1}{\mathrm{We}}\rho\theta\nabla\cdot\left(\frac{\nabla\rho}{\theta}\right)\mathbf{u}\right)_{\Omega} - \left(\nabla\left(\frac{1}{\theta}\right), \frac{1}{2\,\mathrm{We}}|\nabla\rho|^2\mathbf{u}\right)_{\Omega}$$

$$=\int_{\Omega}\frac{1}{\mathrm{We}}\nabla\cdot(\rho\mathbf{u})\nabla\cdot\left(\frac{\nabla\rho}{\theta}\right) - \frac{1}{2\,\mathrm{We}}\nabla\left(\frac{1}{\theta}\right)\cdot\mathbf{u}|\nabla\rho|^2 d\mathbf{x}$$

$$=-\int_{\Omega}\frac{1}{\mathrm{We}\theta}\nabla\left(\nabla\cdot(\rho\mathbf{u})\right)\cdot\nabla\rho - \frac{1}{2\,\mathrm{We}\theta}\nabla\cdot\left(\mathbf{u}|\nabla\rho|^2\right)d\mathbf{x}$$

$$=\int_{\Omega}\frac{-1}{\mathrm{We}\,\theta}\left(\frac{1}{2}|\nabla\rho|^2\nabla\cdot\mathbf{u} + \nabla\rho\otimes\nabla\rho:\nabla\mathbf{u} + \rho\nabla\rho\cdot\nabla\left(\nabla\cdot\mathbf{u}\right)\right)d\mathbf{x}. \quad (7.105)$$

In the derivation of (7.105), integration by part has been performed twice from the second equality to the third equality. The resulting boundary integrals are cancelled due to the boundary conditions. Combing all the terms in (7.99)-(7.101) including the Korteweg stress ς yields

$$-\left(\nabla\left(\frac{\mathbf{u}}{\theta}\right), \varsigma\right)_{\Omega} + \left(\nabla\left(\frac{1}{\theta}\right), \varsigma\mathbf{u}\right)_{\Omega} - \left(\nabla\left(\frac{1}{\theta}\right), \mathbf{\Pi}\right)_{\Omega}$$

$$=-\left(\frac{1}{\theta}, \nabla\mathbf{u}:\varsigma\right)_{\Omega} + \left(\frac{1}{\theta}, \nabla\cdot\mathbf{\Pi}\right)_{\Omega}$$

$$=\int_{\Omega}\frac{1}{\mathrm{We}\,\theta}\left(\frac{1}{2}|\nabla\rho|^2\nabla\cdot\mathbf{u} + \nabla\rho\otimes\nabla\rho:\nabla\mathbf{u} + \rho\nabla\rho\cdot\nabla\left(\nabla\cdot\mathbf{u}\right)\right)d\mathbf{x}. \quad (7.106)$$

236

Now summing (7.99)-(7.101) and making use of the relations (7.102)-(7.106), one has

$$
\int_\Omega \frac{\delta \mathfrak{H}}{\delta \rho}\left[\frac{\partial \rho}{\partial t}\right] + \frac{\delta \mathfrak{H}}{\delta(\rho \mathbf{u})}\left[\frac{\partial(\rho \mathbf{u})}{\partial t}\right] + \frac{\delta \mathfrak{H}}{\delta(\rho E)}\left[\frac{\partial(\rho E)}{\partial t}\right] d\mathbf{x}
$$

$$
= -\int_\Omega \nabla \cdot (\mathfrak{H}\mathbf{u})\, d\mathbf{x} - \left(\nabla\left(\frac{\mathbf{u}}{\theta}\right), \boldsymbol{\tau}\right)_\Omega + \left(\nabla\left(\frac{1}{\theta}\right), \boldsymbol{\tau}\mathbf{u}\right)_\Omega + \left(\frac{1}{\theta}, \rho\mathbf{b}\cdot\mathbf{u}\right)_\Omega
$$

$$
- \left(\frac{1}{\theta}, \rho\mathbf{b}\cdot\mathbf{u}\right)_\Omega + \left(\frac{1}{\theta}, \nabla\cdot\mathbf{q}\right)_\Omega - \left(\frac{1}{\theta}, \rho r\right)_\Omega
$$

$$
= -\int_\Omega \nabla \cdot (\mathfrak{H}\mathbf{u})\, d\mathbf{x} - \int_\Omega \frac{1}{\theta}\boldsymbol{\tau} : \nabla\mathbf{u}\, d\mathbf{x} + \left(\frac{1}{\theta}, \nabla\cdot\mathbf{q}\right)_\Omega - \left(\frac{1}{\theta}, \rho r\right)_\Omega
$$

$$
= -\int_\Omega \nabla \cdot (\mathfrak{H}\mathbf{u})\, d\mathbf{x} - \int_\Omega \frac{1}{\theta}\boldsymbol{\tau} : \nabla\mathbf{u}\, d\mathbf{x} + \int_\Omega \nabla \cdot \left(\frac{\mathbf{q}}{\theta}\right) + \frac{\mathbf{q}\cdot\nabla\theta}{\theta^2} - \frac{\rho r}{\theta}\, d\mathbf{x}.
$$

$$(7.107)$$

Reorganizing the above equation results in

$$
\int_\Omega \left(\frac{\partial \mathfrak{H}}{\partial t} + \nabla \cdot (\mathfrak{H}\mathbf{u}) - \nabla \cdot \left(\frac{\mathbf{q}}{\theta}\right) + \frac{\rho r}{\theta}\right) d\mathbf{x}
$$

$$
= -\int_\Omega \frac{1}{\theta}\boldsymbol{\tau} : \nabla\mathbf{u}\, d\mathbf{x} - \int_\Omega \frac{\nabla\theta\cdot\boldsymbol{\kappa}\nabla\theta}{\theta^2}\, d\mathbf{x}. \qquad (7.108)
$$

$\square$

Remark 7.5.1. *According to (7.60)-(7.63), $Y_i = V_i$ for $i = 2,3,4,5$.*

Remark 7.5.2. *Due to the periodic boundary conditions, the statement (7.5.1) can be simplified as*

$$
\int_\Omega \left(\frac{\partial \mathfrak{H}}{\partial t} + \frac{\rho r}{\theta}\right) d\mathbf{x} = -\int_\Omega \frac{1}{\theta}\boldsymbol{\tau} : \nabla\mathbf{u}\, d\mathbf{x} - \int_\Omega \frac{\nabla\theta\cdot\boldsymbol{\kappa}\nabla\theta}{\theta^2}\, d\mathbf{x}. \qquad (7.109)
$$

Remark 7.5.3. *Even though Theorem 7.5.1 is proved with the periodic bound-ary conditions, the same result can be obtained under other boundary condi-tions, such as the no-slip boundary conditions for the velocity field and the*

237

heat flux boundary condition for the temperature field. The major difficulty with regard to the boundary conditions comes from non-homogeneous essential boundary conditions. Recall that (7.96) is proved by taking the test function of the equation (7.92) as the auxiliary variable V. If there are nonzero essential boundary conditions built in the trial solution space, this technique is no more viable. The same issue arises for the compressible Navier-Stokes equations [178]. This very fact suggests that the strong enforcement of Dirichlet type boundary conditions is not an entropy-dissipative approach. The recently developed weak imposition technique [18] may provide a solution to this issue.

7.6 The semi-discrete formulation

Typical Galerkin method [107] is utilized to discretize the weak problem (7.84)-(7.87) in space. Let $\mathcal{V}_1^h \subset \mathcal{V}_1$, $\mathcal{V}_2^h \subset \mathcal{V}_2$, and $\mathcal{V}_3^h \subset \mathcal{V}_3$ be finite-dimensional approximations of $\mathcal{V}_1$, $\mathcal{V}_2$, and $\mathcal{V}_3$. The h-superscript denotes a mesh parameter. The equations (7.84)-(7.87) are approximated in space as follows.

Find $Y_1^h(t) = \rho^h(t) \in L^2(0, T; \mathcal{V}_1^h) \cap H^1(0, T; L^2(\Omega))$, $Y_{i+1}^h(t) = u_i^h(t)/\theta^h(t) \in L^2(0, T; \mathcal{V}_2^h) \cap H^1(0, T; L^2(\Omega))$ for $i = 1, 2, 3$, $Y_4^h(t) = -1/\theta^h(t) \in L^2(0, T; \mathcal{V}_3^h) \cap H^1(0, T; L^2(\Omega))$, and $Y_6^h = V^h \in L^2(0, T; \mathcal{V}_1^h)$, such that

$$\left(w_1^h, \frac{\partial \rho^h}{\partial t} \right)_\Omega - \left(\nabla w_1^h, \rho \mathbf{u}^h \right)_\Omega = 0, \qquad \forall w_1^h \in \mathcal{V}_1^h, \tag{7.110}$$

$$\left(\mathbf{w}^h, \frac{\partial (\rho^h \mathbf{u}^h)}{\partial t} \right)_\Omega - \left(\nabla \mathbf{w}^h, \rho^h \mathbf{u}^h \otimes \mathbf{u}^h \right)_\Omega$$

$$
-\left(\nabla\cdot\mathbf{w}^h,\,\rho^h V^h\theta^h+\frac{1}{2}\rho^h|\mathbf{u}^h|^2+\frac{1}{\mathrm{We}}\rho^h\theta^h\nabla\cdot\left(\frac{\nabla\rho^h}{\theta^h}\right)\right)_\Omega
$$

$$
-\left(\mathbf{w}^h,\left(V^h\theta^h+\frac{|\mathbf{u}^h|^2}{2}+\frac{1}{\mathrm{We}}\theta^h\nabla\cdot\left(\frac{\nabla\rho^h}{\theta^h}\right)\right)\nabla\rho^h\right)_\Omega-\left(\mathbf{w}^h,\mathfrak{H}^h\nabla\theta^h\right)_\Omega
$$

$$
+\left(\nabla\mathbf{w}^h,\boldsymbol{\tau}^h\right)_\Omega+\left(\nabla\mathbf{w}^h,\boldsymbol{\varsigma}^h\right)_\Omega=\left(\mathbf{w}^h,\rho^h\mathbf{b}\right)_\Omega,
$$

$$
\forall\mathbf{w}^h=(w_2^h;w_3^h;w_4^h)^T\in\left(\mathcal{V}_2^h\right)^3,\quad(7.111)
$$

$$
\left(w_5^h,\frac{\partial(\rho^h E^h)}{\partial t}\right)_\Omega-\left(\nabla w_5^h,\left(\rho^h V^h\theta^h-\theta^h\mathfrak{H}^h+\frac{1}{2\,\mathrm{We}}|\nabla\rho^h|^2+\rho^h|\mathbf{u}^h|^2\right.\right.
$$

$$
\left.\left.+\frac{1}{\mathrm{We}}\rho^h\theta^h\nabla\cdot\left(\frac{\nabla\rho^h}{\theta^h}\right)\right)\mathbf{u}^h\right)_\Omega+\left(\nabla w_5^h,\boldsymbol{\tau}^h\mathbf{u}^h\right)_\Omega+\left(\nabla w_5^h,\boldsymbol{\varsigma}^h\mathbf{u}^h\right)_\Omega
$$

$$
-\left(\nabla w_5^h,\mathbf{q}^h\right)_\Omega-\left(\nabla w_5^h,\boldsymbol{\Pi}^h\right)_\Omega-\left(w_5^h,\mathfrak{h}\right)_{\partial\Omega}=\left(w_5^h,\rho^h\mathbf{b}\cdot\mathbf{u}^h\right)_\Omega+\left(w_5^h,\rho^h r\right)_\Omega,
$$

$$
\forall w_5^h\in\mathcal{V}_3^h,\quad(7.112)
$$

$$
\left(w_6^h,V^h\right)_\Omega=\left(w_6^h,\frac{1}{\theta^h}\left(\nu_{loc}^h-\frac{|\mathbf{u}^h|^2}{2}\right)\right)_\Omega+\left(\nabla w_6^h,\frac{1}{\mathrm{We}\,\theta^h}\nabla\rho^h\right)_\Omega,
$$

$$
\forall w_6^h\in\mathcal{V}_1^h,\quad(7.113)
$$

with $\rho^h(0)=\rho_0^h$, $\mathbf{u}^h(0)/\theta^h(0)=\mathbf{u}_0^h/\theta_0^h$, and $-1/\theta^h(0)=-1/\theta_0^h$ in Ω.

Above, ρ_0^h, $\mathbf{u}_0^h/\theta_0^h$, and $-1/\theta_0^h$ are L^2-projections of $\rho_0(\mathbf{x})$, $\mathbf{u}_0(\mathbf{x})/\theta_0(\mathbf{x})$, and $-1/\theta_0(\mathbf{x})$ onto $\mathcal{V}_1^h$, $\mathcal{V}_2^h$, and $\mathcal{V}_3^h$ respectively. The proof of the following theorem follows straightforwardly from the proof of Theorem 7.5.1. It implies that the spatial discretization guarantees entropy production.

Theorem 7.6.1. *The solutions of the semi-discrete problem* (7.110)-(7.113) *satisfy the following entropy stability condition.*

$$
\int_\Omega\left(\frac{\partial\mathfrak{H}(\rho^h,\theta^h)}{\partial t}+\nabla\cdot\left(\mathfrak{H}(\rho^h,\theta^h)\mathbf{u}^h\right)-\nabla\cdot\left(\frac{\mathbf{q}^h}{\theta^h}\right)+\frac{\rho^h r}{\theta^h}\right)d\mathbf{x}
$$

$$
=-\int_\Omega\frac{1}{\theta^h}\boldsymbol{\tau}^h:\nabla\mathbf{u}^h d\mathbf{x}-\int_\Omega\frac{\nabla\theta^h\cdot\boldsymbol{\kappa}\nabla\theta^h}{(\theta^h)^2}d\mathbf{x}.\qquad(7.114)
$$

Remark 7.6.1. *Henceforth, the same discrete space $\mathcal{V}^h$, up to the prescription of the boundary conditions, is used to approximate $\mathcal{V}_1$, $\mathcal{V}_2$, and $\mathcal{V}_3$. Specifically, NURBS basis functions are used to define the discrete space $\mathcal{V}^h$ within the isogeometric context.*

7.7 The fully discrete formulation

Now the spatial discretization has been shown to be entropy-dissipative. It remains to design the discretizations of the time derivatives such that the temporal scheme can inherit the dissipation property. The most difficult part is the design of the approximation for the term $\partial(\rho E)/\partial t$. If one utilize the classical jump operator to approximate this time derivative, the dissipation of the resulting fully discrete scheme is not provably positive. In my approach, the total energy ρE is first split into four parts:

$$\rho E = \rho \Psi_{loc} - \theta \mathfrak{H} + \frac{1}{2}\rho|\mathbf{u}|^2 + \frac{1}{2\,\mathrm{We}}|\nabla \rho|^2. \qquad (7.115)$$

The approximation for each of the four parts will be carefully designed to ensure the discrete entropy dissipation while maintaining the accuracy. The new discrete approximation of $\partial(\rho E)/\partial t$ can be viewed as a second-order perturbation to the classical discrete approximation (see Lemma 7.7.3). In the proof of discrete dissipation, the special quadrature rules developed in Section 6.6 will be used repeatedly. This again demonstrates the promising potential of the new time integration methods based on the new quadrature rules.

This section is outlined as follows. In Section 7.7.1, the fully discrete

scheme is stated first. In Section 7.7.2, four preliminary lemmas are presented and proved. In Section 7.7.3, the main results are stated. The proofs of the theorems rely heavily on the four lemmas.

7.7.1 The fully discrete scheme

To discretize the semi-discrete problem (7.110)-(7.113) in time, the time interval $\mathcal{I} = (0, T)$ is first divided into N_{ts} subintervals $\mathcal{I}_n = (t_n, t_{n+1})$, $n = 0, \cdots, N_{ts} - 1$, of size $\Delta t_n = t_{n+1} - t_n$. I use

$$
\mathbf{Y}_n^h := \begin{bmatrix} \rho_n^h \\[6pt] \dfrac{u_{1,n}^h}{\theta_n^h} \\[10pt] \dfrac{u_{2,n}^h}{\theta_n^h} \\[10pt] \dfrac{u_{3,n}^h}{\theta_n^h} \\[10pt] -\dfrac{1}{\theta_n^h} \\[10pt] V_n^h \end{bmatrix} \tag{7.116}
$$

to denote the fully discrete solutions of at the time level n. The corresponding primitive variables can be recovered by the following transformation relation.

$$
\rho_n^h = \rho^h(\mathbf{Y}_n^h) = Y_{1,n}^h, \tag{7.117}
$$

$$
u_{i,n}^h = u_i^h(\mathbf{Y}_n^h) = -Y_{i+1,n}^h / Y_{5,n}^h, \quad i = 1, 2, 3, \tag{7.118}
$$

$$
\theta_n^h = \theta^h(\mathbf{Y}_n^h) = -1/Y_{5,n}^h. \tag{7.119}
$$

Next, let me introduce the jump operators for density, linear momentum, and energy over each time step as follows.

$$\llbracket \rho_n^h \rrbracket := \rho_{n+1}^h - \rho_n^h, \tag{7.120}$$

$$\llbracket \rho_n^h \mathbf{u}_n^h \rrbracket := \rho_{n+1}^h \mathbf{u}_{n+1}^h - \rho_n^h \mathbf{u}_n^h, \tag{7.121}$$

$$
\begin{aligned}
\llbracket \rho_n^h E(\rho_n^h, \mathbf{u}_n^h, \theta_n^h) \rrbracket :=& (\rho\Psi_{loc})(\rho_{n+\frac{1}{2}}^h, \theta_{n+1}^h) - (\rho\Psi_{loc})(\rho_{n+\frac{1}{2}}^h, \theta_n^h) \\
&+ (\rho\Psi_{loc})(\rho_{n+1}^h, \theta_{n+\frac{1}{2}}^h) - (\rho\Psi_{loc})(\rho_n^h, \theta_{n+\frac{1}{2}}^h) \\
&- \theta_{n+\frac{1}{2}}^h \left(\mathfrak{H}(\rho_{n+1}^h, \theta_{n+1}^h) - \mathfrak{H}(\rho_n^h, \theta_n^h) \right) \\
&- \frac{\theta_{n+1}^h - \theta_n^h}{2} \left(\mathfrak{H}(\rho_{n+\frac{1}{2}}^h, \theta_{n+1}^h) + \mathfrak{H}(\rho_{n+\frac{1}{2}}^h, \theta_n^h) \right) \\
&+ \frac{(\theta_{n+1}^h - \theta_n^h)^3}{12} \frac{\partial^2 \mathfrak{H}}{\partial \theta^2}(\rho_{n+\frac{1}{2}}^h, \theta_{n+1}^h) \\
&+ \frac{1}{2} \left(\rho_{n+1}^h |\mathbf{u}_{n+1}^h|^2 - \rho_n^h |\mathbf{u}_n^h|^2 \right) \\
&+ \frac{1}{2\,\mathrm{We}} \left(|\nabla \rho_{n+1}^h|^2 - |\nabla \rho_n^h|^2 \right). \tag{7.122}
\end{aligned}
$$

Remark 7.7.1. *Recalling the relation (7.115), the definition of the above energy jump (7.122) can be viewed as a summation of four jump operators:*

$$
\begin{aligned}
\llbracket \rho_n^h E(\rho_n^h, \mathbf{u}_n^h, \theta_n^h) \rrbracket =& \llbracket \rho_n^h \Psi_{loc}(\rho_n^h, \mathbf{u}_n^h, \theta_n^h) \rrbracket - \llbracket \theta_n^h \mathfrak{H}(\rho_n^h, \mathbf{u}_n^h, \theta_n^h) \rrbracket \\
&+ \llbracket \frac{\rho_n^h}{2} |\mathbf{u}_n^h|^2 \rrbracket + \llbracket \frac{1}{2\,\mathrm{We}} |\nabla \rho_n^h|^2 \rrbracket, \tag{7.123}
\end{aligned}
$$

$$
\begin{aligned}
\llbracket \rho_n^h \Psi_{loc}(\rho_n^h, \mathbf{u}_n^h, \theta_n^h) \rrbracket =& (\rho\Psi_{loc})(\rho_{n+\frac{1}{2}}^h, \theta_{n+1}^h) - (\rho\Psi_{loc})(\rho_{n+\frac{1}{2}}^h, \theta_n^h) \\
&+ (\rho\Psi_{loc})(\rho_{n+1}^h, \theta_{n+\frac{1}{2}}^h) - (\rho\Psi_{loc})(\rho_n^h, \theta_{n+\frac{1}{2}}^h), \tag{7.124}
\end{aligned}
$$

$$
\begin{aligned}
\llbracket \theta_n^h \mathfrak{H}(\rho_n^h, \mathbf{u}_n^h, \theta_n^h) \rrbracket =& \theta_{n+\frac{1}{2}}^h \left(\mathfrak{H}(\rho_{n+1}^h, \theta_{n+1}^h) - \mathfrak{H}(\rho_n^h, \theta_n^h) \right) \\
&+ \frac{\theta_{n+1}^h - \theta_n^h}{2} \left(\mathfrak{H}(\rho_{n+\frac{1}{2}}^h, \theta_{n+1}^h) + \mathfrak{H}(\rho_{n+\frac{1}{2}}^h, \theta_n^h) \right) \\
&- \frac{(\theta_{n+1}^h - \theta_n^h)^3}{12} \frac{\partial^2 \mathfrak{H}}{\partial \theta^2}(\rho_{n+\frac{1}{2}}^h, \theta_{n+1}^h), \tag{7.125}
\end{aligned}
$$

$$\llbracket \frac{\rho_n^h}{2}|\mathbf{u}_n^h|^2 \rrbracket = \frac{1}{2}\left(\rho_{n+1}^h|\mathbf{u}_{n+1}^h|^2 - \rho_n^h|\mathbf{u}_n^h|^2\right), \tag{7.126}$$

$$\llbracket \frac{1}{2\,\mathrm{We}}|\nabla\rho_n^h|^2 \rrbracket = \frac{1}{2\,\mathrm{We}}\left(|\nabla\rho_{n+1}^h|^2 - |\nabla\rho_n^h|^2\right). \tag{7.127}$$

The jump operators for the kinetic energy and the surface energy follow the standard definition. The treatments for $\rho\Psi_{loc}$ and $\theta\mathfrak{H}$ are nonclassical and involve a perturbation term. The objective of these definitions will be revealed in Section 7.7.2.

The fully discrete scheme can be stated as follows. In each time step, given $\mathbf{Y}_n^h$ and the time step Δt_n, find $\mathbf{Y}_{n+1}^h$ such that for all $w_1^h \in \mathcal{V}^h$, $\mathbf{w}^h = (w_2^h; w_3^h; w_4^h)^T \in \left(\mathcal{V}^h\right)^3$, $w_5^h \in \mathcal{V}^h$, and $w_6^h \in \mathcal{V}^h$,

$$\mathbf{B}^M(w_1^h; \mathbf{Y}_{n+1}^h) := \left(w_1^h, \frac{\llbracket \rho_n^h \rrbracket}{\Delta t_n}\right)_\Omega - \left(\nabla w_1^h, \rho_{n+\frac{1}{2}}^h \mathbf{u}_{n+\frac{1}{2}}^h\right)_\Omega = 0, \tag{7.128}$$

$$\mathbf{B}^U(\mathbf{w}^h; \mathbf{Y}_{n+1}^h) := \left(\mathbf{w}^h, \frac{\llbracket \rho_n^h \mathbf{u}_n^h \rrbracket}{\Delta t_n}\right)_\Omega - \left(\nabla\mathbf{w}^h, \rho_{n+\frac{1}{2}}^h \mathbf{u}_{n+\frac{1}{2}}^h \otimes \mathbf{u}_{n+\frac{1}{2}}^h\right)_\Omega$$

$$- \left(\nabla \cdot \mathbf{w}^h, \rho_{n+\frac{1}{2}}^h V_{n+\frac{1}{2}}^h \theta_{n+\frac{1}{2}}^h + \frac{1}{2}\rho_{n+\frac{1}{2}}^h |\mathbf{u}_{n+\frac{1}{2}}^h|^2 + \frac{1}{\mathrm{We}}\rho_{n+\frac{1}{2}}^h \theta_{n+\frac{1}{2}}^h \nabla \cdot \left(\frac{\nabla\rho_{n+\frac{1}{2}}^h}{\theta_{n+\frac{1}{2}}^h}\right)\right)_\Omega$$

$$- \left(\mathbf{w}^h, \left(V_{n+\frac{1}{2}}^h \theta_{n+\frac{1}{2}}^h + \frac{|\mathbf{u}_{n+\frac{1}{2}}^h|^2}{2} + \frac{1}{\mathrm{We}}\theta_{n+\frac{1}{2}}^h \nabla \cdot \left(\frac{\nabla\rho_{n+\frac{1}{2}}^h}{\theta_{n+\frac{1}{2}}^h}\right)\right)\nabla\rho_{n+\frac{1}{2}}^h\right)_\Omega$$

$$- \left(\mathbf{w}^h, \mathfrak{H}_{n+\frac{1}{2}}^h \nabla\theta_{n+\frac{1}{2}}^h\right)_\Omega + \left(\nabla\mathbf{w}^h, \boldsymbol{\tau}_{n+\frac{1}{2}}^h\right)_\Omega + \left(\nabla\mathbf{w}^h, \boldsymbol{\varsigma}_{n+\frac{1}{2}}^h\right)_\Omega$$

$$- \left(\mathbf{w}^h, \rho_{n+\frac{1}{2}}^h \mathbf{b}\right)_\Omega = 0, \tag{7.129}$$

$$\mathbf{B}^E(w_5^h; \mathbf{Y}_{n+1}^h) := \left(w_5^h, \frac{\llbracket \rho_n^h E(\rho_n^h, \mathbf{u}_n^h, \theta_n^h) \rrbracket}{\Delta t_n}\right)_\Omega - \left(\nabla w_5^h, \left(\rho_{n+\frac{1}{2}}^h V_{n+\frac{1}{2}}^h \theta_{n+\frac{1}{2}}^h\right.\right.$$

$$\left.\left. - \theta_{n+\frac{1}{2}}^h \mathfrak{H}_{n+\frac{1}{2}}^h + \frac{1}{2\,\mathrm{We}}|\nabla\rho_{n+\frac{1}{2}}^h|^2 + \frac{1}{\mathrm{We}}\rho_{n+\frac{1}{2}}^h \theta_{n+\frac{1}{2}}^h \nabla \cdot \left(\frac{\nabla\rho_{n+\frac{1}{2}}^h}{\theta_{n+\frac{1}{2}}^h}\right)\right.\right.$$

243

$$+ \rho^h_{n+\frac{1}{2}}|\mathbf{u}^h_{n+\frac{1}{2}}|^2\Big)\mathbf{u}^h_{n+\frac{1}{2}}\Big)_\Omega + \Big(\nabla w^h_5, \boldsymbol{\tau}^h_{n+\frac{1}{2}}\mathbf{u}^h_{n+\frac{1}{2}}\Big)_\Omega + \Big(\nabla w^h_5, \boldsymbol{\varsigma}^h_{n+\frac{1}{2}}\mathbf{u}^h_{n+\frac{1}{2}}\Big)_\Omega$$

$$- \Big(\nabla w^h_5, \mathbf{q}^h_{n+\frac{1}{2}}\Big)_\Omega - \Big(\nabla w^h_5, \boldsymbol{\Pi}^h_{n+\frac{1}{2}}\Big)_\Omega - \Big(w^h_5, \rho^h_{n+\frac{1}{2}}\mathbf{b}\cdot\mathbf{u}^h_{n+\frac{1}{2}}\Big)_\Omega$$

$$- \Big(w^h_5, \rho^h_{n+\frac{1}{2}}r\Big)_\Omega = 0, \tag{7.130}$$

$$\mathbf{B}^A(w^h_6; \mathbf{Y}^h_{n+1}) := \Big(w^h_6, V^h_{n+\frac{1}{2}}\Big)_\Omega - \Bigg(w^h_6, \frac{1}{\theta^h_{n+\frac{1}{2}}}\bigg(\frac{1}{2}\Big(\nu_{loc}(\rho^h_n, \theta^h_{n+\frac{1}{2}})$$

$$+ \nu_{loc}(\rho^h_{n+1}, \theta^h_{n+\frac{1}{2}})\Big) - \frac{[\![\rho^h_n]\!]^2}{12}\frac{\partial^2\nu_{loc}}{\partial\rho^2}(\rho^h_n, \theta^h_{n+\frac{1}{2}})\bigg)\Bigg)_\Omega + \Bigg(w^h_6, \frac{1}{\theta^h_{n+\frac{1}{2}}}\frac{\mathbf{u}^h_n\cdot\mathbf{u}^h_{n+1}}{2}\Bigg)_\Omega$$

$$- \Bigg(\nabla w^h_6, \frac{1}{\mathrm{We}\,\theta^h_{n+\frac{1}{2}}}\nabla\rho^h_{n+\frac{1}{2}}\Bigg)_\Omega = 0, \tag{7.131}$$

where

$$\mathbf{Y}^h_{n+\frac{1}{2}} := \frac{1}{2}\Big(\mathbf{Y}^h_n + \mathbf{Y}^h_{n+1}\Big), \tag{7.132}$$

$$\rho^h_{n+\frac{1}{2}} := \rho^h(\mathbf{Y}^h_{n+\frac{1}{2}}), \tag{7.133}$$

$$\mathbf{u}^h_{n+\frac{1}{2}} := \mathbf{u}^h(\mathbf{Y}^h_{n+\frac{1}{2}}), \tag{7.134}$$

$$\theta^h_{n+\frac{1}{2}} := \theta^h(\mathbf{Y}^h_{n+\frac{1}{2}}), \tag{7.135}$$

$$\boldsymbol{\tau}^h_{n+\frac{1}{2}} := \frac{1}{\mathrm{Re}}\Big(\nabla\mathbf{u}^h_{n+\frac{1}{2}} + \big(\nabla\mathbf{u}^h_{n+\frac{1}{2}}\big)^T - \frac{2}{3}\nabla\cdot\mathbf{u}^h_{n+\frac{1}{2}}\mathbf{I}\Big), \tag{7.136}$$

$$\boldsymbol{\varsigma}^h_{n+\frac{1}{2}} := \frac{1}{\mathrm{We}}\Big(\big(\rho^h_{n+\frac{1}{2}}\Delta\rho^h_{n+\frac{1}{2}} + \frac{1}{2}|\nabla\rho^h_{n+\frac{1}{2}}|^2\big)\mathbf{I} - \nabla\rho^h_{n+\frac{1}{2}}\otimes\nabla\rho^h_{n+\frac{1}{2}}\Big), \tag{7.137}$$

$$\mathbf{q}^h_{n+\frac{1}{2}} := -\boldsymbol{\kappa}\nabla\theta^h_{n+\frac{1}{2}}, \tag{7.138}$$

$$\boldsymbol{\Pi} := \frac{1}{\mathrm{We}}\rho^h_{n+\frac{1}{2}}\nabla\cdot\mathbf{u}^h_{n+\frac{1}{2}}\nabla\rho^h_{n+\frac{1}{2}}, \tag{7.139}$$

$$\mathfrak{H}^h_{n+\frac{1}{2}} := \frac{8}{27}\rho^h_{n+\frac{1}{2}}\Bigg(\log\Bigg(\frac{\rho^h_{n+\frac{1}{2}}}{1 - \rho^h_{n+\frac{1}{2}}}\Bigg) - \frac{1}{\gamma - 1}\log(\theta^h_{n+\frac{1}{2}})\Bigg). \tag{7.140}$$

7.7.2 Preliminary lemmas

Let me present and prove four lemmas in this section, which will be utilized in the proof of Theorems 7.7.1 and 7.7.2 in the succeeding section.

Lemma 7.7.1. *For the van der Waals fluid model, the mathematical entropy function $\mathfrak{H}(\rho, \theta)$ given by (7.56) satisfies*

$$\frac{\partial^3 \mathfrak{H}}{\partial \theta^3} < 0. \tag{7.141}$$

Proof.

$$\frac{\partial^3 \mathfrak{H}}{\partial \theta^3} = -\frac{16}{27(\gamma - 1)} \frac{\rho}{\theta^3}. \tag{7.142}$$

The dimensionless temperature θ is always positive and the heat capacity ratio γ is always greater than 1. Hence,

$$\frac{\partial^3 \mathfrak{H}}{\partial \theta^3} < 0. \tag{7.143}$$

$\square$

Lemma 7.7.2. *For the van der Waals fluid model, the local electrochemical potential $\nu_{loc}(\rho, \theta)$ given by (7.54) satisfies*

$$\frac{\partial^3 \nu_{loc}}{\partial \rho^3} > 0. \tag{7.144}$$

Proof.

$$\frac{\partial^3 \nu_{loc}}{\partial \rho^3} = \frac{16\theta}{27} \frac{6\rho^2 - 4\rho + 1}{\rho^3(1 - \rho)^4}. \tag{7.145}$$

245

Since $\theta > 0$ and $6\rho^2 - 4\rho + 1 \geq 1/3$,

$$\frac{\partial^3 \nu_{loc}}{\partial \rho^3} > 0. \tag{7.146}$$

$\square$

Lemma 7.7.3. *Replacing ρ_n^h, $\mathbf{u}_n^h$, and θ_n^h in the definition (7.122) with corresponding time continuous functions $\rho^h(t_n)$, $\mathbf{u}^h(t_n)$, and $\theta^h(t_n)$ and assuming sufficient smoothness in the time direction, one has*

$$\llbracket \rho^h(t_n) E(\rho^h(t_n), \mathbf{u}^h(t_n), \theta^h(t_n)) \rrbracket$$
$$= \Big(\rho^h(t_{n+1}) E(\rho^h(t_{n+1}), \mathbf{u}^h(t_{n+1}), \theta^h(t_{n+1})) - \rho^h(t_n) E(\rho^h(t_n), \mathbf{u}^h(t_n), \theta^h(t_n)) \Big)$$
$$+ \mathcal{O}(\Delta t^3). \tag{7.147}$$

Proof. Recalling the relations (7.123)-(7.127), only the nonclassical jump operators (7.124) and (7.125) need to be analyzed. Let me consider (7.124) first. Taylor expansions lead to

$$(\rho \Psi_{loc})(\rho^h(t_{n+1}), \theta^h(t_{n+1})) = (\rho \Psi_{loc})(\rho^h(t_{n+\frac{1}{2}}), \theta^h(t_{n+\frac{1}{2}}))$$
$$+ \frac{\partial(\rho \Psi_{loc})}{\partial \rho}(\rho^h(t_{n+\frac{1}{2}}), \theta^h(t_{n+\frac{1}{2}})) \left(\rho^h(t_{n+1}) - \rho^h(t_{n+\frac{1}{2}}) \right)$$
$$+ \frac{\partial(\rho \Psi_{loc})}{\partial \theta}(\rho^h(t_{n+\frac{1}{2}}), \theta^h(t_{n+\frac{1}{2}})) \left(\theta^h(t_{n+1}) - \theta^h(t_{n+\frac{1}{2}}) \right)$$
$$+ \frac{1}{2}\frac{\partial^2(\rho \Psi_{loc})}{\partial \rho^2}(\rho^h(t_{n+\frac{1}{2}}), \theta^h(t_{n+\frac{1}{2}})) \left(\rho^h(t_{n+1}) - \rho^h(t_{n+\frac{1}{2}}) \right)^2$$
$$+ \frac{1}{2}\frac{\partial^2(\rho \Psi_{loc})}{\partial \theta^2}(\rho^h(t_{n+\frac{1}{2}}), \theta^h(t_{n+\frac{1}{2}})) \left(\theta^h(t_{n+1}) - \theta^h(t_{n+\frac{1}{2}}) \right)^2$$
$$+ \frac{\partial^2(\rho \Psi_{loc})}{\partial \rho \partial \theta}(\rho^h(t_{n+\frac{1}{2}}), \theta^h(t_{n+\frac{1}{2}})) \left(\rho^h(t_{n+1}) - \rho^h(t_{n+\frac{1}{2}}) \right)$$
$$\left(\theta^h(t_{n+1}) - \theta^h(t_{n+\frac{1}{2}}) \right)$$

246

$$+ \mathcal{O}(\Delta t^3), \tag{7.148}$$

$$(\rho \Psi_{loc})(\rho^h(t_n), \theta^h(t_n)) = (\rho \Psi_{loc})(\rho^h(t_{n+\frac{1}{2}}), \theta^h(t_{n+\frac{1}{2}}))$$
$$+ \frac{\partial(\rho \Psi_{loc})}{\partial \rho}(\rho^h(t_{n+\frac{1}{2}}), \theta^h(t_{n+\frac{1}{2}})) \left(\rho^h(t_n) - \rho^h(t_{n+\frac{1}{2}}) \right)$$
$$+ \frac{\partial(\rho \Psi_{loc})}{\partial \theta}(\rho^h(t_{n+\frac{1}{2}}), \theta^h(t_{n+\frac{1}{2}})) \left(\theta^h(t_n) - \theta^h(t_{n+\frac{1}{2}}) \right)$$
$$+ \frac{1}{2} \frac{\partial^2(\rho \Psi_{loc})}{\partial \rho^2}(\rho^h(t_{n+\frac{1}{2}}), \theta^h(t_{n+\frac{1}{2}})) \left(\rho^h(t_n) - \rho^h(t_{n+\frac{1}{2}}) \right)^2$$
$$+ \frac{1}{2} \frac{\partial^2(\rho \Psi_{loc})}{\partial \theta^2}(\rho^h(t_{n+\frac{1}{2}}), \theta^h(t_{n+\frac{1}{2}})) \left(\theta^h(t_n) - \theta^h(t_{n+\frac{1}{2}}) \right)^2$$
$$+ \frac{\partial^2(\rho \Psi_{loc})}{\partial \rho \partial \theta}(\rho^h(t_{n+\frac{1}{2}}), \theta^h(t_{n+\frac{1}{2}})) \left(\rho^h(t_n) - \rho^h(t_{n+\frac{1}{2}}) \right)$$
$$\left(\theta^h(t_n) - \theta^h(t_{n+\frac{1}{2}}) \right)$$
$$+ \mathcal{O}(\Delta t^3), \tag{7.149}$$

$$(\rho \Psi_{loc})(\rho^h(t_{n+\frac{1}{2}}), \theta^h(t_{n+1})) = (\rho \Psi_{loc})(\rho^h(t_{n+\frac{1}{2}}), \theta^h(t_{n+\frac{1}{2}}))$$
$$+ \frac{\partial(\rho \Psi_{loc})}{\partial \theta}(\rho^h(t_{n+\frac{1}{2}}), \theta^h(t_{n+\frac{1}{2}})) \left(\theta^h(t_{n+1}) - \theta^h(t_{n+\frac{1}{2}}) \right)$$
$$+ \frac{1}{2} \frac{\partial^2(\rho \Psi_{loc})}{\partial \theta^2}(\rho^h(t_{n+\frac{1}{2}}), \theta^h(t_{n+\frac{1}{2}})) \left(\theta^h(t_{n+1}) - \theta^h(t_{n+\frac{1}{2}}) \right)^2$$
$$+ \mathcal{O}(\Delta t^3), \tag{7.150}$$

$$(\rho \Psi_{loc})(\rho^h(t_{n+\frac{1}{2}}), \theta^h(t_n)) = (\rho \Psi_{loc})(\rho^h(t_{n+\frac{1}{2}}), \theta^h(t_{n+\frac{1}{2}}))$$
$$+ \frac{\partial(\rho \Psi_{loc})}{\partial \theta}(\rho^h(t_{n+\frac{1}{2}}), \theta^h(t_{n+\frac{1}{2}})) \left(\theta^h(t_n) - \theta^h(t_{n+\frac{1}{2}}) \right)$$
$$+ \frac{1}{2} \frac{\partial^2(\rho \Psi_{loc})}{\partial \theta^2}(\rho^h(t_{n+\frac{1}{2}}), \theta^h(t_{n+\frac{1}{2}})) \left(\theta^h(t_n) - \theta^h(t_{n+\frac{1}{2}}) \right)^2$$
$$+ \mathcal{O}(\Delta t^3), \tag{7.151}$$

$$(\rho \Psi_{loc})(\rho^h(t_{n+1}), \theta^h(t_{n+\frac{1}{2}})) = (\rho \Psi_{loc})(\rho^h(t_{n+\frac{1}{2}}), \theta^h(t_{n+\frac{1}{2}}))$$
$$+ \frac{\partial(\rho \Psi_{loc})}{\partial \rho}(\rho^h(t_{n+\frac{1}{2}}), \theta^h(t_{n+\frac{1}{2}})) \left(\rho^h(t_{n+1}) - \rho^h(t_{n+\frac{1}{2}}) \right)$$

$$+ \frac{\partial^2(\rho\Psi_{loc})}{\partial\rho^2}(\rho^h(t_{n+\frac{1}{2}}), \theta^h(t_{n+\frac{1}{2}})) \left(\rho^h(t_{n+1}) - \rho^h(t_{n+\frac{1}{2}})\right)^2$$

$$+ \mathcal{O}(\Delta t^3), \tag{7.152}$$

$$(\rho\Psi_{loc})(\rho^h(t_n), \theta^h(t_{n+\frac{1}{2}})) = (\rho\Psi_{loc})(\rho^h(t_{n+\frac{1}{2}}), \theta^h(t_{n+\frac{1}{2}}))$$

$$+ \frac{\partial(\rho\Psi_{loc})}{\partial\rho}(\rho^h(t_{n+\frac{1}{2}}), \theta^h(t_{n+\frac{1}{2}})) \left(\rho^h(t_n) - \rho^h(t_{n+\frac{1}{2}})\right)$$

$$+ \frac{\partial^2(\rho\Psi_{loc})}{\partial\rho^2}(\rho^h(t_{n+\frac{1}{2}}), \theta^h(t_{n+\frac{1}{2}})) \left(\rho^h(t_n) - \rho^h(t_{n+\frac{1}{2}})\right)^2$$

$$+ \mathcal{O}(\Delta t^3). \tag{7.153}$$

Combining the above Taylor expansions, one has

$$\left((\rho\Psi_{loc})(\rho^h(t_{n+1}), \theta^h(t_{n+1})) - (\rho\Psi_{loc})(\rho^h(t_n), \theta^h(t_n))\right)$$

$$- \left((\rho\Psi_{loc})(\rho^h(t_{n+\frac{1}{2}}), \theta^h(t_{n+1})) - (\rho\Psi_{loc})(\rho^h(t_{n+\frac{1}{2}}), \theta^h(t_n))\right.$$

$$\left.+ (\rho\Psi_{loc})(\rho^h(t_{n+1}), \theta^h(t_{n+\frac{1}{2}})) - (\rho\Psi_{loc})(\rho^h(t_n), \theta^h(t_{n+\frac{1}{2}}))\right)$$

$$= \mathcal{O}(\Delta t^3). \tag{7.154}$$

Next, let me analyze the term (7.125).

$$\left(\theta^h(t_{n+1})\mathfrak{H}(\rho^h(t_{n+1}), \theta^h(t_{n+1})) - \theta^h(t_n)\mathfrak{H}(\rho^h(t_n), \theta^h(t_n))\right)$$

$$- \left(\theta^h(t_{n+\frac{1}{2}})\left(\mathfrak{H}(\rho^h(t_{n+1}), \theta^h(t_{n+1})) - \mathfrak{H}(\rho^h(t_n), \theta^h(t_n))\right)\right.$$

$$\left.+ \frac{\theta^h(t_{n+1}) - \theta^h(t_n)}{2}\left(\mathfrak{H}(\rho^h(t_{n+\frac{1}{2}}), \theta^h(t_{n+1})) + \mathfrak{H}(\rho^h(t_{n+\frac{1}{2}}), \theta^h(t_n))\right)\right)$$

$$= \frac{\theta^h(t_{n+1}) - \theta^h(t_n)}{2}\left(\mathfrak{H}(\rho^h(t_{n+1}), \theta^h(t_{n+1})) + \mathfrak{H}(\rho^h(t_n), \theta^h(t_n))\right.$$

$$\left.- \mathfrak{H}(\rho^h(t_{n+\frac{1}{2}}), \theta^h(t_{n+1})) - \mathfrak{H}(\rho^h(t_{n+\frac{1}{2}}), \theta^h(t_n))\right) + \mathcal{O}(\Delta t^3)$$

$$= \frac{(\theta^h(t_{n+1}) - \theta^h(t_n))}{2}\left(\frac{\partial\mathfrak{H}}{\partial\rho}(\rho^h(t_{n+\frac{1}{2}}), \theta^h(t_{n+1})) \left(\rho^h(t_{n+1}) - \rho^h(t_{n+\frac{1}{2}})\right)\right.$$

$$- \frac{\partial \mathfrak{H}}{\partial \rho}(\rho^h(t_{n+\frac{1}{2}}), \theta^h(t_n)) \left(\rho^h(t_n) - \rho^h(t_{n+\frac{1}{2}}) \right) \Bigg) + \mathcal{O}(\Delta t^3)$$

$$= \mathcal{O}(\Delta t^3). \tag{7.155}$$

According to (7.148) and (7.155), it can be concluded that

$$\llbracket \rho^h(t_n) E(\rho^h(t_n), \mathbf{u}^h(t_n), \theta^h(t_n)) \rrbracket$$

$$- \left(\rho^h(t_{n+1}) E(\rho^h(t_{n+1}), \mathbf{u}^h(t_{n+1}), \theta^h(t_{n+1})) \right.$$

$$\left. - \rho^h(t_n) E(\rho^h(t_n), \mathbf{u}^h(t_n), \theta^h(t_n)) \right)$$

$$= \mathcal{O}(\Delta t^3) + \frac{(\theta^h(t_{n+1}) - \theta^h(t_n))^3}{12} \frac{\partial^2 \mathfrak{H}}{\partial \theta^2}(\rho^h(t_{n+\frac{1}{2}}), \theta^h(t_{n+1}))$$

$$= \mathcal{O}(\Delta t^3). \tag{7.156}$$

This completes the proof of the lemma. $\qquad\square$

Lemma 7.7.4. *Given* $\llbracket \rho_n^h \rrbracket$, $\llbracket \rho_n^h \mathbf{u}_n^h \rrbracket$, *and* $\llbracket \rho_n^h E(\rho_n^h, \mathbf{u}_n^h, \theta_n^h) \rrbracket$ *defined in* (7.120)-(7.122), *the following equality holds for some* $\xi_1, \xi_2 \in (0, 1)$.

$$\left(\frac{\llbracket \rho_n^h \rrbracket}{\Delta t_n}, \frac{1}{\theta_{n+\frac{1}{2}}^h} \left(\frac{1}{2} \left(\nu_{loc}(\rho_n^h, \theta_{n+\frac{1}{2}}^h) + \nu_{loc}(\rho_{n+1}^h, \theta_{n+\frac{1}{2}}^h) \right) - \frac{\llbracket \rho_n^h \rrbracket^2}{12} \frac{\partial^2 \nu_{loc}}{\partial \rho^2}(\rho_n^h, \theta_{n+\frac{1}{2}}^h) \right) \right)_\Omega$$

$$- \left(\frac{\llbracket \rho_n^h \rrbracket}{\Delta t_n}, \frac{\mathbf{u}_{n+1}^h \cdot \mathbf{u}_n^h}{2\theta_{n+\frac{1}{2}}^h} \right)_\Omega + \left(\nabla \frac{\llbracket \rho_n^h \rrbracket}{\Delta t_n}, \frac{1}{\mathrm{We}\, \theta_{n+\frac{1}{2}}^h} \nabla \rho_{n+\frac{1}{2}}^h \right)_\Omega + \left(\frac{\mathbf{u}_{n+\frac{1}{2}}^h}{\theta_{n+\frac{1}{2}}^h}, \frac{\llbracket \rho_n^h \mathbf{u}_n^h \rrbracket}{\Delta t_n} \right)_\Omega$$

$$- \left(\frac{1}{\theta_{n+\frac{1}{2}}^h}, \frac{\llbracket \rho_n^h E(\rho_n^h, \mathbf{u}_n^h, \theta_n^h) \rrbracket}{\Delta t_n} \right)_\Omega$$

$$= \int_\Omega \frac{\mathfrak{H}(\rho_{n+1}^h, \theta_{n+1}^h) - \mathfrak{H}(\rho_n^h, \theta_n^h)}{\Delta t_n} d\mathbf{x} + \left(\frac{1}{\theta_{n+\frac{1}{2}}^h \Delta t_n}, \frac{\llbracket \rho_n^h \rrbracket^4}{24} \frac{\partial^3 \nu_{loc}}{\partial \rho^{h3}}(\rho_{n+\xi_1}^h, \theta_{n+\frac{1}{2}}^h) \right)_\Omega$$

$$- \left(\frac{1}{\theta_{n+\frac{1}{2}}^h \Delta t_n}, \frac{\llbracket \theta_n^h \rrbracket^4}{24} \frac{\partial^3 \mathfrak{H}_{loc}}{\partial \theta^{h3}}(\rho_{n+\frac{1}{2}}^h, \theta_{n+\xi_2}^h) \right)_\Omega. \tag{7.157}$$

Proof. Straightforward calculations show that

$$\left(\nabla\frac{[\![\rho_n^h]\!]}{\Delta t_n}, \frac{1}{\mathrm{We}\,\theta_{n+\frac{1}{2}}^h}\nabla\rho_{n+\frac{1}{2}}^h\right)_\Omega = \int_\Omega \frac{|\nabla\rho_{n+1}^h|^2 - |\nabla\rho_n^h|^2}{2\,\mathrm{We}\,\theta_{n+\frac{1}{2}}^h\,\Delta t_n}d\mathbf{x}, \qquad (7.158)$$

and

$$\left(\mathbf{u}_{n+\frac{1}{2}}^h, [\![\rho_n^h\mathbf{u}_n^h]\!]\right)_\Omega - \left([\![\rho_n^h]\!], \frac{1}{2}\mathbf{u}_{n+1}^h\cdot\mathbf{u}_n^h\right)_\Omega$$
$$= \int_\Omega \frac{1}{2}\left(\rho_{n+1}^h|\mathbf{u}_{n+1}^h|^2 - \rho_n^h|\mathbf{u}_n^h|^2\right)d\mathbf{x}. \qquad (7.159)$$

Making use of the above two relations, one can get

$$\left(\frac{[\![\rho_n^h]\!]}{\Delta t_n}, \frac{1}{\theta_{n+\frac{1}{2}}^h}\left(\frac{1}{2}\left(\nu_{loc}(\rho_n^h,\theta_{n+\frac{1}{2}}^h) + \nu_{loc}(\rho_{n+1}^h,\theta_{n+\frac{1}{2}}^h)\right) - \frac{[\![\rho_n^h]\!]^2}{12}\frac{\partial^2\nu_{loc}}{\partial\rho^{h2}}(\rho_n^h,\theta_{n+\frac{1}{2}}^h)\right)\right)_\Omega$$
$$- \left(\frac{[\![\rho_n^h]\!]}{\Delta t_n}, \frac{\mathbf{u}_{n+1}^h\cdot\mathbf{u}_n^h}{2\theta_{n+\frac{1}{2}}^h}\right)_\Omega + \left(\nabla\frac{[\![\rho_n^h]\!]}{\Delta t_n}, \frac{1}{\mathrm{We}\,\theta_{n+\frac{1}{2}}^h}\nabla\rho_{n+\frac{1}{2}}^h\right)_\Omega + \left(\frac{\mathbf{u}_{n+\frac{1}{2}}^h}{\theta_{n+\frac{1}{2}}^h}, \frac{[\![\rho_n^h\mathbf{u}_n^h]\!]}{\Delta t_n}\right)_\Omega$$
$$- \left(\frac{1}{\theta_{n+\frac{1}{2}}^h}, \frac{[\![\rho_n^h E(\rho_n^h,\mathbf{u}_n^h,\theta_n^h)]\!]}{\Delta t_n}\right)_\Omega$$
$$= \left(\frac{[\![\rho_n^h]\!]}{\Delta t_n}, \frac{1}{\theta_{n+\frac{1}{2}}^h}\left(\frac{1}{2}\left(\nu_{loc}(\rho_n^h,\theta_{n+\frac{1}{2}}^h) + \nu_{loc}(\rho_{n+1}^h,\theta_{n+\frac{1}{2}}^h)\right) - \frac{[\![\rho_n^h]\!]^2}{12}\frac{\partial^2\nu_{loc}}{\partial\rho^2}(\rho_n^h,\theta_{n+\frac{1}{2}}^h)\right)\right)_\Omega$$
$$- \left(\frac{1}{\theta_{n+\frac{1}{2}}^h\Delta t_n}, (\rho\Psi_{loc})(\rho_{n+\frac{1}{2}}^h,\theta_{n+1}^h) - (\rho\Psi_{loc})(\rho_{n+\frac{1}{2}}^h,\theta_n^h) + (\rho\Psi_{loc})(\rho_{n+1}^h,\theta_{n+\frac{1}{2}}^h)\right.$$
$$- (\rho\Psi_{loc})(\rho_n^h,\theta_{n+\frac{1}{2}}^h) - \theta_{n+\frac{1}{2}}^h\left(\mathfrak{H}(\rho_{n+1}^h,\theta_{n+1}^h) - \mathfrak{H}(\rho_n^h,\theta_n^h)\right)$$
$$\left.- \frac{[\![\theta_n^h]\!]}{2}\left(\mathfrak{H}(\rho_{n+\frac{1}{2}}^h,\theta_{n+1}^h) + \mathfrak{H}(\rho_{n+\frac{1}{2}}^h,\theta_n^h)\right) + \frac{[\![\theta_n^h]\!]^3}{12}\frac{\partial^2\mathfrak{H}}{\partial\theta^2}(\rho_{n+\frac{1}{2}}^h,\theta_{n+1}^h)\right)_\Omega. \qquad (7.160)$$

Applying the perturbed trapezoidal rule (6.82) to

$$\nu_{loc} = \frac{\partial(\rho\Psi_{loc})}{\partial\rho} \qquad (7.161)$$

gives

$$\int_{\rho_n^h}^{\rho_{n+1}^h} \frac{\partial(\rho\Psi_{loc})}{\partial\rho} d\rho = (\rho\Psi_{loc})(\rho_{n+1}^h, \theta_{n+\frac{1}{2}}^h) - (\rho\Psi_{loc})(\rho_n^h, \theta_{n+\frac{1}{2}}^h)$$

$$= \frac{[\![\rho_n^h]\!]}{2}\left(\nu_{loc}(\rho_n^h, \theta_{n+\frac{1}{2}}^h) + \nu_{loc}(\rho_{n+1}^h, \theta_{n+\frac{1}{2}}^h)\right) - \frac{[\![\rho_n^h]\!]^3}{12}\frac{\partial^2\nu_{loc}}{\partial\rho^2}(\rho_n^h, \theta_{n+\frac{1}{2}}^h)$$

$$- \frac{[\![\rho_n^h]\!]^4}{24}\frac{\partial^3\nu_{loc}}{\partial\rho^{h3}}(\rho_{n+\xi_1}^h, \theta_{n+\frac{1}{2}}^h), \tag{7.162}$$

for $\xi_1 \in (0,1)$. Consequently, (7.160) can be simplified using the above relation as

$$\left(\frac{[\![\rho_n^h]\!]}{\Delta t_n}, \frac{1}{\theta_{n+\frac{1}{2}}^h}\left(\frac{1}{2}\left(\nu_{loc}(\rho_n^h, \theta_{n+\frac{1}{2}}^h) + \nu_{loc}(\rho_{n+1}^h, \theta_{n+\frac{1}{2}}^h)\right) - \frac{[\![\rho_n^h]\!]^2}{12}\frac{\partial^2\nu_{loc}}{\partial\rho^2}(\rho_n^h, \theta_{n+\frac{1}{2}}^h)\right)\right)_\Omega$$

$$+ \left(\frac{[\![\rho_n^h]\!]}{\Delta t_n}, \frac{\mathbf{u}_{n+1}^h \cdot \mathbf{u}_n^h}{2\theta_{n+\frac{1}{2}}^h}\right)_\Omega + \left(\nabla\frac{[\![\rho_n^h]\!]}{\Delta t_n}, \frac{1}{\text{We}\,\theta}\nabla\rho_{n+\frac{1}{2}}^h\right)_\Omega + \left(\frac{\mathbf{u}_{n+\frac{1}{2}}^h}{\theta_{n+\frac{1}{2}}^h}, \frac{[\![\rho_n^h\mathbf{u}_n^h]\!]}{\Delta t_n}\right)_\Omega$$

$$- \left(\frac{1}{\theta_{n+\frac{1}{2}}^h}, \frac{[\![\rho_n^h E(\rho_n^h, \mathbf{u}_n^h, \theta_n^h)]\!]}{\Delta t_n}\right)_\Omega$$

$$= \left(\frac{1}{\Delta t_n}, \frac{[\![\rho_n^h]\!]^4}{24}\frac{\partial^3\nu_{loc}}{\partial\rho^3}(\rho_{n+\xi_1}^h, \theta_{n+\frac{1}{2}}^h)\right)_\Omega - \left(\frac{1}{\theta_{n+\frac{1}{2}}^h\Delta t_n}, (\rho\Psi_{loc})(\rho_{n+\frac{1}{2}}^h, \theta_{n+1}^h)\right.$$

$$- (\rho\Psi_{loc})(\rho_{n+\frac{1}{2}}^h, \theta_n^h) - \theta_{n+\frac{1}{2}}^h\left(\mathfrak{H}(\rho_{n+1}^h, \theta_{n+1}^h) - \mathfrak{H}(\rho_n^h, \theta_n^h)\right)$$

$$\left. - \frac{[\![\theta_n^h]\!]}{2}\left(\mathfrak{H}(\rho_{n+\frac{1}{2}}^h, \theta_{n+1}^h) + \mathfrak{H}(\rho_{n+\frac{1}{2}}^h, \theta_n^h)\right) + \frac{[\![\theta_n^h]\!]^3}{12}\frac{\partial^2\mathfrak{H}}{\partial\theta^2}(\rho_{n+\frac{1}{2}}^h, \theta_{n+1}^h)\right)_\Omega.$$

$$\tag{7.163}$$

Again, applying the perturbed trapezoidal rule (6.83) to

$$\mathfrak{H} = \frac{\partial(\rho\Psi_{loc})}{\partial\theta} \tag{7.164}$$

results in

$$\int_{\theta_n^h}^{\theta_{n+1}^h} \frac{\partial(\rho\Psi_{loc})}{\partial\theta} d\theta = (\rho\Psi_{loc})(\rho_{n+\frac{1}{2}}^h, \theta_{n+1}^h) - (\rho\Psi_{loc})(\rho_{n+\frac{1}{2}}^h, \theta_n^h)$$

251

$$= \frac{[\![\theta_n^h]\!]}{2} \left(\mathfrak{H}(\rho_{n+\frac{1}{2}}^h, \theta_{n+1}^h) + \mathfrak{H}(\rho_{n+\frac{1}{2}}^h, \theta_n^h) \right) - \frac{[\![\theta_n^h]\!]^3}{12} \frac{\partial^2 \mathfrak{H}}{\partial \theta^2}(\rho_{n+\frac{1}{2}}^h, \theta_{n+1}^h)$$
$$+ \frac{[\![\theta_n^h]\!]^4}{24} \frac{\partial^3 \mathfrak{H}}{\partial \theta^3}(\rho_{n+\frac{1}{2}}^h, \theta_{n+\xi_2}^h). \tag{7.165}$$

Using the above relation, relation (7.163) can be rewritten as

$$\left(\frac{[\![\rho_n^h]\!]}{\Delta t_n}, \frac{1}{\theta_{n+\frac{1}{2}}^h} \left(\frac{1}{2} \left(\nu_{loc}(\rho_n^h, \theta_{n+\frac{1}{2}}^h) + \nu_{loc}(\rho_{n+1}^h, \theta_{n+\frac{1}{2}}^h) \right) - \frac{[\![\rho_n^h]\!]^2}{12} \frac{\partial^2 \nu_{loc}}{\partial \rho^2}(\rho_n^h, \theta_{n+\frac{1}{2}}^h) \right) \right)_\Omega$$
$$+ \left(\frac{[\![\rho_n^h]\!]}{\Delta t_n}, \frac{\mathbf{u}_{n+1}^h \cdot \mathbf{u}_n^h}{2\theta_{n+\frac{1}{2}}^h} \right)_\Omega + \left(\nabla \frac{[\![\rho_n^h]\!]}{\Delta t_n}, \frac{1}{\mathrm{We}\, \theta_{n+\frac{1}{2}}^h} \nabla \rho_{n+\frac{1}{2}}^h \right)_\Omega + \left(\frac{\mathbf{u}_{n+\frac{1}{2}}^h}{\theta_{n+\frac{1}{2}}^h}, \frac{[\![\rho_n^h \mathbf{u}_n^h]\!]}{\Delta t_n} \right)_\Omega$$
$$- \left(\frac{1}{\theta_{n+\frac{1}{2}}^h}, \frac{[\![\rho_n^h E(\rho_n^h, \mathbf{u}_n^h, \theta_n^h)]\!]}{\Delta t_n} \right)_\Omega$$
$$= \left(\frac{1}{\Delta t_n}, \frac{[\![\rho_n^h]\!]^4}{24} \frac{\partial^3 \nu_{loc}}{\partial \rho^3}(\rho_{n+\xi_1}^h, \theta_{n+\frac{1}{2}}^h) \right)_\Omega + \left(\frac{1}{\Delta t_n}, \left(\mathfrak{H}(\rho_{n+1}^h, \theta_{n+1}^h) - \mathfrak{H}(\rho_n^h, \theta_n^h) \right) \right)_\Omega$$
$$- \left(\frac{1}{\theta_{n+\frac{1}{2}}^h \Delta t_n}, \frac{[\![\theta_n^h]\!]^4}{24} \frac{\partial^3 \mathfrak{H}}{\partial \theta^3}(\rho_{n+\frac{1}{2}}^h, \theta_{n+\xi_2}^h) \right)_\Omega$$
$$= \int_\Omega \frac{\mathfrak{H}(\rho_{n+1}^h, \theta_{n+1}^h) - \mathfrak{H}(\rho_n^h, \theta_n^h)}{\Delta t_n} d\mathbf{x} + \left(\frac{1}{\theta_{n+\frac{1}{2}}^h \Delta t_n}, \frac{[\![\rho_n^h]\!]^4}{24} \frac{\partial^3 \nu_{loc}}{\partial \rho^3}(\rho_{n+\xi_1}^h, \theta_{n+\frac{1}{2}}^h) \right)_\Omega$$
$$- \left(\frac{1}{\theta_{n+\frac{1}{2}}^h \Delta t_n}, \frac{[\![\theta_n^h]\!]^4}{24} \frac{\partial^3 \mathfrak{H}}{\partial \theta^3}(\rho_{n+\frac{1}{2}}^h, \theta_{n+\xi_2}^h) \right)_\Omega. \tag{7.166}$$

$\square$

Remark 7.7.2. *According to the Lemma 7.7.1 and 7.7.2, the last two terms in (7.157) satisfy*

$$\left(\frac{1}{\theta_{n+\frac{1}{2}}^h \Delta t_n}, \frac{[\![\rho_n^h]\!]^4}{24} \frac{\partial^3 \nu_{loc}}{\partial \rho^3}(\rho_{n+\xi_1}^h, \theta_{n+\frac{1}{2}}^h) \right)_\Omega \geq 0, \tag{7.167}$$

$$\left(\frac{1}{\theta_{n+\frac{1}{2}}^h \Delta t_n}, \frac{[\![\theta_n^h]\!]^4}{24} \frac{\partial^3 \mathfrak{H}}{\partial \theta^3}(\rho_{n+\frac{1}{2}}^h, \theta_{n+\xi_2}^h) \right)_\Omega \leq 0. \tag{7.168}$$

They represent the dissipation introduced by the numerical approximation of the time derivatives.

Remark 7.7.3. *In the proof of Lemma 7.7.4, it can be seen that the discrete approximation of $\partial(\rho E)/\partial t$ is based on the perturbed trapezoidal rules (6.82) and (6.83). One may construct a different scheme by using the perturbed midpoint rules. The resulting numerical dissipation will be slightly different.*

7.7.3 Numerical dissipation and time accuracy

Now, it is ready to state the main results of the fully discrete scheme (7.128)-(7.131).

Theorem 7.7.1. *The solutions of the fully discrete scheme (7.128)-(7.131) satisfy*

$$
\int_\Omega \left(\frac{\mathfrak{H}(\rho_{n+1}^h, \theta_{n+1}^h) - \mathfrak{H}(\rho_n^h, \theta_n^h)}{\Delta t_n} + \nabla \cdot \left(\mathfrak{H}(\rho_{n+\frac{1}{2}}^h, \theta_{n+\frac{1}{2}}^h) \mathbf{u}_{n+\frac{1}{2}}^h \right) - \nabla \cdot \left(\frac{\mathbf{q}_{n+\frac{1}{2}}^h}{\theta_{n+\frac{1}{2}}^h} \right) \right.
$$
$$
\left. + \frac{\rho_{n+\frac{1}{2}}^h r}{\theta_{n+\frac{1}{2}}^h} \right) d\mathbf{x}
$$
$$
= -\int_\Omega \frac{1}{\theta_{n+\frac{1}{2}}^h} \boldsymbol{\tau}_{n+\frac{1}{2}}^h : \nabla \mathbf{u}_{n+\frac{1}{2}}^h d\mathbf{x} - \int_\Omega \frac{\nabla\theta_{n+\frac{1}{2}}^h \cdot \boldsymbol{\kappa} \nabla\theta_{n+\frac{1}{2}}^h}{\left(\theta_{n+\frac{1}{2}}^h\right)^2} d\mathbf{x}
$$
$$
- \int_\Omega \frac{1}{\theta_{n+\frac{1}{2}}^h \Delta t_n} \frac{[\![\rho_n^h]\!]^4}{24} \frac{\partial^3 \nu_{loc}}{\partial \rho^3} (\rho_{n+\xi_1}^h, \theta_{n+\frac{1}{2}}^h) d\mathbf{x}
$$
$$
+ \int_\Omega \frac{1}{\theta_{n+\frac{1}{2}}^h \Delta t_n} \frac{[\![\theta_n^h]\!]^4}{24} \frac{\partial^3 \mathfrak{H}}{\partial \theta^3} (\rho_{n+\frac{1}{2}}^h, \theta_{n+\xi_2}^h) d\mathbf{x}
$$
$$
\leq 0. \tag{7.169}
$$

253

Proof. Taking $w_1^h = V_{n+\frac{1}{2}}^h$ in (7.128), $\mathbf{w}^h = \mathbf{u}_{n+\frac{1}{2}}^h/\theta_{n+\frac{1}{2}}^h$ in (7.129), $w_5^h = -1/\theta_{n+\frac{1}{2}}^h$ in (7.130), $w_6^h = [\![\rho_n^h]\!]/\Delta t_n$ in (7.131) and following the proof of Theorem 7.5.1, it can be shown that

$$
\mathbf{B}^M(V_{n+\frac{1}{2}}^h; \mathbf{Y}_{n+1}^h) + \mathbf{B}^U\Big(\frac{\mathbf{u}_{n+\frac{1}{2}}^h}{\theta_{n+\frac{1}{2}}^h}; \mathbf{Y}_{n+1}^h\Big) + \mathbf{B}^E\Big(-\frac{1}{\theta_{n+\frac{1}{2}}}; \mathbf{Y}_{n+1}^h\Big) - \mathbf{B}^A\Big(\frac{[\![\rho_n^h]\!]}{\Delta t_n}; \mathbf{Y}_{n+1}^h\Big)
$$

$$
= \left(\frac{[\![\rho_n^h]\!]}{\Delta t_n}, \frac{1}{\theta_{n+\frac{1}{2}}^h}\left(\frac{1}{2}\Big(\nu_{loc}(\rho_n^h, \theta_{n+\frac{1}{2}}^h) + \nu_{loc}(\rho_{n+1}^h, \theta_{n+\frac{1}{2}}^h)\Big) - \frac{[\![\rho_n^h]\!]^2}{12}\frac{\partial^2\nu_{loc}}{\partial\rho^2}(\rho_n^h, \theta_{n+\frac{1}{2}}^h)\right)\right)_\Omega
$$

$$
- \left(\frac{[\![\rho_n^h]\!]}{\Delta t_n}, \frac{\mathbf{u}_{n+1}^h \cdot \mathbf{u}_n^h}{2\theta_{n+\frac{1}{2}}^h}\right)_\Omega + \left(\nabla\frac{[\![\rho_n^h]\!]}{\Delta t_n}, \frac{1}{\mathrm{We}\,\theta_{n+\frac{1}{2}}^h}\nabla\rho_{n+\frac{1}{2}}^h\right)_\Omega + \left(\frac{\mathbf{u}_{n+\frac{1}{2}}^h}{\theta_{n+\frac{1}{2}}^h}, \frac{[\![\rho_n^h\mathbf{u}_n^h]\!]}{\Delta t_n}\right)_\Omega
$$

$$
- \left(\frac{1}{\theta_{n+\frac{1}{2}}^h}, \frac{[\![\rho_n^h E(\rho_n^h, \mathbf{u}_n^h, \theta_n^h)]\!]}{\Delta t_n}\right)_\Omega + \int_\Omega \nabla\cdot\Big(\mathfrak{H}(\rho_{n+\frac{1}{2}}^h, \theta_{n+\frac{1}{2}}^h)\mathbf{u}_{n+\frac{1}{2}}^h\Big)\,d\mathbf{x}
$$

$$
+ \int_\Omega \nabla\cdot\left(\frac{\mathbf{q}_{n+\frac{1}{2}}^h}{\theta_{n+\frac{1}{2}}^h}\right) - \frac{\rho_{n+\frac{1}{2}}^h r}{\theta_{n+\frac{1}{2}}}\,d\mathbf{x}
$$

$$
+ \int_\Omega \frac{1}{\theta_{n+\frac{1}{2}}^h}\boldsymbol{\tau}_{n+\frac{1}{2}}^h : \nabla\mathbf{u}_{n+\frac{1}{2}}^h\,d\mathbf{x} + \int_\Omega \frac{\nabla\theta_{n+\frac{1}{2}}^h \cdot \boldsymbol{\kappa}\nabla\theta_{n+\frac{1}{2}}^h}{\Big(\theta_{n+\frac{1}{2}}^h\Big)^2}\,d\mathbf{x} = 0. \tag{7.170}
$$

According to Lemma 7.7.4, the above can be rewritten as

$$
\int_\Omega \left(\frac{\mathfrak{H}(\rho_{n+1}^h, \theta_{n+1}^h) - \mathfrak{H}(\rho_n^h, \theta_n^h)}{\Delta t_n} + \nabla\cdot\Big(\mathfrak{H}(\rho_{n+\frac{1}{2}}^h, \theta_{n+\frac{1}{2}}^h)\mathbf{u}_{n+\frac{1}{2}}^h\Big) - \nabla\cdot\left(\frac{\mathbf{q}_{n+\frac{1}{2}}^h}{\theta_{n+\frac{1}{2}}^h}\right)\right.
$$

$$
\left. + \frac{\rho_{n+\frac{1}{2}}^h r}{\theta_{n+\frac{1}{2}}^h}\right)d\mathbf{x}
$$

$$
= -\int_\Omega \frac{1}{\theta_{n+\frac{1}{2}}^h}\boldsymbol{\tau}_{n+\frac{1}{2}}^h : \nabla\mathbf{u}_{n+\frac{1}{2}}^h\,d\mathbf{x} - \int_\Omega \frac{\nabla\theta_{n+\frac{1}{2}}^h \cdot \boldsymbol{\kappa}\nabla\theta_{n+\frac{1}{2}}^h}{\Big(\theta_{n+\frac{1}{2}}^h\Big)^2}\,d\mathbf{x}
$$

$$
- \int_\Omega \frac{1}{\theta_{n+\frac{1}{2}}^h\Delta t_n}\frac{[\![\rho_n^h]\!]^4}{24}\frac{\partial^3\nu_{loc}}{\partial\rho^3}(\rho_{n+\xi_1}^h, \theta_{n+\frac{1}{2}}^h)d\mathbf{x}
$$

$$+ \int_\Omega \frac{1}{\theta^h_{n+\frac{1}{2}}\Delta t_n} \frac{[\![\theta^h_n]\!]^4}{24} \frac{\partial^3 \mathfrak{H}}{\partial \theta^3}(\rho^h_{n+\frac{1}{2}}, \theta^h_{n+\xi_2})d\mathbf{x}$$

$$\leq 0. \tag{7.171}$$

The last inequality is due to Lemmas 7.7.1 and 7.7.2. $\qquad\square$

Theorem 7.7.2. *The local truncation error in time $\tau(t)$ can be bounded by $|\tau(t)| \leq K\Delta t_n^2$ for all $t_n \in [0, T]$, where K is a constant independent of Δt_n.*

Proof. Consider the mid-point rule applied to the semi-discrete formulation (7.110)-(7.113):

$$\mathbf{B}^M_{mid}(w^h_1; \mathbf{Y}^h) := \left(w^h_1, \frac{[\![\rho^h_n]\!]}{\Delta t_n} \right)_\Omega - \left(\nabla w^h_1, \rho^h_{n+\frac{1}{2}} \mathbf{u}^h_{n+\frac{1}{2}} \right)_\Omega = 0, \tag{7.172}$$

$$\mathbf{B}^U_{mid}(\mathbf{w}^h; \mathbf{Y}^h) := \left(\mathbf{w}^h, \frac{[\![\rho^h_n \mathbf{u}^h_n]\!]}{\Delta t_n} \right)_\Omega - \left(\nabla \mathbf{w}^h, \rho^h_{n+\frac{1}{2}} \mathbf{u}^h_{n+\frac{1}{2}} \otimes \mathbf{u}^h_{n+\frac{1}{2}} \right)_\Omega$$

$$- \left(\nabla \cdot \mathbf{w}^h, \rho^h_{n+\frac{1}{2}} V^h_{mid}\theta^h_{n+\frac{1}{2}} + \frac{1}{2}\rho^h_{n+\frac{1}{2}}|\mathbf{u}^h_{n+\frac{1}{2}}|^2 + \frac{1}{\text{We}}\rho^h_{n+\frac{1}{2}}\theta^h_{n+\frac{1}{2}}\nabla \cdot \left(\frac{\nabla\rho^h_{n+\frac{1}{2}}}{\theta^h_{n+\frac{1}{2}}} \right) \right)_\Omega$$

$$- \left(\mathbf{w}^h, \left(V^h_{mid}\theta^h_{n+\frac{1}{2}} + \frac{|\mathbf{u}^h_{n+\frac{1}{2}}|^2}{2} + \frac{1}{\text{We}}\theta^h_{n+\frac{1}{2}}\nabla \cdot \left(\frac{\nabla\rho^h_{n+\frac{1}{2}}}{\theta^h_{n+\frac{1}{2}}} \right) \right) \nabla\rho^h_{n+\frac{1}{2}} \right)_\Omega$$

$$- \left(\mathbf{w}^h, \mathfrak{H}^h_{n+\frac{1}{2}}\nabla\theta^h_{n+\frac{1}{2}} \right)_\Omega + \left(\nabla\mathbf{w}^h, \boldsymbol{\tau}^h_{n+\frac{1}{2}} \right)_\Omega + \left(\nabla\mathbf{w}^h_{n+\frac{1}{2}}, \boldsymbol{\varsigma}^h_{n+\frac{1}{2}} \right)_\Omega$$

$$- \left(\mathbf{w}^h, \rho^h_{n+\frac{1}{2}}\mathbf{b} \right)_\Omega = \mathbf{0}, \tag{7.173}$$

$$\mathbf{B}^E_{mid}(w^h_5; \mathbf{Y}^h) := \left(w^h_5, \frac{\rho^h_{n+1}E(\rho^h_{n+1}, \mathbf{u}^h_{n+1}, \theta^h_{n+1}) - \rho^h_n E(\rho^h_n, \mathbf{u}^h_n, \theta^h_n)}{\Delta t_n} \right)_\Omega$$

$$- \left(\nabla w^h_5, \left(\rho^h V^h_{mid}\theta^h_{n+\frac{1}{2}} - \theta^h_{n+\frac{1}{2}}\mathfrak{H}^h_{n+\frac{1}{2}} + \frac{1}{2\,\text{We}}|\nabla\rho^h_{n+\frac{1}{2}}|^2 + \rho^h|\mathbf{u}^h_{n+\frac{1}{2}}|^2 \right. \right.$$

$$\left. \left. + \frac{1}{\text{We}}\rho^h_{n+\frac{1}{2}}\theta^h_{n+\frac{1}{2}}\nabla \cdot \left(\frac{\nabla\rho^h_{n+\frac{1}{2}}}{\theta^h_{n+\frac{1}{2}}} \right) \right) \mathbf{u}^h_{n+\frac{1}{2}} \right)_\Omega + \left(\nabla w^h_5, \boldsymbol{\tau}^h_{n+\frac{1}{2}}\mathbf{u}^h_{n+\frac{1}{2}} \right)_\Omega$$

$$+ \left(\nabla w_5^h, \varsigma_{n+\frac{1}{2}}^h \mathbf{u}_{n+\frac{1}{2}}^h \right)_\Omega - \left(\nabla w_5^h, \mathbf{q}_{n+\frac{1}{2}}^h \right)_\Omega - \left(\nabla w_5^h, \mathbf{\Pi}_{n+\frac{1}{2}}^h \right)_\Omega$$
$$- \left(w_5^h, \rho_{n+\frac{1}{2}}^h \mathbf{b} \cdot \mathbf{u}_{n+\frac{1}{2}}^h \right)_\Omega - \left(w_5^h, \rho_{n+\frac{1}{2}}^h r \right)_\Omega = 0, \tag{7.174}$$

$$\mathbf{B}_{mid}^A(w_6^h; \mathbf{Y}^h) := \left(w_6^h, V_{mid}^h \right)_\Omega - \left(w_6^h, \frac{1}{\theta_{n+\frac{1}{2}}^h} \left(\nu_{loc}(\rho_{n+\frac{1}{2}}^h, \theta_{n+\frac{1}{2}}^h) - \frac{|\mathbf{u}_{n+\frac{1}{2}}^h|^2}{2} \right) \right)_\Omega$$
$$- \left(\nabla w_6^h, \frac{1}{\mathrm{We}\, \theta_{n+\frac{1}{2}}^h} \nabla \rho_{n+\frac{1}{2}}^h \right)_\Omega = 0. \tag{7.175}$$

The local truncation error associated with the mid-point rule can be obtained by replacing the time discrete solutions with the corresponding exact time continuous solution:

$$\mathbf{B}_{mid}^M(w_1^h; \mathbf{Y}^h(t)) = \left(w_1^h, \Theta_\rho^{mid} \right)_\Omega, \tag{7.176}$$

$$\mathbf{B}_{mid}^U(\mathbf{w}^h; \mathbf{Y}^h(t)) = \left(w_1^h, \Theta_{\mathbf{u}}^{mid} \right)_\Omega, \tag{7.177}$$

$$\mathbf{B}_{mid}^E(w_5^h; \mathbf{Y}^h(t)) = \left(w_1^h, \Theta_E^{mid} \right)_\Omega, \tag{7.178}$$

$$\mathbf{B}_{mid}^A(w_6^h; \mathbf{Y}^h(t)) = \left(w_1^h, \Theta_A^{mid} \right)_\Omega. \tag{7.179}$$

Assuming sufficient smoothness for the time continuous solutions, one can get

$$\Theta_\rho^{mid} = \mathcal{O}(\Delta t_n^2), \quad \Theta_{\mathbf{u}}^{mid} = \mathcal{O}(\Delta t_n^2)\mathbf{1},$$
$$\Theta_E^{mid} = \mathcal{O}(\Delta t_n^2), \quad \Theta_A^{mid} = \mathcal{O}(\Delta t_n^2). \tag{7.180}$$

Now replacing the time discrete solutions with corresponding time continuous solutions in the fully discrete form (7.128)-(7.131), it can be shown that

$$\mathbf{B}^M(w_1^h; \mathbf{Y}^h(t)) = \left(w_1^h, \Theta_\rho \right)_\Omega, \tag{7.181}$$

$$\mathbf{B}^U(\mathbf{w}^h; \mathbf{Y}^h(t)) = \left(w_1^h, \Theta_{\mathbf{u}} \right)_\Omega, \tag{7.182}$$

256

$$\mathbf{B}^E(w_5^h; \mathbf{Y}^h(t)) = \left(w_1^h, \Theta_E\right)_\Omega, \tag{7.183}$$

$$\mathbf{B}^A(w_6^h; \mathbf{Y}^h(t)) = \left(w_1^h, \Theta_A\right)_\Omega. \tag{7.184}$$

Taylor expansions lead to

$$\frac{1}{2}\left(\nu_{loc}(\rho^h(t_n)) + \nu_{loc}(\rho^h(t_{n+1}))\right) = \nu_{loc}(\rho^h(t_{n+\frac{1}{2}})) + \mathcal{O}(\Delta t_n^2), \tag{7.185}$$

$$\frac{[\![\rho^h(t_n)]\!]^2}{12}\mu''(\rho^h(t_n)) = \mathcal{O}(\Delta t_n^2), \tag{7.186}$$

$$2|\mathbf{u}^h(t_{n+\frac{1}{2}})|^2 - \frac{1}{2}(|\mathbf{u}^h(t_n)|^2 + |\mathbf{u}^h(t_{n+1})|^2) = |\mathbf{u}^h(t_{n+\frac{1}{2}})|^2 + \mathcal{O}(\Delta t_n^2). \tag{7.187}$$

Due to Lemma 7.7.3, one has

$$\frac{\rho_{n+1}^h E(\rho_{n+1}^h, \mathbf{u}_{n+1}^h, \theta_{n+1}^h) - \rho_n^h E(\rho_n^h, \mathbf{u}_n^h, \theta_n^h)}{\Delta t_n} - \frac{[\![\rho_n^h E(\rho_n^h, \mathbf{u}_n^h, \theta_n^h)]\!]}{\Delta t_n}$$

$$= \mathcal{O}(\Delta t_n^2). \tag{7.188}$$

Combing the above results, it follows that

$$\left(w_1^h, \Theta_\rho\right)_\Omega = \left(w_1^h, \Theta_\rho^{mid}\right)_\Omega + \mathcal{O}(\Delta t_n^2) = \mathcal{O}(\Delta t_n^2), \tag{7.189}$$

$$\left(w_1^h, \Theta_\mathbf{u}\right)_\Omega = \left(w_1^h, \Theta_\mathbf{u}^{mid}\right)_\Omega + \mathcal{O}(\Delta t_n^2)\mathbf{1} = \mathcal{O}(\Delta t_n^2)\mathbf{1}, \tag{7.190}$$

$$\left(w_1^h, \Theta_E\right)_\Omega = \left(w_1^h, \Theta_E^{mid}\right)_\Omega + \mathcal{O}(\Delta t_n) = \mathcal{O}(\Delta t_n^2), \tag{7.191}$$

$$\left(w_1^h, \Theta_A\right)_\Omega = \left(w_1^h, \Theta_A^{mid}\right)_\Omega + \mathcal{O}(\Delta t_n^2) = \mathcal{O}(\Delta t_n^2), \tag{7.192}$$

which complete the proof. $\qquad\square$

Remark 7.7.4. *According to the relations (7.185)-(7.188), the fully discrete scheme is a second-order perturbation of the mid-point rule which achieves provably entropy dissipation.*

7.8 Benchmark problems

In this section, two benchmark problems are simulated to verify the theoretical estimates.

7.8.1 Manufactured solution

As a first example, a set of manufactured solutions is constructed for the one-dimensional Navier-Stokes-Korteweg equations to verify the time accuracy. The computations are restricted to the domain $\Omega = (0, 1)$ and the exact density, velocity, and temperature for this problem are chosen as

$$\rho(x, t) = 0.5 + 0.1 \sin(\pi t) \cos(2\pi x), \tag{7.193}$$

$$\mathbf{u}(x, t) = \sin(\pi t) \cos(2\pi x), \tag{7.194}$$

$$\theta(x, t) = 0.85 + 0.1 \sin(\pi t) \sin(4\pi x). \tag{7.195}$$

The forcing terms for the balance equations are obtained by substituting the above exact solutions into the original strong problem (7.40)-(7.42). The corresponding $\mathbf{Y}$ variables can be obtained as

$$Y_1 = \rho = 0.5 + 0.1 \sin(\pi t) \cos(2\pi x), \tag{7.196}$$

$$Y_2 = \frac{\mathbf{u}}{\theta} = \frac{\sin(\pi t) \cos(2\pi x)}{0.85 + 0.1 \sin(\pi t) \sin(4\pi x)}, \tag{7.197}$$

$$Y_3 = -\frac{1}{\theta} = -\frac{1}{0.85 + 0.1 \sin(\pi t) \sin(4\pi x)}. \tag{7.198}$$

The dimensionless numbers for this verification problem are fixed to be Re = 1.0, We = 1.0, $\kappa = 1.0$, and $\gamma = 1.333$. Periodic boundary conditions are enforced on the boundary. The problem is computed with spatial mesh size

$\Delta x = 1.0 \times 10^{-3}$ for polynomial degrees $\mathfrak{p} = 2$ and 3. The time step sizes are taken as 1.0×10^{-1}, 5.0×10^{-2}, 1.0×10^{-2}, 5.0×10^{-3}, and 5.0×10^{-4}. In Table 7.1, the errors in L^2-norm for the quadratic NURBS solutions and the errors in H^1 semi-norm for the cubic NURBS solutions are summarized. It can be observed that the temporal errors converge like $\mathcal{O}(\Delta t^2)$ in both cases. This immediately confirms the time accuracy estimates given in Theorem 7.7.2.

Table 7.1: One-dimensional manufactured solution for the thermal Navier-Stokes-Korteweg equations: Temporal convergence rates at $t = 0.5$.

Temporal errors in L^2 norm with polynomial degree $\mathfrak{p} = 2$

Δt	1.0×10^{-1}	5.0×10^{-2}	1.0×10^{-2}	5.0×10^{-3}	1.0×10^{-3}
$\|Y_1 - Y_1^h\|_{L^2(\Omega)}$	8.00×10^{-4}	1.99×10^{-4}	7.96×10^{-6}	1.99×10^{-6}	7.93×10^{-8}
order	-	2.01	2.00	2.00	2.00
$\|Y_2 - Y_2^h\|_{L^2(\Omega)}$	1.50×10^{-2}	3.77×10^{-3}	1.49×10^{-4}	3.72×10^{-5}	1.48×10^{-6}
order	-	1.99	2.01	2.00	2.00
$\|Y_3 - Y_3^h\|_{L^2(\Omega)}$	6.23×10^{-3}	1.52×10^{-3}	5.95×10^{-5}	1.49×10^{-5}	5.94×10^{-7}
order	-	2.04	2.01	2.00	2.00

Temporal errors in H^1 semi-norm with polynomial degree $\mathfrak{p} = 3$

Δt	1.0×10^{-1}	5.0×10^{-2}	1.0×10^{-2}	5.0×10^{-3}	1.0×10^{-3}
$|Y_1 - Y_1^h|_{H^1(\Omega)}$	5.03×10^{-3}	1.25×10^{-3}	5.00×10^{-5}	1.25×10^{-5}	5.00×10^{-7}
order	-	2.01	2.00	2.00	2.00
$|Y_2 - Y_2^h|_{H^1(\Omega)}$	9.59×10^{-2}	2.58×10^{-2}	9.84×10^{-4}	2.46×10^{-4}	9.84×10^{-6}
order	-	1.89	2.03	2.00	2.00
$|Y_3 - Y_3^h|_{H^1(\Omega)}$	3.04×10^{-2}	7.70×10^{-3}	2.78×10^{-4}	6.95×10^{-5}	2.78×10^{-6}
order	-	1.98	2.06	2.00	2.00

7.8.2   Coalescence of two bubbles

As a second example, I consider a one-dimensional problem without external sources (i.e., $\mathbf{b} = \mathbf{0}$ and $r = 0$) to investigate the entropy dissipation property of the fully discrete scheme. The computational domain of this problem is set to be $\Omega = (0, 1)$. Two vapor bubbles are initially located in the domain with centers at points $C_1 = 0.39$ and $C_2 = 0.61$. The radii of the bubbles are set to be $R_1 = R_2 = 0.1$. The initial density profile is given by the following hyperbolic tangent function.

$$\rho_0(\mathbf{x}) = 0.1 + 0.25 \left[\tanh \left(\frac{d_1(\mathbf{x}) - R_1}{2} \sqrt{\text{We}} \right) \right.$$
$$\left. + \tanh \left(\frac{d_2(\mathbf{x}) - R_2}{2} \sqrt{\text{We}} \right) \right], \tag{7.199}$$
$$d_i(\mathbf{x}) = |\mathbf{x} - C_i|, \quad \text{for } i = 1, 2. \tag{7.200}$$

The initial velocity is zero and the initial temperature is fixed to be $\theta_0 = 0.95$. Periodic boundary conditions are enforced on the boundary $\partial \Omega$. The spatial mesh consists of 10^4 quadratic NURBS functions. In the time direction, the problem is integrated up to $T = 10.0$ with time step sizes $\Delta t = 1.0 \times 10^{-2}$, 5.0×10^{-3}, 2.0×10^{-3}, and 1.0×10^{-5}. The dimensionless numbers are taken as $\text{Re} = 4.0 \times 10^2$, $\text{We} = 1.6 \times 10^5$, and $\gamma = 1.333$; the dimensionless thermal conductivity is taken as $\kappa = 1.0$. The two vapor bubbles will merge together to minimize the surface energy. At the temperature $\theta = 0.95$, the Maxwell states are $\rho_A = 0.193$ and $\rho_B = 0.487$. The initial vapor and liquid densities are $\rho_{v,0} = 0.1$ and $\rho_{l,0} = 0.6$, which are not located at the Maxwell stable states. Hence, the vapor phase will become denser and the liquid phase will

become lighter to minimize the free energy function at this temperature. In the meantime, the phase transition is accompanied with latent heat release and absorption. The thermal effects will change the local temperature distribution, which, in turn, changes the Maxwell states. Eventually, this coupled thermo-mechanical process will reach an equilibrium state. This thermally-coupled bubble dynamics is illustrated in a density-temperature phase diagram in Figure 7.1.
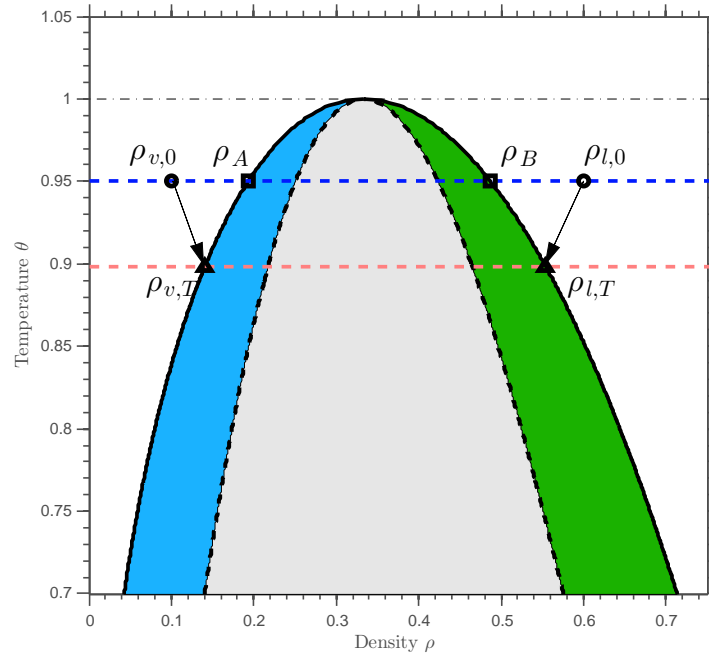

Figure 7.1: Illustration of the thermal bubble dynamics. $\rho_{v,0}$ and $\rho_{l,0}$ are the initial vapor and liquid densities; ρ_A and ρ_B are the Maxwell state at the initial temperature; $\rho_{v,T}$ and $\rho_{l,T}$ are the vapor and liquid densities at time $T = 10.0$.

In Figure 7.2, the evolution of the density profile has been visualized

at times $t = 0.0$, 0.1, 0.5, 1.0, 2.0 and 10.0. It can be observed that the initial interface between the two vapor bubbles gradually vanishes, and the vapor and liquid densities are adjusted to achieve the energy-stable states. In the mean time, the temperature of this system fluctuates. In Figure 7.2 (b), snapshots of the temperature at times $t = 0.0$, 0.1, 0.5, 1.0, 2.0 and 10.0 are depicted. The temperature drops to about 0.876 at time $t = 1.0$, then it raises to 0.898 uniformly at time $t = 10.0$. The Maxwell states at $\theta = 0.898$ are $\rho_v = 0.1403$ and $\rho_l = 0.5546$. Figure 7.2 (a) shows that the density at $t = 10.0$ is very close to the energy stable state at the temperature $\theta = 0.898$. For this problem, the dissipation relation can be written as

$$
\int_\Omega \left(\frac{\mathfrak{H}(\rho_{n+1}^h, \theta_{n+1}^h) - \mathfrak{H}(\rho_n^h, \theta_n^h)}{\Delta t_n} \right) d\mathbf{x}
$$

$$
= - \int_\Omega \frac{1}{\theta_{n+\frac{1}{2}}^h} \boldsymbol{\tau}_{n+\frac{1}{2}}^h : \nabla \mathbf{u}_{n+\frac{1}{2}}^h d\mathbf{x} - \int_\Omega \frac{\nabla \theta_{n+\frac{1}{2}}^h \cdot \boldsymbol{\kappa} \nabla \theta_{n+\frac{1}{2}}^h}{\left(\theta_{n+\frac{1}{2}}^h \right)^2} d\mathbf{x}
$$

$$
- \int_\Omega \frac{1}{\theta_{n+\frac{1}{2}}^h \Delta t_n} \frac{[\![\rho_n^h]\!]^4}{24} \frac{\partial^3 \nu_{loc}}{\partial \rho^3} (\rho_{n+\xi_1}^h, \theta_{n+\frac{1}{2}}^h) d\mathbf{x}
$$

$$
+ \int_\Omega \frac{1}{\theta_{n+\frac{1}{2}}^h \Delta t_n} \frac{[\![\theta_n^h]\!]^4}{24} \frac{\partial^3 \mathfrak{H}}{\partial \theta^3} (\rho_{n+\frac{1}{2}}^h, \theta_{n+\xi_2}^h) d\mathbf{x}
$$

$$
\leq 0. \tag{7.201}
$$

The discrete mathematical entropy are plotted against time in Figure 7.3 (a). It can be observed that $\mathfrak{H}(\rho_n^h, \theta_n^h)$ monotonically decreases with respect to time, which confirms the theoretical estimate given in Theorem 7.7.1. In Figure 7.3 (b), a detailed view of the discrete mathematical entropy in the vicinity of $t = 2.49$ is provided. It can be observed that the differences between the

numerical solutions and the overkill solution decrease with a reduction of time step size.

To verify the time accuracy estimate, overkill solutions were first computed with $\Delta t = 1.0 \times 10^{-5}$. Then the computations were repeated with larger time steps $\Delta t = 5.0 \times 10^{-2}$, 1.0×10^{-2}, 5.0×10^{-3}, 1.0×10^{-3} and 5.0×10^{-4}. The errors at time $t = 1.0$ are listed in Table 7.2. It can be seen that the numerical solutions converge optimally in time to the overkill solutions. This again corroborates the theoretical estimates given in Theorem 7.7.2.

Table 7.2: Coalescence of two bubbles for the one-dimensional thermal Navier-Stokes-Korteweg equations: Temporal errors in L^2-norm at time $t = 1.0$.

Δt	5.0×10^{-2}	1.0×10^{-2}	5.0×10^{-3}	1.0×10^{-3}	5.0×10^{-4}
$\|Y_1 - Y_1^h\|_{L^2(\Omega)}$	8.40×10^{-5}	4.02×10^{-6}	1.02×10^{-6}	4.14×10^{-8}	1.04×10^{-8}
order	-	1.94	1.98	1.99	1.99
$\|Y_2 - Y_2^h\|_{L^2(\Omega)}$	2.69×10^{-4}	6.57×10^{-6}	1.64×10^{-6}	6.54×10^{-8}	1.64×10^{-8}
order	-	2.02	2.00	2.00	2.00
$\|Y_3 - Y_3^h\|_{L^2(\Omega)}$	2.70×10^{-5}	1.50×10^{-6}	3.83×10^{-7}	1.56×10^{-8}	3.93×10^{-9}
order	-	1.92	1.97	1.99	1.99

7.9 Applications

In this section, I investigate the validity of the van der Waals fluid model and the effectiveness of the numerical method by studying three sets of application problems.
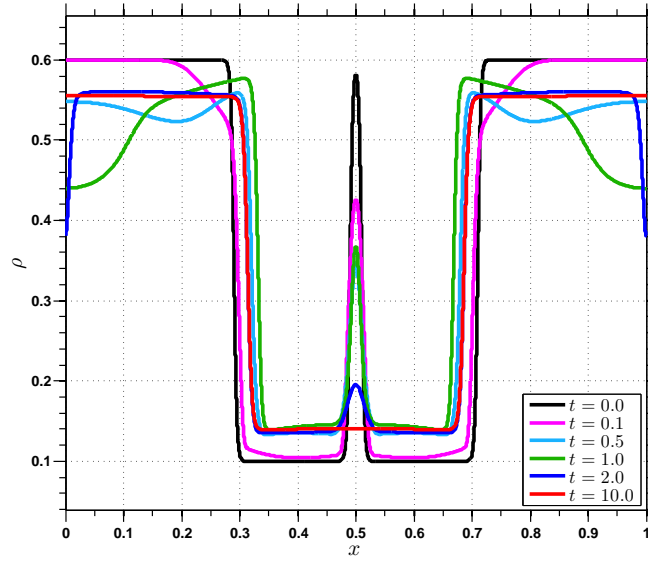
(a)
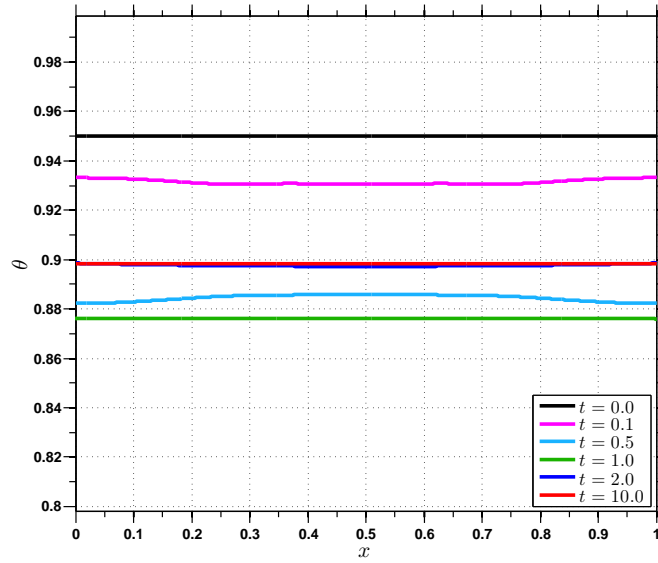
(b)

Figure 7.2: Coalescence of two bubbles for the one-dimensional thermal Navier-Stokes-Korteweg equations: (a) density profiles and (b) temperature profiles at times $t = 0.0$, 0.1, 0.5, 1.0, 2.0 and 10.0.
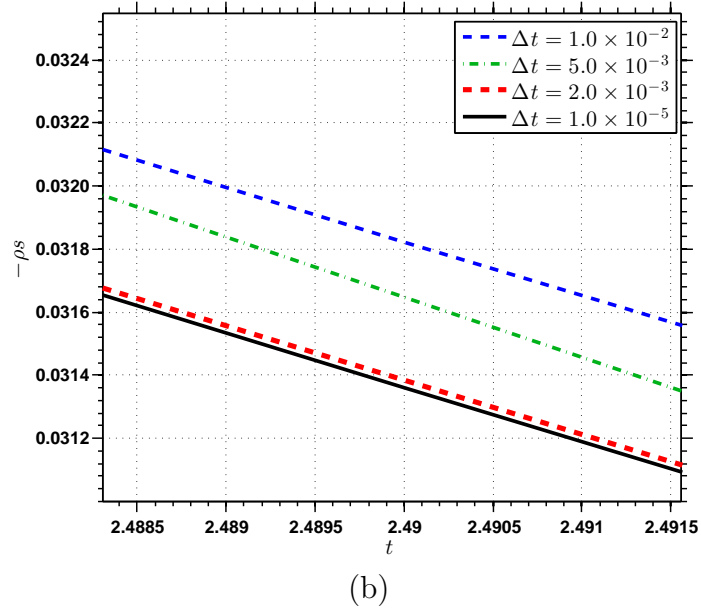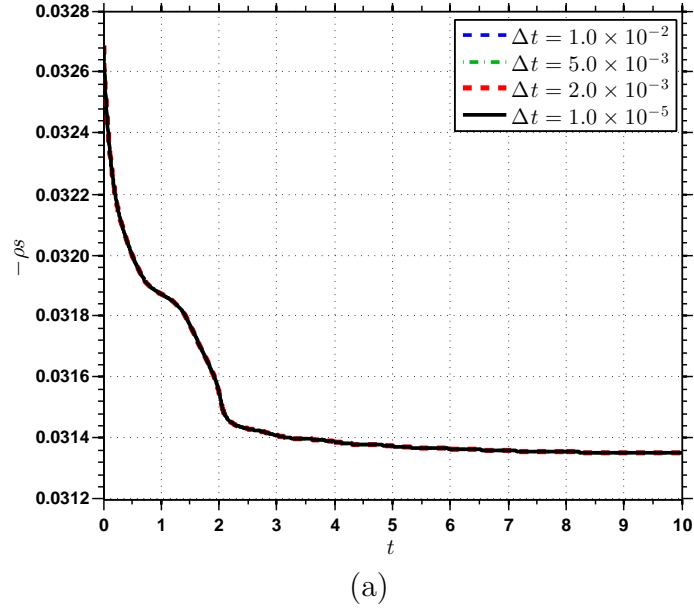
Figure 7.3: Coalescence of two bubbles for the one-dimensional thermal Navier-Stokes-Korteweg equations: Evolution of the discrete entropy. (a) Global view; (b) Detailed view in the vicinity of $t = 2.49$.
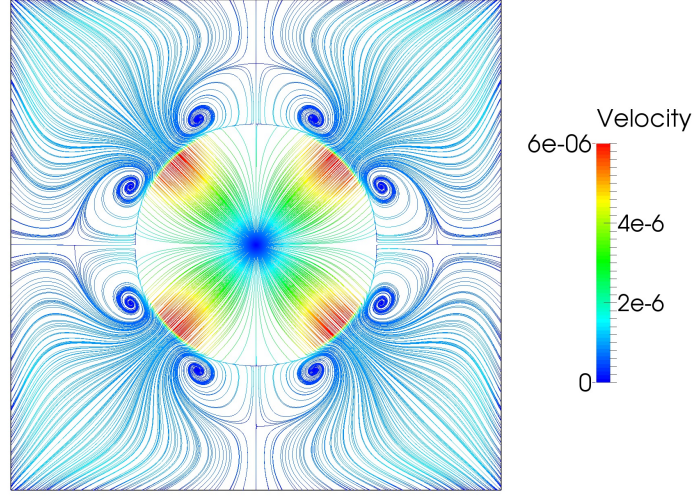
Figure 7.4: Velocity streamlines near a single bubble at time $t = 15.0$: $\theta_{bc} = 0.85$.

7.9.1 Evaporation and condensation of a single bubble

In this example, I numerically investigate the evolution of a single bubble in the presence of temperature variations on the boundary. This problem is fundamental in understanding the complicated thermal-mechanical behavior of the van der Waals fluid model. In this study, the computational domain is restricted to $\Omega = (0, 1)^2$. The center of the vapor bubble is located at the center of the domain, i.e., $C_1 = (0.5, 0.5)$; the radius of the bubble is $R_1 = 0.25$. A hyperbolic tangent function is utilized to give the initial density profile:

$$\rho_0(\mathbf{x}) = 0.3545 + 0.2479 \tanh\left(\frac{d_1(\mathbf{x}) - R_1}{2}\sqrt{\text{We}}\right), \tag{7.202}$$

$$d_1(\mathbf{x}) = |\mathbf{x} - C_1|. \tag{7.203}$$

The initial velocity is set to be zero. The initial temperature is given by

$$\theta_0(\mathbf{x}) = 0.85, \quad \text{if } \mathbf{x} \in \Omega, \tag{7.204}$$

$$\theta_0(\mathbf{x}) = \theta_{bc}, \quad \text{if } \mathbf{x} \in \partial\Omega. \tag{7.205}$$

The boundary conditions for this problem are

$$\nabla\rho \cdot \mathbf{n} = 0, \quad \text{on } \partial\Omega \times (0, T), \tag{7.206}$$

$$\mathbf{u} = \mathbf{0}, \quad \text{on } \partial\Omega \times (0, T), \tag{7.207}$$

$$\theta = \theta_{bc}, \quad \text{on } \partial\Omega \times (0, T). \tag{7.208}$$

According the analysis of the static equilibrium solutions in Section 3.2.3, the hyperbolic tangent function (7.202) is only an approximation to the steady state density profile at the temperature $\theta = 0.85$. Hence, there will be a low-intensity velocity field generated near the interfacial region, which is commonly referred to as the parasitic currents [115]. If $\theta_{bc} \neq 0.85$, as time evolves, thermal diffusion will drive the temperature inside Ω to θ_{bc}. This change of temperature directly leads to the change of the Maxwell states, which further results in condensation or evaporation of the bubble. If $\theta_{bc} > 0.85$, the bubble will evaporate; if $\theta_{bc} < 0.85$, the bubble will condense. In Table 7.3, the Maxwell states at different temperatures are listed. With these values, the radius of the vapor bubble at the new stable configuration can be estimated using the mass conservation relation. Assuming the interfacial region has measure zero, then the total mass in Ω is

$$0.1066 \times 0.25^2\pi + 0.6024 \times (1.0 - 0.25^2\pi) = 0.6024 - 0.031\pi. \tag{7.209}$$

If the Maxwell-state liquid and vapor densities at the temperature θ are denoted as ρ_l^θ and ρ_v^θ. The new radius of the vapor bubble R_{st} is determined by the mass conservation relation

$$\rho_v^\theta \times R_{st}^2 \pi + \rho_l^\theta \times (1.0 - R_{st}^2 \pi) = 0.6024 - 0.031\pi, \qquad (7.210)$$

if ρ_l^θ and ρ_v^θ satisfy $\rho_v^\theta \leq 0.6024 - 0.031\pi \leq \rho_l^\theta$. The solutions of R_{st} for $\theta = 0.95$, 0.90, 0.85, 0.80, and 0.75 are listed in Table 7.3. If $\rho_l^\theta < 0.6024 - 0.031\pi$, the steady state will be a uniform liquid state with density $0.6024 - 0.031\pi$; if $0.6024 - 0.031\pi \leq \rho_v^\theta$, the steady state will be a uniform vapor state with density $0.6024 - 0.031\pi$.

θ	0.95	0.90	0.85	0.80	0.75
ρ_v	0.1930	0.1419	0.1066	0.0799	0.0591
ρ_l	0.4872	0.5524	0.6024	0.6442	0.6808
R_{st}	-	0.1916	0.2500	0.2802	0.3000

Table 7.3: The liquid and vapor densities at the Maxwell states of the van der Waals fluid model at different temperatures. The values are rounded to four decimal places. R_{st} represents the steady-state vapor bubble radius with the given initial density profile (7.202)-(7.203) in the sharp interface limit. When $\theta = 0.95$, a uniform liquid state with density $\rho = 0.5050$ will form at the steady state.

In the numerical simulations, the dimensionless numbers are taken as $\mathrm{Re} = 1.451 \times 10^3$, $\mathrm{We} = 5.263 \times 10^5$, and $\gamma = 1.333$. The dimensionless thermal conductivity is taken as

$$\boldsymbol{\kappa} = \begin{bmatrix} 1.378 \times 10^{-3} & 0.0 \\ 0.0 & 1.378 \times 10^{-3} \end{bmatrix}. \qquad (7.211)$$
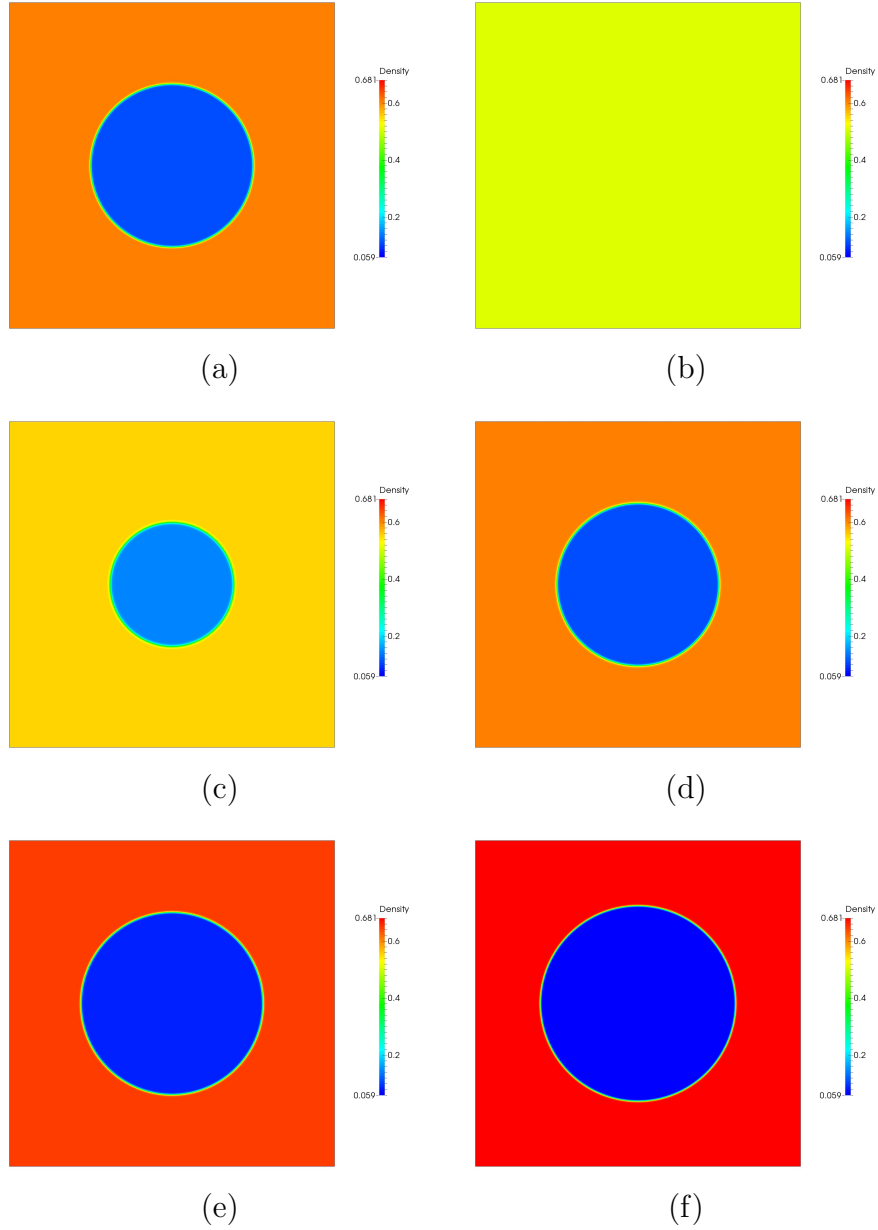
Figure 7.5: Density profiles of a single bubble under different temperature boundary conditions: (a) Initial condition, (b) $\theta_{bc} = 0.95$, (c) $\theta_{bc} = 0.90$, (d) $\theta_{bc} = 0.85$, (e) $\theta_{bc} = 0.80$, (f) $\theta_{bc} = 0.75$.

269

The external body force **b** and the heat source r are fixed to be zero. The spatial mesh is comprised of 512^2 quadratic NURBS elements. The time step size is chosen to be $\Delta t = 1.0 \times 10^{-3}$ and the simulation is integrated up to $T = 2.0 \times 10^2$. In Figure 7.4, the parasitic currents for $\theta_{bc} = 0.85$ at time $t = 15.0$ is depicted. In Figure 7.5, the density profiles at time $t = 200.0$ are depicted. The solution for $\theta_{bc} = 0.95$ at $t = 200.0$ forms a uniform liquid state. From $\theta_{bc} = 0.90$ to $\theta_{bc} = 0.75$, the radius of the bubble increases with the reduction of the boundary temperature. Also, note that the interface width reduces with the decrease of the temperature. This observation confirms the previous estimate in part.

7.9.2   Thermocapillary motion

It has long been known that the motion of interfaces is governed by many forces other than the gravity. These forces may become dominant under special circumstances. For example, composition differences may result in an imbalance of surface tension, which may accordingly lead to a movement of the free surface. This phenomenon can be observed over wine interfaces and is named as the "tears of wine" [192]. Nowadays, the motion of interfaces due to the imbalance of surface tension is generally referred to as the Marangoni effect [173]. Among the many different Marangoni effects, motion driven by the temperature gradient is of keen interest and is often specifically referred to as the thermocapillary effect. Such effect is critical in understanding many complicated physical phenomena, including cavitation [68], boiling [149], and

270

welding [152]. In the seminal paper [207], it was explained that the surface tension will decrease with the increase of the local temperature and the resulting stress imbalance will drive the bubble move in the negative thermal gradient direction. Under this assumption, a theoretical estimate of the bubble velocity for a single bubble in the creeping flow limit has been derived. In addition to the theoretical analysis, there have been several numerical simulation results for the thermocapillary effect, using the level-set method [99] and the front-tracking method [195]. These numerical studies focused on the interface between different components. And a common modeling assumption they adopted is that the surface tension is a function of temperature. So far, there has been very limited study of the thermocapillary motion of a one-component material. In [160], the author has theoretically analyzed the droplet motion under heat gradient. It was explained that the thermocapillary motion of a single-component material is driven by the latent release and absorption. In [158], numerical studies of a dynamic van der Waals model were carried out to investigate the bubble motion under different thermal gradients in a two-dimensional setting. However, the model in [158] ignored the interstitial working flux Π. In this section, I numerically study the thermocapillary effect using the thermodynamically consistent model derived in Chapter 2 and the thermodynamically consistent algorithm derived in this chapter. The resolution in this numerical study is much finer than that of the mesh used in [158]. Additionally, a three-dimensional simulation of the thermocapillary motion is carried out as well in this section.
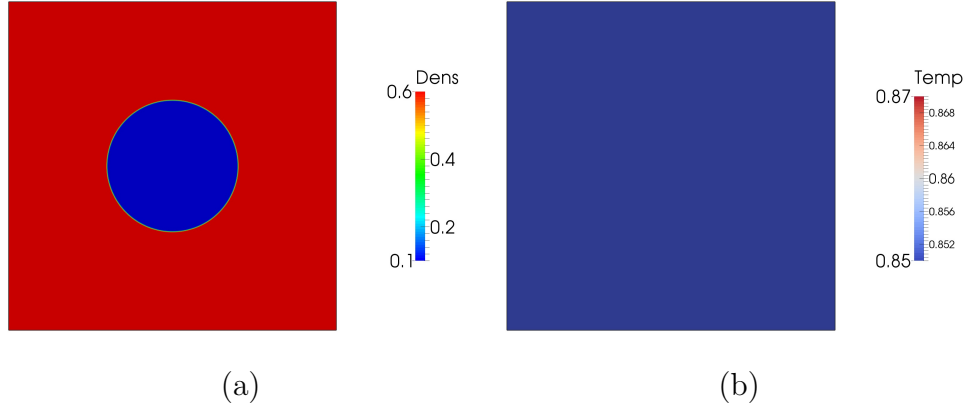
Figure 7.6: Thermocapillary motion of a single bubble in a two-dimensional square: Initial conditions for density (a) and temperature (b).

7.9.2.1 Two-dimensional thermocapillary motion

In the first example, the thermocapillary motion of a single vapor bubble is studied in a two-dimensional square $\Omega = (0,1)^2$. The boundary of Ω is partitioned into three non-overlapping subdivisions:

$$\partial\Omega = \Gamma_v \cup \Gamma_t \cup \Gamma_b, \tag{7.212}$$

$$\Gamma_v := \partial\Omega \cap \left\{ \left\{ \mathbf{x} \in \mathbb{R}^2 | x = 0 \right\} \cup \left\{ \mathbf{x} \in \mathbb{R}^2 | x = 1 \right\} \right\}, \tag{7.213}$$

$$\Gamma_b := \partial\Omega \cap \left\{ \mathbf{x} \in \mathbb{R}^2 | y = 0 \right\}, \tag{7.214}$$

$$\Gamma_t := \partial\Omega \cap \left\{ \mathbf{x} \in \mathbb{R}^2 | y = 1 \right\}. \tag{7.215}$$

The center of the bubble is originally located at $C_1 = (0.5, 0.5)$ and the radius of the bubble is 0.2. The initial density is given by

$$\rho_0(\mathbf{x}) = 0.35 + 0.25 \tanh\left(\frac{d_1(\mathbf{x}) - 0.2}{2} \sqrt{\text{We}} \right), \tag{7.216}$$

272

$$d_1(\mathbf{x}) = |\mathbf{x} - C_1|. \tag{7.217}$$

The initial velocity is fixed to be zero and the initial temperature is

$$\theta_0(\mathbf{x}) = 0.85 \quad \mathbf{x} \in \Omega \cup \Gamma_v \cup \Gamma_b, \tag{7.218}$$

$$\theta_0(\mathbf{x}) = 0.87 \quad \mathbf{x} \in \Gamma_t. \tag{7.219}$$

The boundary conditions for this problem are

$$\nabla \rho \cdot \mathbf{n} = 0, \quad \text{on } \partial\Omega \times (0, T), \tag{7.220}$$

$$\mathbf{u} = \mathbf{0}, \quad \text{on } \partial\Omega \times (0, T), \tag{7.221}$$

$$\theta = 0.85, \quad \text{on } \Gamma_b \times (0, T), \tag{7.222}$$

$$\theta = 0.87, \quad \text{on } \Gamma_t \times (0, T), \tag{7.223}$$

$$-\mathbf{q} \cdot \mathbf{n} = 0, \quad \text{on } \Gamma_v \times (0, T). \tag{7.224}$$

The dimensionless numbers and the dimensionless thermal conductivity are chosen as

$$\text{Re} = 1.738 \times 10^4,$$

$$\text{We} = 3.277 \times 10^6,$$

$$\gamma = 1.333,$$

$$\boldsymbol{\kappa} = \begin{bmatrix} 3.453 \times 10^{-3} & 0.0 \\ 0.0 & 3.453 \times 10^{-3} \end{bmatrix}.$$

The spatial discretization is comprised of 1024^2 quadratic NURBS functions. The time integration is performed with a fixed step size $\Delta t = 5.0 \times 10^{-4}$ up to the final time $T = 500.0$. In Figure 7.6, the initial density and temperature
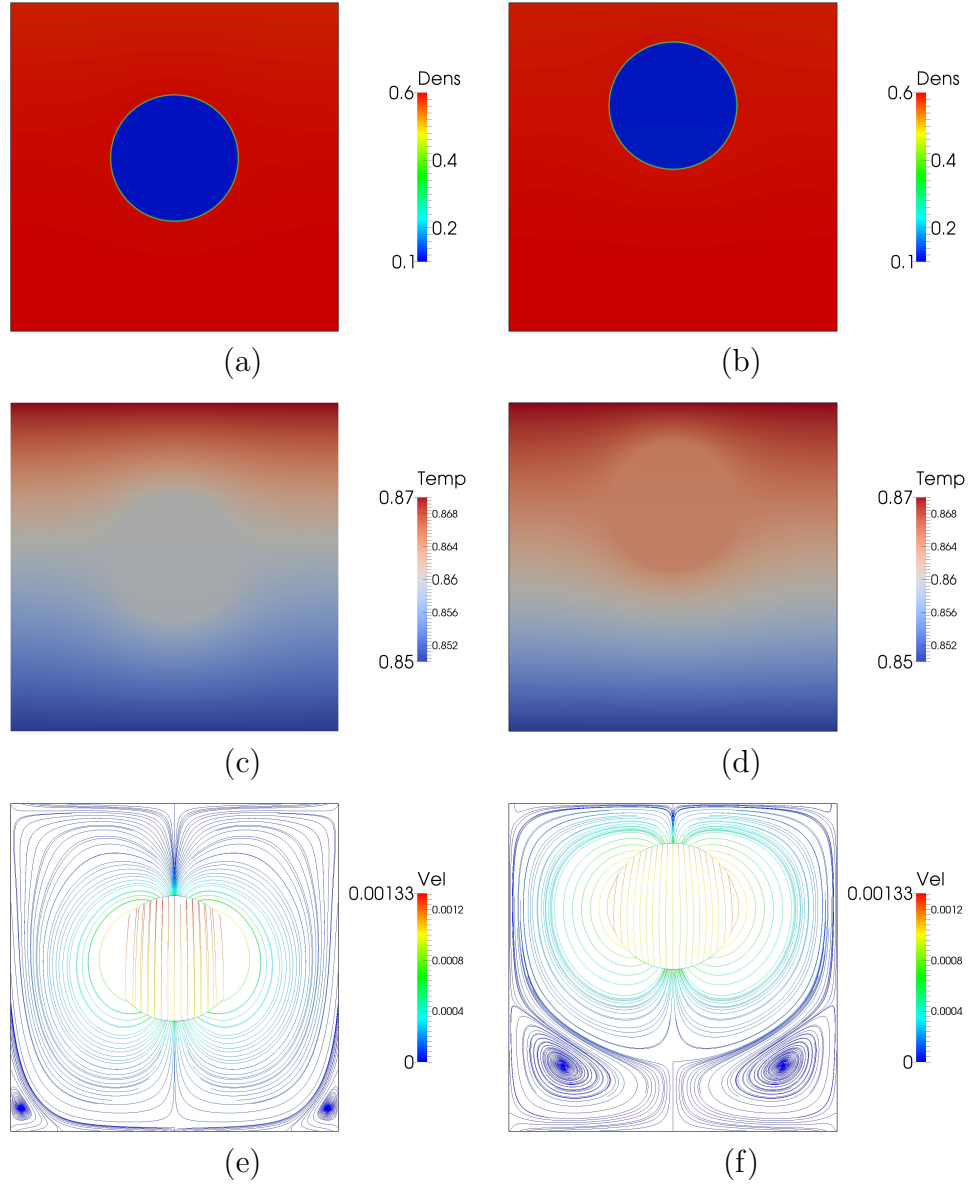
273

Figure 7.7: Thermocapillary motion of a single bubble in a two-dimensional square: Solutions at $t = 5.0 \times 10$ (left column) and $t = 2.0 \times 10^2$ (right column). The first row depicts the density profiles; the second row depicts the temperature profiles; the third row visualizes the velocity streamlines.
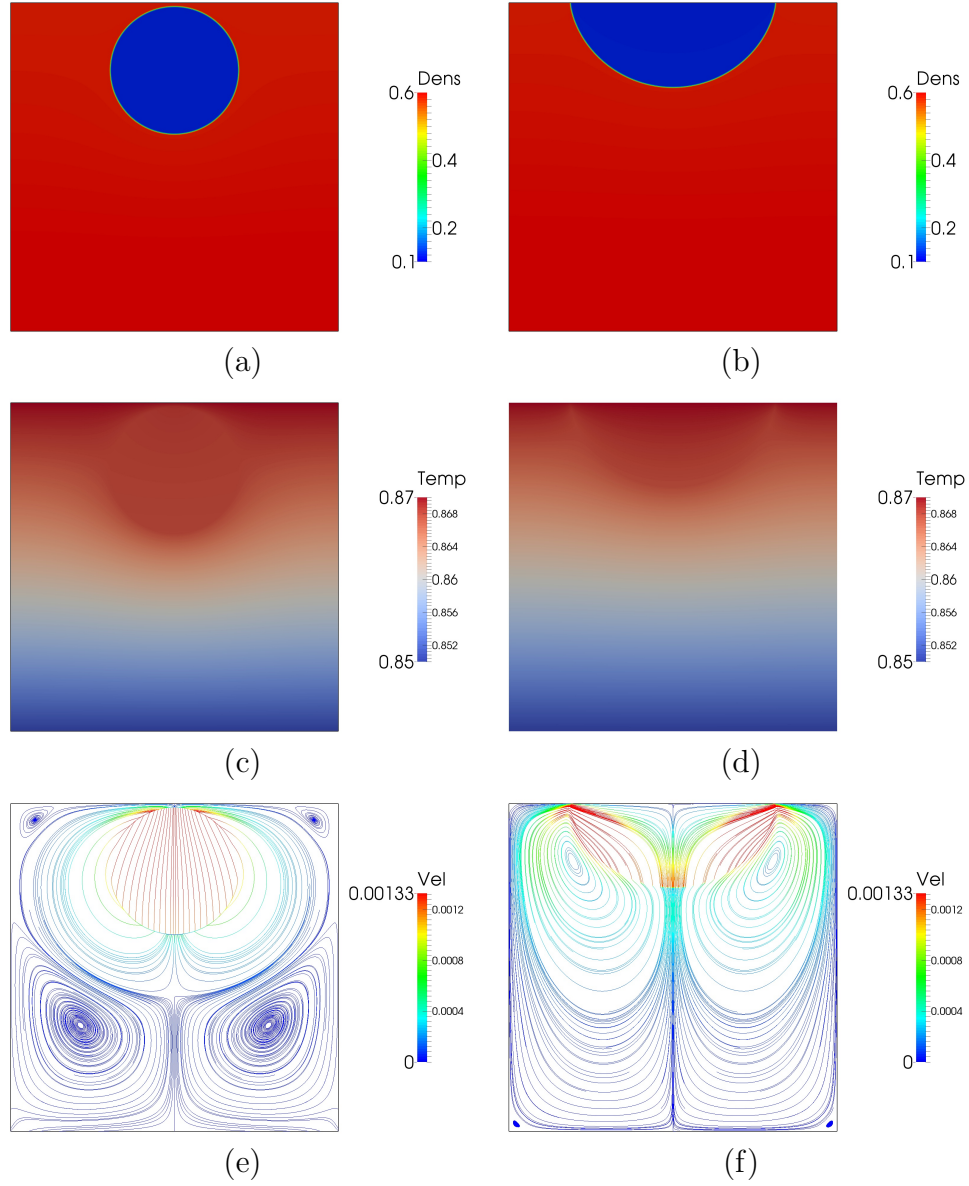
Figure 7.8: Thermocapillary motion of a single bubble in a two-dimensional square: Solutions at $t = 3.0 \times 10^2$ (left column) and $t = 5.0 \times 10^2$ (right column). The first row depicts the density profiles; the second row depicts the temperature profiles; the third row visualizes the velocity streamlines.

profiles have been illustrated. In Figures 7.7-7.8, the resulting density, temperature, and velocity fields have been depicted at various time steps. It is noted that there is a velocity field generated immediately after the simulation starts. The velocity drives the vapor bubble migrate toward the negative thermal gradient direction. Eventually, the vapor bubble attaches the heated wall boundary and forms a hemispheric shape, as is shown in Figure 7.8 (b). It can be observed that, in the liquid phase, there is a temperature gradient generated between the heated top boundary and the cooled bottom boundary. Inside the vapor bubble, the temperature distribution remains homogeneous throughout the whole process. This homogeneous temperature distribution had also been observed by Onuki and was attributed to the latent heat diffusion [158].

7.9.2.2 Three-dimensional thermocapillary motion

As a second example, a three-dimensional numerical simulation of the thermocapillary motion is performed. To the best of the author's knowledge, there has been no published results on this problem in the literature. The computation domain for this study is set to be $\Omega = (0, 0.5) \times (0, 0.5) \times (0, 1)$. The boundary of Ω is partitioned into three non-overlapping subdivisions:

$$\partial\Omega = \Gamma_t \cup \Gamma_b \cup \Gamma_v, \tag{7.225}$$

$$\Gamma_b := \partial\Omega \cap \left\{ \mathbf{x} \in \mathbb{R}^2 | z = 0 \right\}, \tag{7.226}$$

$$\Gamma_t := \partial\Omega \cap \left\{ \mathbf{x} \in \mathbb{R}^2 | z = 1 \right\}, \tag{7.227}$$

$$\Gamma_v := \partial\Omega \cap \left\{ \left\{\mathbf{x} \in \mathbb{R}^2 | x = 0\right\} \cup \left\{\mathbf{x} \in \mathbb{R}^2 | x = 0.5\right\} \right.$$

$$\left. \cup \left\{\mathbf{x} \in \mathbb{R}^2 | y = 0\right\} \cup \left\{\mathbf{x} \in \mathbb{R}^2 | y = 0.5\right\} \right\}. \tag{7.228}$$

The center of the vapor bubble is initially located at $C_1 = (0.25, 0.25, 0.3)$. The bubble radius is set to be 0.2. The initial density and velocity are

$$\rho_0(\mathbf{x}) = 0.35 + 0.25 \tanh\left(\frac{d_1(\mathbf{x}) - 0.2}{2}\sqrt{\mathrm{We}}\right), \tag{7.229}$$

$$d_1(\mathbf{x}) = |\mathbf{x} - C_1|, \tag{7.230}$$

$$\mathbf{u}_0(\mathbf{x}) = \mathbf{0}. \tag{7.231}$$

The initial temperature is

$$\theta_0(\mathbf{x}) = 0.85, \quad \mathbf{x} \in \Omega \cup \Gamma_v \cup \Gamma_b, \tag{7.232}$$

$$\theta_0(\mathbf{x}) = 0.87, \quad \mathbf{x} \in \Gamma_t. \tag{7.233}$$

The boundary conditions for this problem are

$$\nabla\rho \cdot \mathbf{n} = 0, \qquad \text{on } \partial\Omega \times (0, T), \tag{7.234}$$

$$\mathbf{u} = \mathbf{0}, \qquad \text{on } \partial\Omega \times (0, T), \tag{7.235}$$

$$\theta = 0.85, \qquad \text{on } \Gamma_b \times (0, T), \tag{7.236}$$

$$\theta = 0.87, \qquad \text{on } \Gamma_t \times (0, T), \tag{7.237}$$

$$-\mathbf{q} \cdot \mathbf{n} = 0, \qquad \text{on } \Gamma_v \times (0, T). \tag{7.238}$$

The dimensionless numbers and the dimensionless thermal conductivity are taken as

$$\mathrm{Re} = 3.570 \times 10^3,$$

$$\text{We} = 1.383 \times 10^5,$$

$$\gamma = 1.333,$$

$$\boldsymbol{\kappa} = \begin{bmatrix} 1.681 \times 10^{-2} & 0.0 & 0.0 \\ 0.0 & 1.681 \times 10^{-2} & 0.0 \\ 0.0 & 0.0 & 1.681 \times 10^{-2} \end{bmatrix}.$$

The spatial mesh for this problem is comprised of $128 \times 128 \times 256$ quadratic NURBS elements. The time integration is performed up to the final time $T = 200$ with a fixed time step size of $\Delta t = 1.0 \times 10^{-3}$. Figures 7.9-7.13 present snapshots of density isosurfaces, velocity streamlines, and temperature contours at various slices. As soon as the simulation starts, there is a temperature gradient generated in the liquid phase; the temperature field inside the vapor bubble remains nearly homogeneous. Similarly to the two-dimensional counterpart, there is a velocity field generated instantaneously after the top boundary is heated. The initial static vapor bubble is then driven by the velocity toward the heated boundary. At about $t = 160$, the vapor bubble touches the top heated boundary. At $t = 200$, a vapor layer is formed, which separates the heated wall boundary from the bulk liquid phase. The velocity magnitude at $t = 200$ is uniformly small. Hence, the solutions shown in Figure 7.13 can be regarded to be very close to the steady state solutions.

7.9.3 Boiling

Boiling is a phase transition process during which new liquid-vapor interfaces are generated in a bulk liquid region as a result of local thermal variations [63, 165]. These vapor bubbles can be formed from discrete cavities
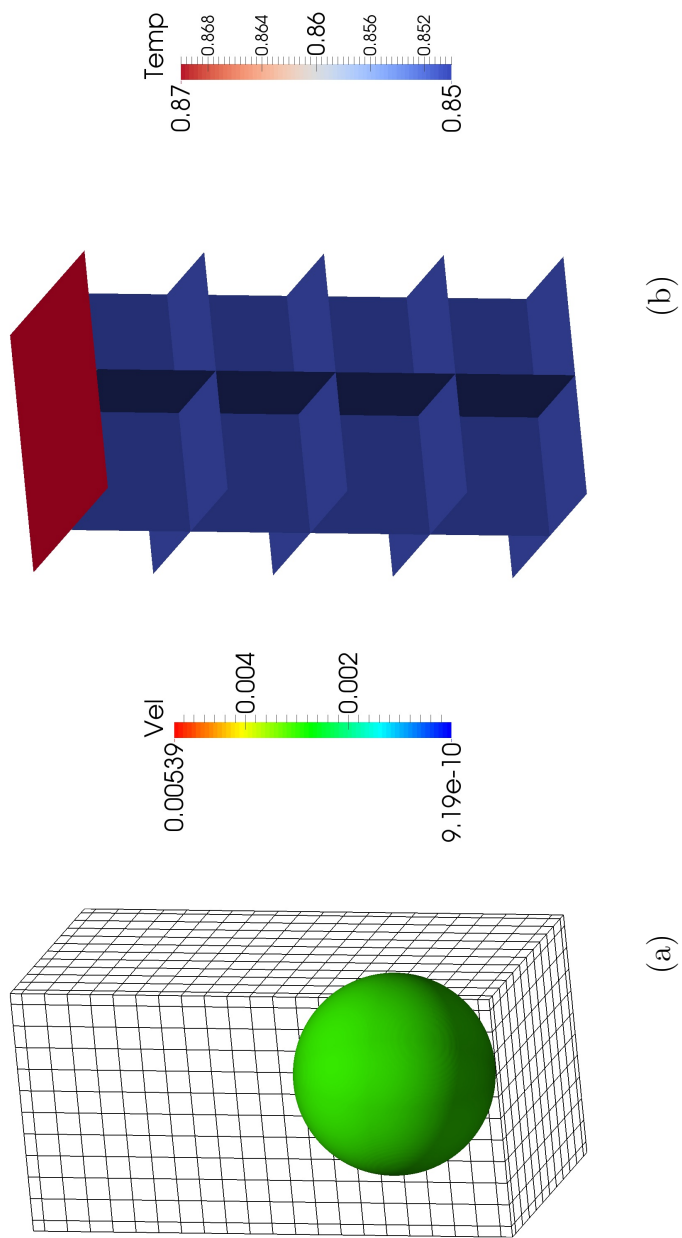
(a)

(b)

Figure 7.9: Three-dimensional thermocapillary motion of a single bubble: Initial conditions for density (a) and temperature (b).
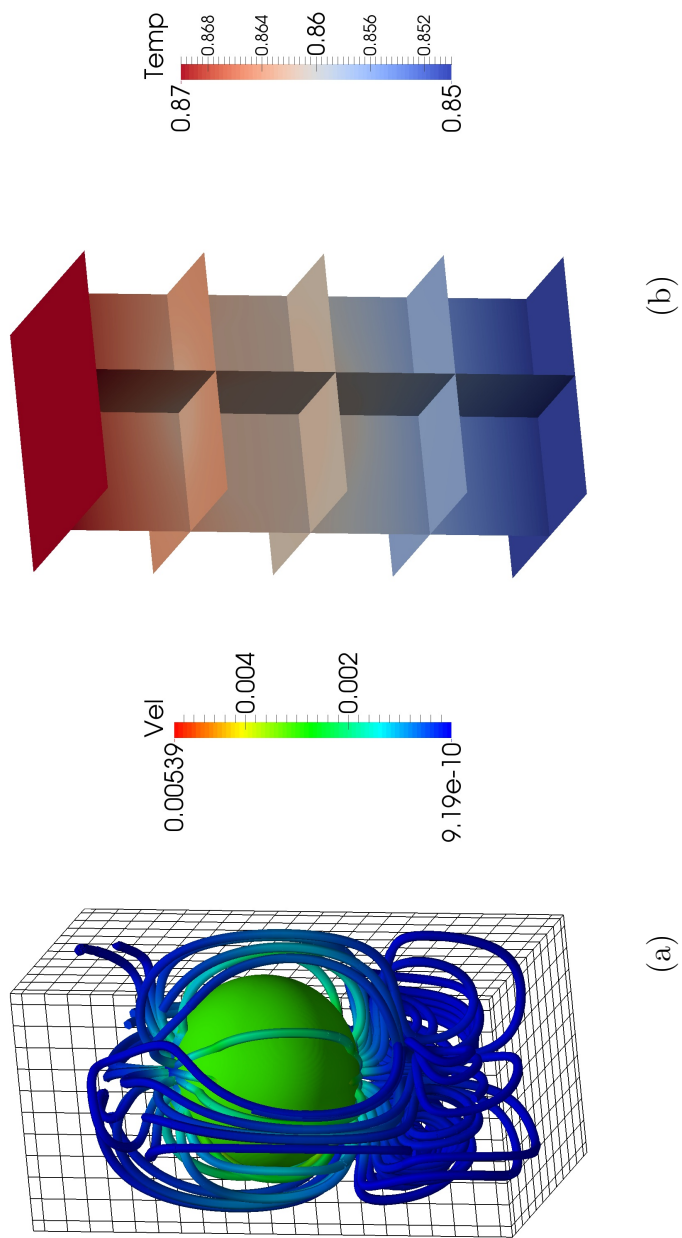
(a)

(b)

Figure 7.10: Solutions of the three-dimensional thermocapillary motion of a single bubble at $t = 80.0$: (a) density isosurface and velocity streamlines, (b) temperature on various slices.
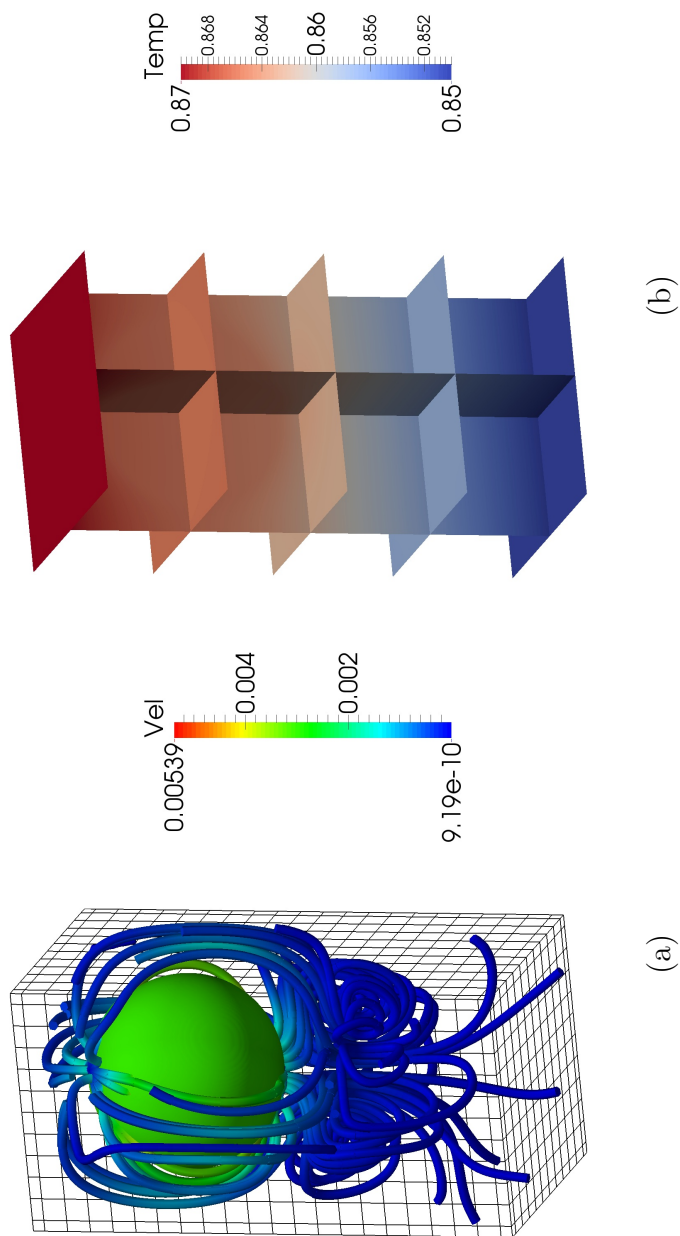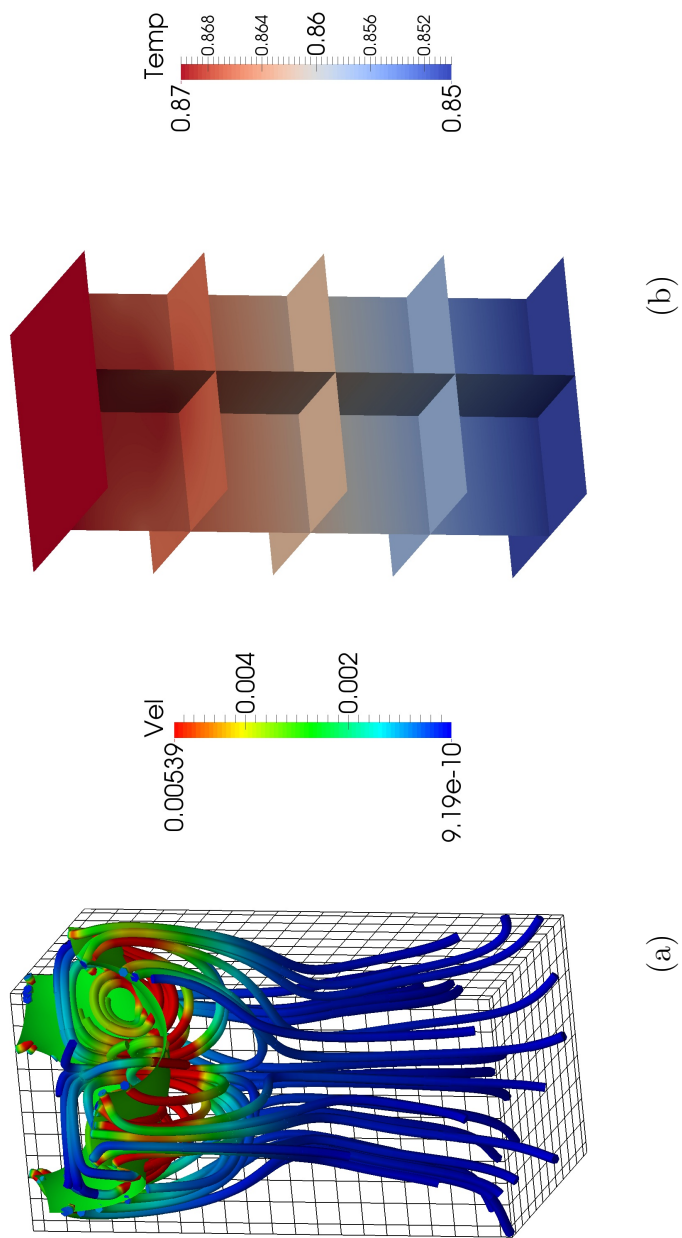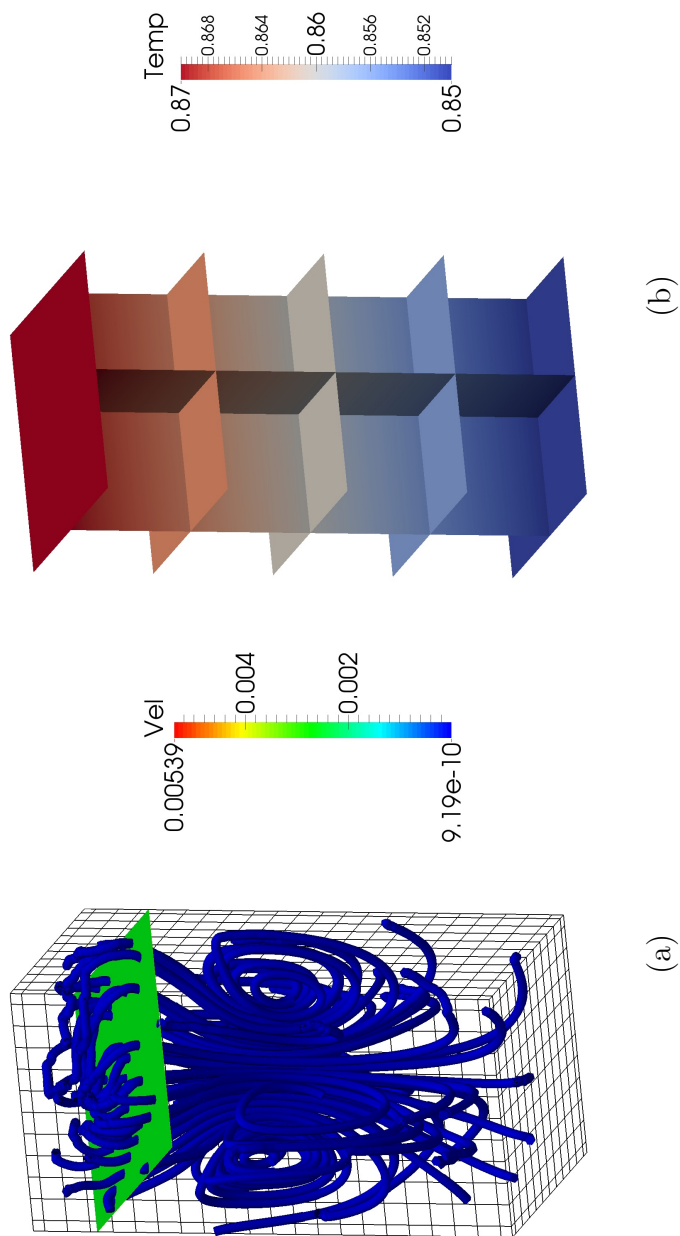
(a)

(b)

Figure 7.11: Solutions of the three-dimensional thermocapillary motion of a single bubble at $t = 120.0$: (a) density isosurface and velocity streamlines, (b) temperature on various slices.

(a)

(b)

Figure 7.12: Solutions of the three-dimensional thermocapillary motion of a single bubble at $t = 160.0$: (a) density isosurface and velocity streamlines, (b) temperature on various slices.

(a)

(b)

Figure 7.13: Solutions of the three-dimensional thermocapillary motion of a single bubble at $t = 200.0$: (a) density isosurface and velocity streamlines, (b) temperature on various slices.

on a heated surface or from a stable superheated vapor layer. The former one is typically referred to as nucleate boiling, while the later one is often named as film boiling. The mode between nucleate boiling and film boiling is called transition boiling. Nucleate boiling is characterized by isolated bubble generation and is the most efficient mode in heat transfer among the three boiling modes. With the increase of the surface temperature, the bubbles on the surface tend to move horizontally and merge together to form a connected layer, which behaves as a thermal isolator between the solid surface and the liquid. Beyond a certain critical surface temperature, a stable vapor film may form between the solid surface and the bulk liquid phase, and vapor bubbles detach from the layer periodically owing to the Rayleigh-Taylor instability. Film boiling is quite dangerous and should be avoided in industry facilities because of its low efficiency in heat transfer. Interested readers are referred to [63] for a thorough discussion of the different boiling modes. Boiling has been extensively employed in energy conversion and exchange facilities, such as power generators, cooling systems for electronic devices, and petroleum refineries. Despite its importance in industry, the fundamental mechanism of boiling, as were admitted by physicists [12, 159] and engineers [65, 118], is still not well understood. During the past decades, experiments have been carried out and empirical correlations have been obtained for engineering designs. However, in view of this phenomenon's disparity of spatiotemporal scales and elusive nature of many subprocesses, the predictive capability of the aforementioned methodologies is rather limited [64].

In the past years, there have been a few but growing numerical studies of boiling. Film boiling has been numerically simulated by the level set method [181], the front tracking method [118], and the volume-of-fluid method [202]. Film boiling is regarded as amenable to analysis, since the governing mechanism is mainly the Rayleigh-Taylor instability. A multiphase solver that can simulate the Rayleigh-Taylor instability should be capable of simulating film boiling. In the aforementioned numerical studies, the simulations all started with a perturbed flat interface as the initial condition for the film boiling. In other words, the film generation process has not been captured by all these methods. On the other side, there is very few work on simulating nucleate boiling, because more physical mechanisms are involved in this phenomenon. A credible nucleate boiling solver is expected to be capable of describing the creation of new interfaces near the nucleation sites, handling the Rayleigh-Taylor instability and the Rayleigh-Bénard instability, and tracking the moving interfaces of bubbles and free surfaces. In [182], the authors have studied the nucleate boiling by specifically designing a model for the region near the nucleate cavities. This model relies on empirical data, including the bubble release rate, the nucleation cite density, etc. Recently, a boiling model has been proposed by using the diffuse-interface concept [159]. In that work, the dependency on empirical data has been significantly reduced. The governing equations are the classical continuum mechanics balance laws endowed with the van der Waals equation of state. However, the model employed does not contain the interstitial working term $\mathbf{\Pi}$, and hence, strictly speaking, the

model in [159] is not thermodynamically consistent. The reported results of [159] shows that the vapor cannot fully contact with the top boundary. All boundaries were wet by the liquid phase during the whole simulation. Since there are very limited information revealed about the numerical method used in that paper, it is unknown why the solutions behaved in such a non-physical way.

In this section, boiling simulations are conducted in two and three dimensions. The model utilized is the thermal Navier-Stokes-Korteweg equations (7.1)-(7.3). To obtain successful boiling simulations, there are several additional modeling considerations. First, the transport parameters should be chosen to be density dependent [159]. Specifically, it is demanded that the dimensionless viscosity $\bar{\mu}$ and the thermal conductivity $\boldsymbol{\kappa}$ are larger in the liquid region than those in the vapor region. In the following simulations, these two material parameters are taken as

$$\bar{\mu} = C_{\mu}^{boil} \rho, \tag{7.239}$$

$$\boldsymbol{\kappa} = C_{\boldsymbol{\kappa}}^{boil} \rho \mathbf{I}, \tag{7.240}$$

with C_{μ}^{boil} and $C_{\boldsymbol{\kappa}}^{boil}$ being constants independent of ρ. Second, gravity effects should be taken into account to generate the buoyant effect. The dimensionless body force $\mathbf{b}$ is fixed as

$$\mathbf{b} = (0; 0; -0.025)^{T}, \tag{7.241}$$

for the three-dimensional case and

$$\mathbf{b} = (0; -0.025)^{T}, \tag{7.242}$$

for the two-dimensional cases. Third, the boundary conditions are designed as follows. The ninety-degree contact angle boundary condition is used for the density variable and the slip boundary condition is applied to the velocity field. To specify the boundary condition for the temperature, the boundary $\partial\Omega$ is first split into three non-overlapping parts:

$$\partial\Omega = \Gamma_t \cup \Gamma_b \cup \Gamma_v, \tag{7.243}$$

$$\Gamma_t = \left\{ \mathbf{x} \in \partial\Omega | \mathbf{n}(\mathbf{x}) \cdot \mathbf{b} < 0 \right\}, \tag{7.244}$$

$$\Gamma_b = \left\{ \mathbf{x} \in \partial\Omega | \mathbf{n}(\mathbf{x}) \cdot \mathbf{b} > 0 \right\}, \tag{7.245}$$

$$\Gamma_v = \left\{ \mathbf{x} \in \partial\Omega | \mathbf{n}(\mathbf{x}) \cdot \mathbf{b} = 0 \right\}. \tag{7.246}$$

With the above partition, the boundary condition for θ is

$$\theta = \theta_h, \quad \text{on } \Gamma_b \times (0, T), \tag{7.247}$$

$$\theta = \theta_c, \quad \text{on } \Gamma_t \times (0, T), \tag{7.248}$$

$$-\mathbf{q} \cdot \mathbf{n} = 0, \quad \text{on } \Gamma_v \times (0, T). \tag{7.249}$$

In the numerical calculations, the Dirichlet boundary conditions for θ on Γ_b and Γ_t should be transformed to the Dirichlet boundary conditions for the entropy variable Y_5 as

$$Y_5 = Y_{5,h} = -\frac{1}{\theta_h}, \quad \text{on } \Gamma_b \times (0, T), \tag{7.250}$$

$$Y_5 = Y_{5,c} = -\frac{1}{\theta_c}, \quad \text{on } \Gamma_t \times (0, T). \tag{7.251}$$

Throughout, the Dirichlet data are chosen as $\theta_h = 0.950$ and $\theta_c = 0.775$. In real situations, the temperature on the solid surface cannot be evenly distributed

due to surface unevenness. To model that effect, the Dirichlet data for Y_5 are perturbed by random functions:

$$Y_{5,h} = -\frac{1}{0.950} + \delta_{Y_{5,h}}(\mathbf{x}), \qquad (7.252)$$

$$Y_{5,c} = -\frac{1}{0.775} + \delta_{Y_{5,c}}(\mathbf{x}), \qquad (7.253)$$

wherein $\delta_{Y_{5,h}}(\mathbf{x})$ and $\delta_{Y_{5,c}}(\mathbf{x})$ are scalar functions with uniform random distributions such that

$$\delta_{Y_{5,h}}(\mathbf{x}) \in [-5.0 \times 10^{-2}, 5.0 \times 10^{-2}], \qquad (7.254)$$

$$\delta_{Y_{5,c}}(\mathbf{x}) \in [-5.0 \times 10^{-3}, 5.0 \times 10^{-3}]. \qquad (7.255)$$

As for the initial conditions, the initial density and temperature are given by hyperbolic tangent functions; the initial velocity is zero. The detailed formulations of the initial conditions are given in the subsequent subsections. These conditions represent a static free surface, with liquid in the bottom region and vapor in the top region. It is worth emphasizing that the initial liquid and vapor densities are all uniformly distributed with no random perturbations. In the classical boiling theory, it was regarded that there should be pre-existing vapor or gas in the imperfections of the heated surface, which serves as boiling onset [63, 165]. In contrast to existing boiling models, there is no artificial manipulation used to serve as boiling onset in this model. The following results will show that the vapor bubble or the vapor film may form automatically without pre-existing nuclei simply due to local temperature variations. This is a fundamental difference between this approach and all other boiling models. It will also be demonstrated that nucleate boiling and film boiling can

be simulated within a unified modeling framework by tuning dimensionless parameters. These modeling features are credited to the thermodynamically consistent nature of the model and the numerical algorithm. It is anticipated that this new methodology may lead to a deeper understanding of boiling.

The rest of this section is organized as follows. In Section 7.9.3.1, a two-dimensional nucleate boiling simulation is presented. In Section 7.9.3.2, a two-dimensional film boiling problem is studied. In Section 7.9.3.3, a three-dimensional boiling simulation is presented.

7.9.3.1 Two-dimensional nucleate boiling

As a first example, I solve the thermal Navier-Stokes-Korteweg equations in a two dimensional rectangular domain $\Omega = (0,1) \times (0, 0.5)$. The material parameters are chosen as

$$\mathrm{We} = 8.401 \times 10^6, \tag{7.256}$$

$$\gamma = 1.333, \tag{7.257}$$

$$C_\mu^{boil} = 1.150 \times 10^{-4}, \tag{7.258}$$

$$C_{\boldsymbol{\kappa}}^{boil} = 1.725 \times 10^{-5}. \tag{7.259}$$

The initial conditions for this problem are

$$\rho_0(\mathbf{x}) = 0.3660 - 0.2971 \tanh \left(\frac{x_2 - 0.35}{2} \sqrt{\mathrm{We}} \right), \tag{7.260}$$

$$\mathbf{u}_0(\mathbf{x}) = \mathbf{0}, \tag{7.261}$$

$$\theta_0(\mathbf{x}) = 0.775. \tag{7.262}$$

In Figure 7.14, the initial conditions for density and temperature have been illustrated. The spatial mesh is comprised of 2048×1024 quadratic NURBS elements. The time step for this problem is fixed to be $\Delta t = 5.0 \times 10^{-4}$ and the problem is integrated up to the final time $T = 1.0 \times 10^2$.
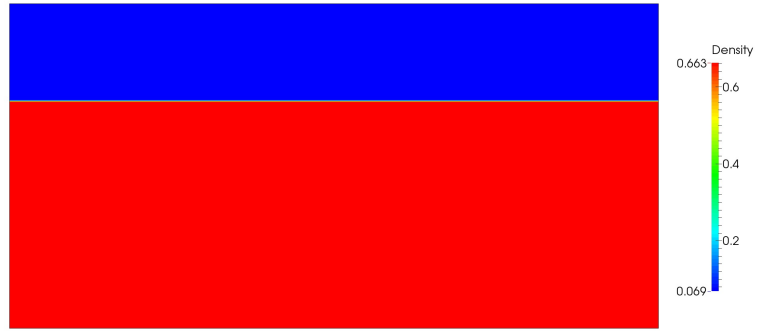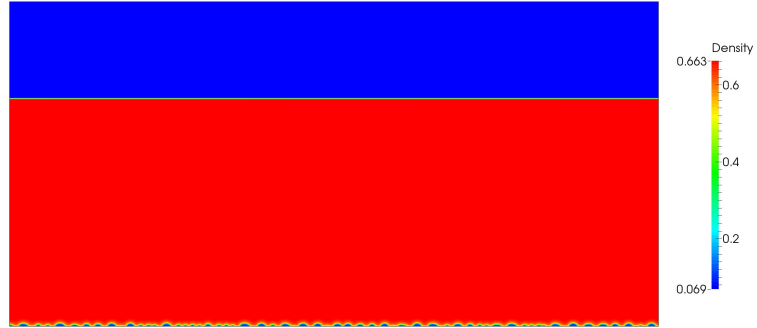

(a)

(b)

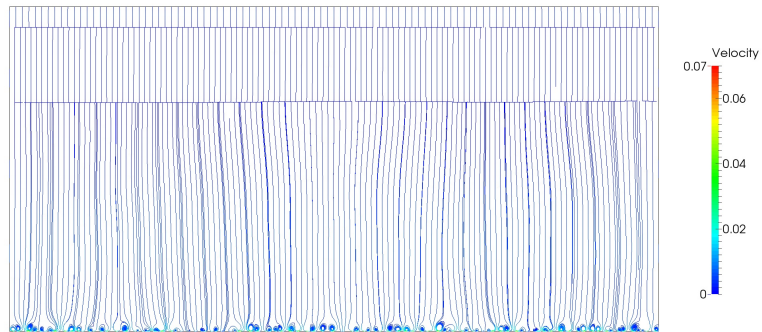Figure 7.14: Initial conditions of the two-dimensional boiling simulation: (a) density, (b) temperature.

In Figures 7.15-7.19, snapshots of the density, temperature, and velocity streamlines are illustrated. It can be observed in Figure 7.15 that tiny vapor bubbles are generated at discrete sites of the heated wall surface at about

(a)

(b)

(c)

Figure 7.15: Solutions of the two-dimensional nucleate boiling simulation at $t = 1.25$: (a) density, (b) temperature, (c) velocity streamlines.
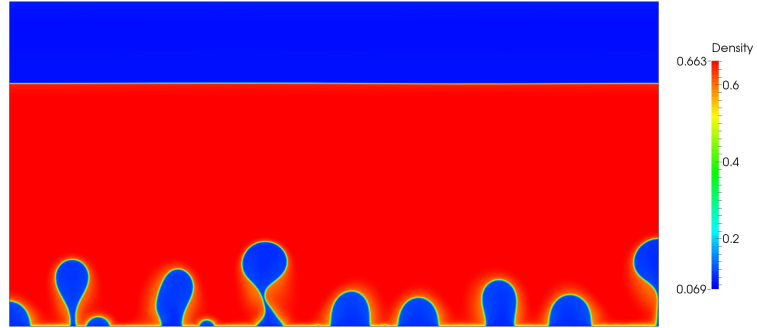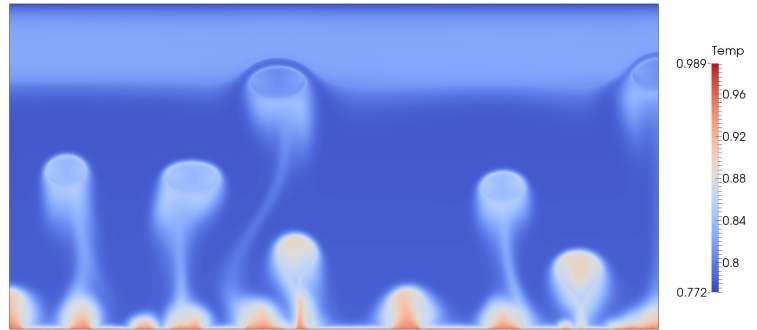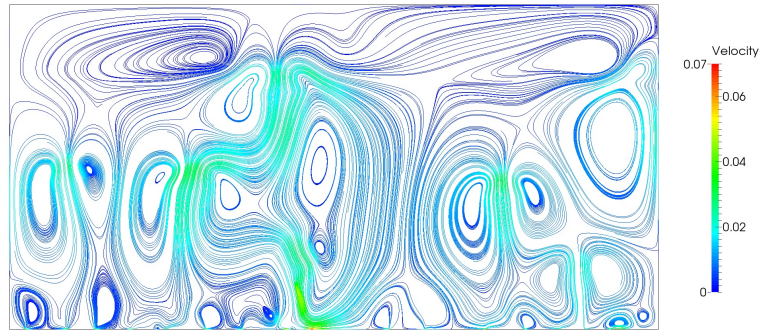
(a)
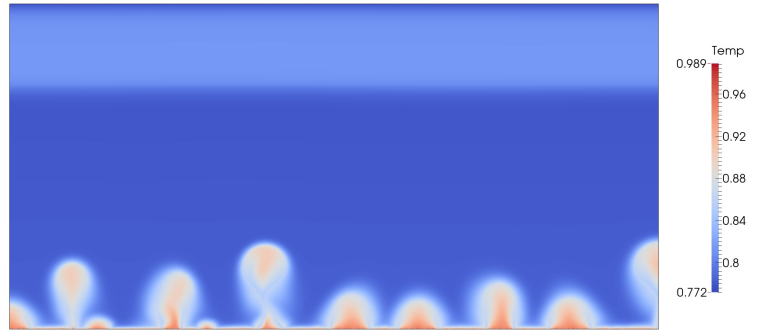
(b)
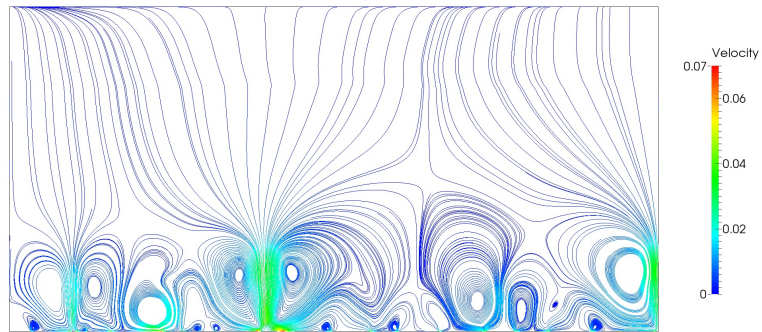
(c)

Figure 7.16: Solutions of the two-dimensional nucleate boiling simulation at $t = 18.75$: (a) density, (b) temperature, (c) velocity streamlines.
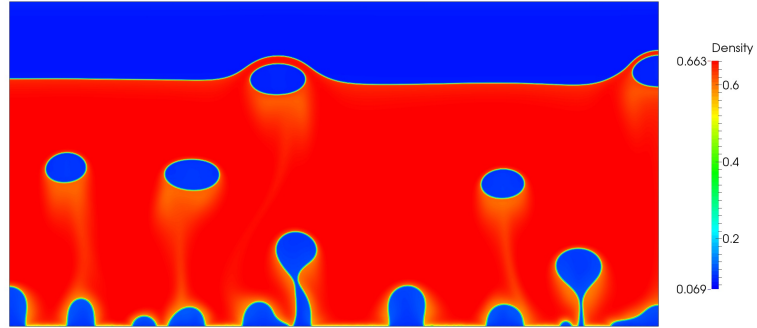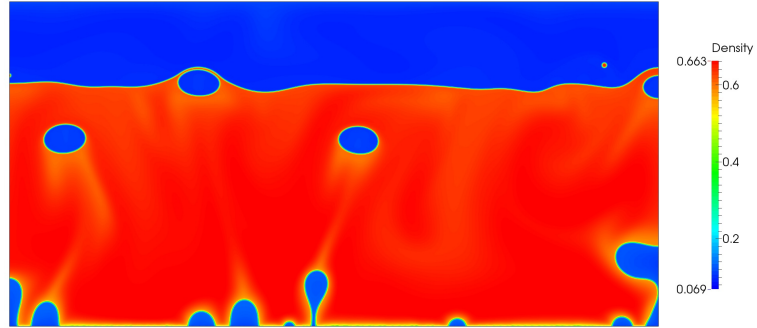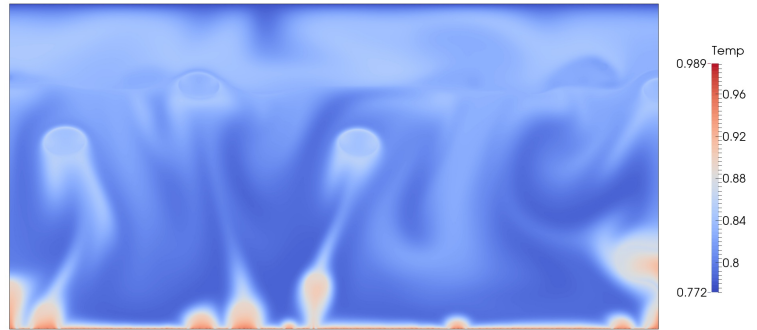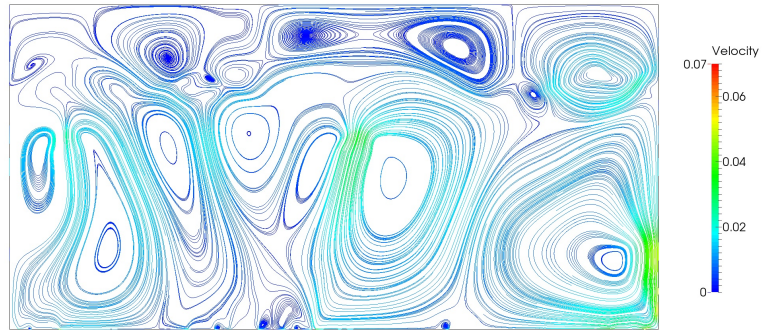
(a)

(b)

(c)

Figure 7.17: Solutions of the two-dimensional nucleate boiling simulation at $t = 31.25$: (a) density, (b) temperature, (c) velocity streamlines.

(a)

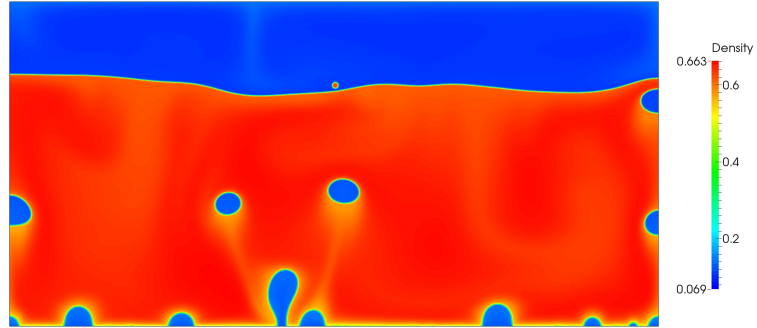

(b)

(c)

Figure 7.18: Solutions of the two-dimensional nucleate boiling simulation at $t = 62.5$: (a) density, (b) temperature, (c) velocity streamlines.

(a)

(b)
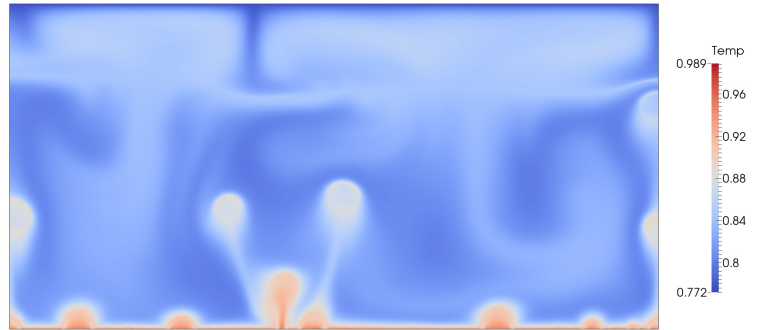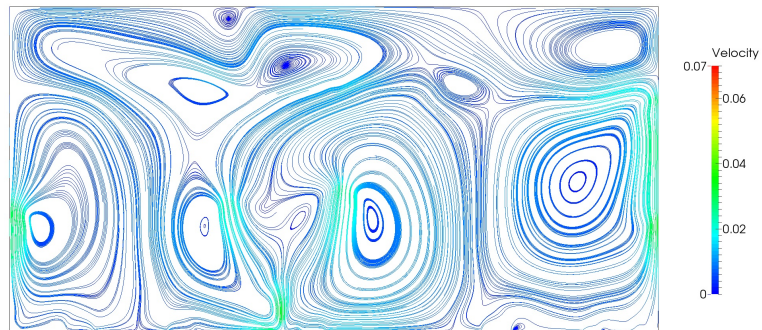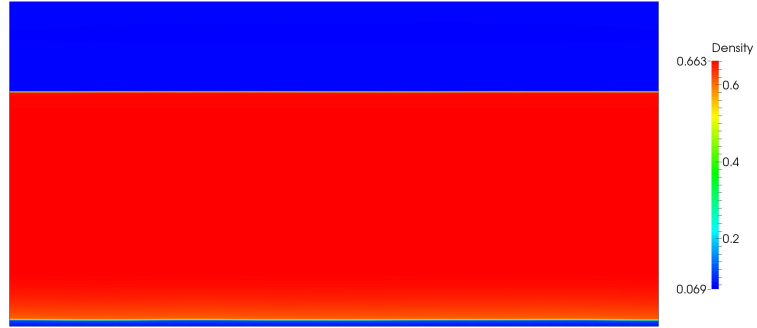

(c)

Figure 7.19: Solutions of the two-dimensional nucleate boiling simulation at $t = 100.0$: (a) density, (b) temperature, (c) velocity streamlines.

$t = 1.25$. These small bubbles soon merge together and form larger vapor bubbles, as is shown in Figure 7.16. The increase of bubble size leads to the growth of the buoyant effect. When the buoyant effect become dominant over the thermocapillary effect, the bubbles start to get detached from the bottom boundary and rise upward. At about $t = 18.75$, the first three bubbles get detached from the bottom. More bubbles are generated on the bottom surface simultaneously. Figures 7.17 and 7.18 show the moments when two bubbles are about to reach the free surface. In Figures 7.18 and 7.19, it can be seen that there are small droplets generated due to the breakage of the liquid film when the vapor bubbles reach the free surface. There are totally 30 bubbles formed in the time interval of $0 < t < 100$.

7.9.3.2   Two-dimensional film boiling

In the second numerical experiment, the same two-dimensional problem considered in Section 7.9.3.1 is simulated again with a different material property parameter C_μ^{boil}. The parameter C_μ^{boil} is chosen to be 4.600×10^{-4}, which is four times larger than the parameter used in the previous example. The simulation is integrated in time up to $T = 5.0 \times 10^2$, because the fluid motion in this example is relatively slower. All the other model and simulation parameters are identical to those in the previous case.
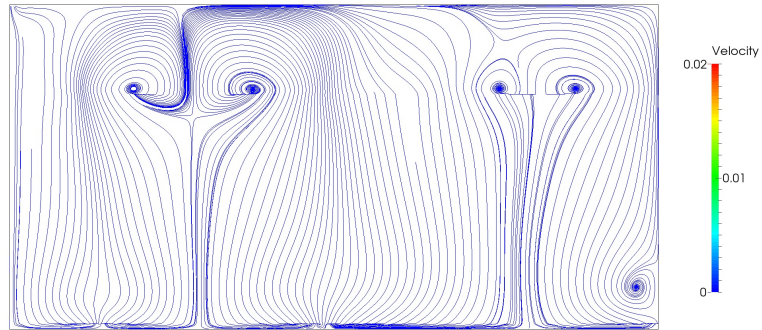
In Figures 7.20-7.24, snapshots of the density, temperature, and velocity streamlines at different time steps are presented. It is worth re-emphasizing that the initial density profile is uniform with no random perturbation, as

(a)

(b)

(c)

Figure 7.20: Solutions of the two-dimensional film boiling simulation at $t = 100.0$: (a) density, (b) temperature, (c) velocity streamlines.

(a)

(b)

(c)

Figure 7.21: Solutions of the two-dimensional film boiling simulation at $t = 175.0$: (a) density, (b) temperature, (c) velocity streamlines.

(a)

(b)

(c)

Figure 7.22: Solutions of the two-dimensional film boiling simulation at $t = 200.0$: (a) density, (b) temperature, (c) velocity streamlines.

(a)

(b)
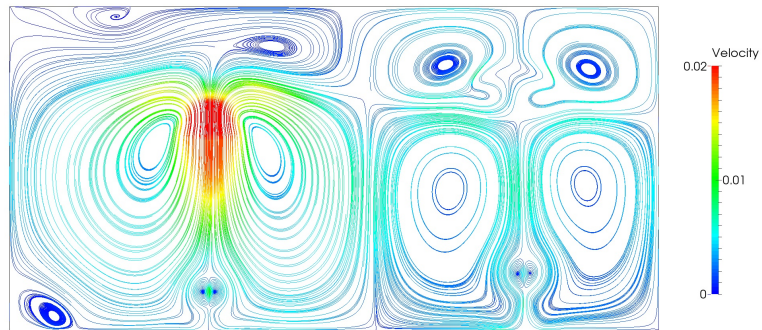
(c)

Figure 7.23: Solutions of the two-dimensional film boiling simulation at $t = 225.0$: (a) density, (b) temperature, (c) velocity streamlines.
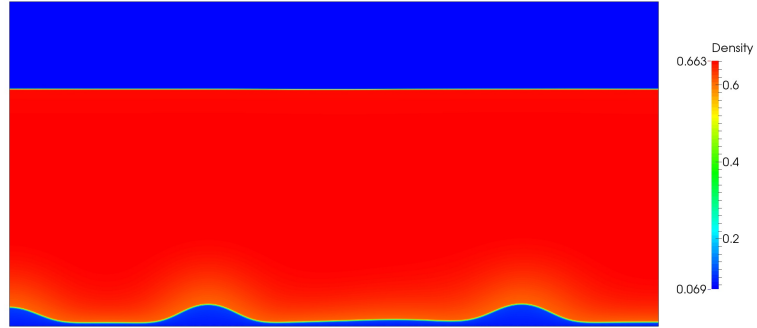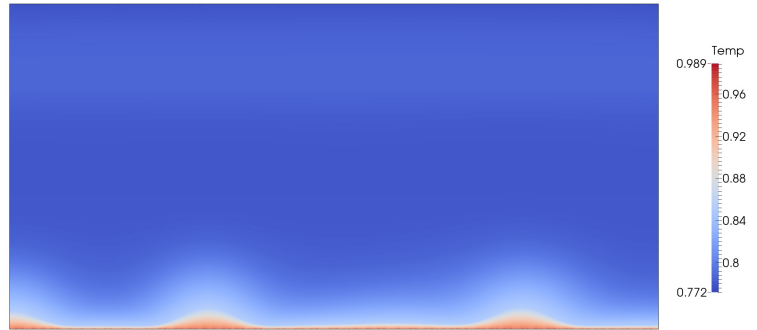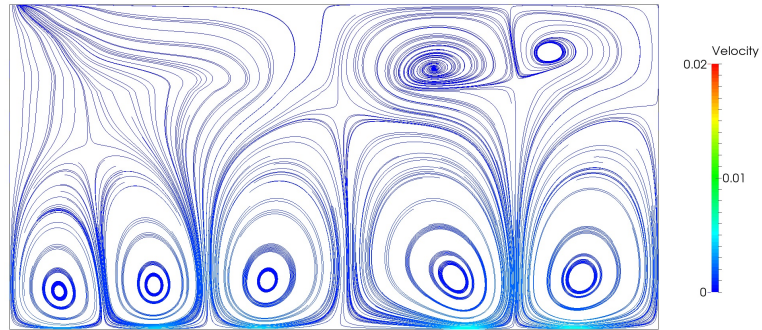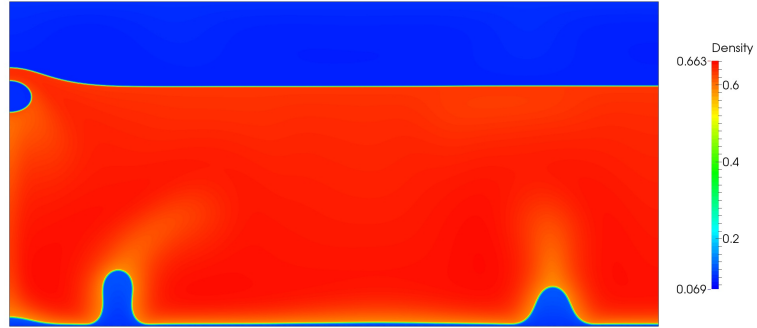
(a)
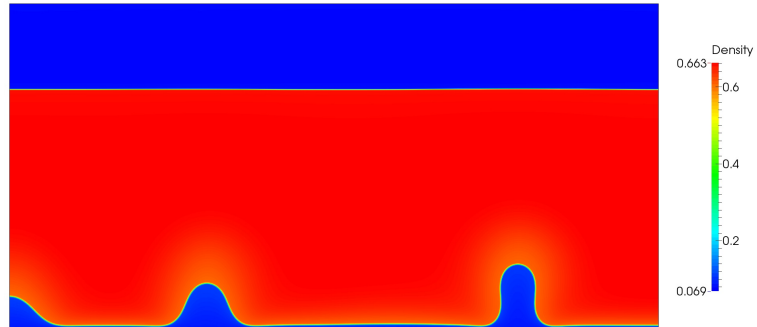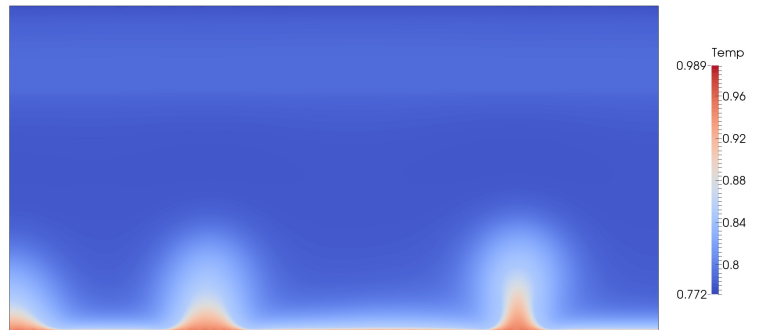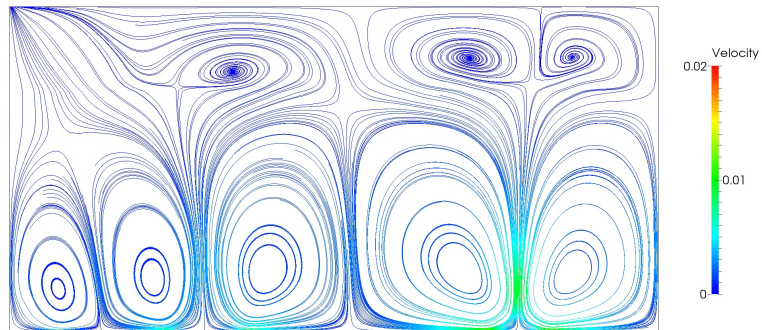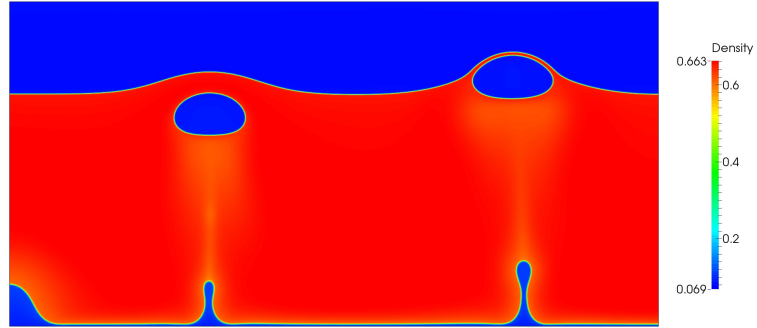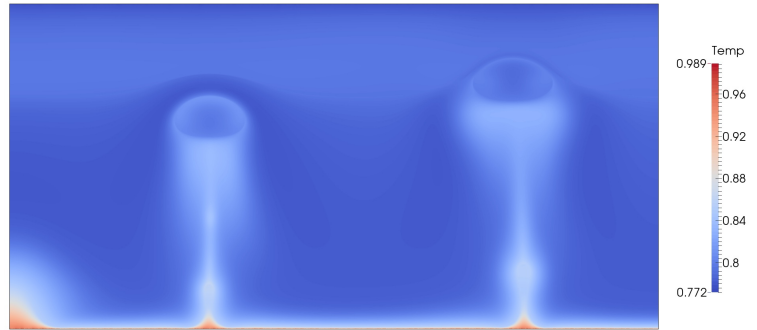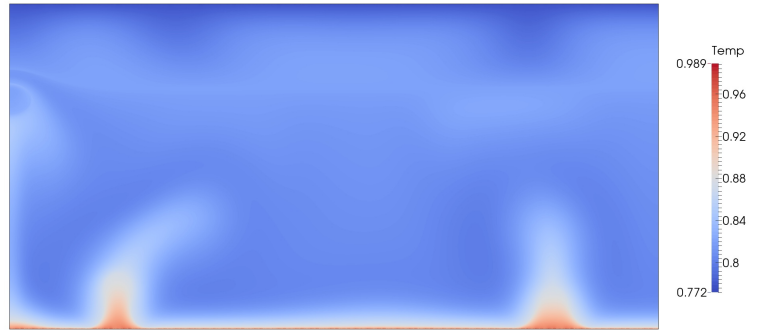

(b)
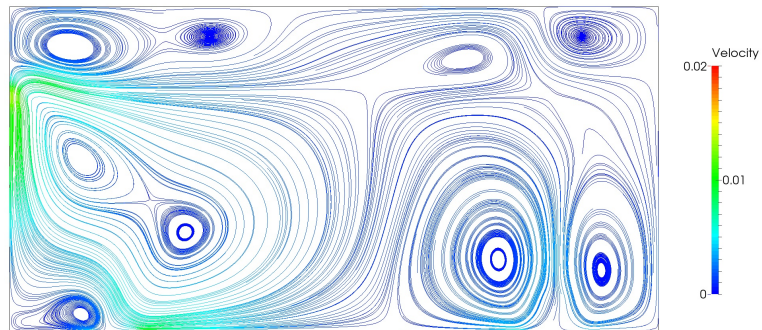
(c)

Figure 7.24: Solutions of the two-dimensional film boiling simulation at $t = 500.0$: (a) density, (b) temperature, (c) velocity streamlines.

is shown in Figure 7.14. Once the simulation starts, there is a thin vapor film generated at the bottom during the early stage of the simulation (Figure 7.20). As time evolves, the interface gradually becomes unstable and there are three mushroom-shaped vapor bubbles formed (Figures 7.21 and 7.22). From $t = 200.0$ to $t = 225.0$, the first two vapor bubbles pinch off from the vapor layer and rise upward in ellipsoidal shapes. As the bubbles get released from the vapor film, two stems are left on the vapor film, where new bubbles are formed. This process repeats itself periodically. Till the final time $t = 500.0$, there are totally seven bubbles generated and detached from the vapor film. The average bubble release rate for this film boiling problem is much less than that of the nucleate boiling counterpart.

7.9.3.3   Three-dimensional boiling

For the three-dimensional problem, the computational domain is restricted to $\Omega = (0, 1) \times (0, 0.5) \times (0, 0.25)$. The material properties are chosen as

$$We = 6.533 \times 10^5, \tag{7.263}$$

$$\gamma = 1.333, \tag{7.264}$$

$$C_\mu^{boil} = 1.289 \times 10^{-4}, \tag{7.265}$$

$$C_\kappa^{boil} = 7.732 \times 10^{-5}. \tag{7.266}$$

The initial conditions for this three-dimensional problem are similar to those of the two-dimensional problem, except the free surface is defined by $x_3 = 0.15$:

$$\rho_0(\mathbf{x}) = 0.33565 - 0.26675 \tanh\left(\frac{x_3 - 0.15}{2}\sqrt{\text{We}}\right), \qquad (7.267)$$

$$\mathbf{u}_0(\mathbf{x}) = \mathbf{0}, \qquad (7.268)$$

$$Y_{5,0}(\mathbf{x}) = -1.2334 - 0.0569 \tanh\left(\frac{x_3 - 0.15}{2}\sqrt{\text{We}}\right). \qquad (7.269)$$

The spatial mesh is comprised of $600 \times 300 \times 150$ quadratic NURBS elements. The problem is integrated in time up to $T = 20.0$ with a fixed time step size $\Delta t = 2.0 \times 10^{-3}$.

Remark 7.9.1. *The initial condition* (7.269) *is in fact a hyperbolic tangent interpolation of* $\theta = 0.85$ *for* $x_2 < 0.15$ *and* $\theta = 0.775$ *for* $x_2 > 0.15$.

In Figures 7.25-7.30, snapshots of density isosurfaces, velocity stream-lines, and temperature isosurfaces are presented at times $t = 0.0, 0.6, 5.0, 11.0$, 14.0 and 20.0. At the initial stage, there is an unstable vapor film formed over the heated wall surface (see Figure 7.26). This film soon separates into isolated vapor bubbles located at random sites on the bottom surface (see Figures 7.27 and 7.28). These bubbles grow in size as time evolves. With the growing of the bubbles, the thermal energy is conducted through the vapor region mainly by convection. Since the simulation domain is very shallow in the z-direction, these bubbles reach the free surface before they get fully released from the bottom. When these high-temperature vapor bubbles reach the cooled top surface, they condense into liquid droplets instantaneously (see Figure 7.29).

At $t = 20.0$, a second round of vapor bubbles is clearly generated on the bottom and the liquid droplets on the top surface get merged together. There is clearly a complex Rayleigh-Bénard mixing structure for the temperature field, as is shown in Figure 7.30.
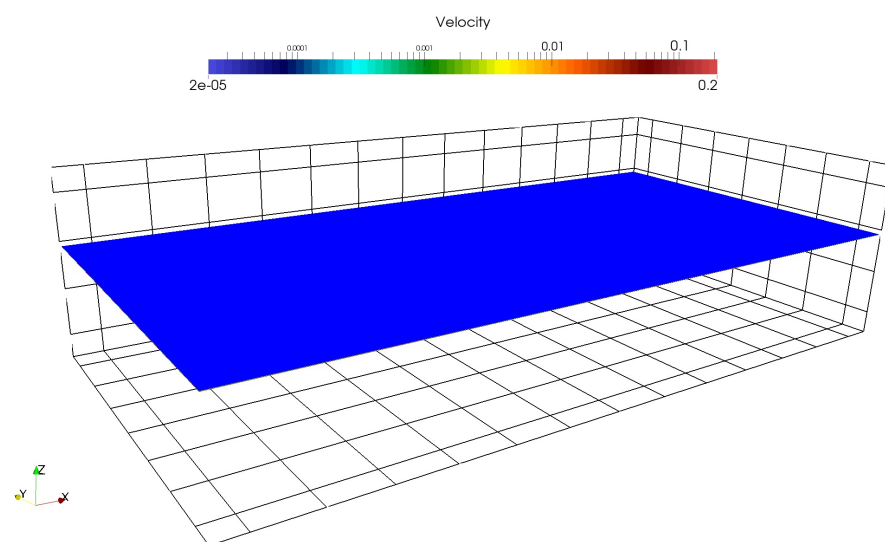
(a)
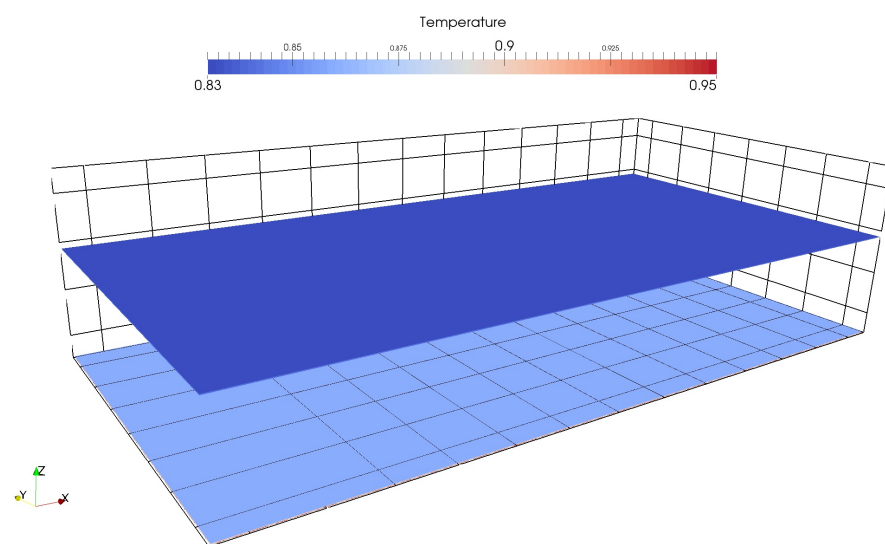
(b)

Figure 7.25: Initial conditions of the three-dimensional boiling: (a) density isosurfaces, (b) temperature isosurfaces.
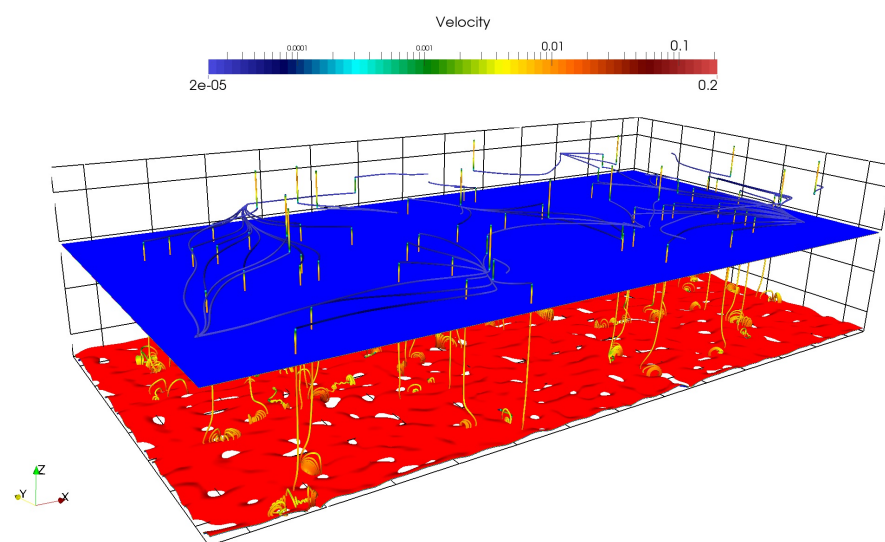
(a)
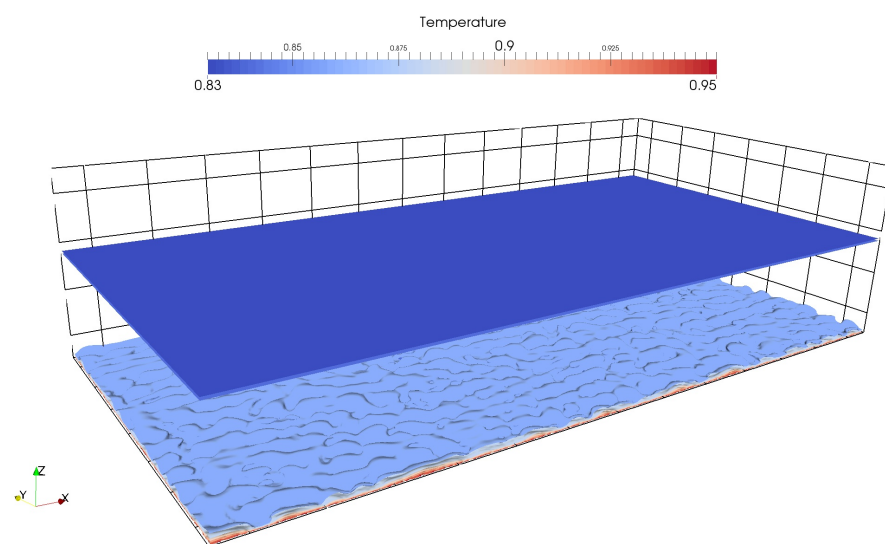
(b)

Figure 7.26: Solutions of the three-dimensional boiling at time $t = 0.6$: (a) density isosurfaces and velocity streamlines, (b) temperature isosurfaces.
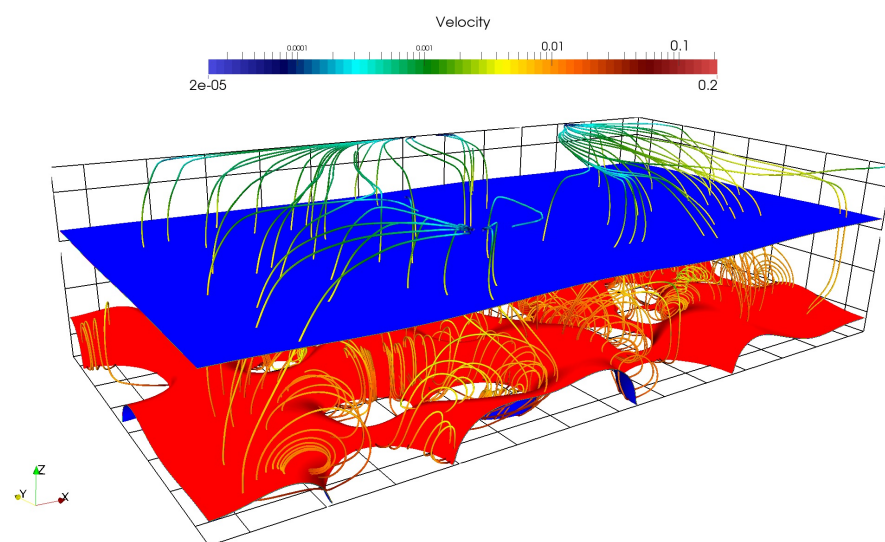
(a)
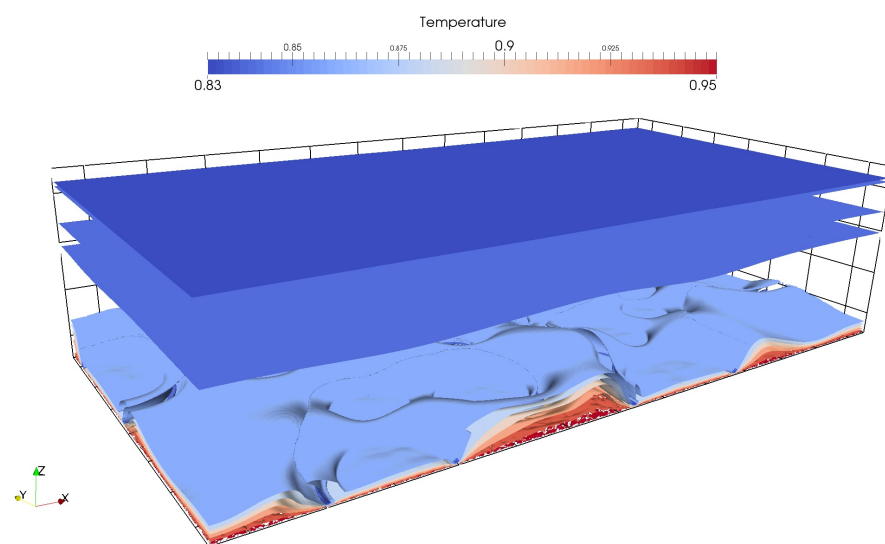
(b)

Figure 7.27: Solutions of the three-dimensional boiling at time $t = 5.0$: (a) density isosurfaces and velocity streamlines, (b) temperature isosurfaces.

307
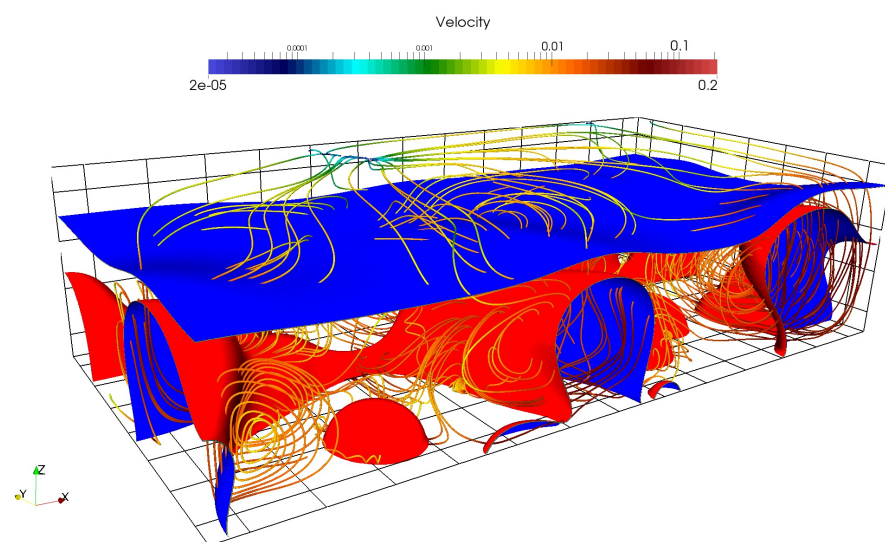
(a)
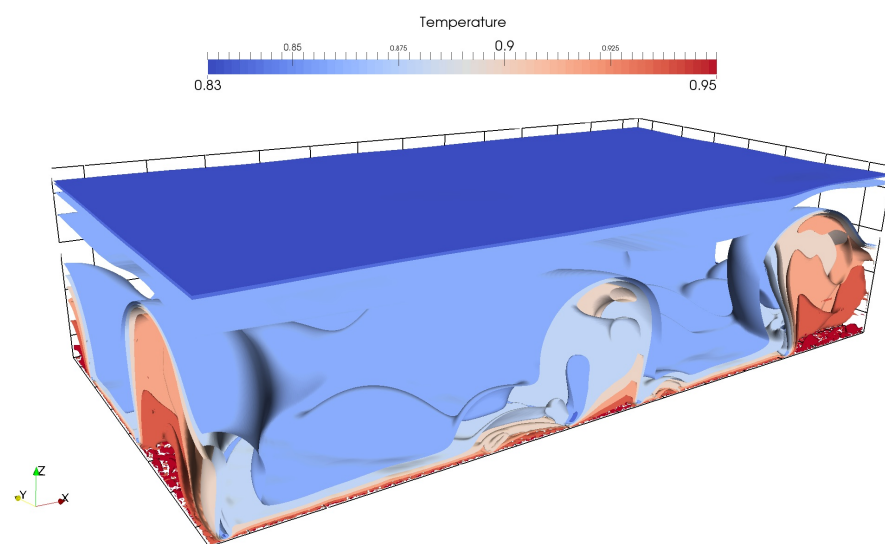
(b)

Figure 7.28: Solutions of the three-dimensional boiling at time $t = 11.0$: (a) density isosurfaces and velocity streamlines, (b) temperature isosurfaces.
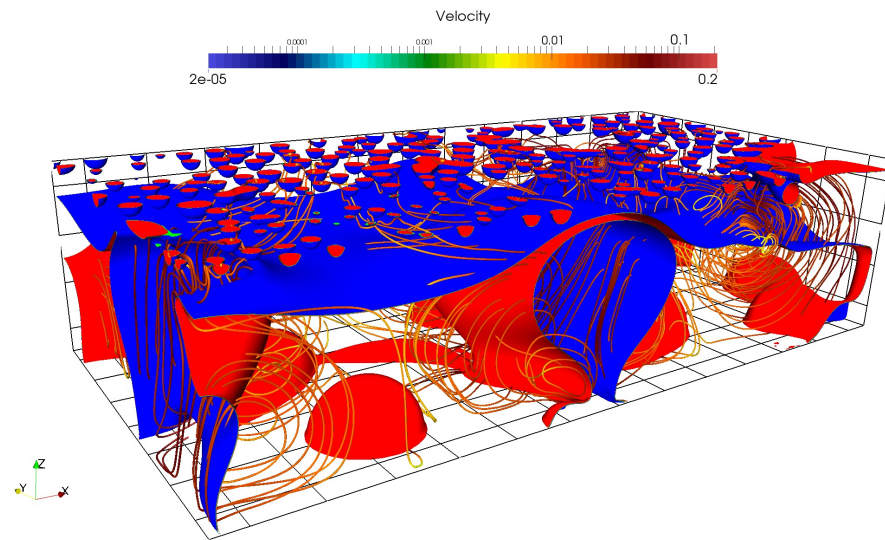
(a)
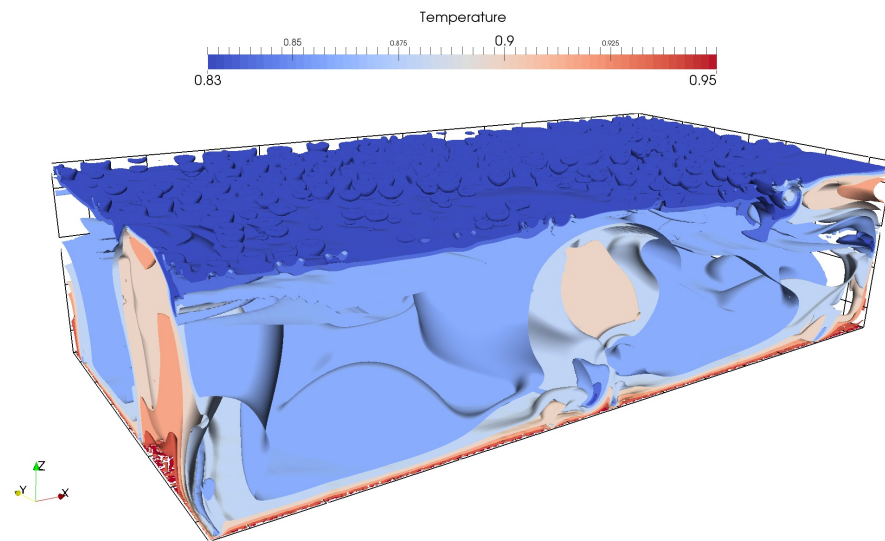
(b)

Figure 7.29: Solutions of the three-dimensional boiling at time $t = 14.0$: (a) density isosurfaces and velocity streamlines, (b) temperature isosurfaces.
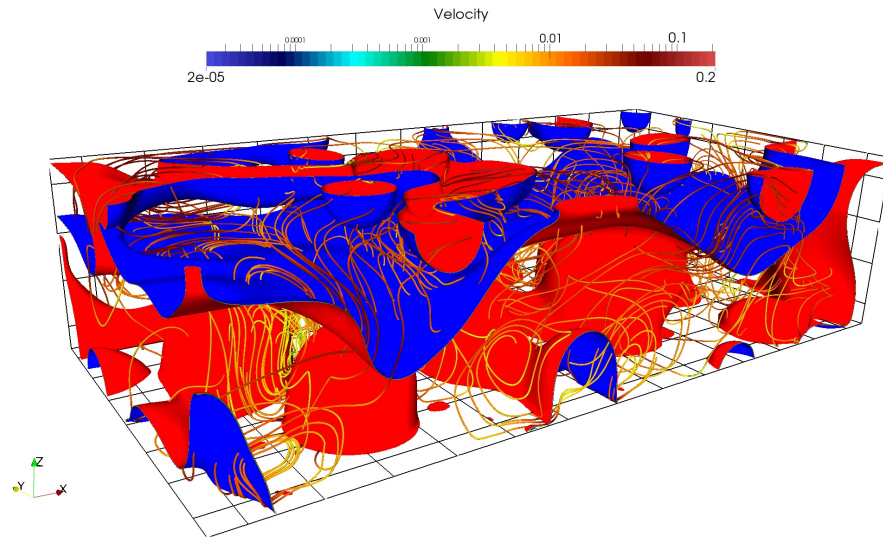
(a)
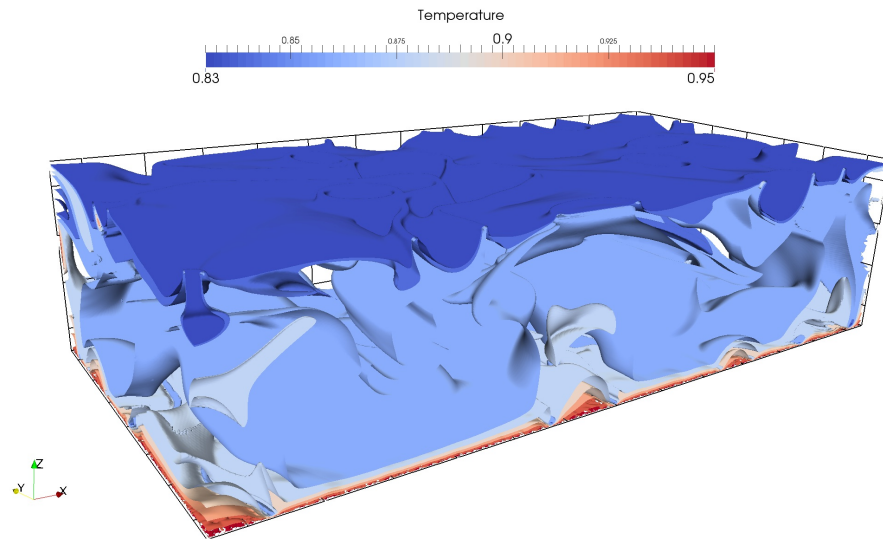
(b)

Figure 7.30: Solutions of the three-dimensional boiling at time $t = 20.0$: (a) density isosurfaces and velocity streamlines, (b) temperature isosurfaces.

310

Chapter 8

Conclusions and future work

> "[...] what is clear and easily comprehended attracts, the
> complicated repels us."
>
> — David Hilbert, 1900

This dissertation presents a comprehensive suite of theoretical and numerical methodologies for the study of multiphase flow problems. In the following, let me conclude the contributions of this dissertation.

A continuum mechanics modeling framework has been systematically developed in Chapter 2. In this framework, the microforce concept [94] has been adopted in order to accommodate the nonlocal surface energies. Within this framework, all the constitutive relations are represented in terms of a free energy potential. The general formulations of the constitutive relations allow the description of a variety of materials, with emphasis on the interfacial effects. Meanwhile, the general constitution formulas intrinsically respect the second law of thermodynamics. Therefore, to close the model, one only needs to design a mathematical formulation for the thermodynamic potential. The resulting constitutive relations together with the balance equations make the system formally well-posed and thermodynamically consistent.

Within this framework, several instantiations have been presented in

Chapter 3. These examples include the perfect gas model, the van der Waals fluid model, the Cahn-Hilliard-type multicomponent fluid model, and a brand-new multicomponent multiphase fluid model. The recovered van der Waals fluid model is identical to the model derived by Dunn and Serrin [69]. The mysterious interstitial work flux introduced by the two authors arises naturally as the microforce power expenditure in this modeling framework. Existing mathematical results on this model has been summarized. The Cahn-Hilliard free energy has been generalized to model multicomponent fluid flow. In particular, the isothermal two-component fluid model is identical to a classical model derived by Lowengrub and Truskinovsky [145]. A brand-new multicomponent multiphase flow model is introduced, with the objective of modeling the air, water, and water vapor system. The thermodynamic potential for this system has been devised to describe the dynamics of both immiscible and miscible interfaces. This modeling procedure may open a door to more faithful models of water mists, boiling flows, cavitating flows, etc.

A general-purpose, parallel computing software, named `PERIGEE`, has been developed in this work. Currently, the software supports scalable transient nonlinear NURBS-based isogeometric analysis. The `PERIGEE` preprocessor makes use of METIS [121] to generate high-quality mesh partitions. State-of-the-art parallel solvers are accessible through PETSc [13]. The analysis data can be post-processed in parallel by VTK [1] and ParaView [104]. The object-oriented programming style of `PERIGEE` eases future implementations of new models. Its strong scalability has been demonstrated to be satisfactory

on the Dell Linux cluster Stampede up to 4096 cores at the Texas Advanced Computing Center.

In Chapter 4, a numerical technique named periodic transformation operator has been developed. This discrete operator can transform a class of open-knot NURBS basis functions to periodic NURBS basis functions. In the meantime, the geometry represented by the original NURBS basis functions is maintained by updating the control points. The update procedure is constructed based on the same periodic transformation operator. In doing so, the strong imposition of periodic boundary conditions is achieved by simply modifying the ID arrays [107]. Moreover, this periodic transformation operator can be combined with the Bézier extraction operator to further simplify the implementation of the element routine for the periodic NURBS basis functions.

In Chapter 5, a passive two-component fluid model is numerical investigated. The purpose of this study is twofold. First, isogeometric analysis together with the generalized-α method and an adaptive time-step scheme is applied to numerically study a simplified Cahn-Hilliard two-component fluid model. In comparison with the existing numerical and experimental results, the two-component Cahn-Hilliard fluid model proposed in Chapter 3 is validated in part. The numerical experiments also demonstrate that the proposed numerical methodology is efficient, accurate, and robust for solving the multicomponent flow problem. Second, the periodic transformation operator is applied to enforce C^1-periodic boundary conditions at the inflow and outflow boundaries of a Taylor-Couette cell. The numerical tests suggest that the pe-

riodic transformation operator developed in Chapter 4 is critical for obtaining qualitatively correct results.

One major contribution of this dissertation is the construction of an entropy-dissipative fully discrete scheme for the Navier-Stokes-Korteweg equations. For problems endowed with non-convex entropy functions, the definition of entropy variables has to be generalized to the functional setting. This generalization leads to a weak formulation that guarantees entropy production. To inherit the dissipation property in the time direction, new time integration schemes based on a family of quadrature rules have been developed. Unlike the space-time time integration method, the new temporal discretization methods do not require convexity for the mathematical entropy function. It can be utilized to construct provably entropy-dissipative schemes, while achieving second-order accuracy in time. The aforementioned properties make the method very promising in constructing numerical schemes for nonlinear non-convex problems. The novel numerical technologies have been first applied to the isothermal Navier-Stokes-Korteweg equations in Chapter 6 and later to the thermal Navier-Stokes-Korteweg equations in Chapter 7. Entropy dissipation and temporal error estimates have been proved and these theoretical results have been corroborated by a number of numerical examples. The numerical techniques have also been utilized to explore a variety of application examples, including the bubble dynamics, the droplet wetting on a solid substrate, the evaporation and condensation of a single bubble, the thermocapillary effects, and the boiling flows. It is worth noting that nowadays boiling simulation is

314

still regarded to be highly difficult. For the existing models, empirical knowledge about boiling is needed to carry out the simulation successfully. In my numerical examples, two and three-dimensional boiling problems, including nucleate boiling and film boiling, have been successfully simulated by solving the thermal Navier-Stokes-Korteweg equations. Owing to the thermodynamically consistent nature of the model, new bubbles are generated and released automatically. Empirical data have largely become unnecessary in this model. This is, to the best of the author's knowledge, the first boiling model that does not require any empirical knowledge. It is anticipated that this methodology may provide a new approach for high-fidelity numerical prediction of boiling curves [64].

There are many promising research directions based on the current work. On the software development side, PERIGEE continues to grow in many directions. New elements, including T-splines [171], hierarchical B-splines [168], and divergence-conforming B-splines [72], are planned to be added. Also, parallel adaptive mesh refinement will be enabled by employing the p4est library [36]. On the modeling side, the van der Waals fluid model will be applied to simulating the cavitating flows. Unlike the boiling flows, cavitation is induced by local pressure variations. One major challenge for this problem is a proper design of the open boundary conditions on the outflow boundary [62]. Furthermore, the van der Waals model is a good approximation for many real fluids, but it is not good enough. There are many modifications for the van der Waals fluid model, the most notable of which is the model proposed by

Serrin [175]. This model is expected to give more accurate material description than the previous models. Thus, it is anticipated that the Serrin's model may provide better predictive capability for problems like boiling flows. In addition to the liquid-vapor fluid model, the multicomponent multiphase fluid model developed in Chapter 3 remains to be explored. It is optimistic that this new model may be applied to studying more intriguing physical problems, like the dynamics of sprays.

Bibliography

[1] The Visualization Toolkit. http://www.vtk.org.

[2] R.A. Adams. *Sobolev Spaces*. Academic Press, 1975.

[3] I. Akkerman, Y. Bazilevs, C.E. Kees, and M.W. Farthing. Isogeometric analysis of free-surface flow. *Journal of Computational Physics*, 230:4137–4152, 2011.

[4] S.M. Allen and J.W. Cahn. A microscopic theory for antiphase boundary motion and its application to antiphase domain coarsening. *Acta Metallurgica*, 27:1085–1095, 1979.

[5] D.M. Anderson, G.B. McFadden, and A.A. Wheeler. Diffuse-interface methods in fluid mechanics. *Annual Review of Fluid Mechanics*, 30:139–165, 1998.

[6] J.D. Anderson. *Hypersonic and High Temperature Gas Dynamics*. New York: McGraw-Hill, 1989.

[7] J.D. Anderson. *Modern Compressible Flow: With Historical Perspective*. McGraw-Hill, 2003.

[8] L.K. Antanovskii. A phase field model of capillarity. *Physics of Fluids*, 7:747, 1995.

[9] R.P. Araujo and D.L.S. McElwain. A mixture theory for the genesis of residual stresses in growing tissues I: A general formulation. *SIAM Journal of Applied Mathematics*, 65:1261–1284, 2005.

[10] T. Arbogast, J. Douglas Jr, and J.E. Santos. Two-phase immiscible flow in naturally fractured reservoirs. *Numerical Simulation in Oil Recovery*, 11:47–66, 1988.

[11] V.E. Badalassi, H.D. Ceniceros, and S. Banerjee. Computation of multiphase systems with phase field models. *Journal of Computational Physics*, 190:371–390, 2003.

[12] A. Badillo. Quantitative phase-field modeling for boiling phenomena. *Physical Review E*, 86:041603, 2012.

[13] S. Balay, S. Abhyankar, M.F. Adams, J. Brown, P. Brune, K. Buschelman, V. Eijkhout, W.D. Gropp, D. Kaushik, M.G. Knepley, L.C. McInnes, K. Rupp, B.F. Smith, and H. Zhang. PETSc users manual. Technical Report ANL-95/11-Revision 3.5, Argonne National Laboratory, 2014.

[14] G. I. Barenblatt. *Similarity, self-similarity, and intermediate assymptotics*. Plenum Press, New York and London, 1979.

[15] Y. Bazilevs, V.M. Calo, J.A. Cottrell, J.A. Evans, T.J.R. Hughes, S. Lipton, M.A. Scott, and T.W. Sederberg. Isogeometric analysis using T-splines. *Computer Methods in Applied Mechanics and Engineering*, 199:229–263, 2010.

[16] Y. Bazilevs, V.M. Calo, J.A. Cottrell, T.J.R. Hughes, A. Reali, and G. Scovazzi. Variational multiscale residual-based turbulence modeling for large eddy simulation of incompressible flows. *Computer Methods in Applied Mechanics and Engineering*, 197:173–201, 2007.

[17] Y. Bazilevs, V.M. Calo, T.J.R. Hughes, and Y. Zhang. Isogeometric fluid-structure interaction: theory, algorithms, and computations. *Computational Mechanics*, 43:3–37, 2008.

[18] Y. Bazilevs and T.J.R. Hughes. Weak imposition of Dirichlet boundary conditions in fluid mechanics. *Computers & Fluids*, 36:12–26, 2007.

[19] Y. Bazilevs, L.B. Da Veiga, J.A. Cottrell, T.J.R. Hughes, and G. Sangalli. Isogeometric analysis: approximation, stability and error estimates for h-refined meshes. *Mathematical Models and Methods in Applied Sciences*, 16:1031–1090, 2006.

[20] J.A. Beattie and O.C. Bridgeman. A New Equation of State for Fluids. I. Application to Gaseous Ethyl Ether and Carbon Dioxide. *Journal of the American Chemical Society*, 49:1665–1667, 1927.

[21] T. Belyschko and T.J.R. Hughes, editors. *Computational methods for transient analysis*. Elsevier Science Publisher B.V., 1983.

[22] M. Benedict, G.B. Webb, and L.C. Rubin. An Empirical Equation for Thermodynamic Properties of Light Hydrocarbons and Their Mixtures I.

Methane, Ethane, Propane and n-Butane. *Journal of Chemical Physics*, 8:334–345, 1940.

[23] S. Benzoni-Gavage. Stability of subsonic planar phase boundaries in a van der Waals fluid. *Archive for Rational Mechanics and Analysis*, 150:23–55, 1999.

[24] C. Blanc and C. Schlick. Accurate Parametrization of Conic by NURBS. *Computer Graphics and Applications*, 16:64–71, 1996.

[25] W.J. Boettinger, J.A. Waren, C. Beckermann, and A. Karma. Phase-Field Simulation of Solidification. *Annual Review of Materials Research*, 32:163–194, 2002.

[26] C. De Boor. On calculation with B-splines. *Journal of Approximation Theory*, 6:50–62, 1972.

[27] M.J. Borden, M.A. Scott, J.A. Evans, and T.J.R. Hughes. Isogeometric finite element data structures based on Bézier extraction of NURBS. *International Journal for Numerical Methods in Engineering*, 87:15–47, 2011.

[28] B. Bourdin, G.A. Francfort, and J. Marigo. The Variational Approach to Fracture. *Journal of Elasticity*, 91:5–148, 2008.

[29] S.W. Bova and G.F. Carey. An entropy variable formulation and applications for the two-dimensional shallow water equations. *International Journal for Numerical Methods in Fluids*, 23:29–46, 1996.

[30] F. Boyer. A theoretical and numerical model for the study of incompressible mixture flows. *Computers and Fluids*, 31:41–68, 2002.

[31] J.U. Brackbill, D.B. Kothe, and C. Zemach. A Continuum Method for Modeling Surface Tension. *Journal of Computational Physics*, 100:335–354, 1992.

[32] C.E. Brennen. *Fundamentals of Multiphase Flows*. Cambridge University Press, 2005.

[33] H. Brenner. Navier-Stokes revisited. *Physica A: Statistical Mechanics and its Applications*, 349:60–132, 2005.

[34] A. Buffa, G. Sangalli, and R. Vazquez. Isogeometric analysis in electromagnetics: B-splines approximation. *Computer Methods in Applied Mechanics and Engineering*, 199:1143–1152, 2010.

[35] F.P. Bundy, W.A. Bassett, M.S. Weathers, R.J. Hemley, H.U. Mao, and A.F. Goncharov. The pressure-temperature phase and transformation diagram for carbon; updated through 1994. *Carbon*, 34:141–153, 1996.

[36] C. Burstedde, L.C. Wilcox, and O. Ghattas. `p4est`: Scalable algorithms for parallel adaptive mesh refinement on forests of octrees. *SIAM Journal on Scientific Computing*, 33:1103–1133, 2011.

[37] F.H. Busse. Non-linear properties of thermal convection. *Reports on Progress in Physics*, 41:1929–1967, 1978.

[38] L.A. Caffarelli and N.E. Muler. An L_∞ bound for solutions of the Cahn-Hilliard equation. *Archive for Rational Mechanics and Analysis*, 133:129–144, 1995.

[39] G. Caginalp and X. Chen. Convergence of the phase field model to its sharp interface limits. *European Journal of Applied Mathematics*, 9:417–445, 1998.

[40] J.W. Cahn. Free Energy of a Nonuniform System. II. Thermodynamic Basis. *Journal of Chemical Physics*, 30:1121–1124, 1958.

[41] J.W. Cahn and J.E. Hilliard. Free energy of a non-uniform system. I. Interfacial free energy. *The Journal of Chemical Physics*, 28:258–267, 1958.

[42] J.W. Cahn and J.E. Hilliard. Free Energy of a Nonuniform System. III. Nucleation in a Two-Component Incompressible Fluid. *The Journal of Chemical Physics*, 31:688–699, 1959.

[43] G. Carrington. *Basic Thermodynamics*. Oxford University Press, 1994.

[44] F. Chalot, T.J.R. Hughes, and F. Shakib. Symmetrization of conservation laws with entropy for high-temperature hypersonic computations. *Computing Systems in Engineering*, 1:495–521, 1990.

[45] C.K. Chan, F. Perrot, and D. Beyens. Effects of hydrodynamics on growth: Spinodal decomposition under uniform shear flow. *Physical Review Letters*, 61:412–415, 2008.

[46] Y.C. Chang, T.Y. Hou, B. Merriman, and S. Osher. A Level Set Formulation of Eulerian Interface Capturing Methods for Incompressible Fluid Flows. *Journal of Computational Physics*, 124:449–464, 1996.

[47] L.Q. Chen. Computer simulation of spinodal decomposition in ternary systems. *Acta Metallurgica et Materialia*, 42:3503–3513, 1994.

[48] L.Q. Chen. Phase-field models for microstructural evolution. *Annual Review of Materials Research*, 32:113–140, 2002.

[49] J. Chung and G.M. Hulbert. A time integration algorithm for structural dynamics with improved numerical dissipation: The generalized-α method. *Journal of Applied Mechanics*, 60:371–375, 1993.

[50] D.A. Cogswell. *A phase-field study of ternary multiphase microstructures*. PhD thesis, Massachusetts Institute of Technology, 2010.

[51] B.D. Coleman and W. Noll. The thermodynamics of elastic materials with heat conduction and viscosity. *Archive for Rational Mechanics and Analysis*, 13:167–178, 1963.

[52] J.A. Cottrell, T.J.R. Hughes, and Y. Bazilevs. *Isogeometric Analysis: Toward Integration of CAD and FEA*. Wiley, 2009.

[53] J.A. Cottrell, T.J.R. Hughes, and A. Reali. Studies of refinement and continuity in isogeometric analysis. *Computer Methods in Applied Mechanics and Engineering*, 196:4160–4183, 2007.

[54] J.A. Cottrell, A. Reali, Y. Bazilevs, and T.J.R. Hughes. Isogeometric analysis of structural vibrations. *Computer Methods in Applied Mechanics and Engineering*, 195:5257–5296, 2006.

[55] R. Courant and K.O. Friedrichs. *Supersonic Flow Shock Waves*. New York : Springer-Verlag, 1948.

[56] M.G. Cox. The numerical evaluation of B-splines. Technical report, National Physics Laboratory DNAC 4, 1971.

[57] V. Cristini, X. Li, J.S. Lowengrub, and S.M. Wise. Nonlinear simulations of solid tumor growth using a mixture model: invasion and branching. *Journal of Mathematical Biology*, 58:723–763, 2009.

[58] L. Cueto-Felgueroso and J. Peraire. A time-adaptive finite volume method for the Cahn-Hilliard and Kuramoto-Sivashinsky equations. *Journal of Computational Physics*, 227:9985–10017, 2008.

[59] R. Danchin and B. Desjardins. Existence of solutions for compressible fluid models of Korteweg type. *Annales de l'Institut Henri Poincare (C) Non Linear Analysis*, 18:97–133, 2001.

[60] L. Dedè, M.J. Borden, and T.J.R. Hughes. Isogeometric Analysis for Topology Optimization with a Phase Field Model. *Archives of Computational Methods in Engineering*, 19:427–465, 2012.

[61] D. Derks, D.G.A.L. Aarts, D. Bonn, and A. Imhof. Phase separating colloid polymer mixtures in shear flow. *Journal of Physics: Condensed Matter*, 20:412–416, 2008.

[62] J.L. Desmarais and J.G.M. Kuerten. Open boundary conditions for the Diffuse Interface Model in 1-D. *Journal of Computational Physics*, 263:393–418, 2014.

[63] V.K. Dhir. Boiling heat transfer. *Annual Review of Fluid Mechanics*, 30:365–401, 1998.

[64] V.K. Dhir. Mechanistic prediction of nucleate boiling heat transfer-achievable or a hopeless task? *Journal of Heat Transfer*, 128:1–12, 2006.

[65] V.K. Dhir, G.R. Warrier, and E. Aktinol. Numerical Simulation of Pool Boiling: A Review. *Journal of Heat Transfer*, 135:1–17, 2013.

[66] D. Diehl. *High Order Schemes for Simulation of Compressible Liquid-Vapor Flows with Phase Change*. PhD thesis, Albert-Ludwigs-Universitat Freiburg, 2007.

[67] H. Ding, P.D.M. Spelt, and C. Shu. Diffuse interface model for incompressible two-phase flows with large density ratios. *Journal of Computational Physics*, 226:2078–2095, 2007.

[68] C. Duan, R. Karnik, M.C. Lu, and A. Majumdar. Evaporation-induced cavitation in nanofluidic channels. *Proceedings of the National Academy of Sciences of the United States of America*, 109:3688–3693, 2012.

[69] J.E. Dunn and J. Serrin. On the thermomechanics of interstitial working. *Archive for Rational Mechanics and Analysis*, 88:95–133, 1985.

[70] S.C. Eisenstat, M.C. Gursky, M.H. Schultz, and A.H. Sherman. Yale sparse matrix package I: The symmetric codes. *International Journal for Numerical Methods in Engineering*, 18:1145–1151, 1982.

[71] C.M. Elliott and S. Zheng. On the Cahn-Hilliard Equation. *Archive for Rational Mechanics and Analysis*, 96:339–357, 1986.

[72] J.A. Evans. *Divergence-free B-spline discretizations for viscous incompressible flows*. PhD thesis, The University of Texas at Austin, 2011.

[73] J.A. Evans, Y. Bazilevs, I. Babuska, and T.J.R. Hughes. n-widths, sup-infs and optimality ratios for the k-version of the isogeometric finite element method. *Computer Methods in Applied Mechanics and Engineering*, 198:1726–1741, 2009.

[74] L.C. Evans. *Partial Differential Equations*. American Mathematical Society, 1998.

[75] D.J. Eyre. An unconditionally stable one-step scheme for gradient systems. www.math.utah.edu/eyre/research/methods/stable.ps.

[76] G. Faccanoni, S. Kokh, and G. Allaire. Approximation of liquid-vapor phase transition for compressible fluids with tabulated EOS. *Comptes Rendus Mathematique*, 348:473–478, 2010.

[77] E. Feireisl. Compressible Navier-Stokes equations with a non-monotone pressure law. *Journal of Differential Equations*, 184:97–108, 2002.

[78] P.C. Fife. Models for phase separation and their mathematics. *Electronic Journal of Differential Equations*, 48:1–26, 2000.

[79] P. Gennes, F. Brochard-Wyart, and D. Quere. *Capillarity and Wetting Phenomena: Drops, Bubbles, Pearls, Waves.* Springer, 2003.

[80] M.G. Gerritsen and L.J. Durlofsky. Modeling fluid flow in oil reservoirs. *Annual Review of Fluid Mechanics*, 37:211–238, 2005.

[81] J.W. Gibbs. On the equilibrium of heterogeneous substances. *American Journal of Science*, 96:441–458, 1878.

[82] J.W. Gibbs. *The collected works of J. Willard Gibbs.* Yale University Press, 1957.

[83] H. Gomez, V.M. Calo, Y. Bazilevs, and T.J.R. Hughes. Isogeometric analysis of the Cahn-Hilliard phase-field model. *Computer Methods in Applied Mechanics and Engineering*, 197:4333–4352, 2008.

[84] H. Gomez, L. Cueto-Felgueroso, and R. Juanes. Three-dimensional simulation of unstable gravity-driven infiltration of water into a porous medium. *Journal of Computational Physics*, 238:217–239, 2013.

[85] H. Gomez and T.J.R. Hughes. Provably unconditionally stable, second-order time-accurate, mixed variational methods for phase-field models. *Journal of Computational Physics*, 230(13):5310–5327, 2011.

[86] H. Gomez, T.J.R. Hughes, X. Nogueira, and V.M. Calo. Isogeometric anslysis of the isothermal Navier-Stokes-Korteweg equations. *Computer Methods in Applied Mechanics and Engineering*, 199:1828–1840, 2010.

[87] H. Gomez and J. Paris. Numerical Simulation of Asymptotic States of the Damped Kuramoto-Sivashinsky Equation. *Physical Review E*, 83:046702, 2011.

[88] H. Gomez, A. Reali, and G. Sangalli. Accurate, efficient, and (iso) geometrically flexible collocation methods for phase-field models. *Journal of Computational Physics*, 262:153–171, 2014.

[89] O. Gonzalez and A.M. Stuart. *A First Course in Comtinuum Mechanics.* Cambridge University Press, 2008.

[90] B. Gonzalez-Ferreiro, H. Gomez, and I. Romero. A thermodynamically consistent numerical method for a phase field model of solidification. *Communications in Nonlinear Science and Numerical Simulation*, 19:2309–2323, 2014.

[91] The HDF Group. Hierarchical data format version 5, 2000-2014.

[92] E.A. Guggenheim. *Mixtures: The Theory of the Equlibrium Properties of Some Simple Classes of Mixtures Solutions and Alloys*. Clarendon Press, 1952.

[93] M.E. Gurtin. On phase transitions with bulk, interfacial, and boundary energy. In *Analysis and Continuum Mechanics*, pages 429–450. Springer, 1989.

[94] M.E. Gurtin. Generalized Ginzburg-Landau and Cahn-Hilliard equations based on a microforce balance. *Physica D: Nonlinear Phenomena*, 92:178–192, 1996.

[95] M.E. Gurtin. On the plasticity of single crystals: free energy, microforces, plastic-strain gradients. *Journal of the Mechanics and Physics of Solids*, 48:898–1036, 2000.

[96] M.E. Gurtin, E. Fried, and L. Anand. *The Mechanics and Thermodynamics of Continua*. Cambridge University Press, 2009.

[97] M.E. Gurtin and H. Matano. On the structure of equilibrium phase transitions within the gradient theory of fluids. *Quarterly of Applied Mathematics*, 46:301–317, 1988.

[98] M.E. Gurtin, D. Polignone, and J. Vinals. Two-phase binary fluids and immiscible fluids described by an order parameter. *Mathematical Models and Methods in Applied Sciences*, 6:815, 1996.

[99] H. Haj-Hariri, Q. Shi, and A. Borhan. Thermocapillary motion of deformable drops at finite Reynolds and Marangoni numbers. *Physics of Fluids*, 9:845–855, 1997.

[100] A. Harten. On the symmetric form of systems of conservation laws with entropy. *Journal of Computational Physics*, 49:151–164, 1983.

[101] T. Hashimoto, K. Matsuzaka, E. Moses, and A. Onuki. String phase in phase-separating fluids under shear flow. *Physical Review Letters*, 74:126–129, 1995.

[102] H. Hattori and D. Li. Solutions for Two-Dimensional System for Materials of Korteweg Type. *SIAM Journal on Mathematical Analysis*, 25:85–98, 1994.

[103] A.J. Hawkins-Daarud. *Toward a Predictive Model of Tumor Growth.* PhD thesis, The University of Texas at Austin, 2011.

[104] A. Henderson. *ParaView Guide, A Parallel Visualization Application.* Kitware Inc., 2007.

[105] C.W. Hirt and B.D. Nichols. Volume of fluid (VOF) method for the dynamics of free boundaries. *Journal of Computational Physics*, 39:201–225, 1981.

[106] P.C. Hohenberg and B.I. Halperin. Theory of dynamic critical phenomena. *Reviews of Modern Physics*, 49:435–479, 1977.

[107] T.J.R. Hughes. *The Finite Element Method: Linear Static and Dynamic Finite Element Analysis.* Prentice Hall, Englewood Cliffs, NJ, 1987.

[108] T.J.R. Hughes, J.A. Cottrell, and Y. Bazilevs. Isogeometric analysis: CAD, finite elements, NURBS, exact geometry and mesh refinement. *Computer Methods in Applied Mechanics and Engineering*, 194:4135–4195, 2005.

[109] T.J.R. Hughes, L.P. Franca, and M. Mallet. A new finite element formulation for computational fluid dynamics: I. Symmetric forms of the compressible Euler and Navier-Stokes equations and the second law of thermodynamics. *Computer Methods in Applied Mechanics and Engineering*, 54(2):223–234, 1986.

[110] T.J.R. Hughes, G. Scovazzi, and T.E. Tezduyar. Stabilized Methods for Compressible Flows. *Journal of Scientific Computing*, 43:343–368, 2010.

[111] D. Jacqmin. Calculation of two-phase Navier-Stokes flows using phase-field modeling. *Journal of Computational Physics*, 155(1):96–127, 1999.

[112] D. Jacqmin. Contact-line dynamics of a diffuse fluid interface. *Journal of Fluid Mechanics*, 402:57–88, 2000.

[113] R.D. James. The propagation of phase boundaries in elastic bars. *Archive for Rational Mechanics and Analysis*, 73:125–158, 1980.

[114] D. Jamet, O. Lebaigue, N. Coutris, and J.M. Delhaye. The second gradient method for the direct numerical simulation of liquid-vapor flows with phase change. *Journal of Computational Physics*, 169:624–651, 2001.

[115] D. Jamet, D. Torres, and J.U. Brackbill. On the theory and computation of surface tension: The elimination of parasitic currents through energy conservation in the second-gradient method. *Journal of Computational Physics*, 182:262–276, 2002.

[116] K.E. Jansen, C.H. Whiting, and G.M. Hulbert. A generalized-α method for integrating the filtered Navier-Stokes equations with a stabilized finite element method. *Computer Methods in Applied Mechanics and Engineering*, 190:305–319, 2000.

[117] D.D. Joseph. Fluid dynamics of two miscible liquids with diffusion and gradient stresses. *European Journal of Mechanics - B/Fluids*, 9:565–596, 1990.

[118] D. Juric and G. Tryggvason. Computations of boiling flows. *International Journal of Multiphase Flow*, 24:387–410, 1998.

[119] A. Karma and W.J. Rappel. Quantitative phase-field modeling of dendritic growth in two and three dimensions. *Physical Review E*, 57:4323, 1998.

[120] G. Karypis and V. Kumar. A fast and highly quality multilevel scheme for partitioning irregular graphs. *SIAM Journal on Scientific Computing*, 20:359–392, 1999.

[121] G. Karypis and V. Kumar. Parallel multilevel k-way partitioning scheme for irregular graphs. *SIAM Review*, 41:278–300, 1999.

[122] C.E. Kees, I. Akkerman, M.W. Farthing, and Y. Bazilevs. A conservative level set method suitable for variable-order approximations and unstructured meshes. *Journal of Computational Physics*, 230:4536–4558, 2011.

[123] J. Kiendl, K.-U. Bletzinger, J. Linhard, and R. Wüchner. Isogeometric shell analysis with Kirchhoff-Love elements. *Computer Methods in Applied Mechanics and Engineering*, 198(49-52):3902–3914, 2009.

[124] J. Kim. Phase field computations for ternary fluid flows. *Computer Methods in Applied Mechanics and Engineering*, 196:4779–4788, 2007.

[125] J. Kim and J. Lowengrub. Phase field modeling and simulation of three-phase flows. *Interfaces and Free Boundaries*, 7:435–466, 2005.

[126] B.S. Kirk. *Adaptive Finite Element Simulation of Flow and Transport Applications on Parallel Computers*. PhD thesis, The University of Texas at Austin, 2007.

[127] D.J. Korteweg. Sur la forme que prennent les équations du mouvement des fluides si l'on tient compte des forces capillaires causées par des

variations de densité considérables mais continues et sur la théorie de la capillarité dans l'hypothèse d'une variation continue de la densité. *Arch. Néerl.*, 6(2):1–24, 1901.

[128] M. Kotschote. Strong solutions for a compressible fluid model of Korteweg type. *Annales de l'Institut Henri Poincare (C) Non Linear Analysis*, 25:679–696, 2008.

[129] G. Kuiper. *Cavitation inception on ship propeller models*. PhD thesis, Delft University of Technology, 1981.

[130] C.M. Landis. Fully coupled, multi-axial, symmetric constitutive laws for polycrystalline ferroelectric ceramics. *Journal of the Mechanics and Physics of Solids*, 50:127–152, 2002.

[131] P.D. Lax. *Hyperbolic Systems of Conservation Laws and the Mathematical Theory of Shock Waves*. SIAM, 1973.

[132] P.D. Lax and R.D. Richtmyer. Survey of the stability of linear finite difference equations. *Communications on Pure and Applied Mathematics*, 9:267–293, 1956.

[133] H.G. Lee and J. Kim. A second-order accurate non-linear difference scheme for the N-component Cahn-Hilliard system. *Physica A: Statistical Mechanics and its Applications*, 387:4787–4799, 2008.

[134] H.G. Lee, J.S. Lowengrub, and J. Goodman. Modeling pinchoff and reconnection in a Hele-Shaw cell. I. The models and their calibration. *Physics of Fluids*, 14:492–513, 2002.

[135] H.G. Lee, J.S. Lowengrub, and J. Goodman. Modeling pinchoff and reconnection in a Hele-Shaw cell. II. Analysis and simulation in the nonlinear regime. *Physics of Fluids*, 14:514–545, 2002.

[136] P.G. LeFloch. *Hyperbolic Systems of Conservation Laws. The theory of classical and nonclassical shock waves.* Birkhäuser, 2002.

[137] P.G. LeFloch and S. Mishra. Kinetic functions in magnetohydrodynamics with resistivity and hall effect. *Acta Mathematica Scientia*, 29:1684–1702, 2009.

[138] N. Leger and A. Vasseur. Relative entropy and the stability of shocks and contact discontinuities for systems of conservation laws with non BV perturbations. *Archive for Rational Mechanics and Analysis*, 201:271–302, 2011.

[139] R.J. Leveque. *Numerical Methods for Conservation Laws.* Birkhauser, 2005.

[140] S. Lipton, J.A. Evans, Y. Bazilevs, T. Elguedj, and T.J.R. Hughes. Robustness of isogeometric structural discretizations under severe mesh distortion. *Computer Methods in Applied Mechanics and Engineering*, 199:357–373, 2010.

[141] C. Liu and J. Shen. A phase field model for the mixture of two incompressible fluids and its approximation by a Fourier-spectral method. *Physica D: Nonlinear Phenomena*, 179:211–228, 2003.

[142] J. Liu, L. Dedè, J.A. Evans, M.J. Borden, and T.J.R. Hughes. Isogeometric Analysis of the Advective Cahn-Hilliard Equation: Spinodal Decomposition Under Shear Flow. *Journal of Computational Physics*, 242:321–350, 2013.

[143] J. Liu, H. Gomez, J.A. Evans, T.J.R. Hughes, and C.M. Landis. Functional Entropy Variables: A New Methodology for Deriving Thermodynamically Consistent Algorithms for Complex Fluids, with Particular Reference to the Isothermal Navier-Stokes-Korteweg Equations. *Journal of Computational Physics*, 248:47–86, 2013.

[144] T.P. Liu. The entropy condition and the admissibility of shocks. *Journal of Mathematical Analysis and Applications*, 53:78–98, 1976.

[145] J. Lowengrub and L. Truskinovsky. Quasi-incompressible Cahn-Hilliard fluids and topological transitions. *Proceedings of the Royal Society A*, 454:2617–2654, 1998.

[146] S. Luckhaus and L. Modica. The Gibbs-Thompson relation within the gradient theory of phase transitions. *Archive for Rational Mechanics and Analysis*, 107:71–83, 1989.

[147] A. Majda. *Compressible Fluid Flow and Systems of Conservation Laws in Several Space Variables.* Springer-Verlag, 1984.

[148] M. Maraldi, G.N. Wells, and L. Molari. Phase field model for coupled displacive and diffusive microstructural processes under thermal loading. *Journal of the Mechanics and Physics of Solids*, 59:1596–1612, 2011.

[149] J.L. McGrew, F.L. Bamford, and T.R. Rehm. Marangoni Flow: An Additional Mechanism in Boiling Heat Transfer. *Science*, 153:1106–1107, 1966.

[150] C.W. Meyer, G. Ahlers, and D.S. Cannel. Initial Stages of Pattern Formation in Rayleigh-Bénard Convection. *Physical Review Letters*, 59:1577–1580, 1987.

[151] C. Miehe, F.E. Hildebrand, and L. Böger. Mixed variational potentials and inherent symmetries of the Cahn-Hilliard theory of diffusive phase separation. *Proceedings of the Royal Society A: Mathematical, Physical and Engineering Science*, 470:1471–2946, 2014.

[152] K.C. Mills, B.J. Keene, R.F. Brooks, and A. Shirali. Marangoni effects in welding. *Philosophical Transactions of the Royal Society of London A*, 356:911–925, 1998.

[153] L. Modica. The gradient theory of phase transitions and the minimal interface criterion. *Archive for Rational Mechanics and Analysis*, 98:123–142, 1987.

337

[154] J.E. Morral and J.W. Cahn. Spinodal decomposition in ternary systems. *Acta Metallurgica*, 19:1037–1045, 1971.

[155] L.O. Naraigh and J. Thiffeault. Bubbles and filaments: Stirring a Cahn-Hilliard fluid. *Physical Review E*, 75:016216.1–016216.11, 2007.

[156] J.T. Oden, A. Hawkins, and S. Prudhomme. General diffuse-interface theories and an approach to predictive tumor growth modeling. *Mathematical Models and Methods in Applied Sciences*, 20:477–517, 2010.

[157] National Institute of Standards and Technology. Thermophysical Properties of Fluid Systems. http://webbook.nist.gov/chemistry/fluid/, 2012. [Online; accessed 15-July-2012].

[158] A. Onuki. Dynamic van der Waals Theory of Two-Phase Fluids in Heat Flow. *Physical Review Letters*, 94:054501, 2005.

[159] A. Onuki. Dynamic van der Waals theory. *Physical Review E*, 75:036304, 2007.

[160] A. Onuki and K. Kanatani. Droplet motion with phase change in a temperature gradient. *Physical Review E*, 72:066304, 2005.

[161] S. Osher and J.A. Sethian. Fronts Propagating with Curvature Dependent Speed: Algorithms Based on Hamilton-Jacobi Formulations. *Journal of Computational Physics*, 79:12–49, 1988.

[162] C. Polizzotto. Gradient elasticity and nonstandard boundary conditions. *International Journal of Solids and Structures*, 40:7399–7423, 2003.

[163] A. Quarteroni, R. Sacco, and F. Saleri. *Numerical Mathematics*. Springer-Verlag, Berlin, 2007.

[164] L. Ratke and P.W. Voorhees. *Growth and Coarsening: Ostwald Ripening in Material Processing*. Springer, 2002.

[165] W.M. Rohsenow. Boiling. *Annual Review of Fluid Mechanics*, 3:211–236, 1971.

[166] Y. Saad and M.H. Schultz. GMRES: A Generalized Minimal Residual Algorithm for Solving Nonsymmetric Linear Systems. *SIAM Journal on scientific and statistical computing*, 7:856–869, 1986.

[167] R. Scardovelli and S. Zaleski. DIRECT NUMERICAL SIMULATION OF FREE-SURFACE AND INTERFACIAL FLOW. *Annual Review of Fluid Mechanics*, 31:567–603, 1999.

[168] D. Schillinger, L. Dedè, M.A. Scott, J.A. Evans, M.J. Borden, E. Rank, and T.J.R. Hughes. An isogeometric design-through-analysis methodology based on adaptive hierarchical refinement of NURBS, immersed boundary methods, and T-spline CAD surfaces. *Computer Methods in Applied Mechanics and Engineering*, 249-252:116–150, 2012.

[169] D. Schillinger, J.A. Evans, A. Reali, M.A. Scott, and T.J.R. Hughes. Isogeometric collocation: Cost comparison with Galerkin methods and extension to adaptive hierarchical NURBS discretizations . *Computer Methods in Applied Mechanics and Engineering*, 267:170–232, 2013.

[170] D.V. Schroeder. *An introduction to thermal physics*. Robin J. Heyden, 2000.

[171] M.A. Scott. *T-splines as a Design-Through-Analysis Technology*. PhD thesis, The University of Texas at Austin, 2011.

[172] M.A. Scott, M.J. Borden, C.V. Verhoosel, T.W. Sederberg, and T.J.R. Hughes. Isogeometric Finite Element Data Structures based on Bézier Extraction of T-splines. *International Journal for Numerical Methods in Engineering,*, 88:126–156, 2011.

[173] L.E. Scriven and C.V. Sternling. The Marangoni effects. *Nature*, 187:186–188, 1960.

[174] T.W. Sederberg, J. Zheng, A. Bakenov, and A. Nasri. T-splines and T-NURCCs. In *ACM Transactions on Graphics*, 2003.

[175] J. Serrin. The Area Rule for Simple Fluid Phase Transitions. *Journal of Elasticity*, 90:129–159, 2008.

[176] J.A. Sethian and P. Smereka. Level Set Methods For Fluid Interfaces. *Annual Review of Fluid Mechanics*, 35:341–372, 2003.

[177] F. Shakib. *Finite element analysis of the compressible Euler and Navier-Stokes equations.* PhD thesis, Stanford University, 1989.

[178] F. Shakib, T.J.R. Hughes, and Z. Johan. A new finite element formulation for computational fluid dynamics: X. The compressible Euler and Navier-Stokes equations. *Computer Methods in Applied Mechanics and Engineering*, 89:141–219, 1991.

[179] A.K. Singhal, M.M. Athavale, H. Li, and Y. Jiang. Mathematical basis and validation of the full cavitation model. *Journal of Fluids Engineering*, 124:617–624, 2002.

[180] M. Slemrod. Admissibility criteria for propagating phase boundaries in a van der Waals fluid. *Archive for Rational Mechanics and Analysis*, 1983:301–315, 81.

[181] G. Son and V.K. Dhir. Numerical Simulation of Saturated Film Boiling on a Horizontal Surface. *Journal of Heat Transfer*, 119:525–533, 1997.

[182] G. Son and V.K. Dhir. Numerical simulation of nucleate boiling on a horizontal surface at high heat fluxes. *International Journal of Heat and Mass Transfer*, 51:2566–2582, 2008.

[183] O. Soriano-Vargas, E.O. Avila-Davila, V.M. Lopez-Hirata, N. Cayetano-Castro, and J.L. Gonzalez-Velazquez. Effect of spinodal decomposition on the mechanical behavior of Fe-Cr alloys. *Materials Science and Engineering: A*, 527:2910–2914, 2010.

341

[184] M.S. Spiegel. *A Stabilized Finite Element Formulation for Multiphase Fluid Flows.* PhD thesis, Stanford University, 2001.

[185] Y. Su and C.M. Landis. Continuum Thermodynamics of Ferroelectric Domain Evolution: Theory, Finite Element Implementation, and Application to Domain Wall Pinning. *Journal of the Mechanics and Physics of Solids*, 55:280–305, 2007.

[186] M.L. Szulczewski, C.W. MacMinn, H.J. Herzog, and R. Juanes. Lifetime of carbon capture and storage as a climate-change mitigation technology. *Proceedings of the National Academy of Sciences of the United States of America*, 109(14):5185–5189, 2012.

[187] E. Tadmor. Skew-selfadjoint form for systems for conservation laws. *Journal of Mathematical Analysis and Applications*, 103:428–442, 1984.

[188] T. Takacs and B. Jüttler. Existence of stiffness matrix integrals for singularly parameterized domains in isogeometric analysis. *Computer Methods in Applied Mechanics and Engineering*, 200:2568–3582, 2011.

[189] T. Tezduyar, S. Aliabadi, and M. Behr. Enhanced-discretization interface-capturing technique (EDICT) for computation of unsteady flows with interfaces. *Computer Methods in Applied Mechanics and Engineering*, 155:235–248, 1998.

[190] T.E. Tezduyar. Finite element methods for flow problems with moving boundaries and interfaces. *Archives of Computational Methods in*

Engineering, 8:83–130, 2001.

[191] A. K. Thakre, W.K. den Otter, J.T. Padding, and W.J. Briels. Spinodal decomposition of asymmetric binary fluids in a micro-Couette geometry simulated with molecular dynamics. *The Journal of Chemical Physics*, 129:074505, 2008.

[192] J. Thomson. On certain curious motions observable on the surfaces of wine and other alcoholic liquours. *Philosophical Magazine*, 10:330–333, 1855.

[193] S. Tremaine. On the origin of irregular structure in saturns rings. *Astronomical Journal*, 125:894–901, 2003.

[194] C. Truesdell and W. Noll. *The Non-Linear Field Theories of Mechanics.* Berlin, Heidelberg, New York: Springer, 1965.

[195] G. Tryggvason, B. Bunner, A. Esmaeeli, D. Juric, N. Al-Rawahi, W. Tauber, J. Han, S. Nas, and Y.J. Jan. A Front-Tracking Method for the Computations of Multiphase Flow. *Journal of Computational Physics*, 169:708–759, 2001.

[196] S.O. Unverdi and G. Tryggvason. A front-tracking method for viscous, incompressible, multi-fluid flows. *Journal of Computational Physics*, 100(1):25–37, 1992.

[197] S.P. van der Pijl, A. Segal, C. Vuik, and P. Wesseling. A mass-conserving Level-Set method for modelling of multi-phase flows. *International Journal for Numerical Methods in Fluids*, 47:339–361, 2005.

[198] J.D. van der Waals. The thermodynamic theory of capillarity under the hypothesis of a continuous variation of density. *Journal of Statistical Physics*, 20:200–244, 1979.

[199] K.G. van der Zee, J.T. Oden, S. Prudhomme, and A. Hawkins-Daarud. Goal-oriented error estimation for Cahn-Hilliard models of binary phase transition. *Numerical Methods for Partial Differential Equations*, 27:160–196, 2010.

[200] G. Vilanova, I. Colominas, and H. Gomez. Coupling of discrete random walks and continuous modeling for three-dimensional tumor-induced angiogenesis. *Computational Mechanics*, 53:449–464, 2014.

[201] A.J. Wagner and J.M. Yeomans. Phase separation under shear in two-dimensional binary fluids. *Physical Review E*, 59:4366–4373, 1999.

[202] S.W.J. Welch and J. Wilson. A Volume of Fluid Based Method for Fluid Flows with Phase Change. *Journal of Computational Physics*, 160:662–682, 2000.

[203] G.N. Wells, E. Kuhl, and K. Garikipati. A discontinuous Galerkin formulation for the Cahn-Hilliard equation. *Journal of Computational Physics*, 218:860–877, 2006.

[204] A.A. Wheeler, W.J. Boettinger, and G.B. McFadden. Phase-field model for isothermal phase transition in binary alloys. *Physical Review A*, 45:7424, 1992.

[205] O. Wodo and B. Ganapathysubramanian. Computationally efficient solution to the Cahn-Hilliard equation: Adaptive implicit time schemes, mesh sensitivity analysis and the 3D isoperimetric problem. *Journal of Computational Physics*, 630:6037–6060, 2011.

[206] A.J.M. Yang, P.D. Fleming, and J.H. Gibbs. Molecular theory of surface tension. *Journal of Chemical Physics*, 64:3732–3747, 1976.

[207] N.O. Young, J.S. Goldstein, and M.J. Block. The motion of bubbles in a vertical temperature gradient. *Journal of Fluid Mechanics*, 6:350–356, 1959.

[208] P. Yue, J.J. Feng, C. Liu, and J. Shen. A diffuse-interface method for simulating two-phase flows of complex fluids. *Journal of Fluid Mechanics*, 515:293–317, 2004.

[209] P. Yue, C. Zhou, and J.J. Feng. Sharp-interface limit of the Cahn-Hilliard model for moving contact lines. *Journal of Fluid Mechanics*, 645:279–294, 2010.

[210] S. Zhou and M.Y. Wang. Multimaterial structural topology optimization with a generalized Cahn-Hilliard model of multiphase transition. *Structural and Multidisciplinary Optimization*, 33:89–111, 2007.

Vita

Ju Liu received the Bachelor of Science degree in Computational Mathematics from Xi'an Jiaotong University in 2008. He immediately entered the Computational and Applied Mathematics program at the University of Texas at Austin under the supervision of Prof. T.J.R. Hughes. His graduate research work has been awarded the Robert J. Melosh medal from the Duke University in 2013. Upon completion of his doctoral degree, he will work as a postdoctoral fellow at the Institute for Computational Engineering and Sciences.

Permanent address: 3378A Lake Austin Blvd
                    Austin, Texas 78703

This dissertation was typeset with LaTeX[†] by the author.

[†]LaTeX is a document preparation system developed by Leslie Lamport as a special version of Donald Knuth's TeX Program.